Optoelectronic Devices with III-Nitride Nanostructures and Monolayer Heterostructures

by

Anthony Aiello

A dissertation submitted in partial fulfillment
of the requirements for the degree of
Doctor of Philosophy
(Electrical and Computer Engineering)
in The University of Michigan
2020

Doctoral Committee:

Professor Pallab Bhattacharya, Chair
Professor Rachel Goldman
Professor Zetian Mi
Professor Jamie Phillips

Anthony F. Aiello

afaiello@umich.edu

ORCID iD: 0000-0001-9663-4128

© Anthony F. Aiello 2020

To my parents

ACKNOWLEDGMENTS

I would first like to express my gratitude for the unwavering support from my parents and family, Mark, Roxanne, Gina, Jim, and my brother Paul. It is not easy being so far from your family all the time. Thank you for standing by my side. Also a special thanks to Dr. Pat Shea, Robert, and Kerstin for your support and friendship. I thank my advisor Professor Pallab Bhattacharya for his constant dedication to the field, motivation to keep moving forward, and providing some of the most advanced resources at my disposal that many universities lack. He has not only lent a great deal in scientific expertise and knowledge, but has helped to shape me into a stronger, more successful person. I am very fortunate to have him as an advisor.

I thank my committee members Prof. Rachel Goldman, Prof. Zetian Mi, and Prof. Jamie Phillips for their valuable comments and time. Prof. Mi has been especially helpful in overseeing our MBE facility and providing expertise where needed. A special thanks to Prof. Zunaid Baten, Prof. Dipankar Saha, Prof. Elaheh Ahmadi, Prof. Robert Hovden, and Prof. Emmanouil Kioupakis for their collaboration on research projects. They would not have been possible without your support.

I am grateful for the support and knowledge from my current and former group members and colleagues: Dr. Thomas Frost, Dr. Aniruddha Bhattacharya, Dr. Arnab Hazari, Dr. Saniya Deshpande, Dr. Zunaid Baten, Dr. Debabrata Das, Dr. Srinivas Vanka, Dr. Xianhe Liu, Dr. Ping Wang, David A. Laleyan, Ayush Pandey, and Yuanpeng Wu. A special thanks to my mentor Dr. Arnab Hazari and also to Dr. Thomas Frost for first introducing me to MBE, fabrication, and

characterization. Dr. Aniruddha Bhattacharya was especially helpful not only for his theoretical insight, but for being a good friend outside of work. David A. Laleyan was always available 24/7 for anything MBE-related and I thank him.

The Lurie Nanofabrication Facility has been instrumental in the success of my research. A special thanks to Dennis Schweiger for always being available and willing to help us on any problem or question we had in the facilities. He is truly a great asset to the program. I am also thankful for the guidance and technical assistance from Dr. Sandrine Martin, Dr. Pilar Herrera-Fierro, Brian Armstrong, Katharine Beach, Terre Briggs, Matthew Oonk, Kevin Owen, Vishva Ray, Tony Sebastian, Dave Sebastian, Steve Sostrom, and Shawn Wright. The LNF team is always there to provide us with state-of-the-art equipment and streamlined processes to make cutting-edge research possible at The University of Michigan.

I am grateful to Lisa Vogel, Elissa Trumbull, Anne Rhodes, Steven Pejuán, and Kristen Thornton for their administrative support throughout my doctoral career. I am also grateful for the financial support received from a Rackham Merit Fellowship, the Blue Sky Initiative program, and the Electrical Engineering and Computer Science (EECS) department. This work would not have been possible without the funding from these sources.

TABLE OF CONTENTS

LIST OF FIGURES

FIGURE

LIST OF TABLES

TABLE

LIST OF APPENDICES

APPENDIX

ABSTRACT

The III-Nitrides have emerged as a leading material group for a wide range of optoelectronic applications including but not limited to commercial solid-state lighting, plastic fiber communication, light detection, RF and high-power switching, deep-UV photonics, single photon sources for quantum computing and cryptography, and the study of exciton dynamics. The versatility of these materials allows them to be epitaxially-grown in bulk (3D), planar (2D), nanowire (1D), or quantum dot (0D) form by careful control of the growth conditions. The composition of the Al(Ga)N and In(Ga)N ternaries allows complete coverage of the deep-UV to IR spectrum. These materials can be grown on a wide range of substrates including free-standing GaN, sapphire, SiC, and silicon. Silicon is most economical and of interest for monolithic integration. However the large lattice mismatch ~17% with GaN requires careful strain engineering to prevent propagation of threading dislocations, which are detrimental to device operation.

In the present study, $Al_{0.56}Ga_{0.44}N/Al_{0.62}Ga_{0.38}N$ multi-quantum well (MQW) heterostructures grown, in collaboration, on GaN/sapphire templates are optically characterized via photoluminescence techniques. These MQW's emit ~280nm and can have obvious benefits in deep-UV applications. The interface roughness between the well/barrier layers is measured and modeled. InGaN/GaN dot-in-nanowires (DINWs) with varying In composition covering the green to IR range are grown on silicon and their optical response measured. High-gain photodetectors are then fabricated using green-emitting DINWs. The photoresponse is measured

and modeled using diffusion and drift theory. It is found that the primary gain of these detectors is due to the modulation of the conducting cross-section of the nanowires upon photoexcitation. InGaN/GaN self-organized quantum dots (QDs) are attractive for their low built-in polarization fields and defect densities, which translates to obvious benefits for lasers and LEDs (i.e. high T_0, low thresholds, decrease in droop, etc.). The ability to grow these QDs on silicon is attractive not just economically, but also for monolithic integration. Here, the growth of device-quality GaN over coalesced GaN nanowires on silicon is demonstrated. Photoluminescence characterization of the green-emitting InGaN/GaN QDs is presented and a LED is demonstrated with a low built-in polarization field ~50kV/cm. These quantum dots are then grown on GaN/sapphire substrates for pump-probe spectroscopy. Excited state absorption and ground state bleaching are observed, which has not been previously reported to our knowledge. The carrier relaxation is analyzed using transient absorption spectroscopy by colleagues at IIT Bombay and the results are discussed. Deep-UV emitting GaN/AlN monolayers are then grown, in collaboration with colleagues, within nanowires on silicon and in planar form as Al(Ga)N on GaN/sapphire for comparison. For the first time, large exciton binding energies ~200meV are measured in these GaN monolayers, in agreement with density functional theory (DFT) and many-body perturbation theory. These structures exhibit strong electron-hole wavefunction overlap and a unique temperature-dependent carrier redistribution that will be discussed. High exciton binding energies are attractive for exciton lasers and polariton devices, microcavities, and for the study of exciton dynamics in GaN to name a few. A deep-UV photodiode with detection from ~200-350nm is demonstrated using these monolayers and its results are presented.

CHAPTER I

Introduction

1.1 Optoelectronic Applications of III-Nitride Materials

The need for commercially-available and widespread use of electrical lighting was first realized in the early 19th century with the inventions of the arc lamp and incandescent lamp as the first electrically-powered light sources. It would take nearly another 100 years for the first visible semiconductor light-emitting diode (LED) to be created, which is credited to an early GaAsP design by Holonyak and Bevacqua working at General Electric in Syracuse, NY [1]. Though emission was centered in the red spectrum, it demonstrated that the LED design was feasible and research quickly expanded to find a solution for the generation of white light. This was typically done by optical pumping of phosphors, which began with fluorescent lamps. However, these are bulky, require a ballast and high-voltage power supply, are incapable of a wide range of color temperatures and luminosity, and are not environmentally-friendly. The solution to all of these problems was to use a semiconductor LED.

White light can be generated using LEDs by two methods. The first method was to use a combination of individual red, green, and blue LEDs. The material of choice in the 70's and 80's was the use of In(Ga)As- and InP-based structures. The problem was that there was no reliable method for the generation of blue light with an LED, in addition to issues with poor material quality and efficiencies. Therefore most of these LEDs remained on the red (warm) side of the spectrum. It wasn't until the 1990's that efficient, high-powered blue LEDs began to be

developed. Today, by far the most common method is the use of a blue LED to optically pump a phosphor coating which is encapsulated on top of the diode. This process is known as down-conversion. These two methods are shown schematically in Figure 1.1(a)-(b) respectively.

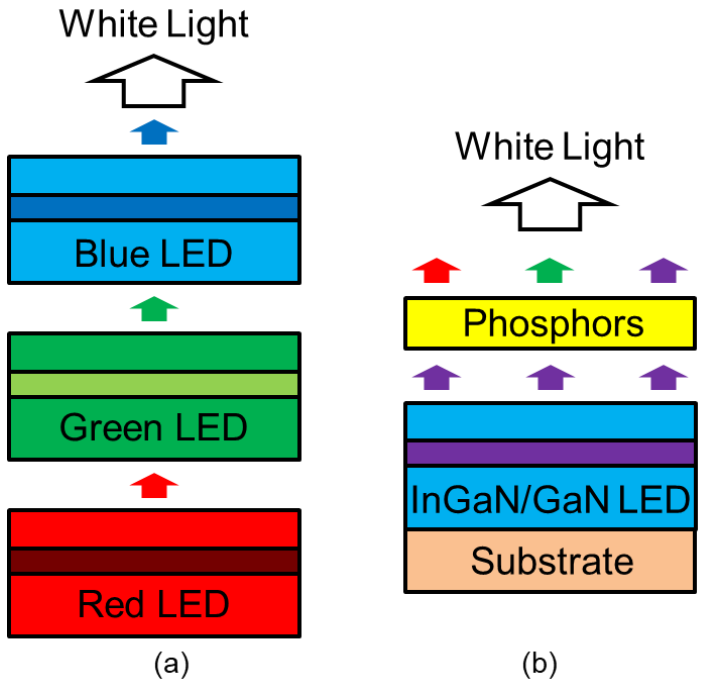

Figure 1.1 Illustration of white light generation using individual LEDs (a) and a blue LED to pump commercial phosphor (b).

The use of phosphor, such as YAG:Ce, requires additional processing steps. Different mixing (concentrations) of the phosphors must also be done to tune the chromaticity and color temperature. Generally, this is fixed for a single package. The phosphor generates a large amount of heat during pumping and the device must have sufficient thermal cooling. The phosphor is generally the lifetime limiter of the LED, although vast improvements in the recent decade have pushed these LED lifetimes to 10+ years. The first blue LED to accomplish this was fabricated from an InGaN/GaN quantum well heterostructure by Nakamura et al. [2]. This required improvements in the crystal quality of the epitaxial layers grown by metal organic vapor-phase

epitaxy (MOVPE) and the p-doping of GaN, which was pioneered heavily by Akasaki and Amano [3-4]. In 2014, Akasaki, Amano, and Nakamura were recognized for their achievements and were awarded The Nobel Prize in Physics. These early developments paved the way for further III-Nitride research into optoelectronic devices. Out of all the currently available semiconductor optoelectronic materials, the III-Nitrides are the only material system that can completely cover the UV-Infrared spectrum. This is shown in Figure 1.2. Al(Ga)N covers the 210-365 nm range and In(Ga)N can be used to cover the 365-1700 nm range. Boron Nitride (h-BH) is also a deep-UV emitter and a III-Nitride. This material however is beyond the scope of this dissertation.

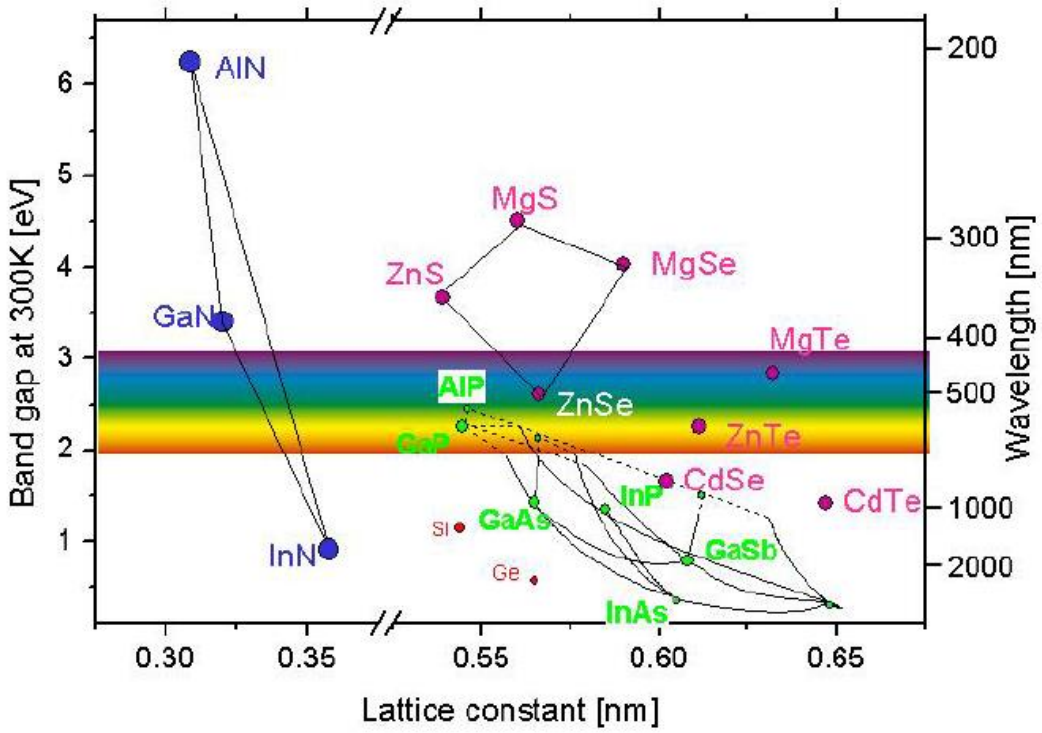

Figure 1.2 Band gap versus lattice constant for various semiconductor material systems. The III-Nitrides are the only system to cover the entire UV-Infrared range. Note that the band gap bowing parameters are not included in the III-Nitride plot [5].

This LED technology has allowed a rapid increase in performance compared to any other white light source technology. Shown in Figure 1.3(a) is the 2012 Technology Roadmap for Solid-State Lighting. Conventional incandescent and halogen sources range between 10-20 lm/W. Fluorescent lamps peak near ~120 lm/W. However these are beginning to be phased out due to environmental factors. In 2019, the luminous efficacy of commercially-available LEDs surpassed that of any other technology and was on track with the roadmap of Figure 1.3(a). The performance of some of these products are shown in Figure 1.3(b), surpassing 200 lm/W. Lumileds and OSRAM are two of the largest manufacturers of commercial LEDs.

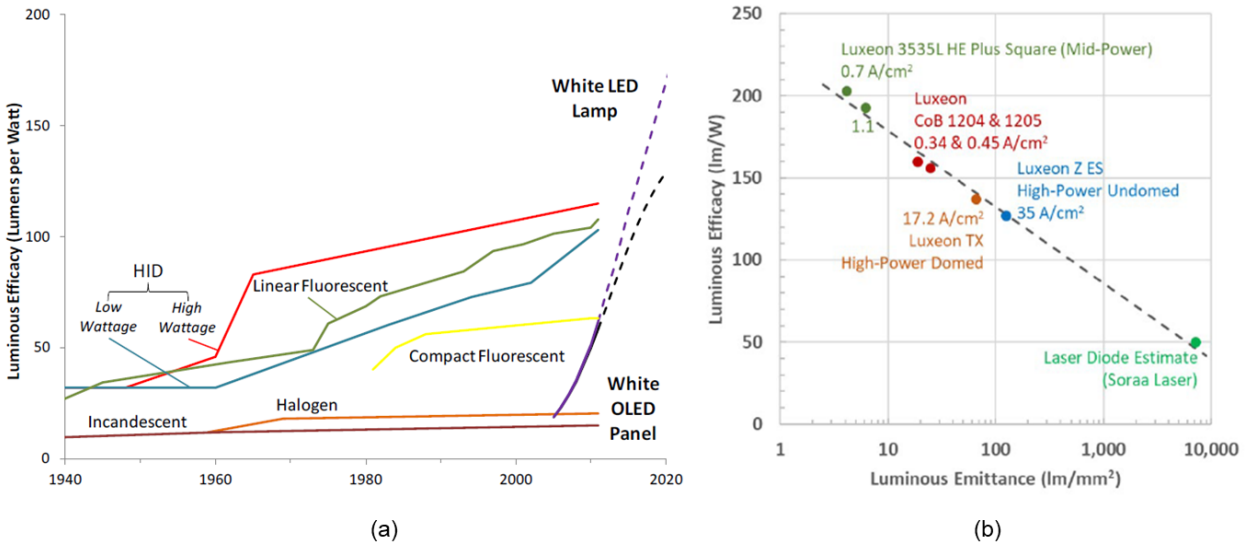

Figure 1.3 (a) 2012 U.S. Department of Energy Technology Roadmap for Solid-State Lighting showing the luminous efficacy of various light source technologies versus year. The dashed line is a prediction model [6]. (b) 2019 luminous efficacy versus luminous emittance for current state-of-the-art white LEDs [7].

Laser applications became the next stepping stone with III-Nitrides following the first InGaN/GaN quantum well (QW) laser emitting at ~410 nm by Nakamura's group [8]. Commercial blue lasers using this technology quickly found their place in optical data recording (i.e. Blu-ray), projectors, and medical applications. With the use of the Al(Ga)N alloy, the

wavelength could be extended into the ultraviolet for micromachining, advanced cosmetics, sterilization, as well as military use such as the detection of biological agents (i.e. anthrax). But the real challenge was extending the wavelength towards red. The first green InGaN/GaN QW laser emitting at 531 nm was developed on semi-polar GaN [9]. This was an attempt at solving the "green gap" problem, which will be discussed in section 1.2.3. However, the use of QWs to push past green remained a challenge for several reasons. The built-in polarization field becomes very high (~1-2 MV/cm) and thus the electron-hole wavefunction overlap suffers. This in turn causes a very high threshold current density as well as blue-shifting with injection due to the quantum confined Stark effect (QCSE). Further increasing the indium composition of the QW can cause clustering effects which degrade device performance. By adjusting the epitaxy conditions to grow InGaN/GaN quantum dots (QDs) rather than QWs, the polarization field could be reduced to < 100 kV/cm. In addition, defect densities could be mitigated as well due to the nature of strain relaxation of the QDs. Thus the first red-emitting InGaN/GaN QD laser was demonstrated [10]. The structure used seven periods of $In_{0.4}Ga_{0.6}N$/GaN QDs embedded within an $In_{0.02}Ga_{0.98}N$ waveguide and cladding using a combination of $In_{0.18}Al_{0.82}N$ (lattice-matched to GaN) and $Al_{0.07}Ga_{0.93}N$. This is shown in Figure 1.4(b). The average QD diameter and height are 37 nm and 5 nm respectively. An atomic-force microscopy (AFM) image is shown in Figure 1.4(b). The emission peaks at 630 nm and is shown in Figure 1.4(c).

GaN-based polariton lasers using microcavities were achieved at room temperature [11]. The ability to spontaneously generate coherent and monochromatic emission makes polariton lasers unique. The infrared wavelengths of 1.3 μm and 1.55 μm are of particular interest for long-haul communications. 1.3 μm has minimal dispersion in fiber while 1.55 μm exhibits the least absorption. GaAs- and InP-based systems remain the industry standard for this application.

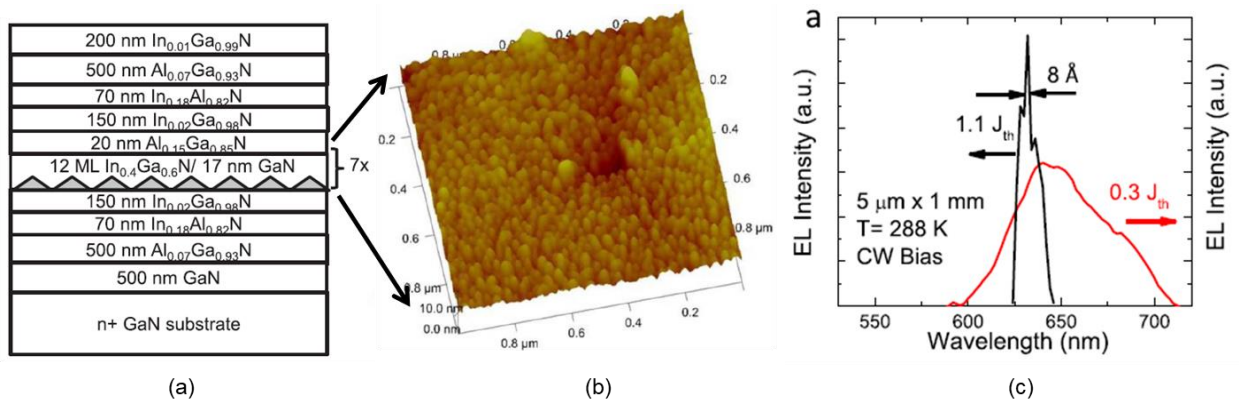

Figure 1.4 (a) InGaN/GaN QD laser heterostructure from [10], (b) AFM of an uncapped QD layer, and (c) spectral characteristics above and below threshold [10].

However, 1.3 μm lasing with InGaN/GaN disk-in-nanowire heterostructures on silicon has been shown which is of interest for silicon photonics and optical interconnects [12]. The III-Nitrides can also be used in UV-visible and infrared photodetectors. AlGaN can be used, for instance, in a metal-semiconductor-metal (MSM) structure with a cutoff wavelength up to 365 nm and noise equivalent powers comparable to GaP and Si photodiodes [13]. UV detection is necessary for certain communications that require UV light, flame detection, and ozone sensing to name a few. There is also interest to use In(Ga)N to extend detection into the infrared where use in communications, the military, and space are obvious. Currently, InAs/GaAs quantum dot infrared photodetectors (QDIPs) are being pursued for commercial infrared imaging alongside HgCdTe detectors. The QDIP design differs in that it relies on intraband transitions for the infrared absorption. These infrared detectors however are generally grown on non-silicon substrates and require a flip-chip bump bonding process to the CMOS readout circuitry. High-speed InGaAs detectors are currently the industry-standard for fiber-optic communications via 1.3 and 1.55 μm wavelengths. This material has also replaced germanium for most detection applications in this wavelength range due to better reliability and overall performance. However LN_2-cooled germanium detectors are still commonly used for radiation detection and

spectroscopy and still manufactured by companies such as Mirion, Ortec, and Teledyne Judson. Silicon is currently the industry-standard material for detection in the wavelength range of 200-1100nm and has generally replaced GaAsP due to better performance and substrate type. It can be found in a variety of device types such as PiN and avalanche photodiodes, simple photoconductors, and in CMOS CCD arrays for cameras and imaging applications and has noise-equivalent powers better than 10^{-15} $W/Hz^{1/2}$ and pA-range dark currents. Hamamatsu is one of the largest worldwide suppliers of these detectors, which can be found in various OEM solutions from companies such as Thorlabs, Newport, Horiba, and Teledyne. Vacuum tubes in the form of photomultiplier tubes and streak cameras are still common in spectroscopy due to their very high responsivity. Common photocathode materials include multialkali (S-20 nomenclature), Cs-based, GaAsP, as well as InGaAs. However, these are bulky, fragile, and generally require a separate high-voltage power supply module and optional cooling systems from thermoelectric coolers, water, or LN_2.

GaN in both N-polar and Ga-polar structures has found its way into high power and radio-frequency (RF) transistors, notably high electron mobility transistors (HEMTs) [14-16]. Though outside the scope of this dissertation as it is not an optoelectronic device, the recent technology should be mentioned as it is becoming a commercial standard for many high power and RF applications. They can be found in consumer power supplies, hybrid and battery-powered automobiles, and radar and power amplifiers operating beyond X-band frequencies. This is of particular interest to the military for use in various tactical aircraft.

1.2 Background of III-Nitrides

The research of III-Nitride development started ~30 years ago and there were many

challenges that the community faced before commercialization of any device could proceed. One of the earliest challenges was achieving high crystalline quality and efficient p-type doping in GaN. Planar heterostructures were also found to have very large built-in polarization fields, as previously mentioned. Devices such as lasers which require defect densities < 10^6 cm^{-2} are generally grown homoepitaxially, which can be costly, and large substrates >50 mm are generally unavailable. These materials can be grown on other substrates such as silicon and sapphire, however the growth must be carefully engineered to mitigate defect propagation from the substrate interface.

1.2.1 Polarization and Crystal Structure

Gallium nitride is stable in its wurtzite (hexagonal) crystal form. It can exist in an unstable zinc-blende (cubic) state similar to GaAs and InP if the epitaxy conditions are adjusted. However there is no real benefit of using zinc-blende GaN as the wurtzite form is of much higher crystalline quality and can be found in most, if not all, commercial GaN devices. The unit cell is shown in Figure 1.5(a) for a Ga-polar structure. The lattice constants along the c- and a-axis are 0.52 nm and 0.32 nm respectively. GaN is typically grown along the c-axis which is indicated by the [0001] arrow in Figure 1.5(a). For N-polar the convention would be $[000\bar{1}]$ and in this case the unit cell would be terminated by nitrogen atoms. Unlike many other material systems, the III-Nitrides are susceptible to built-in polarization fields which can reach the MV/cm range for planar heterostructures. As can be seen in the unit cell, there is an absence of inversion symmetry along the c-axis direction. In addition, there exists a large difference in electronegativity between the gallium and nitrogen atoms. This causes a spontaneous polarization to be present from the formation of a dipole moment.

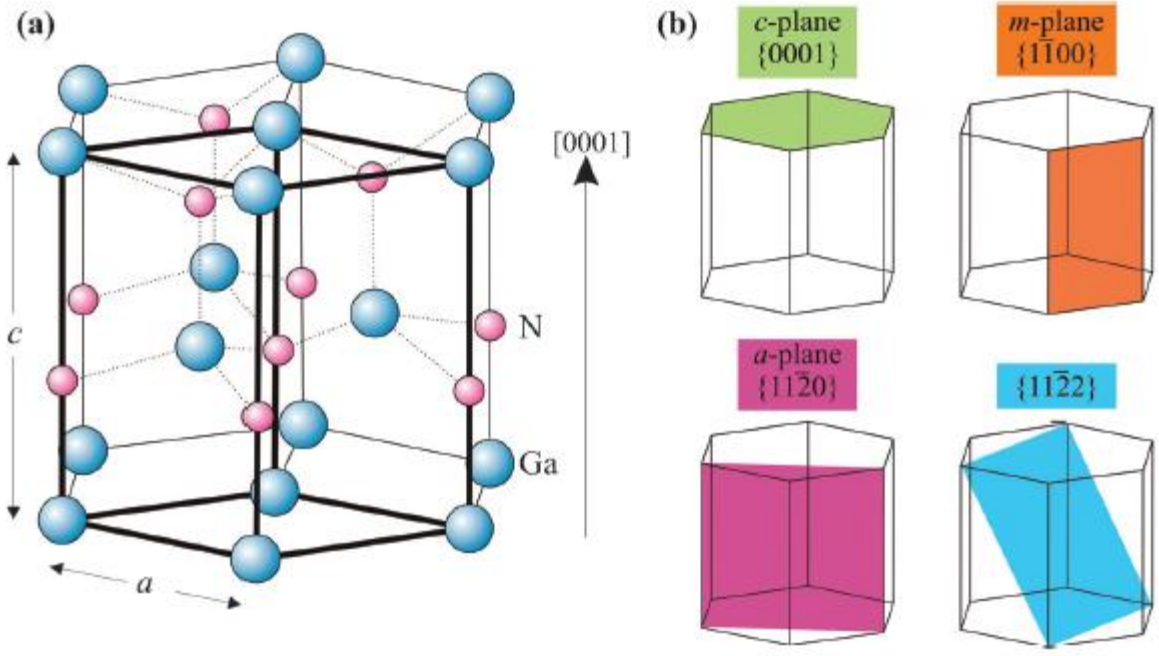

Figure 1.5 (a) Unit cell of gallium nitride grown along the c-axis in wurtzite form. (b) Schematic of the various crystallographic orientations which GaN can be grown [17].

In addition to the spontaneous component of the polarization, a piezoelectric force may also exist during the epitaxy of strained layers. If grown along the c-axis, it is the lattice constant along the a-axis direction that is responsible for tensile or compressive strain. For instance, the lattice constants along the a-axis for AlN and InN are 0.31nm and 0.35nm respectively. Thus the respective lattice mismatch is nearly 2% and 10% to GaN and is a primary reason why In(Ga)N exhibits larger polarization fields and clustering as the indium concentration is increased. The lattice mismatch of GaN to silicon is nearly 17%, which can make the growth of high quality epitaxial layers on silicon challenging. The high strain associated with In(Ga)N/GaN interfaces generally induces a larger polarization field than the spontaneous component and can adversely affect optoelectronic devices such as lasers and LEDs. A large amount of band-bending can exist throughout the device structure, resulting in poor electron-hole wavefunction overlap. This can cause problems such as high threshold current densities for lasers and a reduction in the overall

radiative efficiency, a primary challenge for reaching the infrared with III-Nitrides. A diagram of the conduction and valence bands for Ga-polar and N-polar AlGaN/GaN heterostructures is shown in Figure 1.6(a)-(b) respectively.

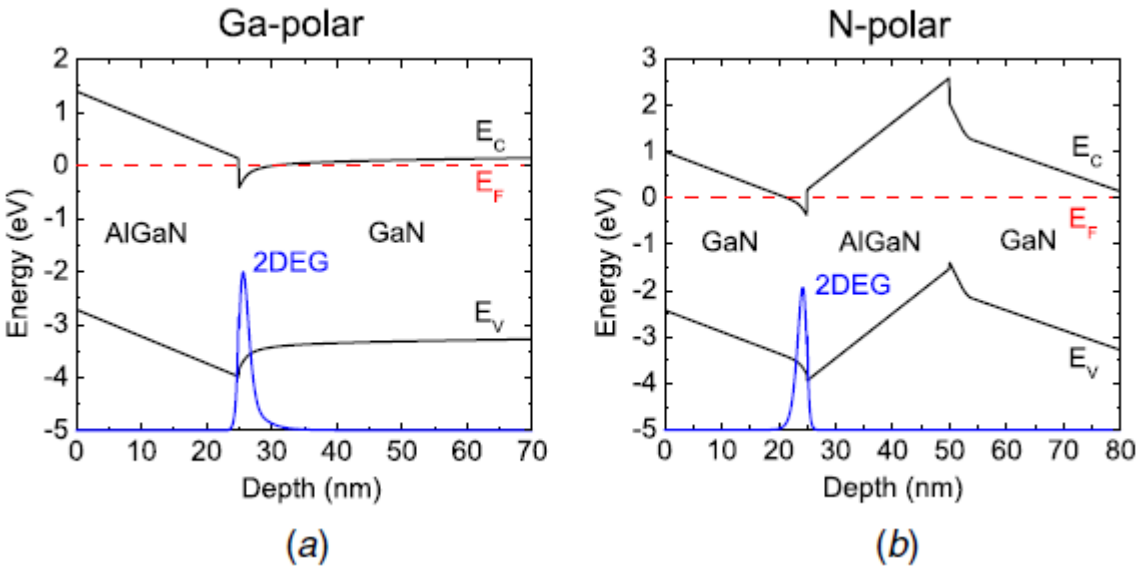

Figure 1.6 Conduction and valence bands of an AlGaN/GaN heterostructure under Ga-polar (a) and N-polar (b) conditions [16].

LED design generally incorporates an AlGaN electron blocking layer (EBL) to prevent the leakage of electrons past the active region. However, the band-banding as shown in Figure 1.6 can pull the EBL down, reducing its effect on blocking electrons, thus causing carrier leakage and a reduction in the external quantum efficiency (EQE) which can translate into droop, which will be discussed later. In addition, as the carrier injection is increased, this polarization field is screened, which reduces the band-bending and causes a blue-shift of the emission wavelength. This phenomenon is known as the quantum confined Stark effect, as previously mentioned, and causes wavelength stability concerns in lasers and LEDs.

There have been several attempts at mitigating or even completely eliminating the polarization field in these materials. One of the most common methods is to grow along different directions of the GaN lattice, which are shown in Figure 1.5(b) [9, 18]. Zero net polarization

exists along the m-plane and a-plane directions and a semi-polar structure exists if growth is done along the $[11\bar{2}2]$ direction. However, these substrates can be difficult to grow with extremely low defect densities, which is required for lasing and achieving population inversion, thus they can cause a reduction in the radiative efficiency. Another method is to take advantage of the epitaxial strain and grow quantum dots in a 3D growth mode rather than 2D, which has been shown to reduce the polarization field by orders of magnitude. These QDs can be grown on planar layers or embedded within GaN nanowires and this will be discussed.

1.2.2 P-doping

One of the main challenges facing epitaxial growth of device structures using III-Nitrides was the p-type doping of GaN-based material. In the early days of GaN research, metalorganic chemical vapor deposition (MOCVD) was the method of choice for crystal growth. However, the reactor chambers generally had high background concentrations of oxygen and hydrogen. Oxygen is incorporated into the GaN lattice alongside nitrogen vacancies which causes unintentional n-type doping. It is much easier to dope GaN with Si, as the activation energy is ~20 meV. The most common p-dopant however is Mg with an activation energy of ~200 meV. With hydrogen in the growth chamber, Mg-H complexes may form, causing additional difficulty in p-doping. Several breakthroughs in doping were achieved at the time which paved the way for laser and LED development [2-4]. A high hole concentration is required for proper carrier injection in such devices. Doping the material too high with Mg can invert the polarity of gallium nitride and cause excess defect formation. Another growth technique called plasma-assisted molecular beam epitaxy (PAMBE) was able to increase the hole concentration at least an order of magnitude compared to MOCVD. This is primarily due to the fact that growth can be

performed at lower temperatures ~700 °C for high quality GaN compared to temperatures in excess of 1000 °C. MBE chambers can also achieve ultrahigh vacuum pressures ~10^{-11} Torr, which is nearly free of impurities such as oxygen and hydrogen. High hole concentrations ~10^{18} cm^{-3} or better have been demonstrated using both Ga-rich conditions, such as with a metal modulation epitaxy technique, and N-rich conditions at lower growth temperatures and a high nitrogen overpressure [19-20].

1.2.3 "Green Gap"

From Figure 1.2, it is obvious that the only material system that can theoretically cover the UV-IR range are the III-Nitrides. The GaAs and InP families are restrained to the Red-IR range. By tuning the indium composition of In(Ga)N, high wavelengths can be achieved at the cost of the quantum efficiency. Increasing the indium composition greatly enhances the strain, polarization, and can also cause defect formation. This induces carrier leakage and delocalization as well as Auger recombination, which all translates to a reduction in the radiative efficiency. A plot of the EQE versus emission wavelength of various III-Nitride and $(Al_xGa_{1-x})_{0.52}In_{0.48}P$ high-power LEDs is shown in Figure 1.7. The drop in EQE between both material systems is centered in the green spectral range and this is known as the "green gap" in the optoelectronic community and is typically associated with planar and polar structures. As previously discussed, changing the growth mode or a different quantum structure such as QDs or using GaN of different polar orientations are ways to get around this problem. Some of the semipolar work from J. Speck's group at UCSB is included in Figure 1.7.

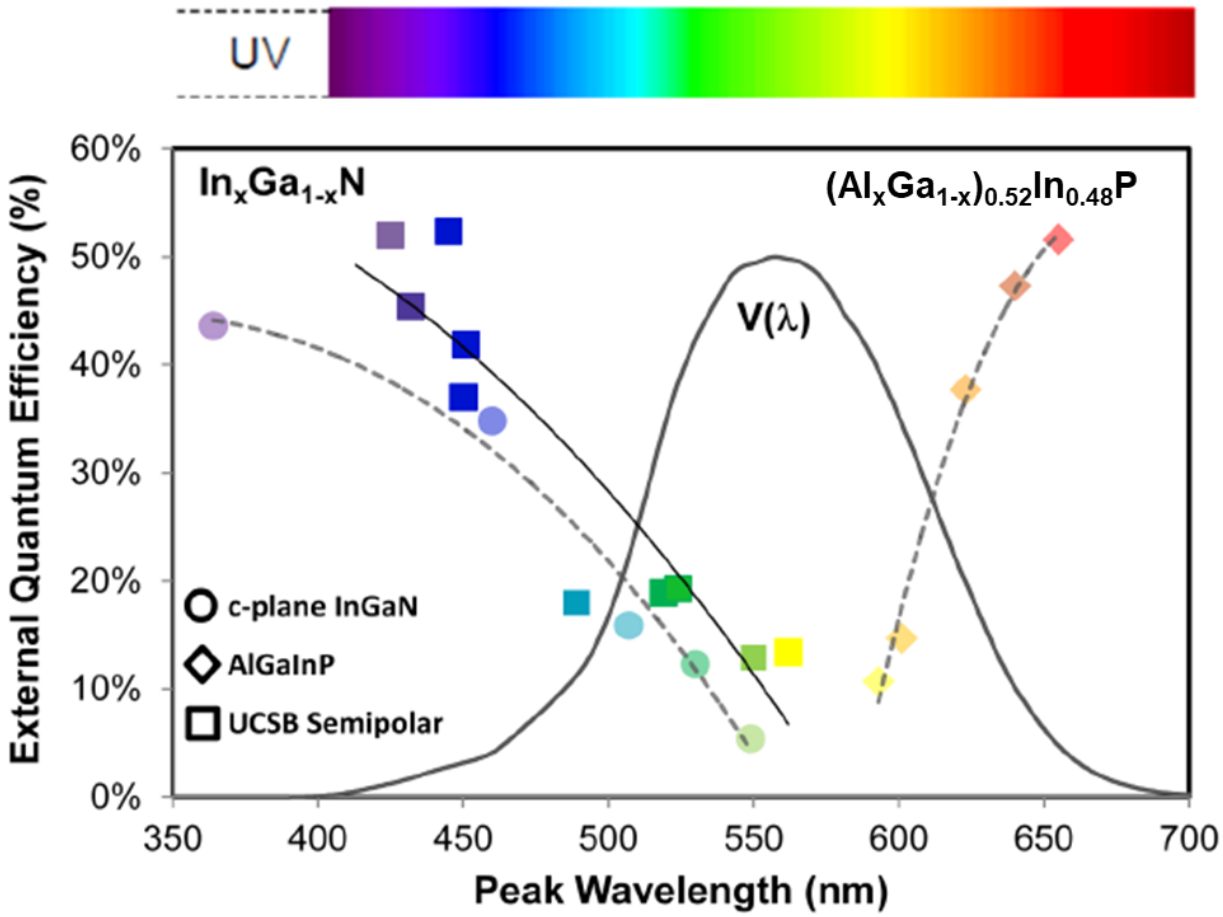

Figure 1.7 Measured EQE of various state-of-the-art high power visible LEDs from InGaN and AlGaInP. V(λ) is the luminous eye response from Commission Internationale de l'Éclairage (CIE). Adapted from [21].

Increasing the carrier injection often results in a reduction of the EQE at emission wavelengths above ~500 nm. This is known as droop and is most common among planar QW heterostructure LEDs, again due to high built-in polarization fields, Auger recombination, and carrier leakage. InGaN/GaN quantum dots have been shown to mitigate all of these effects.

1.2.4 Substrates

GaN-based structures can be grown on a wide range of substrates and the choice of substrate is typically dependent on the type of device required. Lasers require very low defect

densities $<10^6$ cm^{-2} and thus are typically grown homoepitaxially on free-standing GaN. These substrates are costly and are generally not found above 2" diameter wafers, which may pose a limitation on high production volumes. Free-standing GaN with a variety of doping and polarities are available from companies such as Kyma, NGK, Lumilog, Sumitomo, and Ammono. Silicon wafers can be used as substrates and are economical, available in a wide variety of wafer diameters, and are ideal for silicon photonics and monolithic integration. However the lattice mismatch is ~17% with GaN. Nanowires can be grown nearly defect-free on silicon. However if planar structures are desired, special techniques such as Al(Ga)N/GaN superlattices or In(Ga)N/GaN interfaces must be used to mitigate defect propagation and cracking, which can lead to defect-related Auger recombination. Lasers, LEDs, and detectors have all been demonstrated on silicon with III-Nitrides. Sapphire has a 3.4% lattice mismatch to GaN and GaN/sapphire templates grown by VPE are commercially available from many companies such as Kyma, Powerway Wafer, MSE, DOWA, and Nitride Semiconductors. These are acceptable for LEDs, but are generally not used for lasers since sapphire cannot be cleaved and dislocation densities can be ~10^8 cm^{-2} or higher. Silicon carbide is the other common substrate used in epitaxy with a 3.9% lattice mismatch. CREE is the largest supplier of commercial SiC substrates. GaN on SiC is also susceptible to high defect densities, but this can be mitigated with proper strain engineering. SiC offers excellent thermal conductivity for heat sinking and is available in semi-insulating substrates. It is currently the standard for commercial GaN power and RF devices.

1.3 Reaching the Deep-UV

The applications for deep-UV optoelectronics have been previously discussed. There are many ways to reach these wavelengths using the III-Nitrides. Hexagonal boron nitride can also

be used, however it will not be discussed here. Al(Ga)N MQW heterostructures are by far the most common method to achieve deep-UV electroluminescence (EL). Such a structure and its associated EL at various current injections is shown in Figure 1.8(a). These sub-300 nm wavelengths require a substantial increase in the aluminum concentration of the AlGaN ternary, and this can pose some challenges during epitaxy. Aluminum has a very high sticking coefficient and can cause issues such as interface roughness and clustering. It must be grown at high grown

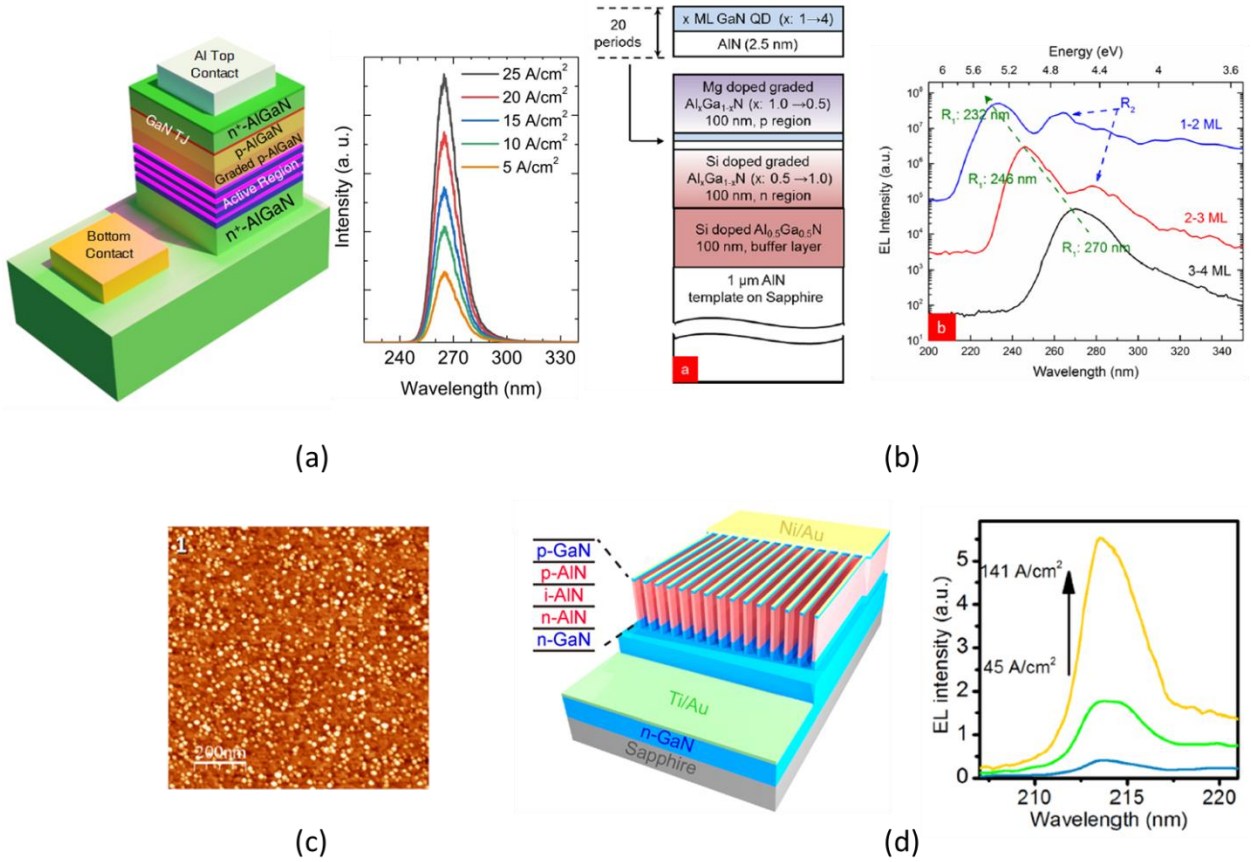

Figure 1.8 (a) Deep-UV ~265 nm multi-quantum well LED schematic and electroluminescence at various injections [22]. (b) Monolayer GaN/AlN LED schematic with 232-270 nm emission [23]. (c) AFM image of GaN/AlN quantum dots [24]. (d) Schematic of an AlN nanowall LED with 214 nm electroluminescence [25].

temperatures to maintain crystalline quality and is also more difficult to p-dope than GaN. Is has also been recently demonstrated, both theoretically and experimentally that GaN monolayers embedded in Al(Ga)N exhibit very large quantum confinement and high exciton binding

energies. Figure 1.8(b) demonstrates such an LED structure. These monolayers will be discussed in detail in Chapters 4-5 and can be grown in either planar or nanowire structures. GaN quantum dots grown on AlN can theoretically achieve deep-UV wavelengths from the associated quantum confinement and these have demonstrated. An AFM image of such QDs is shown in Figure 1.8(c). Other creative methods include electron-beam lithography and etching to define AlN nanowalls to achieve ~214 nm electroluminescence. An issue with AlN is that the emission is primarily directed perpendicular to the c-axis, opposite that of GaN and InGaN emission. This can make light extraction challenging. The use of AlGaN quantum wells will be further discussed in Chapter 2 with regards to material characterization followed by the characterization of GaN monolayers in Chapter 4 and monolayer photodiode characterization in Chapter 5.

1.4 Disk-in-Nanowires and Quantum Dots

Planar GaN layers epitaxially grown on silicon substrates are subject to very large defect densities and threading dislocations due to the large lattice mismatch that exists between GaN and silicon. There are various techniques to achieve device-quality GaN on silicon such as the use of Al(Ga)N/GaN superlattices and In(Ga)N which act as defect filters. However these growth techniques can be complex and time consuming, often requiring epitaxial thicknesses well over 1 μm, which can require a long growth time with PAMBE due to the slower growth rates compared to MOCVD and VPE systems. By adjusting the growth parameters to N-rich (i.e. III/V ratio < 1), GaN nanowires can be grown near defect-free on silicon in the Volmer-Weber growth mode. This occurs when a large lattice mismatch exists and causes the formation of 3D adatom islands. Under N-rich growth conditions, a thin ~2 nm thick amorphous Si_xN_y layer forms over the silicon first, which helps alleviate the strain before GaN growth. Once the 3D islands form,

impinging Ga adatoms are kinetically driven across the substrate surface and contribute primarily to axial growth along the c-axis. Adatoms impinging along the nanowire sidewalls are generally desorbed. Lowering the growth temperature can increase the radial growth rate and result in larger diameter nanowires. Too high a growth temperature and the Ga will only desorb from the surface. The growth rate is controlled by tuning the metal flux. A schematic of the nanowire growth is shown in Figure 1.9(a) and a phase diagram of the growth is shown in Figure 1.9(b) for nanocolumns (NC).

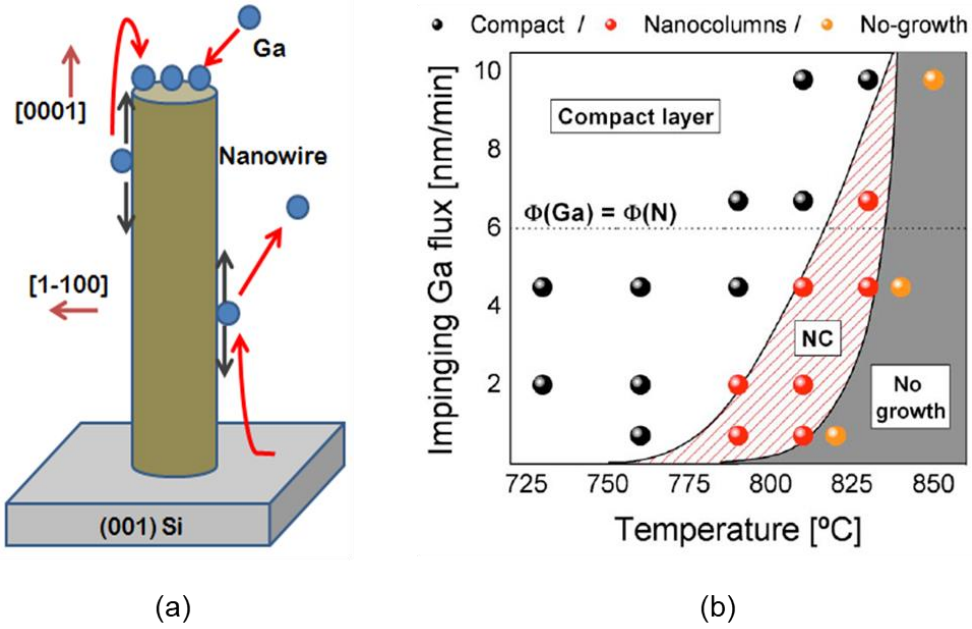

Figure 1.9 (a) Schematic of GaN nanowire Volmer-Weber growth on silicon demonstrating the various pathways of Ga adatoms [26]. (b) Phase diagram of GaN growth on (111) Si. The N flux is fixed at 6 nm/min [27].

A plan-view scanning electron microscopy (SEM) image of GaN nanowires grown along the c-axis under N-rich conditions is shown in Figure 1.10(a). A transmission electron microscopy (TEM) image showing the formation of the amorphous silicon nitride layer between silicon and GaN is shown in Figure 1.10(b). The large surface to volume ratio mitigates extended

defects compared to planar layers. There is also a lower built-in polarization field due to the radial relaxation of strain.

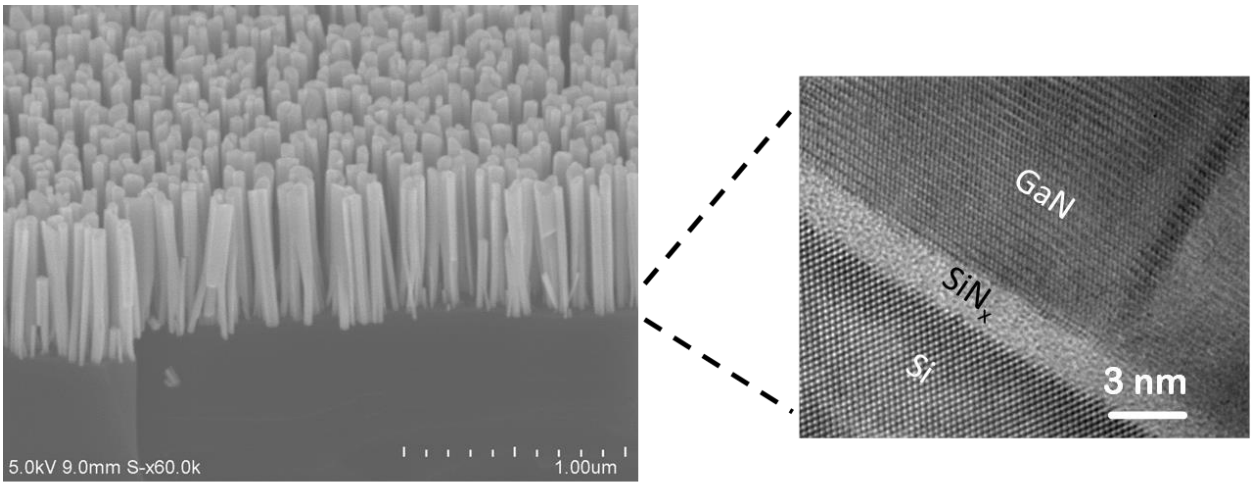

Figure 1.10 (a) Plan-view SEM image of self-assembled GaN nanowires grown on (001) silicon by PAMBE. (b) TEM image showing formation of silicon nitride layer between the silicon and GaN. Courtesy of Prof. Wei Guo.

To make light emitters across the visible spectrum, thin In(Ga)N disks can be inserted in these nanowires. Generally, the growth temperature is lowered to allow sufficient indium incorporation so the emission wavelength can be tuned. Inserting multiple periods of these disks separated by ~10 nm of GaN barriers increases the light output. These disk regions are typically 50-80 nm in diameter and 2-3 nm thick. Temperature-dependent photoluminescence (PL) of typical disk-in-nanowires (DINW) with 525 nm emission is shown in Figure 1.11(a) and the respective carrier lifetimes measured from time-resolved photoluminescence (TRPL) are plotted in Figure 1.11(b). A measured room-temperature transient is shown in the inset and these are analyzed with a stretched exponential. An increase of the radiative lifetime is observed, which is typically seen with InAs and InGaN quantum dots as a result of electron-hole scattering. TEM

imaging was performed to analyze these InGaN disk regions and this is shown in Figure 1.11(c). It was discovered that these InGaN regions form QDs rather than QW-like disks. This explained the nature of the radiative lifetime observed. The electron-hole scattering is schematically shown

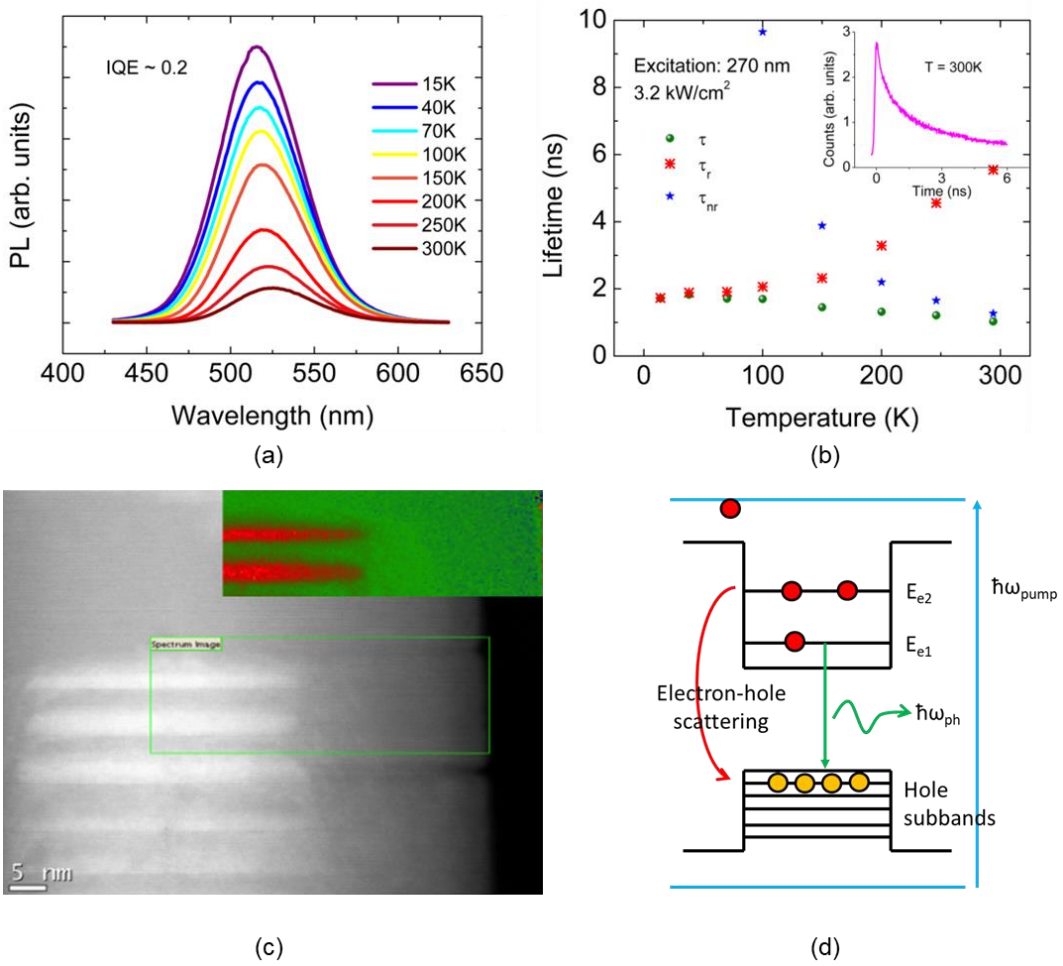

Figure 1.11 (a) Temperature-dependent PL of DINW emitting in the green. (b) Carrier lifetimes versus temperature measured from TRPL. Inset shows measured transient at 300 K. (c) TEM image of a single DINW showing formation of InGaN QDs [28]. (d) Schematic of electron-hole scattering mechanism in QDs.

in Figure 1.11(d). At cryogenic temperatures, cold holes sit at the ground state and electrons excited at higher states by a pump can scatter with these holes and relax to their ground state where they can recombine radiatively. However, as the temperature increases, some holes are thermally-excited to slightly higher states, leaving less holes to scatter with electrons. This

reduces the scattering rate, thus increasing the radiative lifetime. These DINWs have many of the benefits of QDs and several optoelectronic devices have been demonstrated with them.

InGaN/GaN self-assembled quantum dots form under the Stranski-Krastanov growth mode when a critical indium composition of 18% is reached. Initially, a 2D wetting layer several monolayers thick is grown, which then merges into 3D islands which form the QDs. These quantum dots generally only form under N-rich conditions and can easily be suppressed if the metal fluxes are too high, resulting in 2D growth. A phase diagram is shown in Figure 1.12 demonstrating the 2D-3D transition for GaN growth by PAMBE. For InGaN, the growth temperature will be shifted lower, but the process is very similar. The transition is monitored

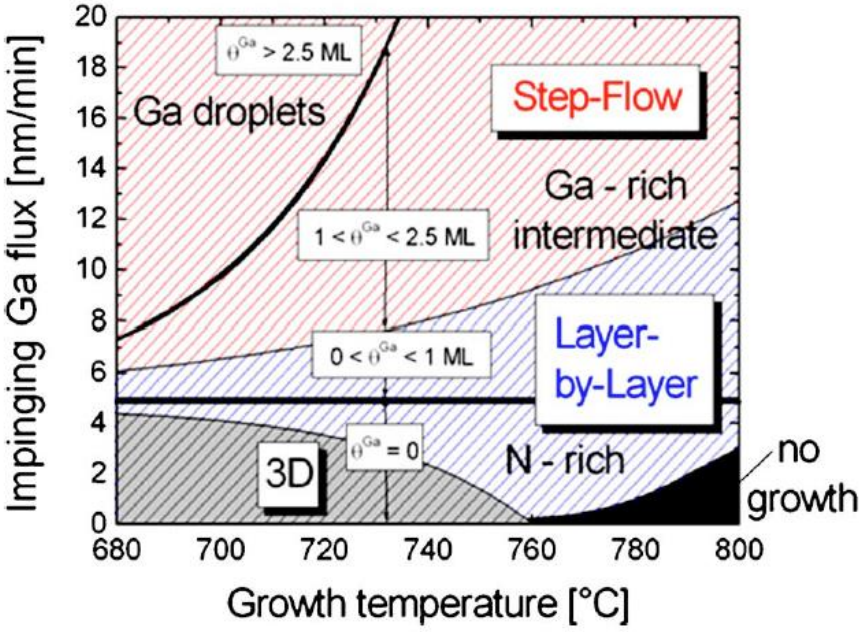

Figure 1.12 Growth diagram of GaN grown by PAMBE on GaN/sapphire substrates. N flux is held constant at 4.8 nm/min [29].

using a reflection high energy electron diffraction (RHEED) pattern. This will be further discussed in Chapter 2. But the transition is typically marked by a brightening of the RHEED Bragg spots and a spotty diffraction pattern.

The strain relaxation of the QDs results in a substantially reduced polarization field

which is beneficial to optoelectronic devices as previously mentioned. Even the In(Ga)As/Ga(Al)As system has taken advantage of QDs for use in state-of-the-art lasers, demonstrating reduced threshold current densities, wide wavelength tuning, improved modulation bandwidths, chirp, and linewidth enhancement factors. InGaN/GaN QDs have successfully shown emission in the red as in Figure 1.4 and their radiative properties are generally superior to their planar counterparts. They will be further discussed in later chapters.

1.5 Current Status of III-Nitride Photodetectors

Commercially-available Al(Ga)N- and In(Ga)N-based photodetectors can be most commonly found in a Schottky-type device structure from companies such as EOC, Luna, and Kyosemi. These devices are primarily grown out of quantum well and bulk heterostructures on GaN-compatible substrates and offer visible-blind detection down to the UV-C spectral range without the need of optical filters. These photodiodes offer similar responsivities compared to their silicon counterparts, dark currents as low as ~1 pA, and noise-equivalent powers ~10^{-17} $W/Hz^{1/2}$ which exceeds that of silicon. The Schottky device structure also allows them to be used in high-speed applications. In(Ga)N is used to extend detection past the UV-A band and into the 500 nm range. They are becoming popular in applications involving radiometry, UV detection and monitoring (i.e. sterilization lamp monitors), and various medical and military uses. In addition, PiN and avalanche photodiodes as well as NiN GaN-based photodetectors can be grown and fabricated. The use of nanowires allows these detectors to be grown on silicon substrates instead of GaN or SiC and can improve the overall gain of the detector. Chapters 4 and 5 will demonstrate UV-visible detection using such III-Nitride nanowire heterostructures on silicon.

1.6 Dissertation Overview

The primary focus of this dissertation is to examine various III-Nitride quantum structures grown by PAMBE. This includes AlGaN quantum well heterostructures, GaN/Al(Ga)N monolayer structures grown in planar form on AlN templates and in self-assembled nanowire form on silicon, InGaN/GaN disk-in-nanowires grown on silicon, and finally InGaN/GaN quantum dots grown on both planar GaN/silicon and GaN/sapphire substrates. TEM and SEM analysis will be presented throughout for characterizing the structural interfaces. X-ray diffraction analysis is also used to analyze the material composition and crystalline quality. Optical characterization is used extensively throughout this dissertation to present photoluminescence and time-resolved photoluminescence behavior of all the structures. Pump-probe transient absorption spectroscopy is used for the first time to analyze the carrier dynamics of InGaN/GaN quantum dots grown on GaN/sapphire substrates. Two types of devices are fabricated and their results presented. A visible-blind photodetector using InGaN/GaN DINWs is fabricated and electrically characterized. A deep-UV PiN photodiode using GaN/AlN monolayers embedded in nanowires on silicon is also demonstrated and characterized. Finally, an InGaN/GaN QD LED on a planar GaN/silicon substrate with emission ~480 nm is grown and fabricated and its results are presented.

Chapter 2 will first introduce a brief history of PAMBE and its use for III-Nitride crystal growth. Some of the mechanics and functionality of a typical system will be discussed as well as the benefits compared to MOCVD methods and how it is used today with regards to research and production. Growth techniques to achieve planar, nanowire, and quantum dot structures will be presented. Lastly, $Al_{0.56}Ga_{0.44}N/Al_{0.62}Ga_{0.38}N$ multi-quantum well heterostructures for deep-UV emitters will be optically and structurally characterized. In-depth TEM imaging will be presented

to compare measured interface roughness with that of a model constructed from measured photoluminescence data. The interface roughness of such structures in MBE can play an important role in the luminescence properties.

Chapter 3 presents the optical and structural characterization of GaN monolayers. Two types of structures are grown. One is a planar GaN/$Al_{0.65}Ga_{0.35}N$ heterostructure and the other is a self-assembled GaN nanowire array with 3 periods of GaN/AlN monolayers embedded within. TEM and SEM imaging indicates the existence of GaN monolayers. Theoretical calculations using many-body theory are performed to compare measured exciton binding energies of both structures to that of theory. Extensive microphotoluminescence and time-resolved measurements are analyzed. It is found that these structures exhibit very strong quantum confinement properties and high exciton binding energies exceeding 200 meV, which agree with theory. Such structures are of interest for deep-UV emitters/detectors and exciton devices.

Chapter 4 describes the growth of an $In_{0.42}Ga_{0.58}N$/GaN disk-in-nanowire photodetector structure grown on silicon. The photoluminescence of these disks peaks at 565 nm and the detector structure exhibits a strong photoresponse across the visible spectrum, with various peaks which are associated to the interband transitions within the disk regions. The measured photocurrent is analyzed and modeled. Two gain components are found which include the conventional gain due to recycling of carriers and a second component involving the modulation of the conducting cross-section of the nanowires, which dominates the gain. A peak responsivity and gain of 1450 A/W and ~10^3 is measured, respectively. The results are presented.

Chapter 5 demonstrates the use of GaN monolayers in nanowires grown on silicon as a photodiode structure. The GaN regions are grown at a thickness of 2 monolayers to enhance the light absorption. The diodes exhibit rectifying characteristics in the measured current-voltage

data. The monolayer photoluminescence peaks at ~280 nm and the device exhibits a strong deep-UV photoresponse. The quantum efficiency is presented and peaks at 0.6 % and the noise-equivalent power (NEP) is found to be $4.3 \times 10^{-11} W/Hz^{1/2}$. A high speed response measurement is performed using an acousto-optic modulator. The measured -3 dB bandwidth is found to be 120 kHz and likely limited by the RC time constant.

Chapter 6 discusses the epitaxial growth and characterization of InGaN/GaN quantum dots. These dots are first grown on a coalesced GaN nanowire buffer on silicon. They are characterized with temperature-dependent PL and TRPL as well as AFM. The peak of the luminescence is ~480 nm. An LED structure is then grown using this template and the measured electroluminescence agrees with the PL peak. A small blueshift of 2.4 nm is measured with increasing injection, which indicates a reduced polarization field compared to quantum wells. Droop is observed which can be attributed to defect-assisted Auger recombination. These devices demonstrate that InGaN/GaN can be grown over device-quality GaN/silicon. Similar $In_{0.27}Ga_{0.73}N$/GaN QDs grown on GaN/sapphire substrates are characterized with pump-probe spectroscopy. From the transient absorption measurements, ground state bleaching and excited state absorption are found to be characteristic mechanisms associated with the quantum dot states and barrier layers. The results are presented and discussed.

Chapter 7 concludes the present work and provides two possible future projects. GaN monolayers may be of interest as the gain media in an exciton laser due to the very high binding energy. Single-photon sources and detectors are important for applications involving space, spectroscopy, quantum computing, and quantum key distribution. A room-temperature single photon source using InGaN/GaN quantum dots on silicon may be of interest.

CHAPTER II

Epitaxial Growth and Interface Roughness in Al(Ga)N/Al(Ga)N Heterostructures

2.1 Introduction

A wide variety of crystal growth techniques exist that enable the realization of GaN-based semiconductor device technologies including optoelectronics and transistors. Recent decades have seen tremendous improvements in epitaxy system design, much of it due to the rapid acceleration of computers and integrated circuits. Epitaxy system users no longer had to manually control shutters and effusion cell power supplies throughout several hours of growth. A computer could run a custom recipe precisely and with repeatability. Effusion cell design became so well-vetted that molecular beam fluxes could be controlled to within a percent of a degree. Computer-aided design (CAD) allowed the production as well as simulation of MBE components (i.e. bearings, filaments, valves, heaters, crucibles, etc.) with extreme precision. And with this advancement of electronics came the availability of advanced RF plasma sources, which became the de facto standard for PAMBE, now a serious competitor to MOCVD. Each growth technique has its own advantages over the other with regards to parameters such as growth rate, substrate temperature, background impurities, in-situ monitoring, and p-doping efficiency. The history and use of PAMBE for III-Nitride growth will be briefly discussed. Methods of growing various heterostructures and nanostructures will be presented. A planar AlGaN/AlGaN quantum well heterostructure is grown and characterized optically and by TEM. The interface roughness is measured and analyzed, as previously published in [30].

2.2 Molecular Beam Epitaxy of III-Nitride Semiconductors

As discussed in Chapter 1, the III-Nitride material system can completely cover the bandgap range of ~0.6-6.2 eV as shown in Figure 2.1, which includes the bowing parameters. In addition, the $In_{0.18}Al_{0.82}N$ ternary provides a large refractive index difference with GaN while maintaining lattice-matching conditions. This is important for laser waveguide and cladding layers for mode confinement. GaN is also of interest for power and RF applications due to its high breakdown electric field and saturation velocity (3.3 MV/cm and $2.5x10^7$ cm/s respectively). PAMBE is of interest due to very sharp interfaces which can be obtained during

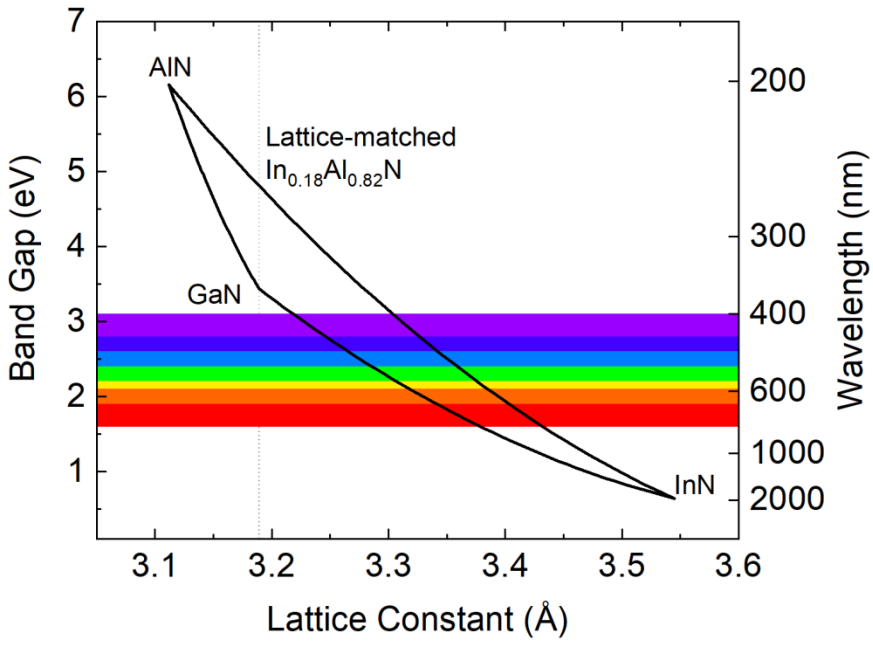

Figure 2.1 Bandgap versus a-plane lattice constant for the III-Nitrides.

growth in addition to ultralow impurity levels which enhance the device electrical characteristics. The lower growth temperatures associated with PAMBE provides the capability of obtaining higher concentrations of indium, especially important for visible-IR optoelectronics. However, these advantages are at a cost of having lower growth rates typically <1 μm/hr compared to that of MOCVD which can range ~50-100 μm/hr. Thus PAMBE is generally not chosen for

production and high volume work. Growth conditions and substrates can be altered to select Ga- or N-polar structures, though the majority of commercial devices are grown on the Ga-polar side. A photo of a Veeco GEN 930 PAMBE system at The University of Michigan is shown in Figure 2.2. This is a research-grade system, obvious from its floor size. Production systems are available, such as Veeco's GEN200 and GEN2000 systems, which can house two separate growth chambers and 4" or 6" substrate handling for maximum throughput. The crucibles are

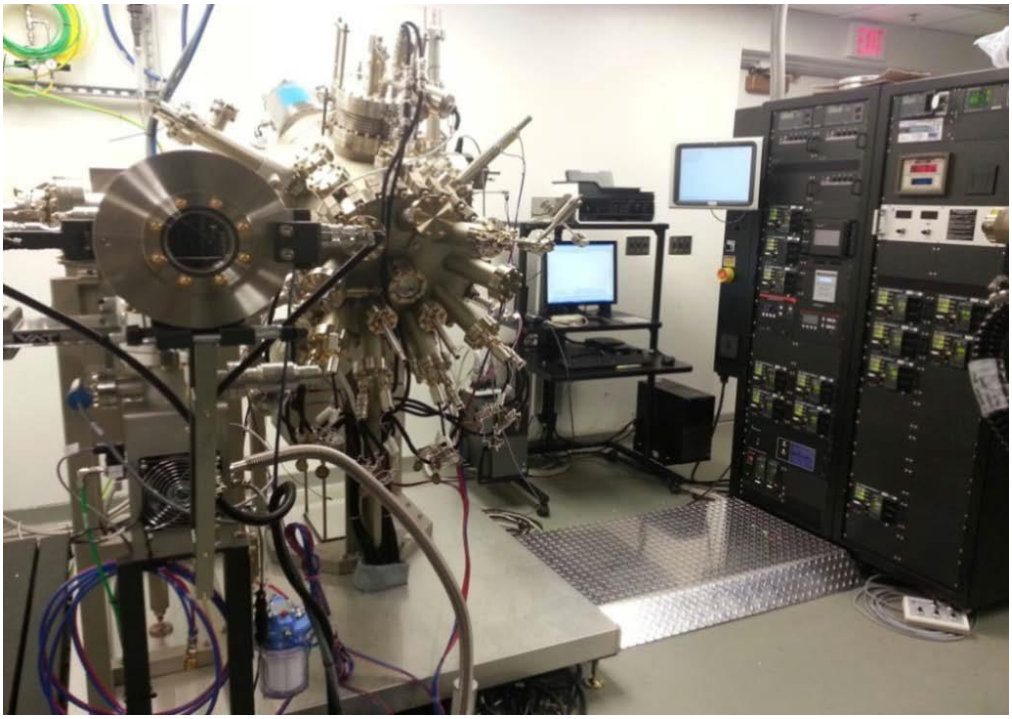

Figure 2.2 Veeco GEN930 PAMBE system.

generally much larger, up to ~10,000 g, to support longer campaigns and cell stabilities. Research-grade systems, such as the GEN930 3" capable system, have a single, low-volume growth chamber and much smaller capacity crucibles. Early systems were often manufactured by Varian, Perkin-Elmer, Riber, and various custom Japanese designs. Campaigns generally last ~1 year with everyday use. Prior to loading into the growth chamber, substrates must first undergo an intro bake in a separate chamber at ~200 °C to remove water vapor while being pumped by a

turbo-molecular pump backed by a dry pump. The substrates can then be transferred to a buffer chamber, sometimes called a preparation chamber, supported by an ion pump. A second bake to degas contaminants is performed at ~500 °C until the background pressure decreases to a stable value. Once this is complete, the substrate is ready for growth. The process of MBE itself can be thought of as a type of vacuum evaporation. Growth relies on a heated substrate and the sources alike under ultra-high vacuum (UHV). The sources are heated to obtain the desired vapor pressure and a shutter is translated clear of the cell aperture so that the molecular beam is directed towards the heated substrate, which is positioned at a distance well within the mean-free path length of the molecules. From there, the surface kinetics take over to govern the crystal growth. Due to the nature of the UHV environment associated with MBE, many in-situ measurements can be performed, such as RHEED and mass spectrometry. The III-Nitrides generally grow in wurtzite form along the c-axis as it is most kinetically stable. Zinc-blende GaN can be grown and is known to lack any built-in polarization field, which has obvious benefits [31]. But wurtzite GaN is typically of superior quality.

2.2.1 Brief History

The first published use of the term MBE is believed to be that by Al Cho and his colleagues in 1970 to differentiate their GaAs work from that of MOCVD and other methods [32]. Much of the earliest work on MBE was done at Plessey Labs, Bell Labs, and later IBM and other groups [33]. The earliest MBE research on III-Nitrides is largely attributed to groups such as that by Yoshida et al. in Japan in 1975 [34]. They reported AlN growth on sapphire substrates using reactive evaporation with ammonia. The real interest however, is the use of PAMBE. One of the earliest reports of this method comes from Robert Davis et al. working at North Carolina

State University in 1989 [35]. The active nitrogen species was generated by a plasma operating at 2.45 GHz. The nitrogen gas was supplied by the boil-off from liquid nitrogen stored in a dewar, not from a compressed gas tank housing ultrapure nitrogen more commonly used today. Nonetheless, this would become the standard method of PAMBE in the years to come.

2.2.2 The MBE System

Growth Chamber Layout

A simplified schematic of a typical PAMBE growth chamber is shown in Figure 2.3. These systems are capable of reaching background pressures ~10^{-11} Torr after a complete bake-out routine, which means ultralow impurity levels. Such low pressures allow the use of mass analyzers, such as a residual gas analyzer (RGA), to monitor impurities such as oxygen, hydrogen, and water. It will also detect helium, which is useful for leak checking after a system venting and bake-out. Chamber pumping is accomplished by a combination of a cryogenic pump, ion pump, as well as the liquid nitrogen cryo panels. Some systems are equipped with titanium sublimation pumps in addition to the above, as titanium is an excellent getter under UHV systems. The gate valve in Figure 2.3 connects to the preparation chamber (not shown) and allows for transfer of the substrate to the substrate manipulator, which is heated and can also rotate during growth to ensure uniformity. Mechanical feedthroughs for motion are generally magnetically coupled so that UHV pressures can be achieved. The effusion cells, also known as Knudsen cells (K-cells) are positioned facing the substrate. The crucibles are generally made of high-temperature materials such as pyrolytic boron nitride (pBN). Pneumatic shutters are put in place to rapidly impede the molecular beam, allowing for sharp interfaces. The RF plasma source provides active nitrogen species. The gas flow and plasma power are controlled for the desired

growth window. Some systems can also supply CBr_4 for carbon doping. The liquid nitrogen cryo panels trap unwanted impurities being outgassed from the sources, which aid in maintaining UHV. The most common method of measuring the beam fluxes is done by use of an ion gauge (beam flux monitor) positioned on the substrate manipulator, which is then indexed to the flux

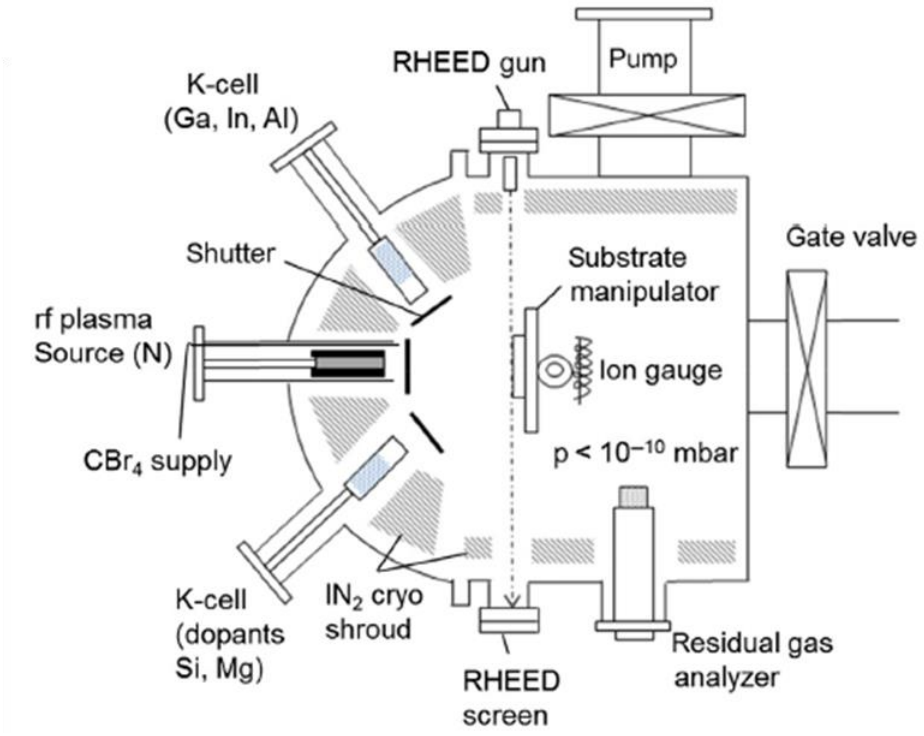

Figure 2.3 Cross-sectional schematic of a typical PAMBE system. Only the growth chamber is shown with two Knudsen cells (K-cells) for illustration [36].

measurement position. These flux measurements are system-specific and are known as beam equivalent pressures. A RHEED gun is an additional benefit of MBE for in-situ monitoring of the substrate surface. The reflected electron beam is directed at a phosphor screen for viewing by eye or with a camera.

The Plasma Source

A schematic of an RF plasma source is shown in Figure 2.4(a). A common operating

frequency for a MBE nitrogen plasma is 13.56 MHz. The plasma is typically generated within a pBN bulb, which must be replaced at regular intervals due to plasma etching. The cell requires water cooling due to the high RF power used (300-500 W) and a matching network minimizes the reflected power. Some manufacturers include deflection plates to prevent unwanted electrons and ions from reaching the substrate. By adjusting the nitrogen flow and plasma power, the growth rate can be tuned as shown in Figure 2.4(b). Gas is supplied by regulated ultrapure >99.999% ("5 nines") nitrogen.

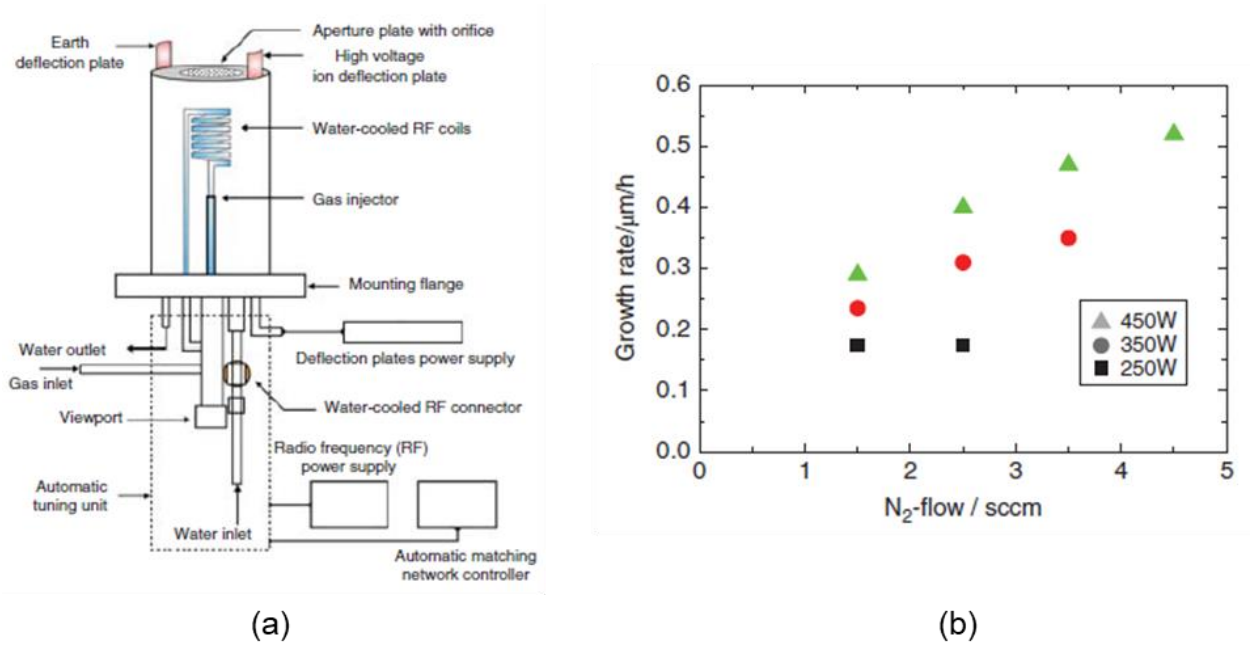

Figure 2.4 (a) Schematic of a typical RF plasma source and (b) growth rate as a function of gas flow and plasma power. A Veeco Unibulb source was used [33].

Substrate Temperature

The actual growth temperature at the substrate surface can differ from the thermocouple reading at the heater side by as much as 100 °C. Many MBE systems are equipped with infrared pyrometers, such as the Ircon Modline series in the GEN930 system. They are generally positioned in line with the substrate during growth. A window that is transparent to IR is positioned in-between. The correct emissivity value of the substrate must be known for accurate

readings. In addition, radiation from the effusion sources and substrate heater filament could cause inaccuracies. It is often common to calibrate the pyrometer reading to that of the 1x1 to 7x7 reconstruction of (111) silicon, visible by RHEED on a clean, oxide-free wafer. This occurs at ~860 °C [37]. Growth temperature calibration can also be done using the melting point of metals, alloying temperature, and the associated surface reconstruction. Aluminum is commonly used for this method by evaporating Al onto a silicon substrate in the growth chamber and monitoring the RHEED pattern for alloying at ~577 °C.

2.3 Epitaxial Techniques

III-Nitrides can be grown in all dimensions using PAMBE from bulk to various quantum-confined structures. 2D layer growth will first be briefly discussed, followed by 1D nanowire growth on silicon and finally 0D quantum dot growth on GaN/sapphire substrates. RHEED monitoring is the most important tool for the crystal grower while targeting these various growth regions.

2.3.1 Epitaxial Layers

Smooth, defect-free planar layers are best achieved right beneath the boundary of the Ga droplet region, as shown in Figure 1.12. Excess Ga will build up on the surface above this boundary, causing micron-size Ga droplets to form on the surface, which can impede growth underneath he droplets and lead to a large number of dislocations. Periodic interruptions ~5-10 sec in duration, generally in the absence of metal and nitrogen flux, are performed to clear the surface of excess metal buildup. The RHEED is remains dim and streaky. As growth moves more nitrogen-rich within the intermediate boundary, the Ga adatom mobility begins to decrease. A Ga

adlayer acting as a wetting layer is constantly present on the surface, but is not enough to cause droplet formation. RHEED patterns get brighter as the conditions become more N-rich. Under metal-rich conditions, only the 1x1 pattern is seen for Ga-polar growth as shown in Figure 2.5(a). As the conditions move more N-rich, the 2x2 pattern becomes visible as shown in Figure 2.5(b). If a sufficiently high Mg flux is added, the polarity may invert. Shown in Figure 2.5(c) is the 6x6 N-polar GaN RHEED pattern after the polarity is inverted from a large Mg concentration. An AFM image of smooth, pit-free Ga-polar GaN grown on a GaN/sapphire substrate is shown in Figure 2.5(d).

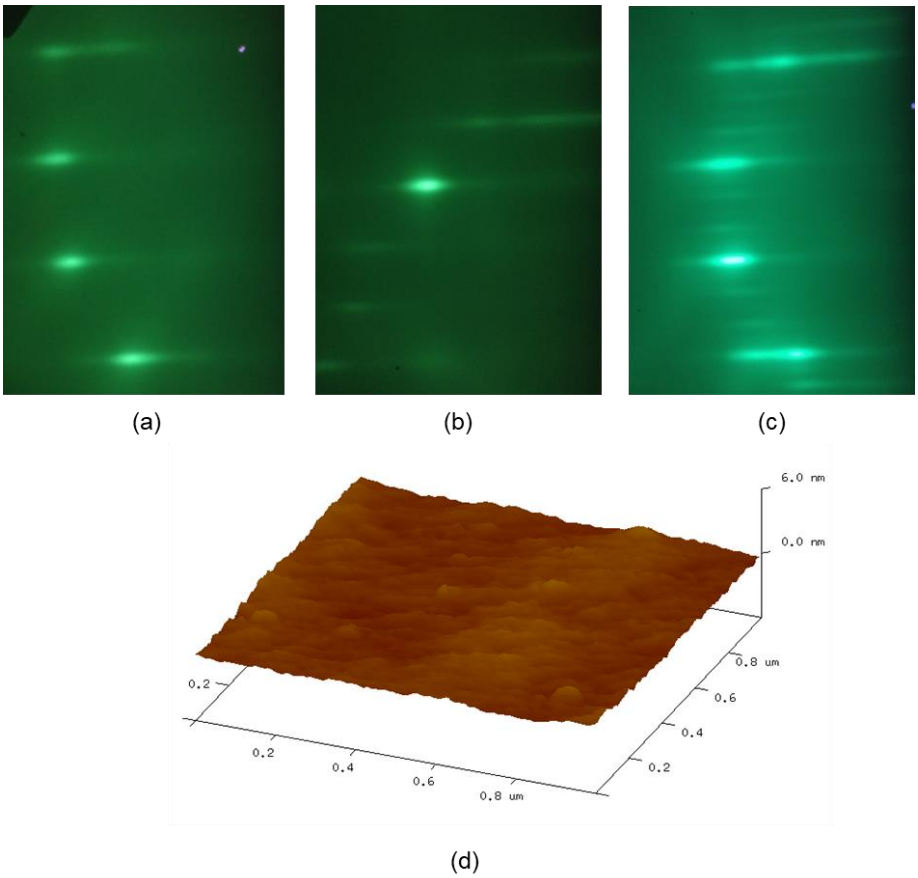

Figure 2.5 (a) 1x1 RHEED pattern of GaN under Ga-rich conditions. (b) 2x2 RHEED pattern under N-rich conditions. (c) 6x6 pattern of N-polar GaN after polarity inversion from Mg. (d) AFM of GaN grown under metal-rich conditions demonstrating smooth morphology.

The RHEED intensity also varies as the growth transitions between the different modes of Figure 1.12. When a CCD camera is mounted at the RHEED screen, the intensity can be monitored as a function of time. In the Ga-rich region when more than one monolayer (ML) of Ga exists on the surface, the RHEED intensity decreases and the pattern remains dim and streaky. In the layer-by-layer growth mode, <1 ML of Ga coverage is maintained on the surface and multiple RHEED intensity oscillations can be observed, where one period equals 0.5 ML of growth. As the III/V ratio continues to decrease << 1, growth transitions to a 3D mode, characterized by a rough surface due to low adatom mobility and a bright and spotty RHEED pattern. These RHEED intensity patterns are shown in Figure 2.6.

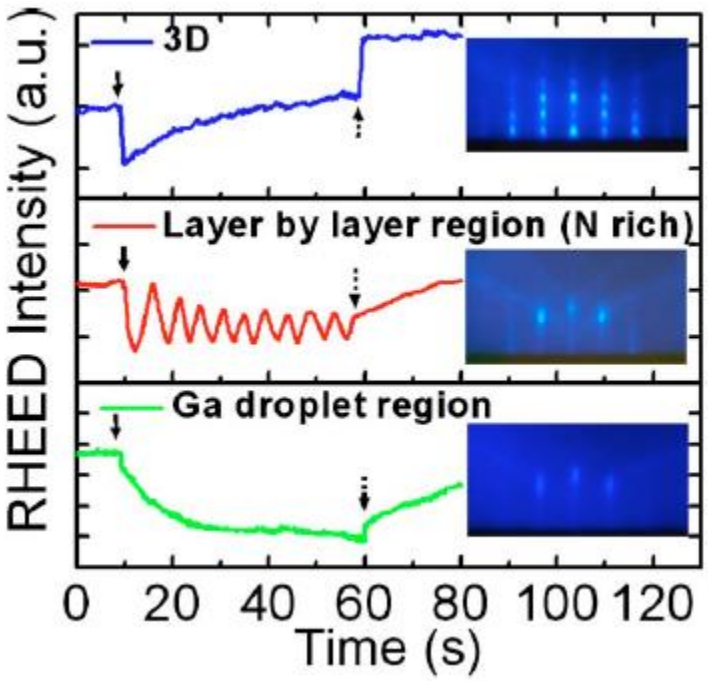

Figure 2.6 RHEED intensity versus time under various growth conditions. Insets show the respective RHEED pattern. Growth done on a Veeco GEN2 system at The University of Michigan [20].

2.3.2 Nanowires on Silicon

Self-assembled 1D GaN nanowires can be grown defect-free on silicon in the Volmer-Weber growth mode under the large lattice mismatch. The growth kinetics were described in Chapter 1 and shown in Figure 1.9. They are generally grown under N-rich conditions (i.e. 400W and 1 sccm) and at a higher temperature of ~800 °C to limit the surface mobility but enhance the axial growth rate. InGaN/GaN disks can be inserted at a lower growth temperature ~600 °C for light emitters/detectors. They grow along the c-axis and have hexagonal faces. A plan-view and top-view SEM image is shown in Figure 2.7 (a) and (b) respectively of disk-in-nanowires grown on (001) silicon. The RHEED pattern during nanowire growth is typically semicircular and spotty as shown in Figure 2.7(c).

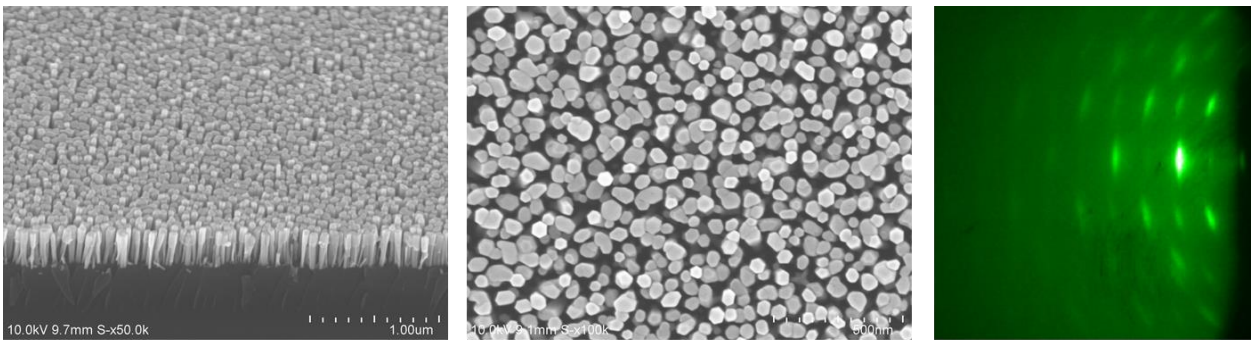

Figure 2.7 (a) Plan-view SEM image at 45° of InGaN/GaN disk-in-nanowires. (b) Top-view SEM image of the nanowires. (c) RHEED pattern during nanowire growth.

2.3.3 Self-Organized Quantum Dots

Self-organized InGaN/GaN quantum dots grow in the Stranski-Krastanov growth mode under slightly N-rich conditions when the indium concentration exceeds 18% when grown over GaN. The thickness of the initial 2D wetting layer depends on the indium composition, which can be as low as ~3 ML for a high indium concentration or ~10 ML for a lesser concentration. During the wetting layer, RHEED oscillations can be observed, which can be used to determine

the thickness and growth rate. Once the critical thickness is reached for the 2D-3D transition, the RHEED intensity increases and then saturates. The RHEED pattern itself will become a spotty 1x1 pattern. The RHEED oscillations and pattern are shown in Figure 2.8 (a) and (b) respectively. The RHEED typically becomes spotty between ~15-25 sec after opening the shutters. Continued growth after this time enhances the dot size, causing a slight red shift. Too long a growth time will cause coalescing of the quantum dots and poor luminescence properties due to defects. A 3D and 2D AFM scan is shown in Figure 2.8 (c) and (d) respectively.

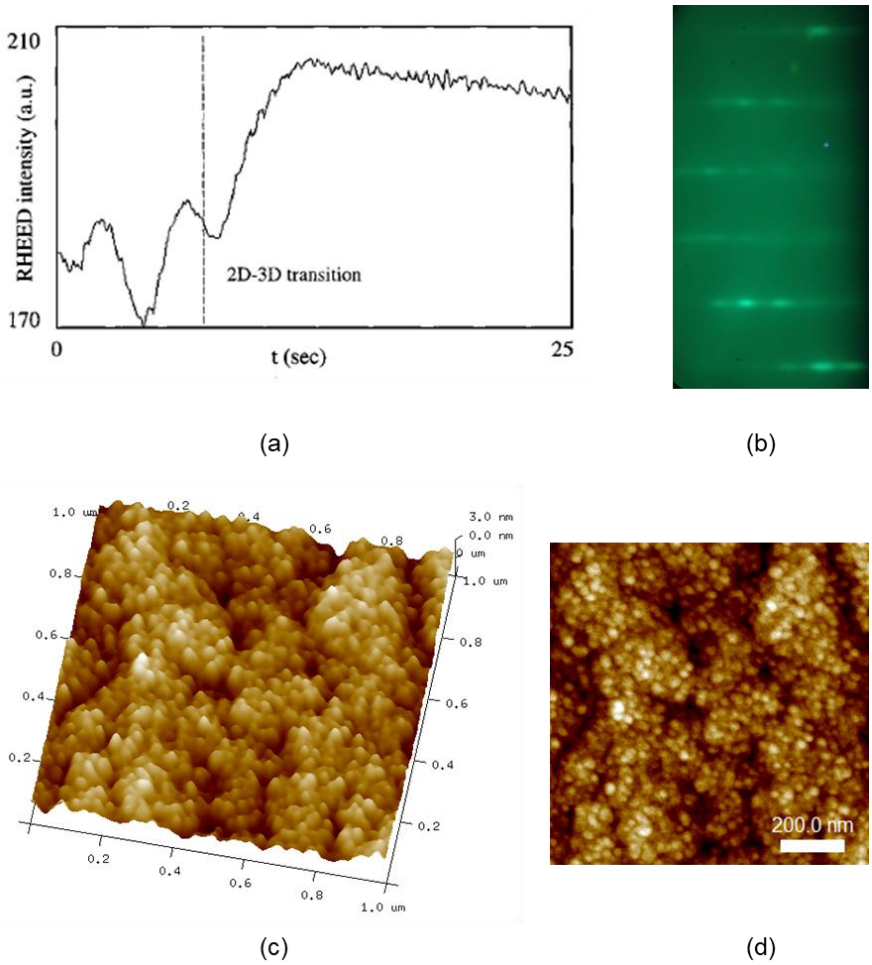

Figure 2.8 (a) RHEED intensity for InGaN/GaN quantum dots [38]. (b) Spotty 1x1 RHEED pattern of quantum dots. (c) 3D and (d) 2D AFM scan of InGaN QDs.

2.4 Optical and Interface Characteristics of $Al_{0.56}Ga_{0.44}N/Al_{0.62}Ga_{0.38}N$ Multiquantum Wells with ~280 nm Emission

Introduction

The materials of choice for light sources emitting in the deep ultraviolet (DUV) region of the spectrum (210-360 nm) are the AlGaN alloys and their heterostructures and multiquantum wells [39-40]. Deep UV light emitting diodes are required for a number of critical applications [41]. These include sterilization and water purification, curing of polymers, Raman spectroscopy, medical applications, high-density optical recording and white light generation. Other applications will emerge as reliable lasers are developed. $Al_xGa_{1-x}N/Al_yGa_{1-y}N$ quantum wells for deep UV LEDs have been grown both by MOCVD [42-43] and PAMBE [44-45], usually under Ga-rich conditions on AlN-on-sapphire templates. The effects of nitrogen and oxygen on the electrical properties of the films and the role of the high density of defects on the optical properties have been reported by a few groups [46-47]. It is also understood that the metallic Ga layer on the surface aids in the absorption and ultimate incorporation of adatoms, lattice, dopant and impurity, on the growing surface [48]. The objective of this work was to analyze the interface roughness of $Al_{0.56}Ga_{0.44}N/Al_{0.62}Ga_{0.38}N$ multiquantum wells grown by MBE by studying the optical properties and structural characteristics of the quantum wells with internal quantum efficiency (IQE) ~30%. Molecular beam epitaxy allows for the growth of high quality films with high doping efficiency in high Al-content alloys [49]. This is of importance for future realization of deep-UV LEDs using similar growth methods with high Al compositions. Specifically, the dynamic luminescence characteristics from temperature-dependent and time resolved photoluminescence measurements and the analysis of the photoluminescence data to establish the role of alloy broadening and interface roughness on the observed luminescence has been investigated. Transmission and reflectance measurements have been performed on the

MQW heterostructure and bulk well and barrier samples respectively. Complementary scanning transmission electron microscopy (STEM) confirms crystalline AlGaN MQWs with step edges of 1-3 atomic layers at heterojunction interfaces.

Epitaxy

The MQW heterostructures, shown schematically in Figure 2.9(a) (i), were grown on AlN templates on sapphire in a Veeco GEN 930 PAMBE system by Ayush Pandey in Prof. Zetian Mi's research group at The University of Michigan. The Al compositions are chosen such that the peak PL emission wavelength was at ~280 nm. From that, the barrier composition was chosen for optimal confinement while mitigating the reduction in doping efficiency at these higher Al compositions. The growth of the AlN buffer layer was done at ~880 °C, while the temperature was reduced to ~780 °C for growth of the subsequent layers. Using two Al cells, an Al beam equivalent pressure (BEP) of ~$3x10^{-8}$ Torr was used for the growth of the AlN and overlying $Al_{0.62}GA_{0.38}N$ layer, while the shutter of one of the Al cells was closed for the growth of the lower Al content well regions. The Ga flux was maintained at a total III/V ratio of ~1.5 which corresponded to a growth rate of ~80 nm/hr. The RHEED pattern was monitored in-situ, to ensure that epitaxial growth was under slightly metal rich conditions. Periodic interruptions in the growth were incorporated to remove any excess Ga in the form of droplets from the surface, including immediately before and after the quantum well layers. During these interruptions, all shutters were closed to allow the excess Ga to desorb, which was verified by observing the RHEED pattern becoming brighter. Moustakas et al [49] have reported that growing AlGaN alloys by MBE under Ga rich conditions is similar to liquid phase epitaxy, rather than a physical vapor deposition process, as there is a layer of liquid Ga on the surface into which Al, N and

dopant atoms will dissolve, before they crystallize on the AlGaN epitaxial layer surface. However, any non-uniformity in the Ga layer thickness prior to the interruption will result in compositional non-homogeneity [50] and will also contribute to surface roughness. Single undoped $Al_xGa_{1-x}N$ (x=0.56 and 0.62) layers were also grown under identical conditions on AlN-on-sapphire templates to perform PL, reflectance and transmission measurements to ascertain the alloy compositions. The thicknesses are arbitrarily chosen such that the growth is not pseudomorphic and the photoluminescence is characteristic of the bulk intrinsic material properties.

Experimental Procedure

Photoluminescence measurements were carried out by exciting the sample at 236 nm with a frequency-tripled Ti: sapphire laser tuned to 708 nm with an 80 MHz repetition rate and 100 fs pulse width. The emission is collected and analyzed by a 0.75 m monochromator with a resolution of 0.03 nm and detected by a photomultiplier tube (PMT). The laser beam is focused to a 72 μm spot size on the sample. The peak excitation intensity is fixed at 1 kW/cm^2 for all measurements. The intensity is chosen to obtain optimal signal to noise ratio as temperature is increased while ensuring the PL signal remains stable. Temperature-dependent PL measurements were made by mounting the sample in a closed-cycle helium cryostat. Time-resolved photoluminescence transients were measured at different temperatures to determine the carrier lifetimes and their radiative and non-radiative components. The transient signal is detected with a thermoelectrically-cooled fast hybrid photomultiplier tube with a detection range of 220-650 nm and a timing jitter <50 ps. Room temperature reflectance and transmission measurements have also been made on the MQW samples and on the single $Al_{1-x}Ga_xN$ layers by Dr. Aniruddha

Bhattacharya, former colleague in Prof. Pallab Bhattacharya's research group. These measurements were made with a variable-angle spectroscopic ellipsometer over the wavelength range of 193-1687 nm. For the reflectance measurements, the angles of incidence and specular reflection were 45° (the smallest angle of incidence attainable in the system). The reflectance spectra were calibrated with a highly reflective Si wafer as the reference sample. For the transmission measurements, the angles of incidence and detection were maintained to be perfectly normal to the sample surface and the back sides of the samples were also polished.

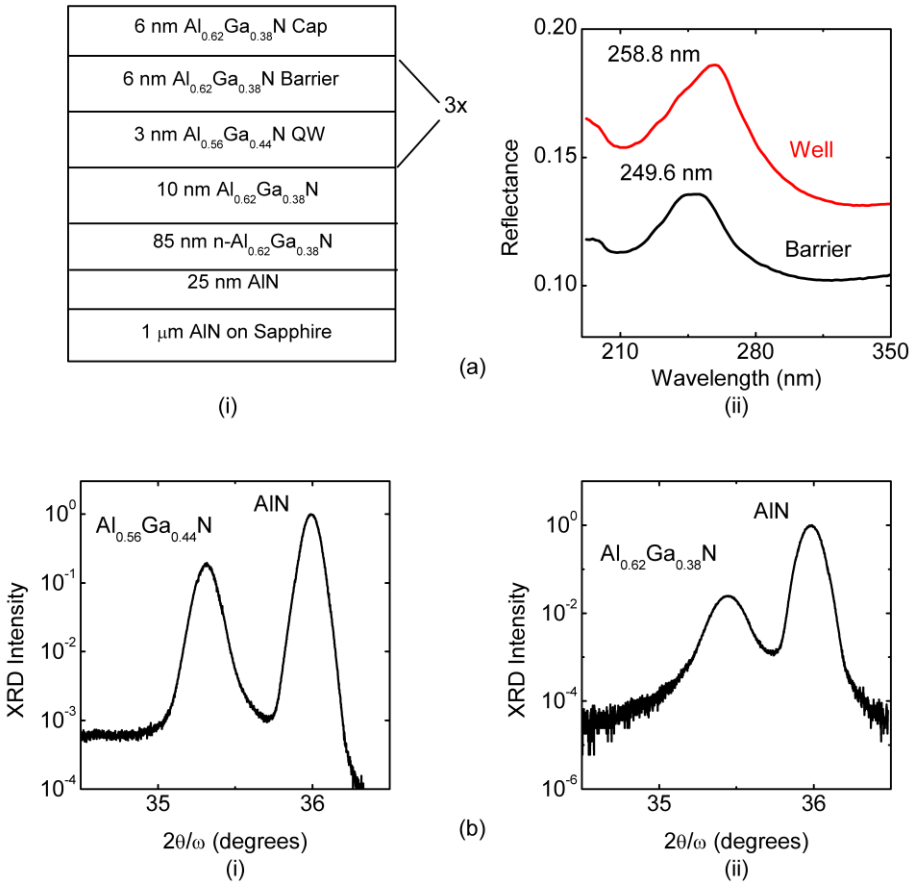

Figure 2.9 (a) Schematic representation of the MQW heterostructure with three $Al_{0.56}Ga_{0.44}N/Al_{0.62}Ga_{0.38}N$ quantum wells grown over an AlN on sapphire template (i) and the optical reflectance recorded at 45° of thick $Al_{0.56}Ga_{0.44}N$ and $Al_{0.62}Ga_{0.38}N$ layers grown separately representing the bulk well and barrier compositions with respective peaks at 258.8nm and 249.6nm (ii); (b) XRD results of the bulk well (i) and the bulk barrier (ii) grown over the AlN on sapphire templates.

Analysis

Results from the reflectance measurements on the AlGaN single layers with compositions identical to the well and barrier regions of the MQW samples are shown in Figure 2.9(a) (ii). The corresponding X-ray diffraction (XRD) measurement results on the well and barrier layers are shown in Figure 2.9(b), (i), and (ii), respectively. XRD data is courtesy of Ayush Pandey. Based on the (0002) XRD data, the lattice constant of the AlGaN layer has been calculated from the relative peak position to the AlN peak. Vegard's law was then applied to approximate the composition of the epilayer. The reflectance and XRD data confirm that the alloy compositions in the well and barrier of the MQW are $Al_xGa_{1-x}N$ with x = 0.55 + 0.01 and 0.62 ± 0.01, respectively. Shown in Figure 2.10(a) are the room temperature PL and transmission (inset) spectra obtained from an $Al_{0.56}Ga_{0.44}N/Al_{0.62}Ga_{0.38}N$ MQW sample. A shift of 31 nm (535 meV) is observed between the dominant PL peak at 284 nm and the transmittance edge at 253 nm. Such a large shift has previously been reported for AlGaN MQWs, possibly due to the significant disorder present within the AlGaN alloy grown [51-52]. A second weaker transition observed in the PL spectrum at ~270 nm is believed to originate from the $Al_{0.62}Ga_{0.38}N$ barrier and buffer layers and the spectral position is in the exact agreement with that of the peak in the spectrum measured with the single $Al_{0.62}Ga_{0.38}N$ layer. The dominant PL transition has been analyzed and consists of several transitions originating most possibly from compositional fluctuations. The linewidth of the main transition (largest integrated area) is derived to be 224.7 meV ± 0.4 meV. The results of temperature-dependent PL measurements on the MQW sample are shown in Figure 2.10(b). An approximate internal quantum efficiency of ~30% is estimated from the data, assuming that non-radiative channels are frozen at 13.5 K. The variation of the peak emission energy of the luminescence with temperature is plotted in the inset of Figure 2.10(b). The solid

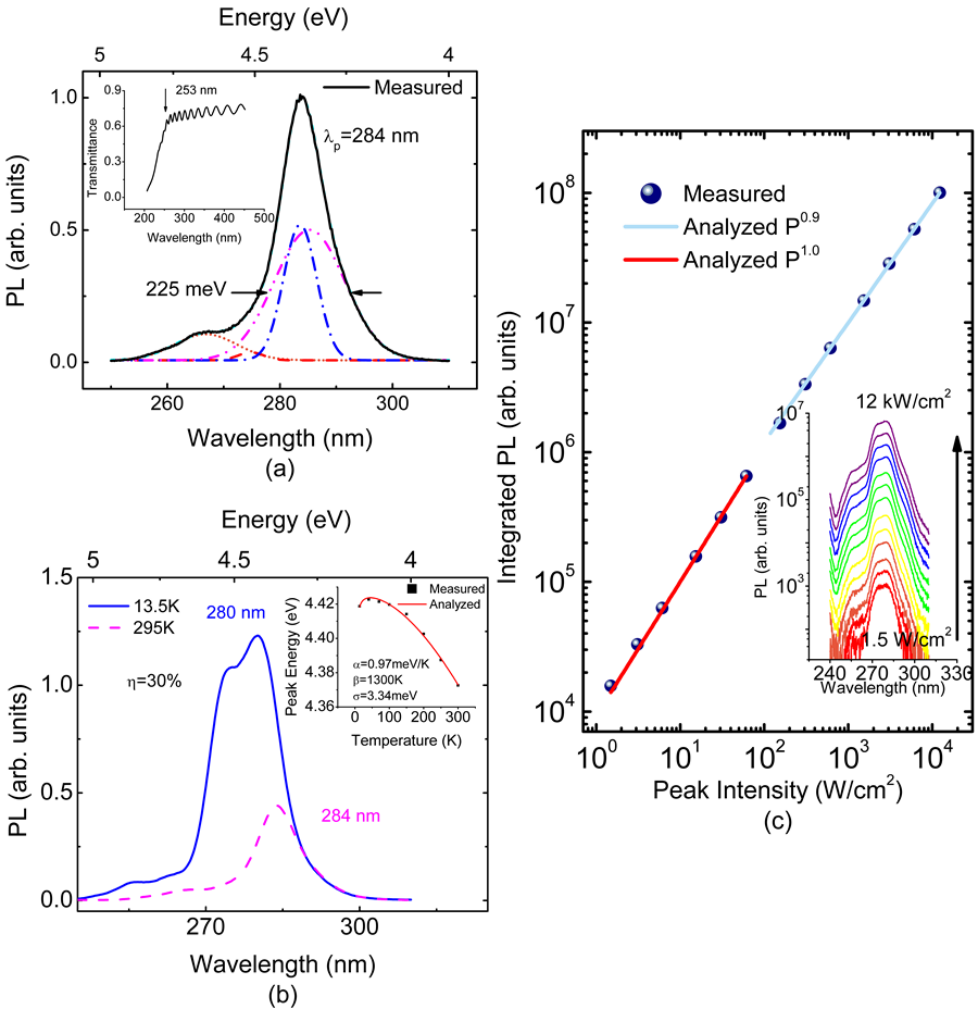

Figure 2.10 (a) Photoluminescence spectra of the MQW heterostructure with the Gaussian analysis shown as the dashed lines. The transmission of the heterostructure is shown in the inset with the edge at 253nm; (b) low-temperature photoluminescence of the MQW heterostructure with the temperature-dependent Varshni analysis with localization effects shown in the inset. Values of α, β, and σ are extracted to be 0.97meV/K, 1300K, and 3.34meV respectively; (c) measured integrated photoluminescence with peak excitation intensity. The luminescence is spectrally integrated across 265-310nm. The inset shows measured spectra in log-linear scale from 1.5W/cm^2 to 12kW/cm^2 excitation intensity.

curve represents analysis of the measured data in accordance with the Varshni equation including localization effects [53]. Good agreement is observed with the values of α, β and σ listed in the figure. Here, σ is a parameter related to the Stokes shift of the luminescence. In particular, the value of σ = 3.34 meV suggests the presence of compositional inhomogeneities and localization effects, including those at the MQW interfaces. Optical excitation dependent PL measurements

were made on the MQW samples at 14 K. The measured variation of integrated PL intensity with excitation density is shown in Figure 2.10(c). The intensity follows a power law relationship of the form $I \sim P_{inc}^{0.9}$, where the luminescence has been spectrally integrated across the wavelength range of 265-310 nm. Above 60 W/cm^2, the value of the slope decreases from 1.0 to 0.9. The fact that no blue shift of the luminescence peak with excitation was observed over the range of excitation density, depicted in the inset of Figure 2.10(c), suggests that at least one of the levels involved in the radiative transition is a confined state, possibly at the interface.

The Schrödinger equation was solved using a scalar form of the Hamiltonian [54], assuming that the built-in electric field is evenly distributed across the interfaces. The field is calculated using reported values of the constants [55]. Pseudomorphic growth over the thick underlying AlN layer is assumed. For a barrier and well composition of x = 0.62 (E_g = 4.968 eV) and 0.56 (E_g = 4.791 eV) respectively, the spontaneous and piezoelectric polarizations are 0.064 C/m^2 and 0.0040 C/m^2 for the barrier and -0.060 C/m^2 and 0.0053 C/m^2 for the well. This results in a built-in electric field of ~640 kV/cm using a value of ε_r equal to 8.65 in the well. The effective masses of the electron, heavy-hole, and light-hole are derived to be 0.273m_o, 2.59m_o, and 2.11m_o, using Vegard's law. The transition energy E_{e1}-E_{hh1} is ~4.83 eV (256.7 nm) at 295 K for a 2.9 nm well (actually determined to be 2.9 nm ± 0.3 nm from transmission electron microscopy to be described later), assuming ΔE_c:ΔE_v equal to 67:33 [56]. This agrees well with the transmittance measurement result as shown in the inset of Figure 2.10(a). The first electron bound state E_{e1} is ~44 meV above the conduction band edge and the first heavy-hole bound state E_{hh1} is ~5.5 meV below the valence band edge with the band-bending due to polarization. There is a second electron bound state E_{e2} located at ~164 meV.

With both well and barrier materials of the MQW being AlGaN alloys of high Al content,

it is most likely that interface roughness will be present [57]. The extent of this roughness was investigated by analyzing the measured PL data. At the same time the role of alloy scattering was ascertained to analyze the overall PL line widths. The 295 K data are chosen due to other peaks emerging in the spectra at cryogenic temperatures, which distort the true linewidth of the transition of interest. Therefore, any thermal broadening that may exist is not separately analyzed. The total inhomogeneous linewidth broadening is obtained from a Gaussian analysis of the 295 K photoluminescence data of the MQW heterostructure shown in Figure 2.10(a). The linewidth from alloy broadening can be described by [58]:

$$\sigma^a = \sqrt{\sigma_1^2 + \sigma_2^2} \tag{2.1}$$

where

$$\sigma_1 = \sigma_{B1}^a \frac{\Delta_{QW}}{\Delta_{B1}} \frac{1}{\sqrt{P}} \tag{2.2}$$

and

$$\sigma_2 = \sigma_{B2}^a \frac{\Delta_{QW}}{\Delta_{B2}} \frac{1}{\sqrt{1-P}}. \tag{2.3}$$

Here $\sigma_{B1}{}^a$ and $\sigma_{B2}{}^a$ are, respectively, the PL line widths of single layers of AlGaN with compositions equal to those in the barrier and well regions of the MQW. The measured values of $\sigma_{B1}{}^a$ and $\sigma_{B2}{}^a$ for single alloy layers of thickness 170-nm and 85-nm are 223 meV and 167 meV, respectively. These high values of PL linewidth in single layers indicate large alloy broadening in AlGaN with high Al-content. Δ_{QW} is the change in the electron-hole sub-band energy with alloy composition, Δ_{B1} and Δ_{B2} represent the change in bandgap with alloy composition for the barrier and well respectively, and P is the fraction of wavefunction in the barrier. The linewidth due to interface roughness can be described by [58].

$$\sigma_{IR} \cong \delta_1 \frac{\partial E^{eh}}{\partial w}\Big|_{w=w_0} \tag{2.4}$$

where δ_1 describes the average height of the interface roughness, E^{eh} is the electron to heavy-hole sub-band energy, w is the well width, and w_o is the average well width derived from high-resolution TEM imaging to be discussed later. The value of P is found to be 0.319. For a well width of 2.9 nm, the total linewidth due to alloy broadening σ^a is calculated to be 179.5 meV. Attributing the remaining 45.2 meV ± 0.4 meV of the total linewidth to be due to interface roughness, δ_1 is found to be 1.10 nm ± 0.01 nm. In comparison, σ_{IR} with 0.6 nm of interface roughness is found to be 25 meV. Calculated line widths due to interface roughness and alloy scattering as a function of well width are plotted in Figure 2.11(a). These calculations have been made assuming that the PL originates from the E_{e1}-E_{hh1} transition, which corresponds to the measured transmission edge of the quantum well. However, in the absence of luminescence data originating from such a transition, the measured linewidths used in the calculation have been taken from the observed dominant transitions.

To verify the interface roughness, high-angle annular dark-field scanning transmission electron microscopy (HAADF-STEM) was performed of a grown sample in cross section, that shows the three pairs of AlGaN MQW within Figure 2.11(b) (i). The microscopy was performed by Prof. Robert Hovden's group at the Michigan Center for Materials Characterization (MC2). The QW layers are ~3 nm with ~5 nm AlGaN barriers above and below, shown in Figure 2.11(b) (ii). The brighter HAADF intensity of the QWs reflects their increased Ga concentration (Ga elastically scatters more strongly than Al). Atomic-scale step edges at the terminating QW surfaces are shown in Figure 2.11(b) (iii) with a height of ~0.3-1 nm (~1-3 atomic layers). The maximum height in this range agrees well with the calculated value of δ_1 quoted earlier. HAADF-STEM collected across six different growth regions estimates the total growth thickness of the QW to be 2.9 nm ± 0.3 nm. The variation in thickness is due to the presence of ~1-3

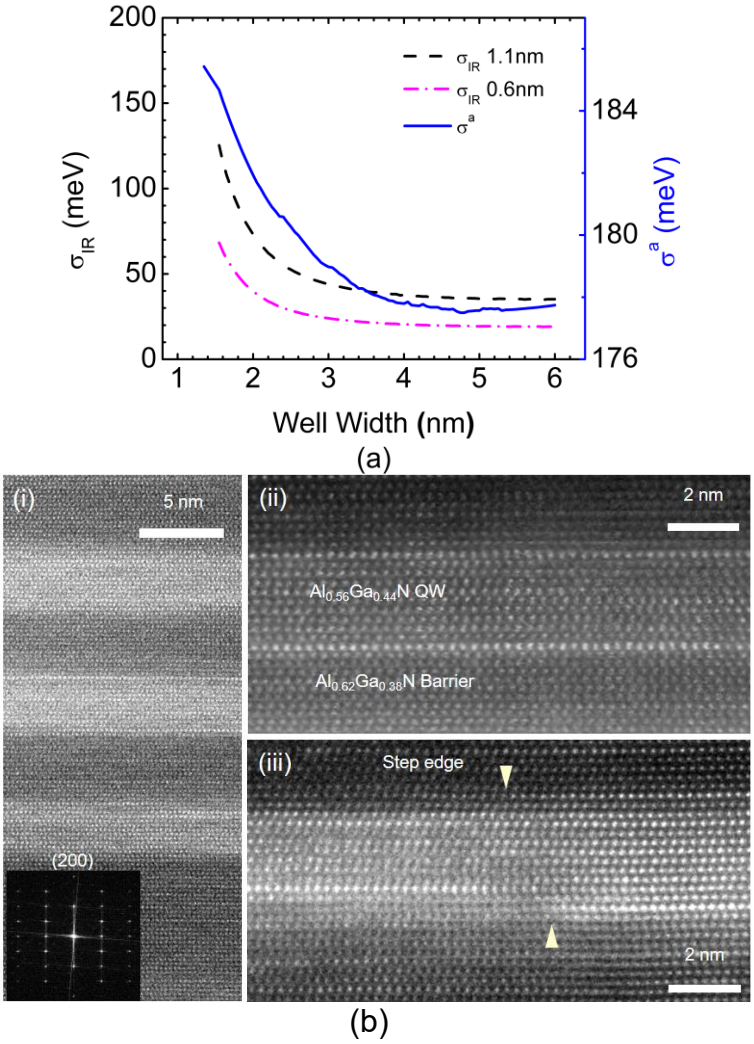

Figure 2.11 (a) Calculated photoluminescence linewidths as a function of well width broadened due to interface roughness (dashed curves) and alloy scattering (solid curve), respectively. The dashed curves have been calculated at two different values of interface roughness. (b) Quantum well AlGaN structure revealed in cross-section by HAADF-STEM. Three quantum wells of ~3 nm are separated by ~5 nm AlGaN barriers (i). Atomic resolution imaging shows sharp interfaces at top and bottom of QW (ii). Step edges commonly occurred with step sizes of 1-3 unit cells. Growth direction upward along vertical (iii).

atomic layers stepped on either top or bottom QW layers. Some Ga-rich atomic layers appear intermittently present within the Al-rich AlGaN barriers and buffer region. Similarly, Ga-rich termination was observed at the top and bottom plane of each quantum well. It is perhaps important to note that the effects of interface roughness might become more severe for $Al_xGa_{1-x}N/Al_yGa_{1-y}N$ quantum wells designed for emission at shorter wavelengths. This prediction is

motivated by similar experimental studies made on GaAs-based systems, wherein the values of interface roughness have been found to increase with increasing values of Al composition in the barrier [59]. This phenomenon is partially exacerbated by the greater challenges introduced in the heteroepitaxy of III-V compound semiconductors having higher Al compositions.

The data obtained from temperature dependent TRPL measurements is now discussed. The lifetime τ is extracted from the measured transient PL data by the stretched exponential model: $I(t) = I_0 e^{-(t/\tau)^{\beta}}$, where β is the stretching parameter and a value of $\beta<1$ indicates inhomogeneity and/or polarization effects. In this analysis the value of β is in the range of 0.87 – 0.9. The radiative and non-radiative lifetimes, τ_r and τ_{nr}, respectively, are derived from the values of τ and the quantum efficiency η, where $\tau_r = \tau/\eta$ and $1/\tau = 1/\tau_r + 1/\tau_{nr}$. The internal quantum efficiency as a function of temperature is shown in Figure 2.12(a), where it is assumed that η is 100 % at the lowest temperature of 13.5 K. The lifetimes are plotted in Figure 2.12(b) as a function of temperature, wherein the measured PL transients at two temperatures are shown in the inset. The increase of radiative lifetime with temperature is similar to that observed for InAs/GaAs [60-61] and InGaN/GaN [62] self-organized quantum dots and for InGaN/GaN dot-in-nanowire heterostructures [63]. In systems with discrete states, whose energy separation is larger than the LO phonon energy, photo-excited electrons in the continuum or the excited states cannot relax to the ground state by usual phonon scattering. The dominant mechanism to cool high energy electrons is electron-hole scattering, whereby hot electrons scatter with cold ground state holes and relax to the ground state. The energized holes are excited to higher energy hole states, from which they relax rapidly by multiphonon emission. It may be noted that there is usually a continuum of hole states due to degeneracy and band mixing. Occupation of the electron ground state, which participates in the PL transition, depends on the rate of electron-hole

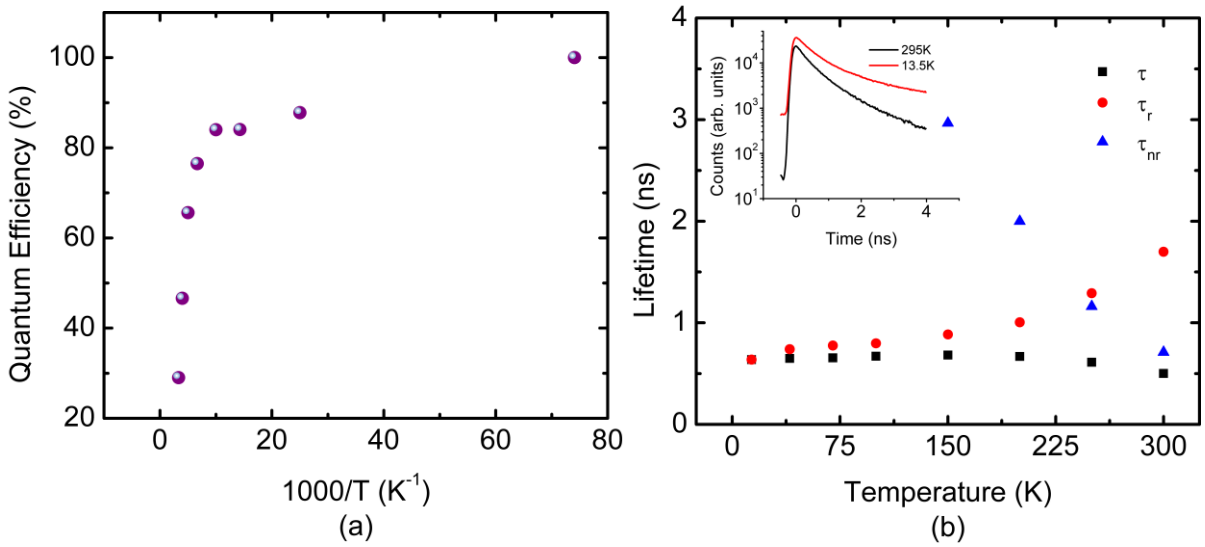

Figure 2.12 (a) Calculated quantum efficiency as a function of 1000/T assuming 100% IQE at 13.5K. (b) Extracted carrier lifetimes as a function of temperature for the MQW sample. Inset shows the measured photoluminescence transients at the lowest and highest temperatures recorded at the peak emission wavelength.

scattering and hole occupation of the ground states. The scattering rate is high at low temperatures, but decreases with increase of temperature due to thermal excitation of cold holes from the ground states. This will result in an increase of the radiative lifetime, which has been observed previously for InAs/GaAs QDs. The observed increase of radiative lifetime with temperature in the $Al_{0.56}Ga_{0.44}N/Al_{0.62}Ga_{0.38}N$ MQW further confirms that the observed luminescence originates from confined states which exist either in the form of compositional non-uniformities or as interface roughness at the MQW interfaces.

2.5 Summary

In conclusion, an overview and history of PAMBE has been presented and examples of how to grow III-Nitride epitaxial layers, nanowires, and quantum dots were shown. The luminescent properties of $Al_{0.56}Ga_{0.44}N/Al_{0.62}Ga_{0.38}N$ quantum wells were investigated by steady-

state and time-resolved photoluminescence measurements and high-resolution TEM imaging. From analysis of the results, the average height of the roughness at the well-barrier interfaces was estimated. The observed increase of radiative lifetime with temperature suggests that the shift in luminescence from the transmission edge originates from confined states at the interface. Despite MBE being capable of sharp interfaces, some monolayer fluctuations can be present within the active region of a device and these may impact the device characteristics.

Chapter III

Optical Characterization of GaN Monolayers

3.1 Introduction

Deep-ultraviolet light sources are important for high density-optical storage, artificial photosynthesis and water purification, in addition to solid state lighting [39-41, 64-69]. The conventional technique is to fabricate devices with AlN, high Al-containing AlGaN alloys and quantum wells using these materials [42-45, 70-74]. In addition to problems associated with p-doping, light emission from these materials along the c-plane is extremely weak, as opposed to GaN. The preferred emission direction is from the a-plane due to differences in the valence bandstructure between AlN and GaN [65-66, 75-76]. In principle, emission in the deep-UV wavelengths can also be obtained from GaN layers of thickness 1-2 atomic monolayers, sandwiched by AlN or AlGaN barrier layers. The quantum confinement energy of carriers in such a "thin" quantum well has been shown to be large, leading to a large electronic bandgap in the deep-UV range [23, 77-80]. The strong confinement of electrons and holes in the two-dimensional (2D) GaN region can also lead to a large exciton binding energy, calculated to be ~200 meV, ~10 times that in bulk GaN [81-84]. However, this result has not been borne out experimentally with GaN/AlN quantum wells, where the GaN layer thickness is 1-2 monolayers (MLs). A large exciton binding energy is advantageous for the study of room temperature polariton lasing, micro-cavity devices, exciton lasers, and 2D devices [85-87]. Large exciton binding energies in the range of 0-1.5 eV have been reported for many organic semiconductors

for use in organic light-emitting diodes and solar cells [88]. ZnO, a wide band-gap semiconductor, is known to have an exciton binding energy at ~60 meV and room temperature lasing has been demonstrated [89]. More recently, transition metal dichalcogenides (TMDCs), in particular WS_2, was shown to have a binding energy of ~0.71 eV in the form of a monolayer [90].

In the present study the optical properties of GaN/AlN disk-in-nanowire arrays grown on silicon substrates by molecular beam epitaxy (MBE) have been investigated, as previously reported [91]. These self-assembled nanowires grow catalyst-free on silicon [28, 63, 92-93]. It has also been shown that p-doping of Al(Ga)N nanowires can be achieved for device applications [94-95]. The samples investigated have 3 GaN disks of 1 ML thickness, separated by thick (10 nm) AlN barriers. Temperature- and excitation-dependent and time-resolved photoluminescence measurements have been made and the measurement results have been analyzed. The exciton binding energy is measured to be ~160-260 meV and the peak photoluminescence is at a photon energy of ~5.2 eV, agreeing with theoretical calculations. Measurements have also been made on planar GaN/$Al_{0.65}Ga_{0.35}N$ quantum wells, where the GaN layer is ~1-2 ML thick. Similar results were obtained and the exciton binding energy is estimated to be 95 meV.

Using first principles methods based on density functional theory (DFT) and many-body perturbation theory, Bayerl et al have shown that in near-two dimensional (monolayer and bilayer) GaN bounded by AlN barrier layers of varying thickness the electronic and optical gaps and the exciton binding energy are greatly enhanced due to the extreme quantum confinement [82, 84]. Consequently, the polarization-induced separation of electrons and holes in the GaN layer is reduced, resulting in higher radiative efficiency and smaller spectral shift of the peak luminescence due to quantum-confined Stark effect (QCSE). The biaxial compressive strain in

the GaN layer also alters the carrier effective masses. More importantly, the emission of polarized light in the vertical direction (perpendicular to the c-plane) with E⊥c is not hampered. This attribute might also be useful for UV detectors.

3.2 Epitaxial Growth of Monolayer Structures

The nanowire and planar samples for the study were grown by molecular beam epitaxy. The nanowire array, schematically shown in Figure 3.1(a), was grown, in collaboration by Yuanpeng Wu, on (111) Si substrates starting with 60 nm of GaN at 810 °C. 150 nm of AlN is then grown at 870 °C followed by the growth of GaN ML at 820 °C and 10 nm AlN at 820 °C. The GaN/AlN is repeated 2 more times to have 3 GaN ML disks. Three periods were chosen to balance the low level of light emission and its detection for a single period versus growth related inhomogeneities for a larger number of periods. The average nanowire diameter is 35 nm and the area density is $6x10^9$ cm^{-2}. An SEM image of the as-grown nanowires is shown in Figure 3.1(a)(ii), courtesy of Yuanpeng Wu. Growth of the planar heterostructure, shown in Figure 3.1(b), is carried out by Ayush Pandey in Prof. Zetian Mi's group on an AlN/sapphire template. 20 nm of an AlN buffer layer is first grown at 750 °C followed by 120 nm of $Al_{0.65}Ga_{0.35}N$ at 690 °C. A short growth interruption (~10 sec) under N_2 plasma results in the formation of a very thin GaN layer, on which 20 nm of $Al_{0.65}Ga_{0.35}N$ is grown. Atomic-resolution scanning transmission electron microscope (STEM) measurements (Figure 3.1(a)-(b)) indicate that the GaN disk is 1 ML in the nanowire sample and the GaN layer thickness in the planar sample is ~1-2 ML. The HAADF intensity profile for each STEM image suggests that the nanowire interface is cleaner than that of the planar sample. TEM imaging was done by Prof. Robert Hovden's research group.

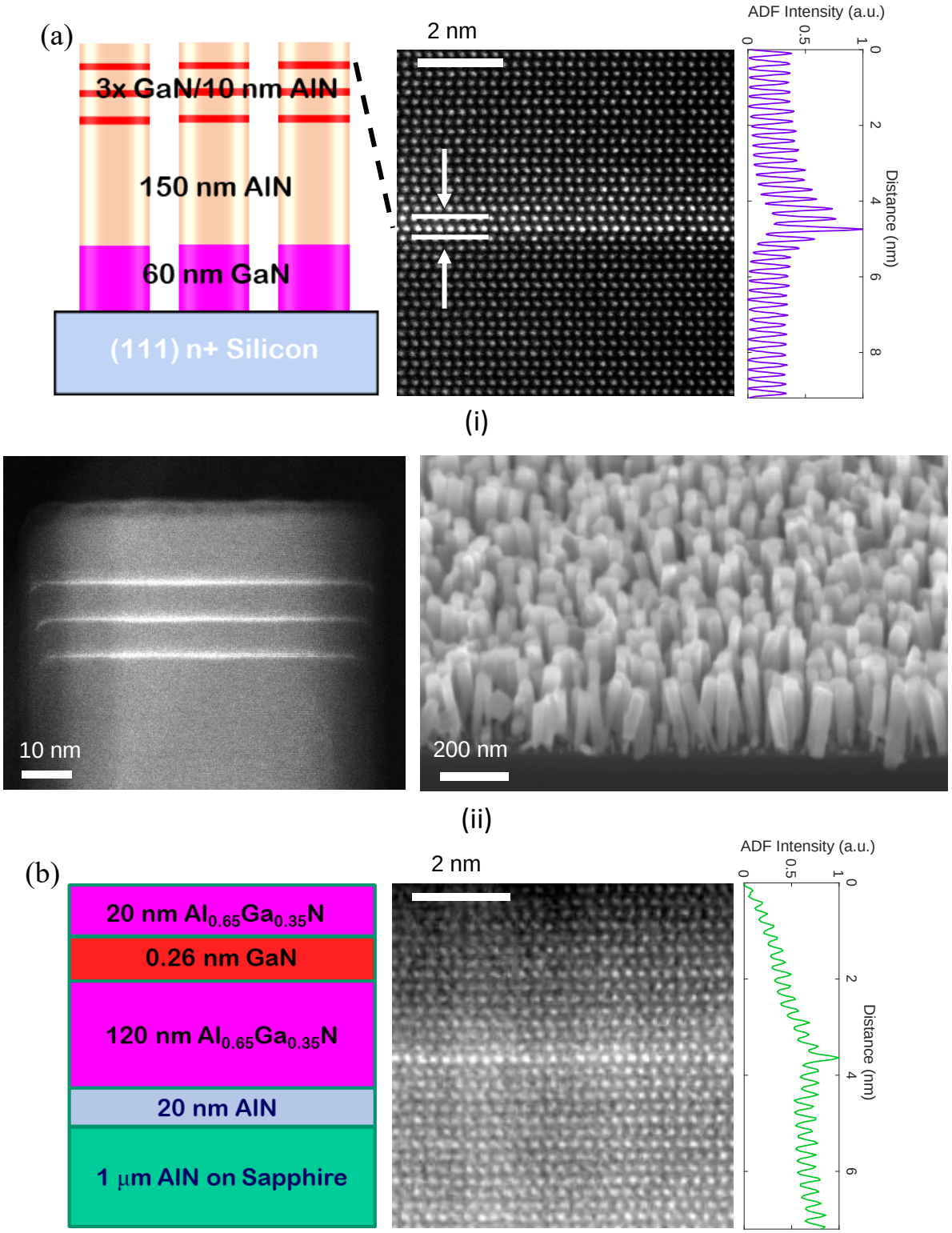

Figure 3.1 Schematic heterostructure and high-angle annular dark-field (HAADF) STEM image of the monolayer GaN in (a) (i) a single AlN nanowire, and (b) a planar GaN/$Al_{0.65}Ga_{0.35}N$ heterostructure, both grown by plasma-assisted molecular beam epitaxy. Integrated HAADF profile intensity shown alongside image. STEM operated at 300 keV, 29 mrad semiconvergence angle (a) (ii) Plan-view SEM image (*right*) of the nanowire array and STEM image (*left*) of the 3 periods of a single nanowire.

Note the slow increase of background intensity in Figure 3.1(b) is due to thickness changes in the specimen. The ML quantum well in Figure 3.1(b) was imaged in a separate specimen grown under the same conditions and chemistry.

3.3 Theoretical Calculations

Atomistic calculations based on density functional and many-body perturbation theory are performed to model the electronic and excitonic properties of the GaN/AlN and GaN/AlGaN samples. The calculations were performed by Prof. Emmanouil Kioupakis' research group at The University of Michigan. The computational methodology follows the lines of references [82, 84]. To simulate the $Al_{0.65}Ga_{0.35}N$ barriers, they were approximated with an ordered $Al_{0.67}Ga_{0.33}N$ alloy and a $(\sqrt{3} \times \sqrt{3})R60^{\circ}$ supercell was employed as illustrated in Figure 3.2. The calculated results for the band gap and exciton binding energy are listed in Table 3.1, and are in good agreement with the measured PL emission energies for both heterostructures, which are to be discussed.

TABLE 3.1 Electronic gap, optical gap, and exciton binding energy for GaN/Al(Ga)N heterostructures as measured by the PL emission peak at 300 K and calculated with many-body perturbation theory. The exciton binding energy is estimated by comparing the electronic gap and the PL emission peak.

	GaN/AlN [84]	$GaN/Al_{0.65}Ga_{0.35}N$
Electronic gap	5.44 eV	4.88 eV
Binding energy	0.21 eV	0.20 eV
Optical gap	5.23 eV	4.68 eV
PL emission peak	5.18-5.28 eV	4.785 eV
Estimated binding energy	0.16-0.26 eV	0.095 eV

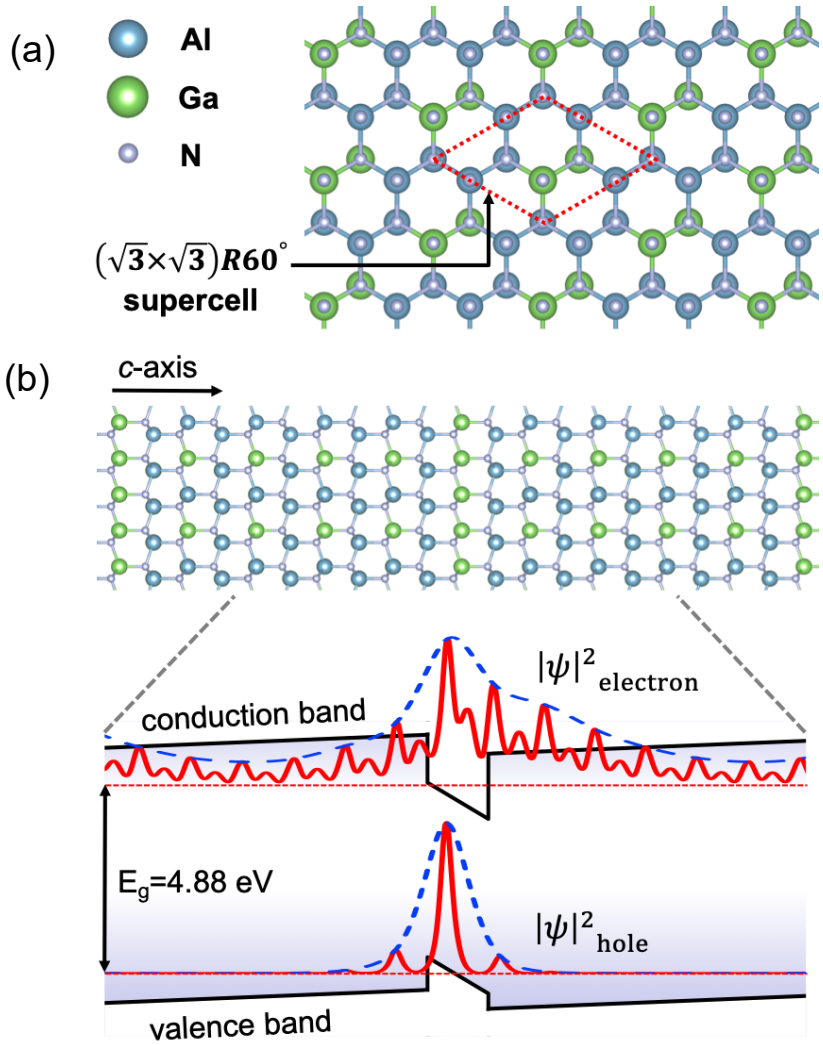

Figure 3.2 (a) Schematic of a $(\sqrt{3}\times\sqrt{3})R60^{\circ}$ supercell used to model the electronic and excitonic properties of monolayer GaN wells in $Al_{0.67}Ga_{0.33}N$ barriers; (b) structure and band diagram of GaN/$Al_{0.67}Ga_{0.33}N$ heterostructure along the *c*-axis. Extreme quantum confinement effect increases the electronic gap of GaN to 4.88 eV and blueshifts the luminescence into the deep UV. Electron and hole wavefunctions ($|\psi|^2$ solid lines) are localized in the monolayer GaN well. Polarization-field-induced separation of electrons and holes reduces the overlap of electron and hole envelope functions ($|\psi|^2$ dashed lines). Courtesy Prof. Emmanouil Kioupakis.

Carrier localization by composition fluctuations can strongly affect the properties of nitride alloys [96]. To explore the effects of barrier disorder on the measured properties and to validate the simulation results obtained with ordered alloy barriers, the DFT band-extrema energies and wave functions of the ordered structure are compared to disordered $Al_{0.67}Ga_{0.33}N$ barriers simulated with a special quasi-random structure (SQS) [97-98], and with five random

alloy structures that are stoichiometric within each plane. The results show that the band-gap reduction resulting from alloy fluctuation is small (15 meV) both for the SQS and for the random structures, much lower than the localization energy (70 meV) of 3D alloys [96]. Moreover, both electron and hole wave functions are extended within the plane even under the presence of barrier compositional fluctuations. The results demonstrate that carrier localization within the plane due to barrier composition fluctuations is weak, while the main origin of in-plane localization of carriers is well-width fluctuations [82].

3.4 Optical Characterization and Analysis

Temperature and excitation-dependent and time-resolved photoluminescence measurements were performed with 6.2 eV (200 nm) excitation provided by the fourth harmonic output of a 80 MHz/70 fs Ti: sapphire laser, focused to a spot size of 20 μm or 5 μm with suitable optics. The excitation for temperature-dependent PL measurements was fixed to 10 W/cm^2. Luminescence signals were analyzed by a 0.75 m monochromator with a resolution of 0.02 nm and detected by a UV-enhanced PMT. The transient signals from TRPL measurements were detected by a high-speed single photon counter with a temporal resolution of 50 ps. The nanowire sample will first be discussed followed by the planar heterostructure sample.

3.4.1 Nanowires with GaN/AlN Monolayers

The variation of luminescence with temperature recorded with a ~20 μm excitation spot diameter (corresponding to an excitation intensity of 10 W/cm^2) is shown in Figure 3.3(a). The spectrum recorded at 4 K with a 5 μm pinhole is shown in Figure 3.3(b) and is analyzed with multiple Gaussian profiles. The narrow peak at 5.38 eV corresponds to a Gaussian profile with a

linewidth of 3 meV. The variation of the peak emission energy with temperature obtained from the data of Figure 3.3(a) is plotted in Figure 3.3(c). Similar data obtained from measurements with the 5 μm pinhole are plotted in Figure 3.3(d). Also plotted in Figure 3.3(c)-(d) are the

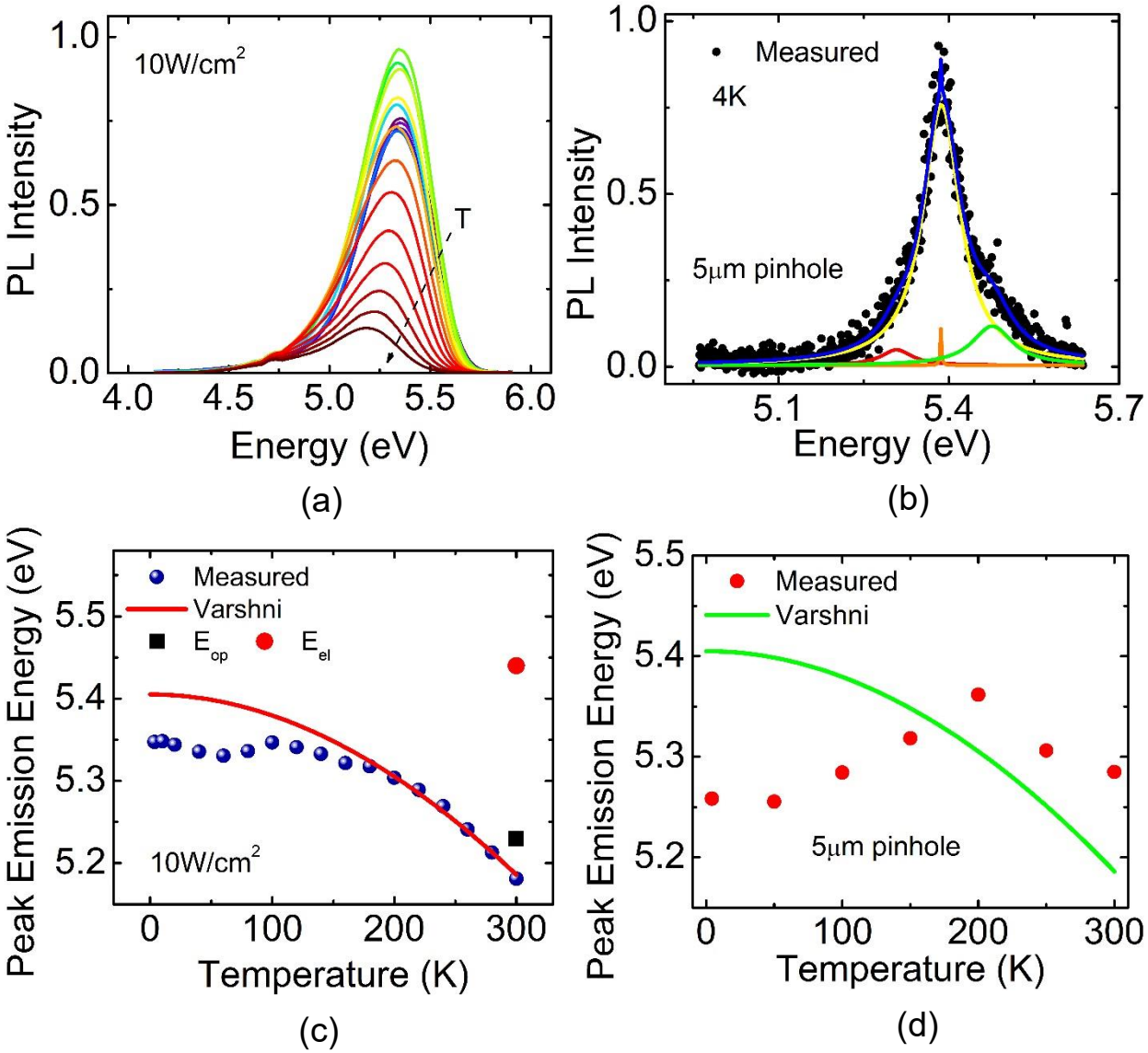

Figure 3.3 Photoluminescence results from GaN/AlN nanowire array: (a) temperature dependence. Dashed line indicates direction of increasing temperature; (b) spectrum recorded at 4 K with 5 μm pinhole and Gaussian analysis; (c) and (d) variation of peak emission energy with temperature from spectra of (a) and those recorded with 5 μm pinhole. The solid curves represent the variation calculated with the Varshni equation. The calculated electronic and optical gaps at 300 K are also shown in (c).

calculated variation of effective bandgap energy according to the Varshni equation, where E_0, α,

and β are 5.41 eV, 10 meV/K, and 3800 K respectively [53, 99]. The trend of the data suggests that at the lowest temperatures the photoexcited carriers are strongly confined in a lower energy localized state, probably existing at the monolayer barrier interfaces. With increasing temperature the carriers are transferred to the bound states in the GaN monolayer and the emission energy follows the trend of the Varshni law at higher temperatures. Similar behavior has been observed for InGaN/GaN quantum wells [100]. Also plotted in Figure 3.3(c) are the calculated electronic and optical gaps, E_{el} and E_{op} respectively, in a GaN ML bounded by thick (10-12 ML) AlN barriers. It is clear that the measured PL emission energy is very close to the calculated optical gap and is ~260 meV below the calculated electronic gap. In Figure 3.3(d), the emission energy at 300 K is ~160 meV below the calculated electronic gap. These energy differences are believed to correspond to the exciton binding energy E_{bx}. Exciton formation can be prevented due to screening by the photoexcited carriers. It is estimated that at the excitation power of 10 W/cm^2, the carrier density is smaller than the Mott density of 2.3x10^{13} cm^{-2} in GaN. An E_{bx} of 200 meV is assumed, which results in an effective Bohr radius a_B^{eff} of 0.4 nm [85-86].

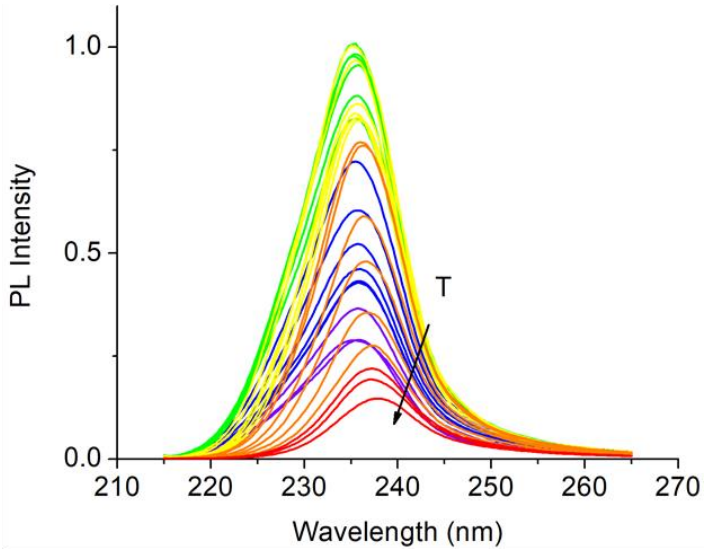

Figure 3.4 Temperature-dependent PL of a 10-period nanowire sample with GaN/AlN embedded monolayers under similar growth conditions as the 3-period sample of Figure 3.3. Arrow indicates direction of increasing temperature. Excitation is identical. No pinhole is used here.

For comparison, a 10-period nanowire sample is grown under nearly identical growth conditions. The temperature-dependent PL of this sample is shown in Figure 3.4. The room-temperature peak is at 238 nm (5.21 eV) which agrees almost exactly with the optical gap in Table 3.1. The PL intensity also appears to exhibit a similar trend of increasing with temperature

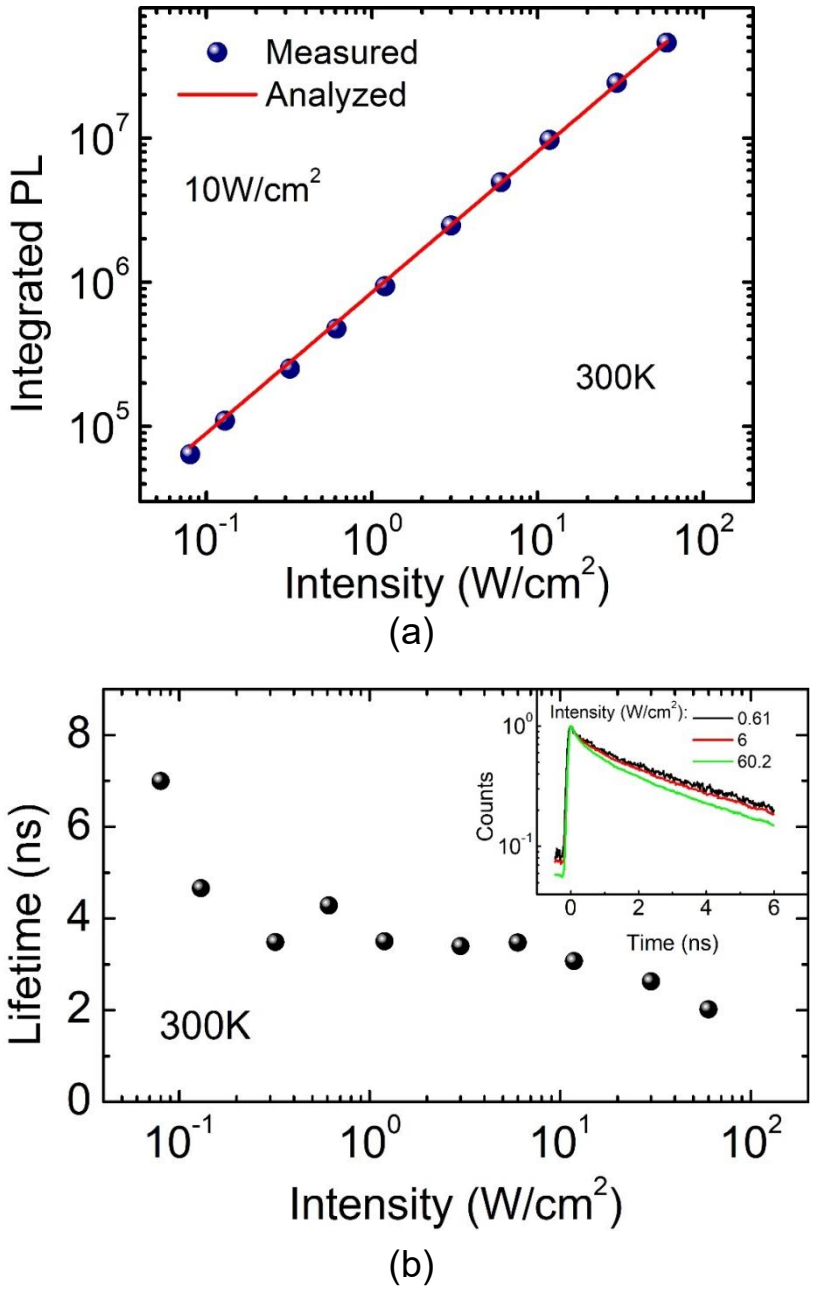

Figure 3.5 Variation of (a) integrated photoluminescence intensity, and (b) recombination lifetime with excitation intensity at 300 K in monolayer GaN nanowire sample. The measured photoluminescence transients are shown in the inset of (b).

to some extent, which will be discussed later. Figure 3.5(a) depicts the measured linear dependence of the integrated PL intensity, I_{PL}, on excitation at 300 K, according to $I_{PL} \propto P^{0.98}$, where P is the laser intensity. The variation of measured recombination lifetime τ with excitation intensity at 300 K is shown in Figure 3.5(b). The transient data is analyzed using a stretched exponential, $I_{PL} \propto e^{-(t/\tau)^{\gamma}}$, where t is time and γ varies between 0.47-0.64. Typical transients obtained from TRPL measurements are shown in the inset. There is an initial decrease of τ with increasing excitation, which is most possibly due to the quantum confined Stark effect (QCSE). While the polarization field is expected to be large between GaN and AlN, the QCSE may be small due to the strong quantum confinement. Beyond an excitation of 0.3 W/cm^2 the lifetime is relatively invariant with excitation. The invariant τ and the linear variation of

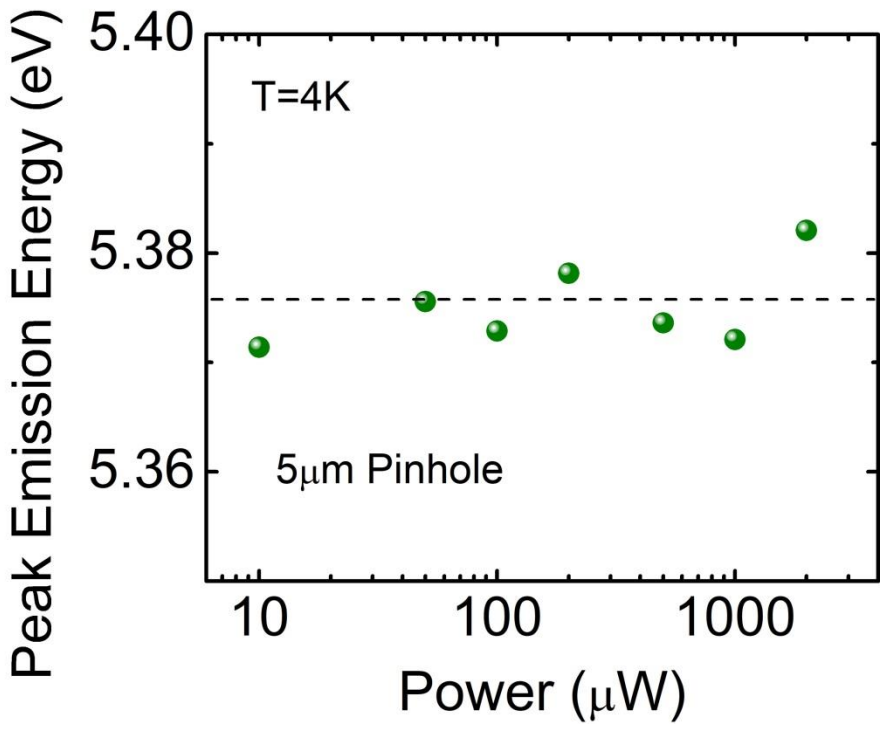

Figure 3.6 Peak emission energy from measured photoluminescence of 3-period GaN/AlN nanowire sample measured at 4 K. Dashed line is a guide to the eye.

integrated PL with excitation point to a strongly confined exciton transition. The relatively large

values of τ at 300 K seen in Figure 3.5(b) reflect a small rate of non-radiative recombination in the GaN ML disks. The peak emission energy as a function of the laser excitation power is also plotted in Figure 3.6 at 4 K. It is relatively invariant with excitation, which is an indicator of extreme confinement and that the exciton binding energy is not reduced by excess carriers or phonons.

3.4.2 Planar Heterostructure with GaN/$Al_{0.65}Ga_{0.35}N$ Monolayers

The characteristics of the planar GaN/$Al_{0.65}Ga_{0.35}N$ monolayer heterostructure are next described. The $Al_{0.65}Ga_{0.35}N$ barrier composition is verified by XRD. The temperature-dependent PL spectra is measured with a 5 μm pinhole and shown in Figure 3.7. The emission peak at 300 K is 4.785 eV. Various weaker shoulders can be seen in the recorded spectra, which are likely due to various states within the GaN monolayers, which is to be discussed. The variation of the

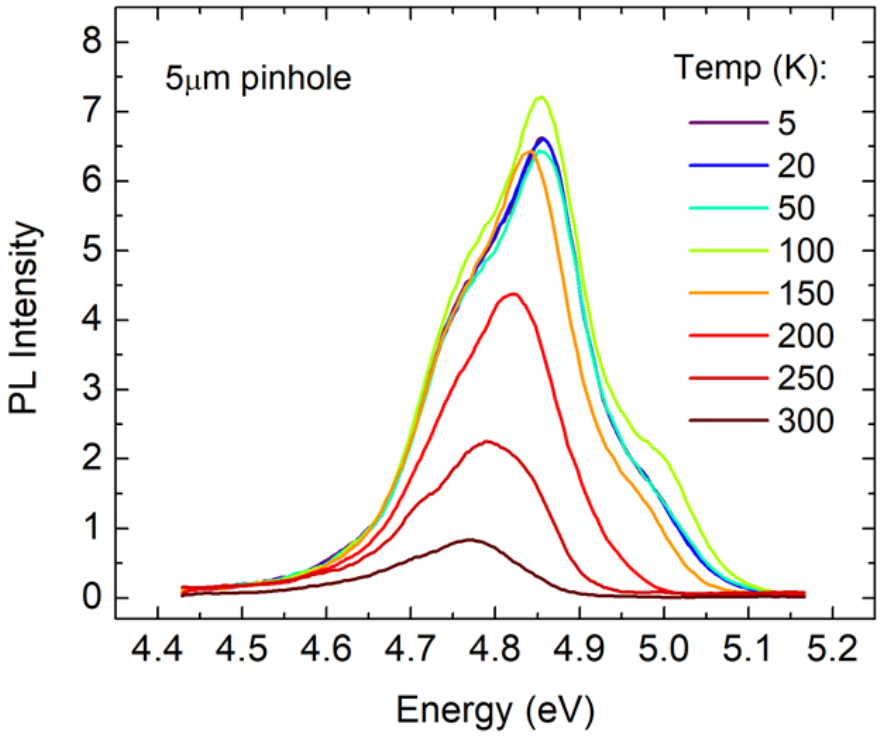

Figure 3.7 Temperature-dependent photoluminescence of planar GaN/$Al_{0.65}Ga_{0.35}N$ monolayer heterostructure resolved through a 5 μm pinhole.

PL peak energy with temperature, measured with a 5 μm pinhole, is shown in Figure 3.8(a) and the PL spectrum recorded at 4 K is shown in the inset. The solid curve is plotted in accordance with the Varshni equation, where E_0, α, and β are 4.87 eV, 1.88 meV/K, and 1600 K respectively.

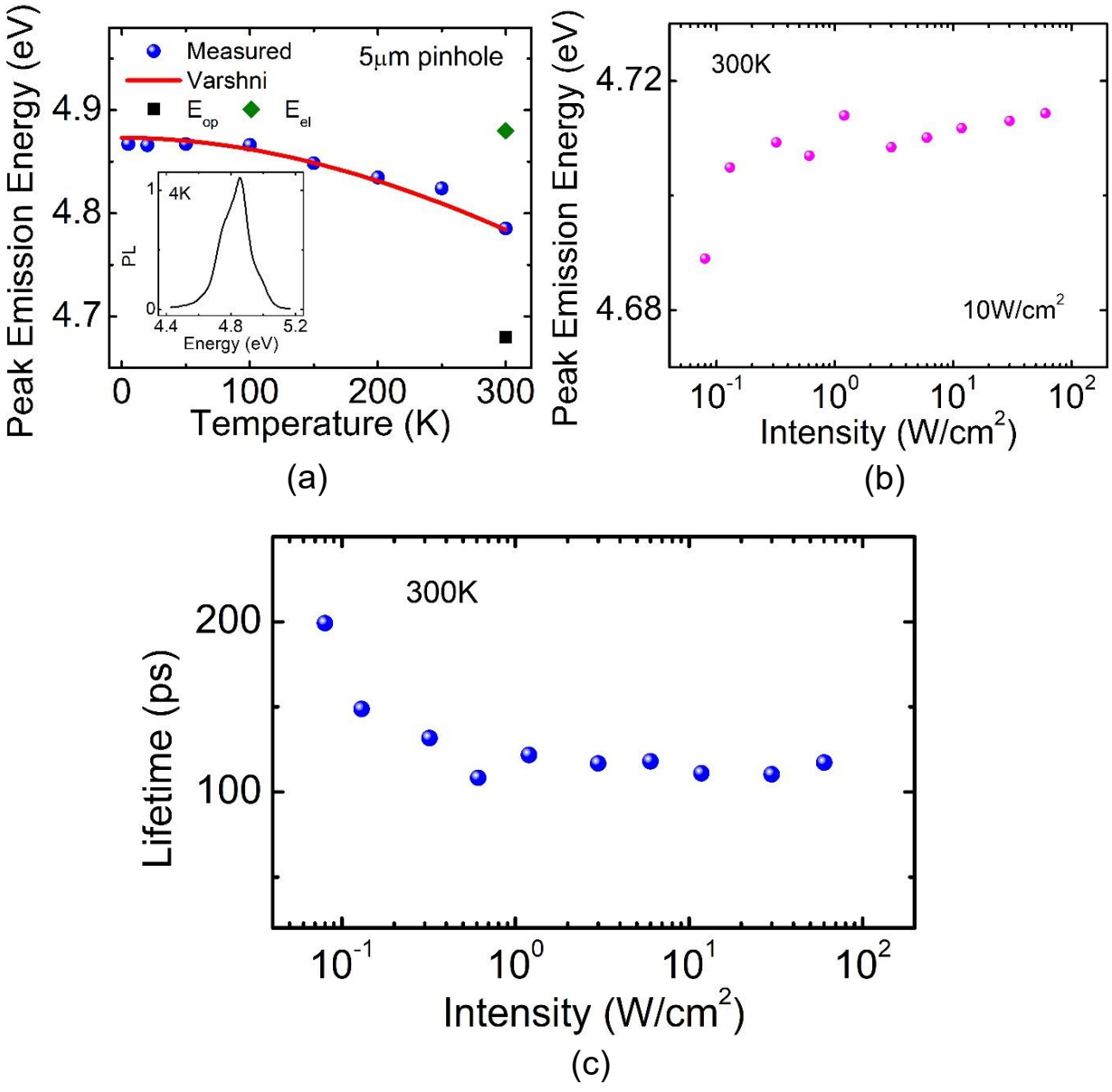

Figure 3.8 (a) Variation of photoluminescence peak emission energy with temperature in planar monolayer GaN sample with the measured spectra shown in the inset. The calculated variation in accordance with the Varshni equation and the calculated electronic and optical gaps are also shown; variation of integrated photoluminescence intensity (b) and recombination lifetime (c) with excitation intensity at 300 K in the same sample.

It is observed that carrier confinement in localized states at very low temperatures and their redistribution to GaN ML states at higher temperatures are very small and the measured data are in good agreement with the Varshni curve. The calculated electronic and optical gaps at 300 K in the ML GaN planar layer with $Al_{0.65}Ga_{0.35}N$ barriers are shown. The measured peak emission energy of 4.785 eV at 300 K is again closer to, and slightly higher than, the calculated optical gap of 4.68 eV and 95 meV smaller than, the calculated electronic gap of 4.88 eV. It is therefore believed that the exciton binding energy E_{bx} is ~95 meV in the GaN monolayer. The value is lower than the 160 meV value estimated from the nanowire ML sample and indicates that interface roughness might be responsible for making the true thickness of the GaN layer in the planar sample to be ~1-2 ML. The measured variations of the peak emission energy and the recombination lifetime with excitation intensity at 300 K are depicted in Figure 3.8(b)-(c), respectively. The small decrease of lifetime τ and increase of emission energy with excitation for low values of the latter are due to QCSE. For higher values of excitation intensity, both parameters remain relatively constant, indicating excitonic behavior. It may be noted, however, that the values of τ, between 100-200 ps, are much smaller than those measured in the nanowire samples and indicate a much larger rate of non-radiative recombination in the planar sample, as expected, due to the presence of large densities of defects and dislocations. Finally, the temperature dependence of the integrated PL intensity is shown in Figure 3.9(a)-(b) for the nanowire and planar samples, respectively. The unusual feature in the data is the peaking of the PL intensity at ~90 K in both samples, though to a lesser degree in the planar sample. At low temperatures the photoluminescence originates from radiative recombination of carriers confined in the localized states. As mentioned earlier, in the context of the data shown in Figure 3.3(c)-(d), there is a redistribution of the photoexcited carriers to the bound states of the GaN

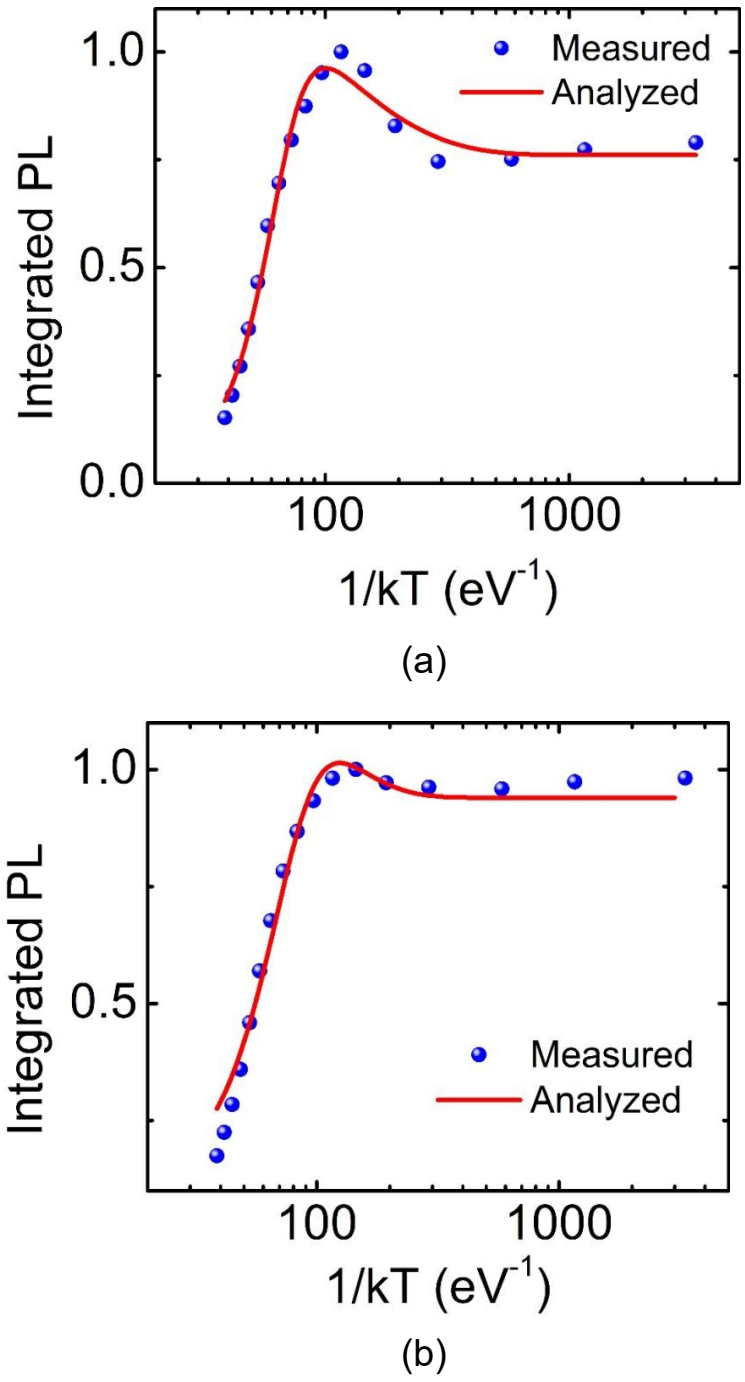

Figure 3.9 Plot of integrated photoluminescence intensity versus inverse temperature for (a) nanowire and (b) planar sample.

monolayer. Carriers could also be redistributed from other localizations in the local environment. Both processes can lead to an increase in PL intensity from the GaN ML. With further increase of temperature the rate of non-radiative recombination increases and the PL

intensity decreases. Similar behavior has been reported with InGaN quantum dots [101]. The activation energy, E_2, derived from this portion of the overall curve in both samples is ~60-80 meV, analyzed from the Arrhenius equation $I_{PL} \propto 1/(1+Ae^{-E1/kT}+Be^{-E2/kT})$, where A and B are constants, T is temperature, k is the Boltzmann constant, and E_1 and E_2 are activation energies describing the low and high temperature regions respectively. A similar trend can be seen with the measured recombination lifetimes from TRPL as a function of temperature, shown in Figure 3.10 for both samples. At cryogenic temperatures, short lifetimes ~3 ps are due to strong confinement and wave function overlap at localized states. As the temperature increases between 100-200 K, carriers transfer to monolayer states. This process is accompanied by an increase of the radiative lifetime. Similar results were obtained with the 10-period nanowire sample, shown

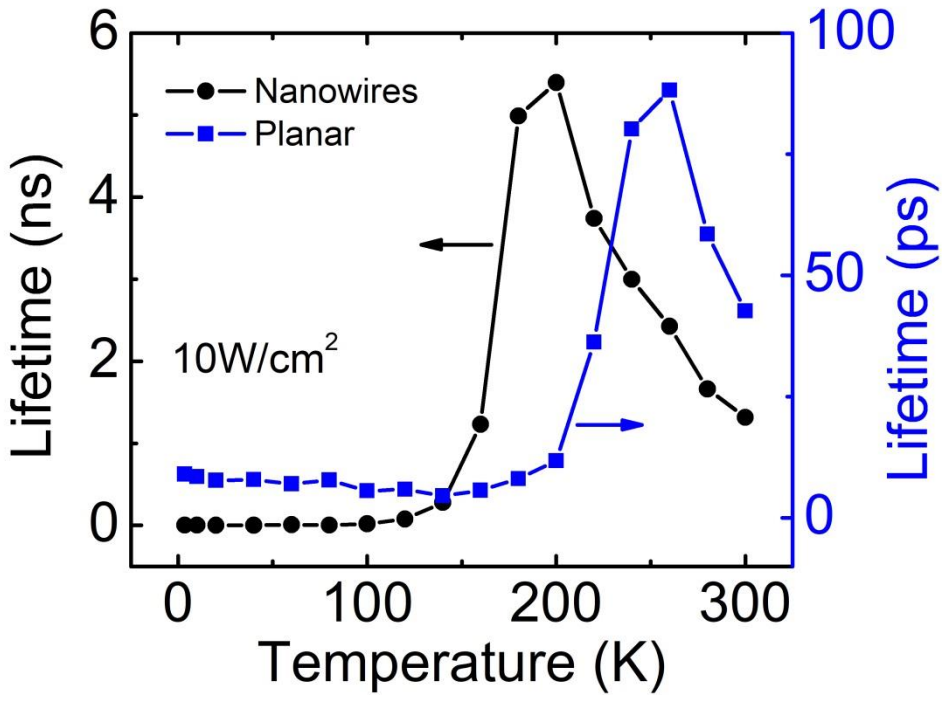

Figure 3.10 Measured recombination lifetimes for the nanowire and planar samples as a function of temperature using the stretched exponential function. No pinhole is used here. The nanowire and planar sample lifetimes are plotted on the left and right y-axis, respectively.

in Figure 3.11. The variation of the integrated photoluminescence intensity with 1/T is more extreme compared to the 3-period sample, as expected, shown in Figure 3.11(a). Increasing the

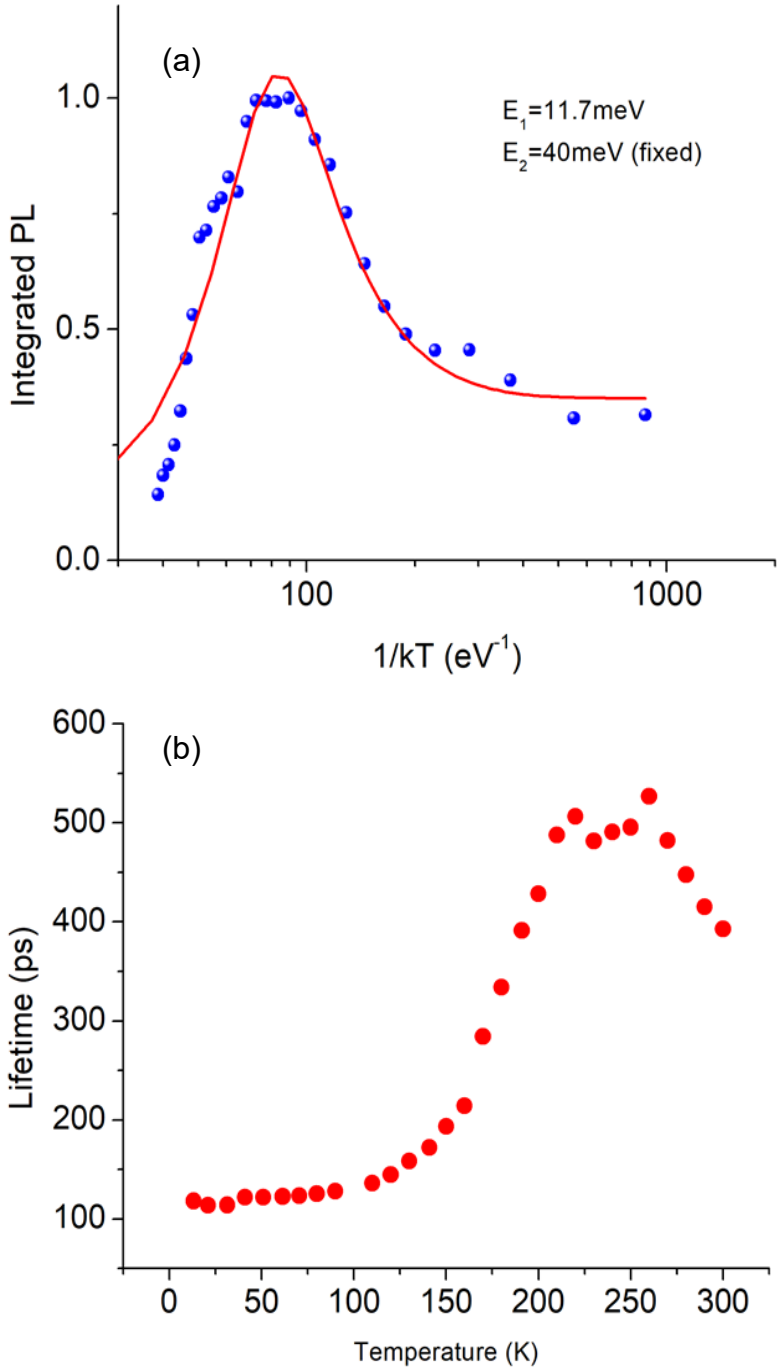

Figure 3.11 (a) Variation of the integrated photoluminescence intensity for the 10-period nanowire sample as a function of 1/T and (b) measured recombination lifetime from TRPL versus temperature.

number of periods introduces additional monolayer fluctuations and non-uniformities, which adversely affects the purity of the luminescence. The overall intensity, however, is higher due to the increased number of disks playing a role in the radiative recombination. This may be beneficial to light emitters as well as detectors. This also translates into a lower recombination lifetime, which is evident in Figure 3.11(b). The shape of the curve is rather similar to that of the planar layer, which is also prone to more fluctuations.

3.5 Summary

In conclusion, large exciton binding energies in GaN monolayers have been experimentally demonstrated through temperature-dependent and time-resolved photoluminescence measurements on GaN/AlN nanowire array and GaN/$AlN_{0.65}Ga_{0.35}N$ planar samples grown by molecular beam epitaxy. The thickness of the GaN layers are in the range of 1-2 monolayers as seen from high-resolution TEM imaging. Comparing the measured PL emission energies with the calculated electronic and optical gap, and from temperature- and excitation-dependent and time-resolved PL data, it is evident that the observed photoluminescence at room temperature is excitonic in nature. Peak emission is observed in the deep UV, at 5.18-5.28 eV and 4.785 eV at 300 K for the nanowire and planar samples, respectively. Efficient junction diodes for deep-UV light sources and detectors can therefore be realized with both planar and nanowire heterostructures with emission/detection direction along the c-axis. Electrically-injected excitonic and polaritonic devices operating at room temperature can also be investigated.

Chapter IV

Disk-in-Nanowire Visible Photodetectors on Silicon

4.1 Introduction

Applications such as biophotonics, fluorescence spectroscopy, flame monitoring in the visible wavelengths and hydrocarbon combustion control require a robust high gain visible photodetector [102-103]. The III-nitride materials and in particular the InGaN alloys are suitable since the alloying of GaN with In lowers the bandgap to the visible range [104]. The alloys, in the form of nanowire or disk-in-nanowire random arrays have been grown very successfully on (001) and (111) Si substrates by radio-frequency plasma-assisted molecular beam epitaxy [104]. Light sources, both light-emitting diodes and edge-emitting diode lasers with peak emission ranging from 480 nm to 1.3 μm, fabricated with the InGaN/GaN DINW arrays on Si have been reported [12, 105-107]. Both III-nitride and ZnO nanowire photodetectors in the UV range have been characterized, with the response of some devices extending to the visible range [108-115]. The devices include photoconductors and junction diodes, single nanowire diodes and devices made with nanowire ensembles and GaN/AlN DINW devices. Most of these devices also exhibit large gain, defined as the ratio of the number of photoexcited electrons to the number of absorbed photons. For detectors with InGaN/GaN DINW it is desirable to maximize the absorption volume and this can be achieved by using an array instead of a single nanowire and by having multiple disks in the nanowires. In this work photodetectors with InGaN/GaN DINW arrays epitaxially grown on (001) silicon substrates have been characterized, as previously

reported in [116]. Multiple $In_{0.42}Ga_{0.58}N$ disks were incorporated in the GaN nanowires and the photoluminescence emission peak from the disks was observed at ~565 nm. From transmission electron microscopy high-angle annular dark-field imaging and from the measured dynamic characteristics of edge-emitting diode lasers, it is evident that single quantum dots are formed in the InGaN disk regions of the nanowire heterostructures [28]. The devices, largely photoconductive in nature, are characterized by very large gain and responsivity. Uniquely, the photocurrent spectra, measured as functions of temperature and bias, are characterized by distinct peaks, which correspond to electron-hole interband transitions within the InGaN dots formed in the disk regions. The spectra have been analyzed with a model based on the continuity equations. The measured large gains have also been accounted for by taking into account the normal photoconductive gain due to electron-hole separation and also the modulation of the nanowire cross-section by trapping of photogenerated holes upon illumination [108, 114-115, 117].

4.2 Epitaxy of Photodetector Heterostructure

The photoconductor heterostructure shown in Figure 4.1 was grown on n^+ (001) Si substrate in a Veeco PAMBE system equipped with standard Ga, In, and Ge effusion cells including an RF plasma N_2 source. The substrate temperature is monitored by an infrared pyrometer calibrated to the RHEED 1x1 to 7x7 transition of (111) Si. Ga and N_2 fluxes are calibrated in N_2-rich and Ga-rich environments, respectively, at low temperature where the Ga desorption is negligible. The Si substrate is first solvent cleaned and then etched in HF to remove the native oxide. It is then degassed first at 200 °C for 60 minutes then at 450 °C for 60 minutes. A high-temperature oxide desorption step in the growth chamber is done at 850 °C for 20 minutes to remove any residual native oxide. Growth is done under N_2-rich conditions and the

RF plasma power and N_2 flow is fixed at 350 W and 1 sccm (6 nm/min) respectively. First, 260 nm of n-GaN nanowires are grown at 780 °C at a Ga flux of 3 nm/min with Ge-doping concentration of $2x10^{18}$ cm^{-3}. The active region consists of six pairs of undoped $In_{0.42}Ga_{0.58}N$/GaN disks grown at 600 °C. The disks and barriers are 3 nm and 12 nm thick, respectively, which have been previously calibrated [28]. The Ga flux during the disk and barrier growth steps is 2.5 nm/min and 2.6 nm/min, respectively, and the In flux is held at $3x10^{-8}$ Torr during the growth step. The top 100 nm unintentionally-doped n-GaN region is grown at 660 °C with a Ga flux of 2.6 nm/min to complete the n-i-n photodetector heterostructure. A low Mg flux is added for a low hole concentration while maintaining an overall n-type region. From scanning electron microscopy, the nanowire fill factor, area density, and average disk diameter are determined to be 0.4, $2x10^{10}$ cm^{-2} and 50 nm, respectively. Measured photoluminescence from the grown sample is shown in Figure 4.3(a), with the luminescence peak observed at 565 nm.

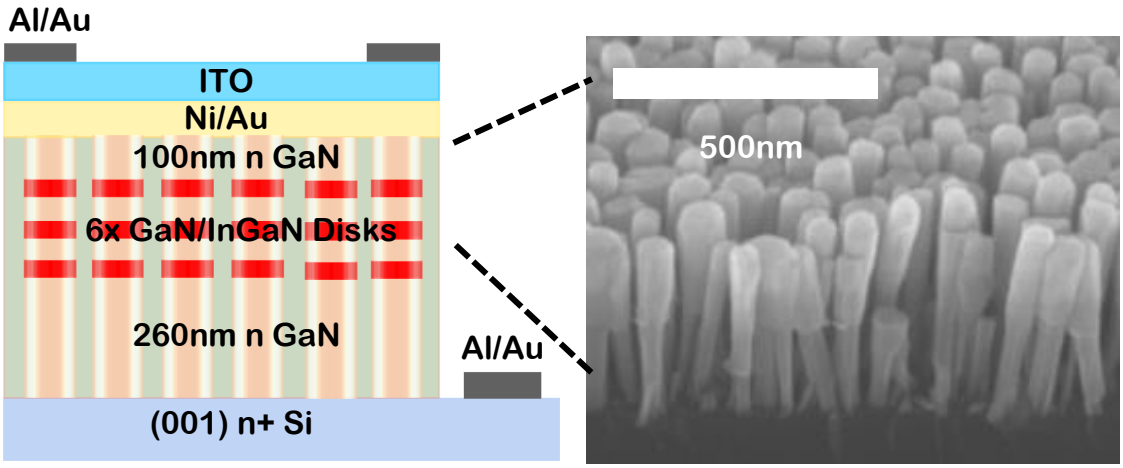

Figure 4.1 Schematic of fabricated disk-in-nanowire photodetector on (001) silicon. Plan-view SEM of the nanowires is also shown. The nanowire length is ~500 nm.

4.3 Photodetector Fabrication

To fabricate photodetectors, parylene is first deposited over the nanowires which helps in planarizing the structure, passivating the surfaces, and preventing metal from evaporating in

between the nanowires during contact formation. Reactive ion etching (RIE) is done to expose the nanowire tips for the top contact and to form 600 µm x 600 µm mesas defined by standard

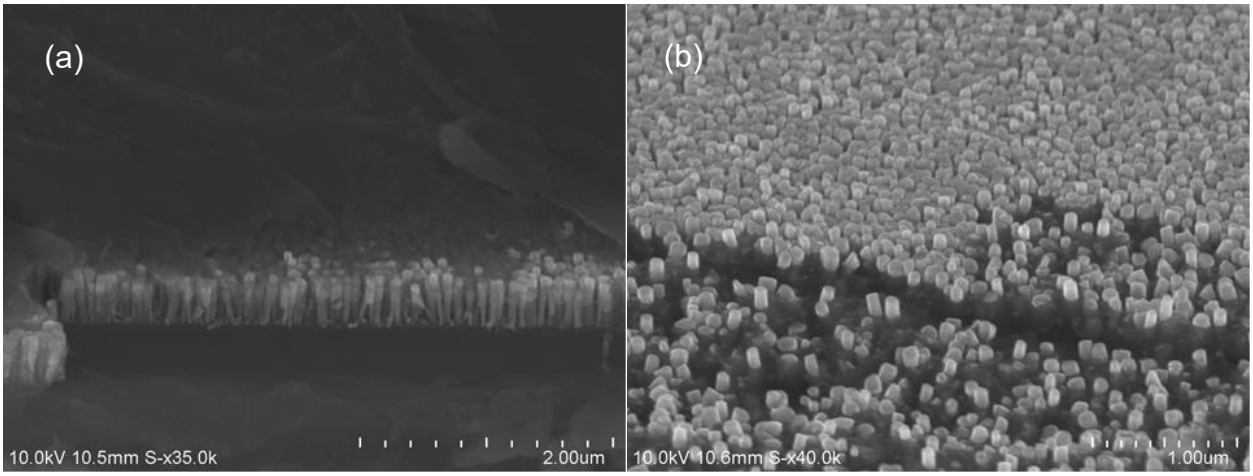

Figure 4.2 (a) Nanowires after 60 sec of parylene RIE and (b) 94 sec of RIE exposing most of the nanowire tips for device contact.

photolithography. Etching of the parylene is shown in the SEM images of Figure 4.2. After 94 sec, most of the nanowire tips are exposed while the gaps in between are filled. An HCl etch is done to remove native oxide from the GaN and then 5 nm/5 nm Ni/Au is deposited for the top contact and annealed in a 4:1 N_2:O_2 ambient at 550 °C. A 230 nm thick indium tin oxide (ITO) layer is deposited for current spreading over the Ni/Au and then annealed in Ar at 450 °C. The bottom contact on the Si substrate is formed by depositing 100 nm/10 nm of Al/Au, which also covers the Ni/Au/ITO top contact. Lift-off is used for all metallization steps. The bottom contact can be assumed to be ohmic since the conduction bands of the n-doped GaN nanowire and the n-doped Si are almost aligned. The device is schematically represented in Figure 4.1.

4.4 Photodetector Characteristics

Current-voltage (I-V) characteristics of the devices were measured in the dark using a picoammeter and applying bias to the top contact while holding the substrate at 0 V. Photocurrent is measured under illumination with 1 µW at 375 nm from a tunable light source. At this

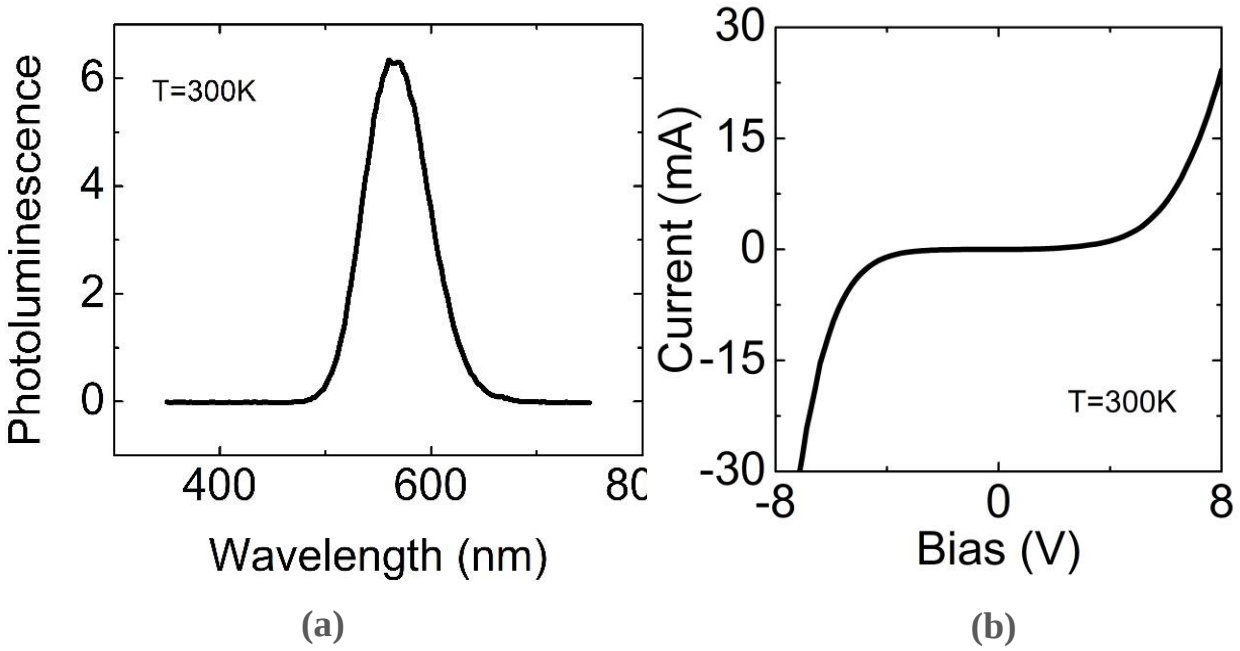

Figure 4.3 (a) Measured room temperature photoluminescence at 300 W/cm^2 excitation. Linewidth is ~280 meV. (b) Measured I-V characteristics of a device in linear scale. Bias is applied to the top of the nanowire mesa.

wavelength the photoexcitation is confined to the InGaN disk regions and the GaN nanowires are transparent. Typical dark I-V characteristics are shown in Figure 4.3(b). There is a slight asymmetry between the characteristics at positive and negative bias, that may be due to a non-ideal ohmic contact at the top end of the nanowires. The dark zero-bias resistance is measured to be 200 kΩ. The value of the dark current is relatively high, in spite of the InGaN disk/GaN barrier heterostructures. Leakage along the surface of the nanowires is believed to be the main cause of this. The current increase under illumination and a photovoltaic effect is observed at zero bias. The measured open-circuit voltage V_{oc} is 780 μV. The band-bending across the InGaN disk region, to be discussed in the following, at zero bias is believed to cause the photovoltaic effect. A cross-over of the dark and photo current occurs at a bias of 1.1 V, which indicates a decrease of the device series resistance upon illumination. This decrease is a result of modulation (reduction) of the surface depletion layer width along the n-GaN nanowire lateral

surfaces due to hole trapping and an effective increase of the nanowire conduction area. Electroluminescence is also observed under forward bias, shown in Figure 4.4. The peak is ~580 nm and exhibits a slight blue shift with injection due to built-in polarization. An image of a probed device is shown as the inset.

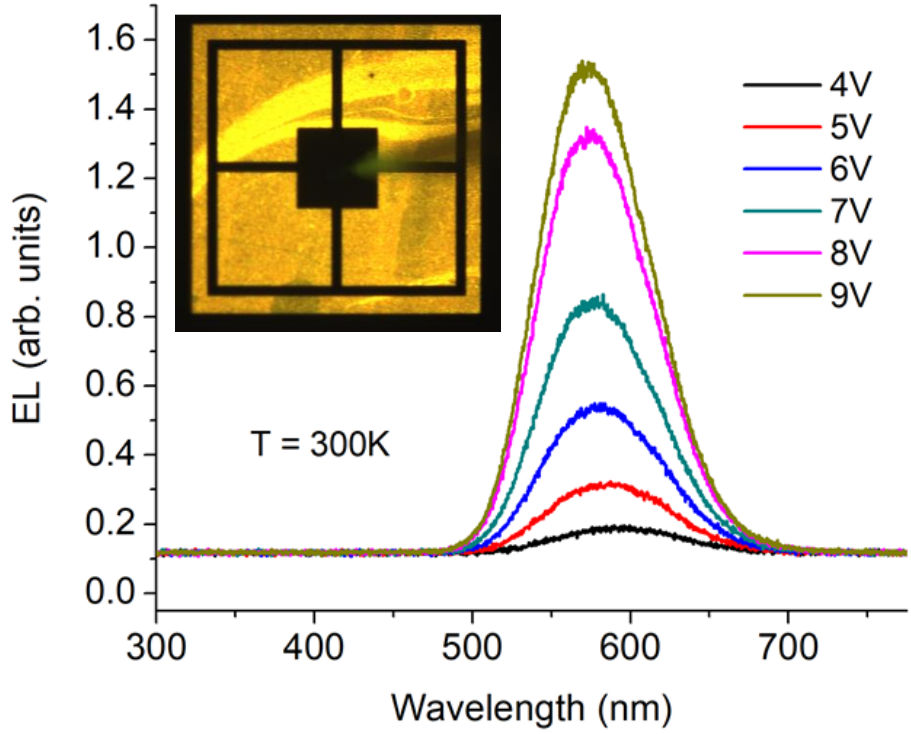

Figure 4.4 Measured room-temperature electroluminescence of the photodetector under forward bias at various injections. EL is collected by fiber coupling to a spectrometer. Inset shows a probed device under forward bias.

4.4.1 Measured Photocurrent

Photocurrent spectra at various negative biases are measured by focusing the output of a tunable tungsten-halogen white light source on to the top surface of the detector mounted on a thermoelectric cooler. A typical measured spectrum, normalized by the response of the system, and with the dark current subtracted, at a bias of -3 V is shown in Figure 4.5(a). The high-energy cut-off is attributed to the characteristics of the excitation source. The decaying photocurrent at the lower energy side is attributed to defects and doping (unintentional) related states. On

analyzing it (Figure 4.5(b)) with the formulation for an Urbach tail [118]:

$$I_{ph}(E) = I_{ph0}e^{(E-E_g)/E_u} \tag{4.1}$$

where E is the photon energy and E_g is the bandgap, a value of the Urbach energy E_u= 206 meV is derived. This is close to the reported value of 190 meV for $In_{0.42}Ga_{0.58}N$ [119]. The photocurrent spectra measured as a function of bias and temperature are shown in Figure 4.5(c)-

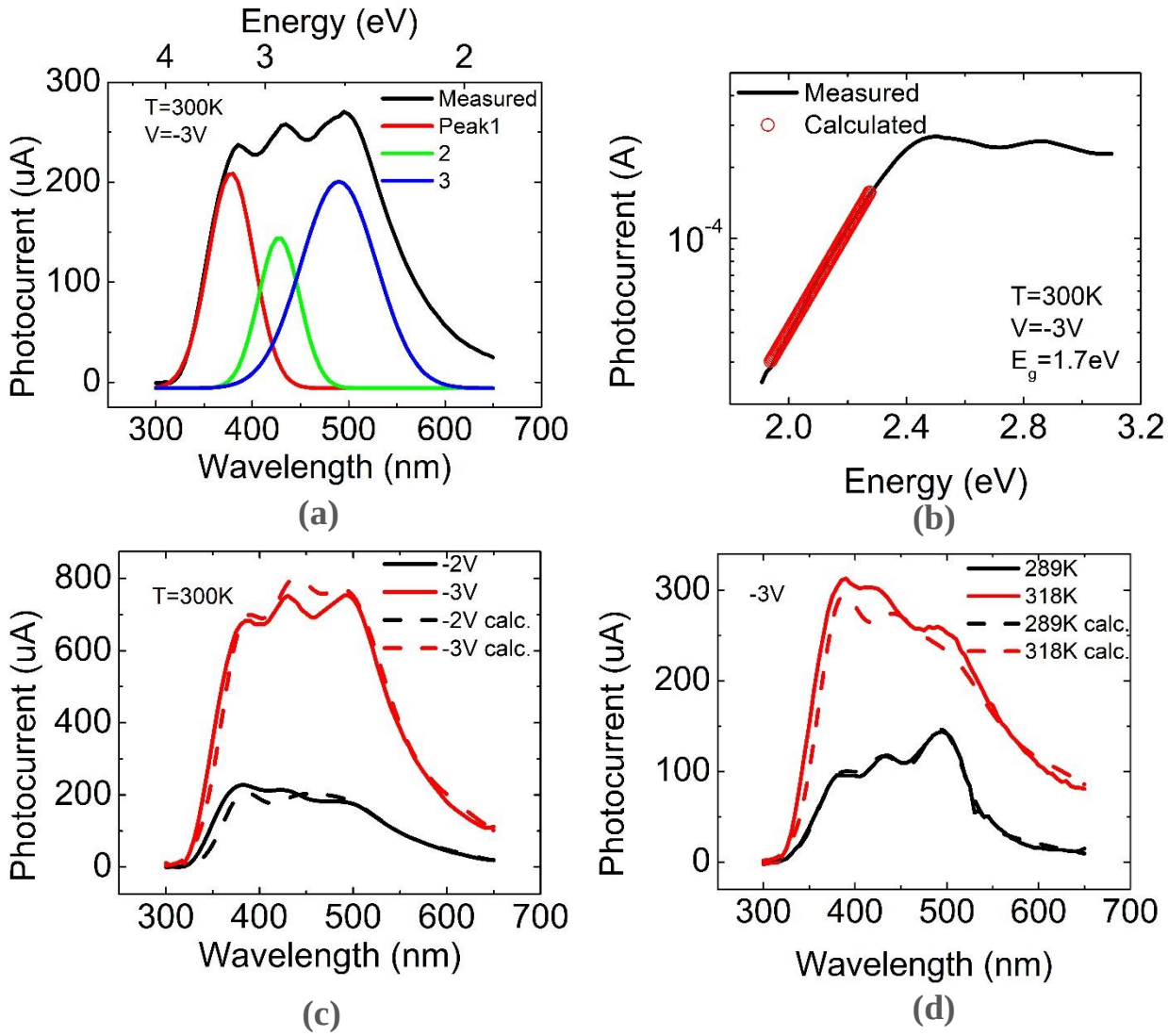

Figure 4.5 (a) Gaussian modeling of measured photocurrent at -3 V at 300 K. (b) Modeling of the Urbach tail results in an energy, E_u, of 206 meV. (c) Measured photocurrent as a function of bias at 300 K. (d) Measured photocurrent as function of temperature at -3 V. Dashed lines are calculated from the analysis.

(d) respectively. It is evident in Figure 4.5(a)-(d) that there are three distinct peaks in the photocurrent spectra. These multiple peaks, which have not been previously reported, are attributed to interband absorption involving quasi-bound electron and hole states. It is also observed that the relative strength of the peaks is strongly dependent on bias and temperature due to varying carrier capture and emission rates. It is the emitted carriers that contribute to the photocurrent. Analysis of these data is described in the following.

4.4.2 Responsivity

The calculated responsivity as a function of bias and temperature derived from the measured data are shown in Figure 4.6(a)-(b). The optical power incident on the sample is measured with a calibrated photodiode. A nanowire fill factor of 0.4 and a geometric factor of

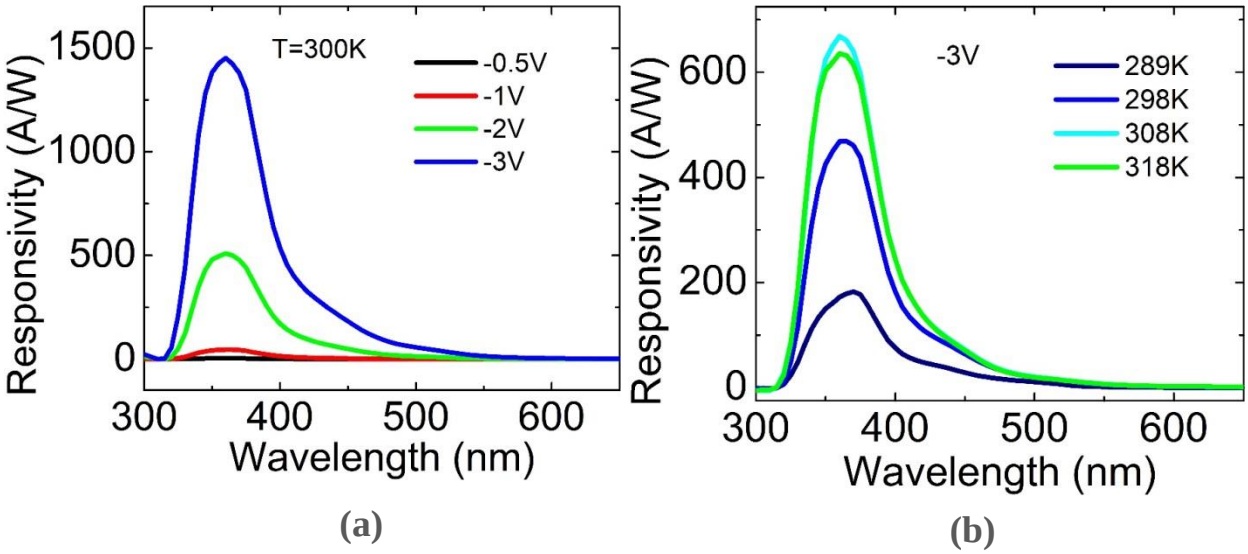

Figure 4.6 (a) Calculated responsivity as a function of bias. The peak is at 360 nm at -3 V. (b) Calculated responsivity as a function of temperature.

0.9 are also taken into account. A maximum responsivity of ~1450 A/W is measured at room temperature at a bias of -3 V. The dependence of responsivity on temperature and bias is again dependent on the carrier dynamics in the InGaN quantum dots. The increase of responsivity with

temperature indicates that the emission of photogenerated carriers, that contribute to the photocurrent, from the quantum dots is not by tunneling. The large values of responsivity is an assertion of large gain in the devices resulting from normal photoconductive gain due to electron-hole separation and the modulation of the nanowire conduction width. These effects will be analyzed in the following.

4.4.3 Transient Response

To study the device photoresponse, the time-dependent photocurrent of the device was measured by illuminating it with 375 nm light of 1 μW incident power for ~550 sec. At this time the detector attains the steady-state photocurrent. The transient response is shown in Figure 4.7(a). The decay is analyzed using two exponentials from which the decay time is extracted to be 454sec. The rise time is measured to be 190sec. The current rise and decay times are a

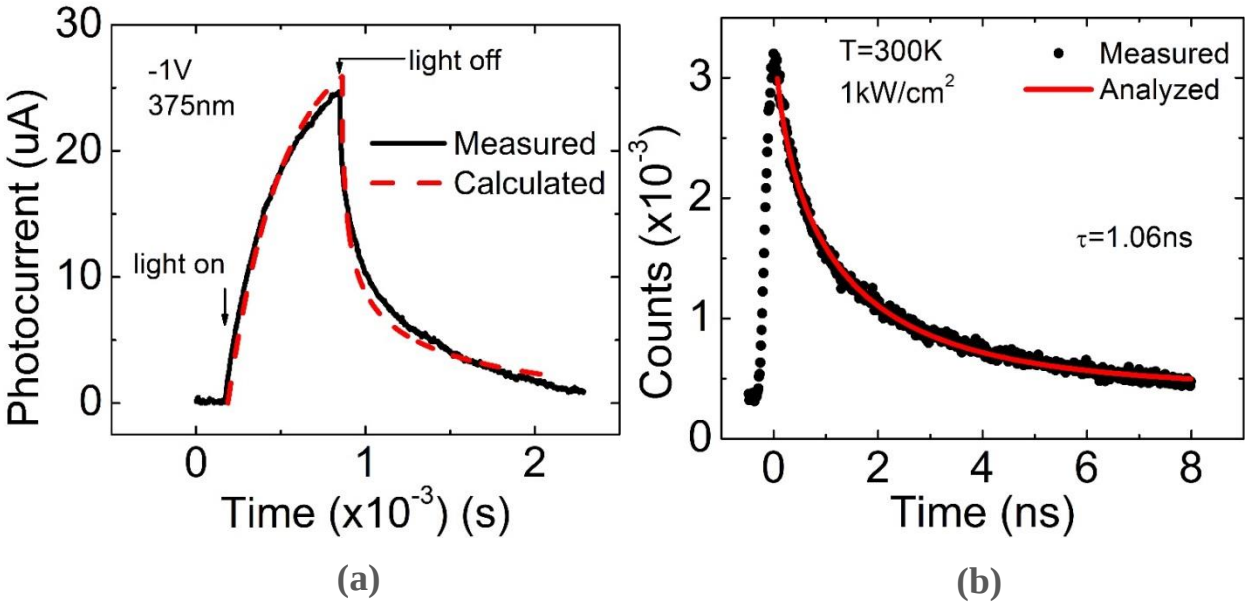

Figure 4.7 (a) Measured and calculated steady-state photocurrent transient response. Illumination is 1 μW at 375 nm. Arrows indicate the start and stop of illumination. (b) Measured time-resolved photoluminescence of the as-grown nanowires excited with 200 nm. Data is modeled using a stretched exponential with a lifetime of 1.06 ns.

measure of the carrier trapping and de-trapping times, respectively, in the surface states along the nanowire walls and carrier exchange at defects or traps in other sections of the device [114, 120]. In contrast, the photoluminescence decay time of the disk-in-nanowire array at room temperature, determined from time-resolved photoluminescence measurement and the stretched exponential model (Figure 4.7(b)) is 1.06 ns, which includes both radiative and non-radiative recombination. This value of the recombination lifetime is in agreement with previous studies and reports [104, 121]. The recombination lifetime in the GaN nanowires section is also ~1 ns.

In order to analyze the measured photocurrent spectra, it is necessary to identify the observed multiple peaks. Gaussian fitting of the measured photocurrent spectrum shown in Figure 4.5(a) reveals three distinct transitions shown in the figure, with peaks at ~383 nm, 430 nm and 492 nm. Electron and hole bound state energies in the strained InGaN/GaN disk regions, assumed to be quantum wells, were estimated by solving the coupled Schrödinger-Poisson equations self-consistently in an iterative manner. From the calculated energies of the quasi-bound electron, heavy-hole and light-hole states, transition wavelengths of 381 nm and 431 nm, that are in agreement with the measured values above, correspond to E2-LH2 and E1-HH3 transitions, respectively. The measured 492 nm transition peak corresponds to the E1-HH1 transition wherein the electron or heavy-hole state is believed to be bound to a defect in the disk region.

4.4.4 Photoresponse Modeling and Gain

The measured photoresponse was analyzed in collaboration with Prof. Zunaid Baten at Bangladesh University of Engineering and Technology. The photocurrent is a result of the transport of photogenerated carriers in the quantum dots within the disks across the nanowires to

the contacts. Depending on the applied bias and the consequent band profile across the disk region, the transport will be drift- or diffusion-limited. The corresponding equations describing the transport are [103]:

$$\frac{d\rho_d}{dt} = G - U_{SRH} - \frac{\rho_d}{\tau_{ed}} + \frac{\rho_b}{\tau_{cd}} = 0 \tag{4.2}$$

$$\frac{d\rho_b}{dt} = -U_b + \frac{\rho_d}{\tau_{ed}} - \frac{\rho_b}{\tau_{cd}} - \frac{1}{q}\frac{dJ_p}{dx} = 0 \tag{4.3}$$

$$J_p = -qD_p \frac{d\rho_b}{dx} \tag{4.4}$$

$$J_p = -qGL_{p,d} \tag{4.5}$$

where Equations 4.2-4.4 describe diffusive transport when the disks are in the flat-band region of the band diagram and Equation 4.5 describes drift of the photogenerated carriers in the tilted band region. In these equations, ρ_d and ρ_b are the hole densities in the dot and barrier regions respectively, G is the photo-generation rate, U_{SRH} is the Shockley-Read-Hall recombination rate

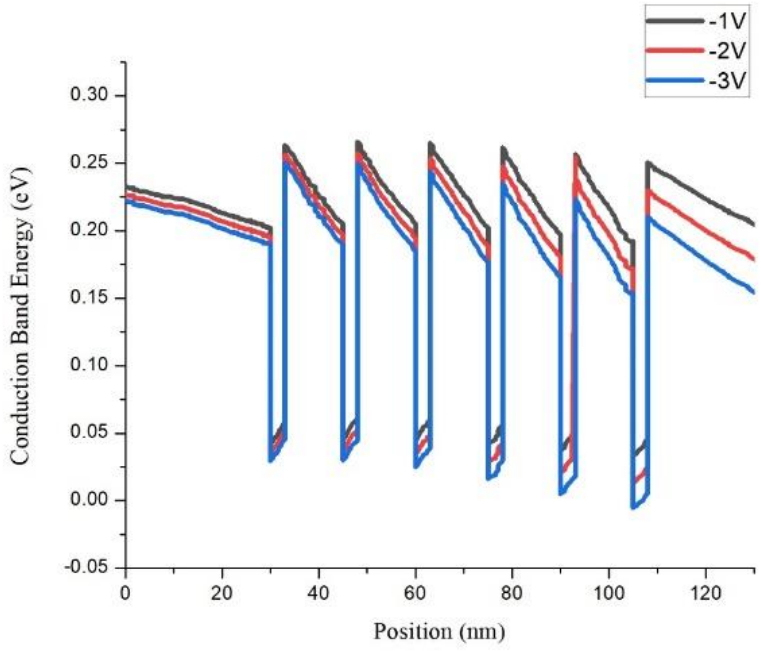

Figure 4.8 Conduction band profile of the heterostructure under different applied biases. Courtesy Prof. Zunaid Baten.

inside the dot, τ_{ed} and τ_{cd} are the escape and capture times of holes from the dot, U_b is the bulk recombination rate, $L_{p,d}$ is the diffusion length of holes in the dots, and D_p is the bulk diffusion coefficient. The band profiles as a function of applied bias were calculated by solving the coupled Poisson and continuity equations in a self-consistent manner and are shown in Figure 4.8. The profiles determine the relative number of disks in the tilted band and flat band regions and consequently the contributions of drift and diffusion to the total photocurrent. The steady state solution of Equations 4.2-4.4 is used to calculate the diffusive component of photocurrent [103]. For this, the capture and escape times, τ_{cd} and τ_{ed} respectively, corresponding to the different bound state transitions are considered as fitting parameters [122]. The linewidths of the different peaks considered here are obtained from the Gaussian fitting shown in Figure 4.5(a). The magnitude of the photocurrent corresponding to the different peaks is calculated using the rate equation based model described above. The calculated bias-dependent photocurrent spectra, as shown in Figure 4.5(c), are in very good agreement with the measured data.

The measured temperature dependence of the photocurrent at an applied bias of -3 V has also been analyzed considering the temperature variation of the escape and capture times. In general, the escape rate increases with temperature. The calculated photocurrent spectra are shown in Figure 4.5(d) alongside the measured data, where the overall photocurrent increases with increase of temperature. It is also observed that the peak at 383 nm (E2-LH2) increases in intensity at a faster rate than the peak at 430 nm (E_1-HH3) and that at 492 nm (possibly E1-HH1 bound to defect). This behavior is related to the relative variation of emission and capture rate of carriers (holes) associated with the different bound states. The variation of the escape and capture times with temperature and bias for the three transitions, as obtained from the analysis, are plotted in Figure 4.9(a)-(d). The value of the escape time varies from 0.8 μs to 1 ns whereas

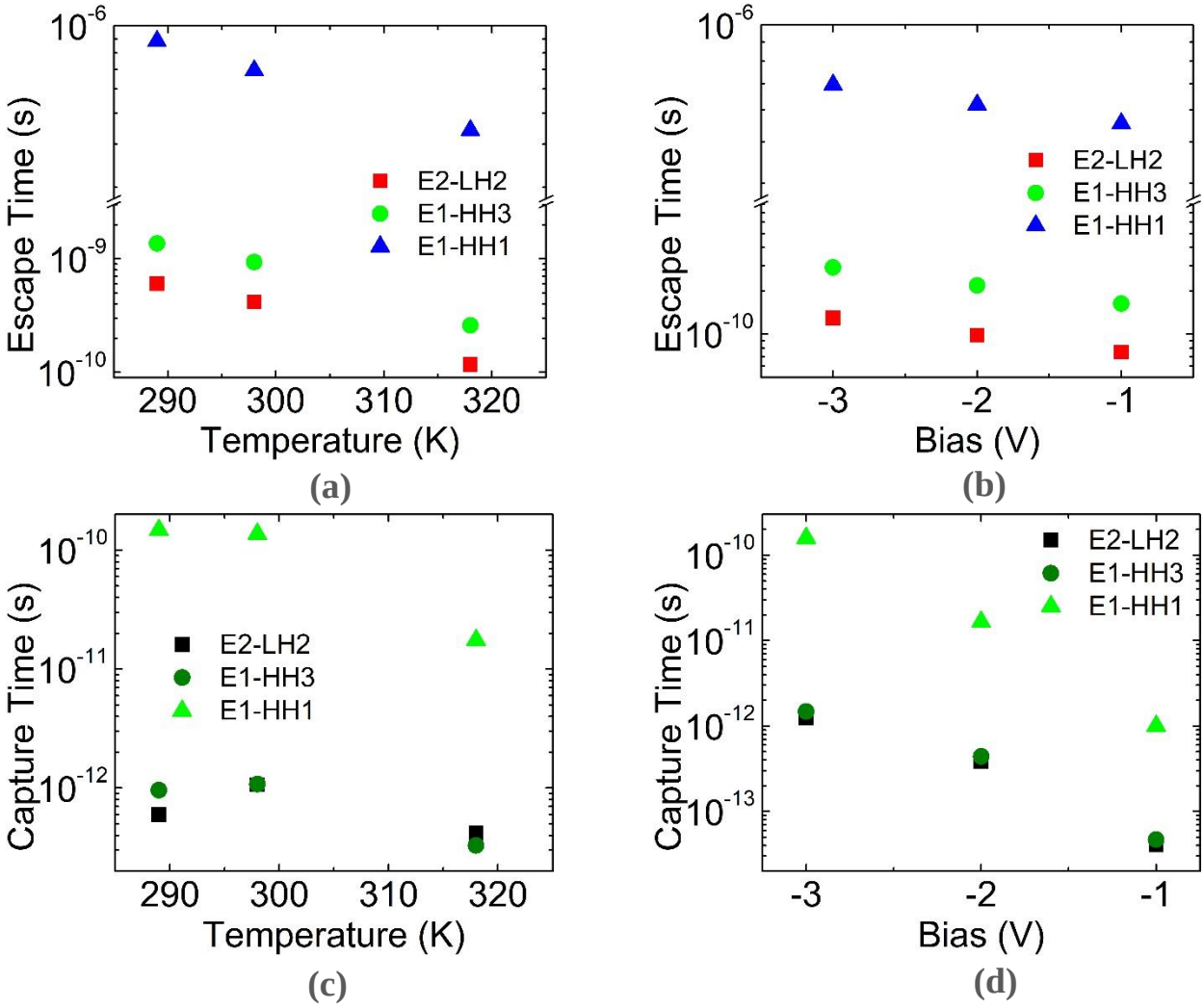

Figure 4.9 (a) Calculated escape times as a function of temperature at each intersubband transition. (b) Escape times as a function of bias at 300 K. (c) Capture times as a function of temperature. (d) Capture times as a function of bias at 300 K.

the capture time varies in the range of 0.5 ps to 100 ps. The capture time τ_{cd} of all the transitions decrease with increase of temperature. An identical trend has been experimentally observed and reported for InGaN/GaN multi-quantum wells [123]. The escape time τ_{ed} also decreases with increase of temperature for all the transitions. The bias dependence of τ_{cd} and τ_{ed} (both decreasing with increasing bias) for all three transitions is most likely related to the variation of the polarization field and band bending in the disk region with bias. It may be noted that the values

of both τ_{cd} and τ_{ed} are significantly larger for the defect-bound state transition than those for other transitions, which probably reflects the relative difficulty of carrier capture and emission into and from such a state. It should also be noted that the values of the escape times of holes shown in Figure 4.9(a)-(b) are 1-2 orders of magnitude larger than the values calculated by using a thermionic emission model [109]. While the emission rate increases with temperature, the larger values of the escape times reflect carrier capture into a deep potential well in the quantum dot formed in the disk region.

4.4.5 Gain

The gain of the photodetectors is now calculated, for which a surface depletion model [114-115, 117] is invoked wherein it is assumed that surface states on the nanowire walls give rise to a depletion region along the perimeter and pin the Fermi level. Assuming that the GaN nanowire sections in the photo detector are uniformly doped, the photoconductive gain can be expressed as [115, 117]:

$$G = G_1 + G_2 = \frac{\tau}{\tau_t}\frac{S}{\pi d^2/4} + \frac{nL\Delta S}{\tau_t P_{abs}/\hbar\omega} \tag{4.6}$$

where τ is the photogenerated electron-hole recombination lifetime, τ_t is the electron transit time, P_{abs} is the optical power absorbed in the nanowire, S is the undepleted surface area of the nanowire, n is free carrier density, L is the nanowire length, d is the diameter of the nanowire, and $\hbar\omega$ is the photon energy. The first term expresses the conventional photoconductive gain resulting from the recycling of carriers. The second term arises from the modulation (increase) of the conducting cross-section of the nanowires upon photoexcitation due to partial screening of the charge in the surface depletion regions by the trapped photogenerated holes. This modulation also decreases the nanowire resistance to current flow and increases the slope of the I(V) curve,

resulting in the cross-over of the dark and photocurrent. The plots of G_1 and G_2 and the total gain G as a function of bias are depicted in Figure 4.10. It is obvious that the modulation of the

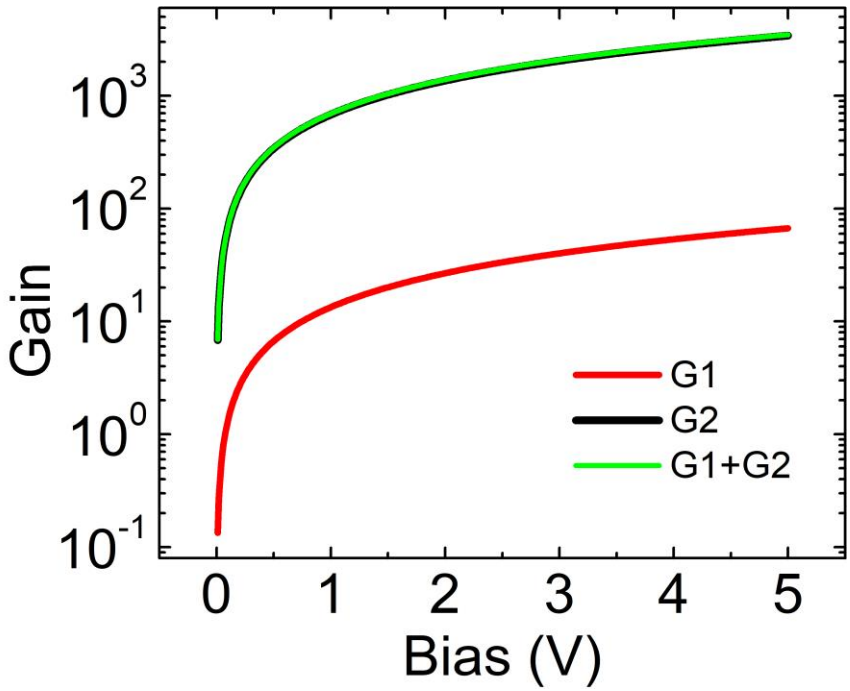

Figure 4.10 Calculated total photoconductive gain where G1 corresponds to transit time gain and G2 corresponds to surface modulation gain in accordance with Equation 4.6.

nanowire cross-section dominates the photoconductive gain. The value τ is taken as 1 ns, as measured by TRPL, in agreement with previous reports [104]. The transit time τ_t is calculated assuming a mobility of 550 $cm^2/V{\cdot}s$ in GaN. The power absorbed is estimated from the incident power and the absorption coefficient of $5x10^4$ cm^{-1} in InGaN [124]. The value of n is assumed to be $5x10^{17}$ cm^{-3}. A useful figure of merit for the performance of photodetectors is the noise equivalent power (NEP), which is a measure of the minimum detectable signal [125]. The calculated NEP for the measured devices is $7.8x10^{-12}$ $WHz^{-1/2}$ with 375 nm illumination at a bias of -3 V and 1 Hz, which corresponds to a detectivity, D^*, of $4.9x10^9$ $cmHz^{1/2}W^{-1}$ at room temperature. The values used for calculating NEP are provided in Table 4.1. Since these detectors are grown and fabricated on silicon, it is useful to compare the NEP with that of state-of-the-art

TABLE 4.1 Values for NEP Calculation.

Definition	Symbol	Value
Incident energy	hν	3.3eV
Incident steady-state power	P_0	1μW
Internal quantum efficiency	η	0.035
Gain	Γ_G	2000
Recombination Lifetime	τ	1ns
Conductivity of photoconductive region	G_c	5μS
Total light-induced current	I_0	230μA

visible silicon detectors, which is on the order of 10^{-16}-10^{-15} $WHz^{-1/2}$ for photodiodes [126-127]. GaP photodiodes used for ultraviolet detection have similar NEP metrics [128]. The calculated NEP is comparable to other GaN-based photodetectors [129-131] as well as PbSe, PbS, and ZnS quantum dot based photodetectors on silicon [132-138].

The transient device photoresponse was modeled considering the temporal modulation of the surface depletion of the nanowire. Following the analysis of Sanford [121], the device transient photocurrent is expressed as:

$$I_{ph}(t) = \frac{N_d \mu q A(t) V}{L} \tag{4.7}$$

where *A(t)* is the time-dependent undepleted cross-sectional area of the nanowire surface, μ is carrier mobility, V is bias, and N_d is the electron concentration. The term *A(t)* is calculated using the following rate equation:

$$\frac{dA(t)}{dt} = -\beta(t) A(t) n C_n \, exp\left(-\frac{\phi(t)}{kT}\right) \tag{4.8}$$

In this relation $\beta(t)$ is a dimensionless fitting parameter, and C_n is the electron-hole capture coefficient defined as $C_n = \sigma_n \sqrt{\frac{8kT}{\pi m}}$, where σ_n is the capture cross section, k is Boltzmann constant, T is the measurement temperature and m is the carrier effective mass. In Equation 4.8,

time dependent bending of the conduction band at nanowire surface is denoted as $\phi(t)$, which is obtained from the following relation:

$$\phi(t) = \frac{qn}{2\varepsilon}\left[\frac{R^2 - R_c^2}{2} - R_c^2\, ln\left(\frac{R}{R_c}\right)\right] \tag{4.9}$$

Here ε is material dielectric constant, R is radius of the nanowire and R_c is the radius of the effective conducting region under illumination. As has been described in the main text, R and R_c

TABLE 4.2 Parameter Values Used in the Photoresponse Analysis.

Definition	Symbol	Value
Bandgap of GaN	E_{gGaN}	3.39 eV
Electron Effective Mass (GaN)	me_{GaN}	$0.2m_0$
Heavy Hole Effective Mass (GaN)	mhh_{GaN}	$2m_0$
Light Hole Effective Mass (GaN)	mlh_{GaN}	$0.6m_0$
Lattice Constant (GaN)	a_{GaN}	0.3189 nm
Relative Permittivity (GaN)	ϵ_{GaN}	9.2
Bandgap of InN	E_{gInN}	0.77 eV
Electron Effective Mass (InN)	me_{InN}	$0.2m_0$
Heavy Hole Effective Mass (InN)	mhh_{InN}	$2.3m_0$
Light Hole Effective Mass (InN)	mlh_{InN}	$0.89m_0$
Lattice Constant (InN)	a_{InN}	0.3548 nm
Relative Permittivity (InN)	ϵ_{InN}	15.3
Conduction Band Offset	ΔE_c	$0.7E_g$
Valence Band Offset	ΔE_v	$0.3E_g$
Polarization charge density	P_{pol}	$6.3835\text{x}10^7$ C/cm^2
Polarization Electric Field	E_{pz}	51.6 MV/m
Bulk Recombination Lifetime in GaN	τ_b	0.2778 ns
Hole Diffusion Coefficient in GaN	D_p	$9\text{x}10^{-4}$ cm^2/s
Radiative Recombination Lifetime	τ_r	5.5 ns
Non-radiative Recombination Lifetime	τ_{nr}	1.3 ns
Shockley Read Hall Recombination Rate	U_{SRH}	10^8 s^{-1}
Carrier Concentration during Illumination	N_d	$3.95\text{x}10^{18}$ cm^{-3}
Carrier Concentration during Dark State	N_d	$2.8\text{x}10^{18}$ cm^{-3}
Capture Cross Section	σ_n	$3.5\text{x}10^{-22}$ cm^2

are obtained by self-consistent analysis using the approach described by Zhang [114]. The calculated transient photocurrent is plotted alongside the measured data in Figure 4.7(a). The values of parameters used in the different analyses and calculations are listed in Table 4.2.

Upon photoexcitation, electron-hole pairs are generated in the InGaN/GaN disk regions of the nanowires and they undergo drift and diffusion while being transported along the GaN nanowire sections to the opposite contacts. Normal photoconductive gain results from the imbalance of the electron-hole recombination lifetime and the transit time in the nanowires. Additionally, some holes are trapped in the nanowire surface states and modulate the conducting volume, thereby decreasing the resistance. The capture and emission processes also give rise to the transient photocurrent behavior shown in Figure 4.7(a).

Finally, it is worth mentioning that the strong peaks, attributed to interband transitions involving electron and hole bound states in the InGaN dots, observed in the photocurrent spectra at room temperature suggest that intersubband photoconductivity at infrared wavelengths may be measured in these photodetectors. Considering that the devices are grown and fabricated on silicon raises the possibility of a silicon-based infrared array imaging technology.

4.5 Summary

In conclusion, the characteristics of photoconductive detectors fabricated with InGaN/GaN disk-in-nanowire arrays grown on (001) silicon substrates by molecular beam epitaxy have been investigated. The measured photocurrent spectra at room temperature in the visible range exhibit distinct peaks which are attributed to interband transitions due to photon absorption involving quasi-bound states in the elongated quantum dots formed in the disk regions. The devices exhibit very large gains, largely due to modulation of the conducting cross-

section of the GaN nanowires upon photoexcitation caused by trapping of holes at the surface states. These devices are promising for silicon-based infrared (IR) detectors based on intersubband transitions within the InGaN disks.

Chapter V

Deep Ultraviolet Monolayer GaN/AlN Disk-in-Nanowire Array Photodiode on Silicon

5.1 Introduction

Solar-blind and visible-blind (~250-365 nm) photodetectors operating in the ultraviolet and deep-UV spectral ranges are important for oil spill, flame and missile detection [102, 139]. Integrated on a silicon complementary metal-oxide-semiconductor (CMOS) chip, the detectors can be useful for environmental sensing and security-related applications. While a Ag-doped Si visible-blind short-wavelength detector based on enhanced sub-bandgap photoresponse has been demonstrated, the materials of choice for such detectors are the III-nitrides [140]. Accordingly, Schottky barrier diodes, p-i-n diodes and avalanche photodiodes with GaN active region have been reported [131, 141]. The ternary alloy AlGaN with a bandgap larger than GaN is a more suitable material for the absorption region and the performance characteristics of high-gain AlGaN solar-blind avalanche photodiodes have been reported [142]. However, use of AlGaN alloys with high Al-content in the design and fabrication of photodiodes generally has a few drawbacks. First, the preferred choice of substrate is AlN/sapphire and not Si [143]. Second, p-doping of the AlGaN alloys remains to be a problem [73-74]. Finally, due to differences in the valence bandstructure between GaN and AlN, top-illumination of the photodetectors is not the preferred direction of excitation [65, 76].

It has been shown that GaN, InGaN and AlGaN nanowires grown on (001) and (111) Si have a very low density of extended defects due to the large surface-to-volume ratio [28, 92].

Additionally, the radial relaxation of strain during epitaxial growth leads to small polarization fields in the nanowire heterostructures [93, 107]. Chapters 3 and 4 report the photoluminescence characteristics of AlN nanowires containing GaN disks of one monolayer (ML) thickness [91] and an InGaN/GaN nanowire photodetector on silicon for UV-visible detection [116], respectively. Light-emitting diodes utilizing these GaN monolayers with sub-250 nm emission have also been demonstrated [144-145]. The ML GaN/AlN self-assembled disk-in-nanowire arrays are grown on Si substrates by molecular beam epitaxy. As a consequence of the extreme confinement in the ML GaN disk region the confinement energy of carriers in the disk is very large, leading to a large bandgap and exciton binding energy. An optical bandgap of 5.18 eV and an exciton binding energy of 260 meV have been measured at room temperature in the ML GaN, in excellent agreement with theoretical calculations [82-84]. The measured characteristics of a GaN/AlN disk-in-nanowire array photodiode on Si substrates, with ~2 ML GaN disks as the absorption media, are presented as reported in [146]. The devices are operated with top illumination and exhibit deep-UV photoresponse in the 200-300 nm spectral range.

5.2 Molecular Beam Epitaxy of Photodiode

The ML GaN/AlN disk-in-nanowire p-n diode arrays were grown on n^+ (111) Si substrates in a MBE system equipped with standard effusion cells and a radio-frequency (RF) nitrogen plasma source. Epitaxy was done in collaboration by Yuanpeng Wu in Prof. Zetian Mi's research group. The substrate temperature was monitored with an infrared pyrometer. Growth of the nanowire array was initiated with a 100 nm Si-doped GaN region at a substrate temperature of 780 °C. 150 nm of Si-doped AlN is then grown at 875 °C followed by the growth of 2 ML GaN at 870 °C and 10 nm AlN at 870 °C. The GaN/AlN is repeated 2 more times to have three 2

ML GaN disks. 40 nm of Mg-doped AlN is then grown followed by 3 nm of Mg-doped GaN to form the top p-contact layer. A schematic of the grown disk-in-nanowire array is shown in Figure 5.1.

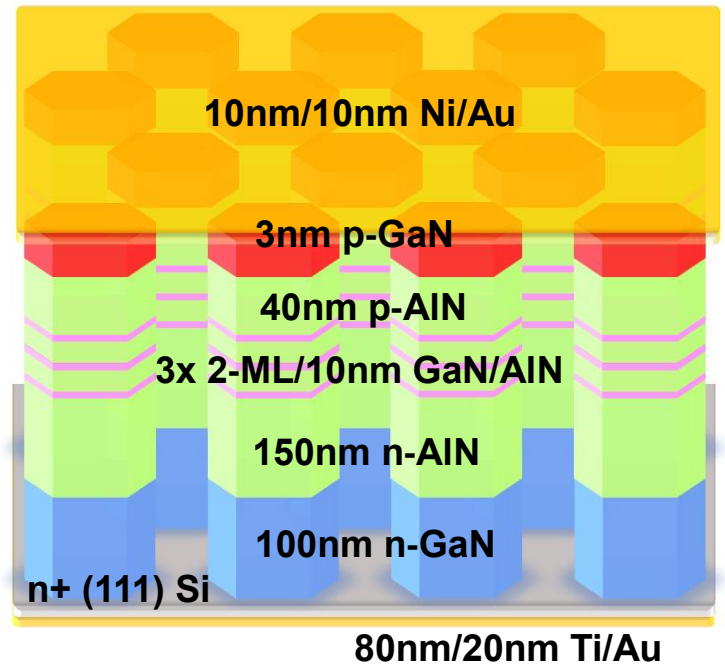

Figure 5.1 Schematic of fabricated disk-in-nanowire deep-UV photodiode epitaxially-grown on silicon.

5.3 Characterization of Monolayer Disk-in-Nanowires

TEM and SEM imaging of the nanowires is shown next for structural characterization. Photoluminescence measurements are then analyzed for characterization of the luminescence properties.

5.3.1 Structural Characterization

A scanning electron microscope image is shown in Figure 5.2(a). The average nanowire diameter is 35 nm and the area density is ~$2x10^{10}$ cm^{-2}. It may be noted that while a 1 ML GaN disk region would enable absorption at shorter wavelengths, the GaN disk thickness in this study

was chosen to be 2 ML to enhance light absorption and the corresponding photoconductivity. A high-angle annular dark field scanning transmission electron microscope (HAADF-STEM) image of a single AlN nanowire, grown under identical conditions with a ~2 ML GaN disk region is depicted in Figure 5.2(b). STEM imaging was performed at the Michigan Center for Materials Characterization. A STEM image of an AlN nanowire having 3 periods of 1-ML GaN, grown under identical conditions, is shown as an inset, repeated from Figure 3.1(a)(ii) for completeness.

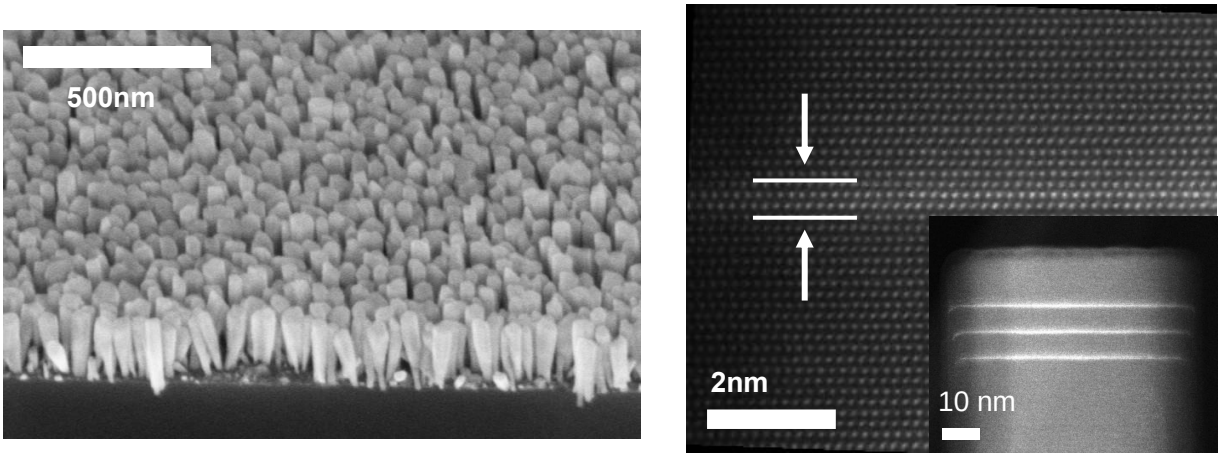

Figure 5.2 (a) Plan-view SEM image of the as-grown nanowire array. (b) STEM image showing formation of 2 monolayers of GaN within an AlN nanowire. Inset shows low-magnification image of all 3 periods for the case of 1-ML GaN. Courtesy of Yuanpeng Wu.

5.3.2 Optical Characterization

Photoluminescence (PL) and time-resolved photoluminescence (TRPL) measurements were performed with 6.2 eV (200 nm) excitation provided by the fourth harmonic output of an 80 MHz 100 fs Ti: sapphire laser, focused to a spot size of ~20 μm. The excitation was fixed to ~10 W/cm^2. Luminescence signals were analyzed by a 0.75 m monochromator with a resolution of 0.02 nm and detected by a UV-enhanced PMT. The transient signals from TRPL measurements were detected by a high-speed single photon counter with a temporal resolution of 50 ps. The

room-temperature photoluminescence spectrum is shown in Figure 5.3(a). The PL peak from the ML GaN disks is at 278 nm with a weak peak at 240 nm and a shoulder at 295 nm, which are believed to be due to monolayer fluctuations throughout the nanowire array. This will be discussed later in the context of the photocurrent spectra. Room-temperature PL spectrum for a Si-doped AlN nanowire array, grown under identical conditions, is shown as an inset. The peak is at 210 nm with no other transitions visible. The increase in signal after 300 nm is due to the 2nd harmonic of the 193 nm laser background. The measured and analyzed TRPL data at room temperature are shown in Figure 5.3(b). The transient response is analyzed using a bi-exponential decay model. The fast and slow recombination lifetime values are 240 ps and 1.08 ns respectively. The faster recombination time reflects screening of the built-in polarization and thus better overlap of the electron and hole wavefunctions. As carriers recombine, the field is slowly restored, resulting in a longer recombination lifetime.

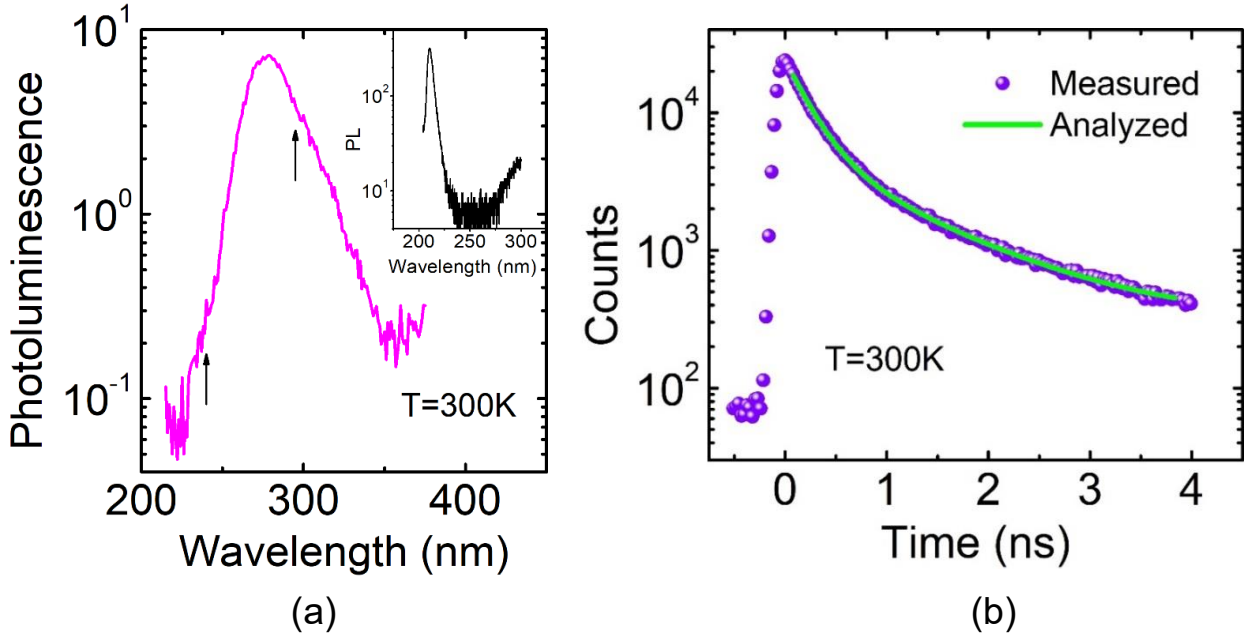

Figure 5.3 (a) Room-temperature photoluminescence spectrum of the nanowire array. Arrows indicate low and high energy shoulders. Inset shows room-temperature PL of Si-doped AlN nanowire array, courtesy of Yuanpeng Wu. (b) Measured and analyzed time-resolved photoluminescence of the as-grown nanowires.

Temperature-dependent photoluminescence is also performed using a continuous-flow liquid helium cryostat. The measured spectra are shown in Figure 5.4(a). The ratio of the PL intensities at 300 K and 4.3 K is 0.27 and the peak at 300 K is 4.63 eV. A blueshift with decreasing temperature is observed due to the temperature-dependence of the bandgap. This is plotted in Figure 5.4(b) and analyzed with the Varshni relation with α and β values of 2.76 meV/K and 2000 K respectively.

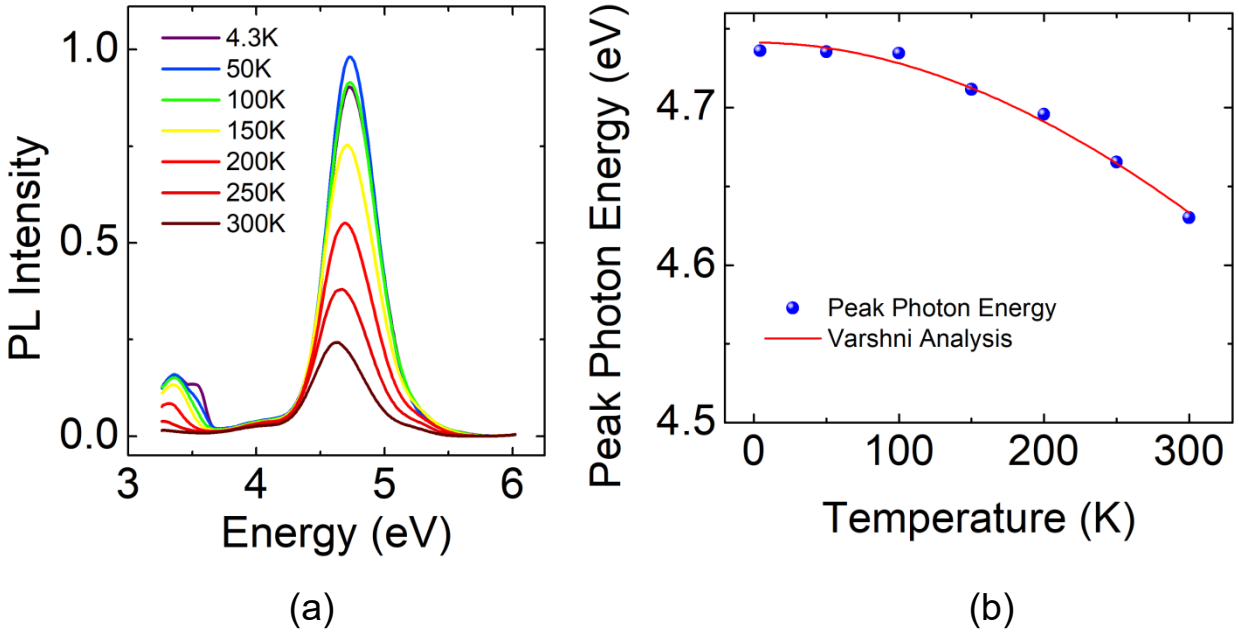

Figure 5.4 (a) Measured temperature-dependent photoluminescence of as-grown nanowire array and (b) peak emission energy as a function of temperature analyzed with the Varshni relation.

5.4 Photodiode Fabrication

Fabrication of the nanowire photodiodes is initiated by forming the top p-contact using standard photolithography. Mesa-shaped diodes of size 1 mm^2 and 0.09 mm^2 are defined with 10 nm Ni/10 nm Au p-contact metallization by electron beam evaporation. Following that, 80 nm Ti/20 nm Au is evaporated on the backside of the silicon substrate to form the n-contact. The

device structure is shown in Figure 5.1. The absolute value of the current-voltage characteristics of a 1 mm^2 nanowire photodiode measured at room temperature in the dark and under illumination (λ = 230 nm) are shown in Figure 5.5(a) in log scale. The reverse leakage current at -8 V bias is 100 nA and the turn-on voltage is ~4 V. It is noticed that the dark current and photocurrent cross over at a forward bias of 1.75 V, indicated by the arrow in Figure 5.5(a). This anomalous behavior results from a decrease of the series resistance upon illumination due to a reduction of the surface depletion layer width along the lateral surfaces of the AlN nanowires, caused by hole trapping at surface states and an effective increase of the nanowire conduction area [115-116]. The zero-bias resistance of the photodiode in the dark is ~ 1 GΩ, taken from the dynamic resistance shown in Figure 5.5(b), and the on-resistance is 60 Ω, taken as 1/slope of the I-V curve under high bias. The ideality factors are also extracted at low bias between 1-3 V and moderate bias of 3-5 V, indicated by the dashed lines in Figure 5.5(a). At low bias the ideality

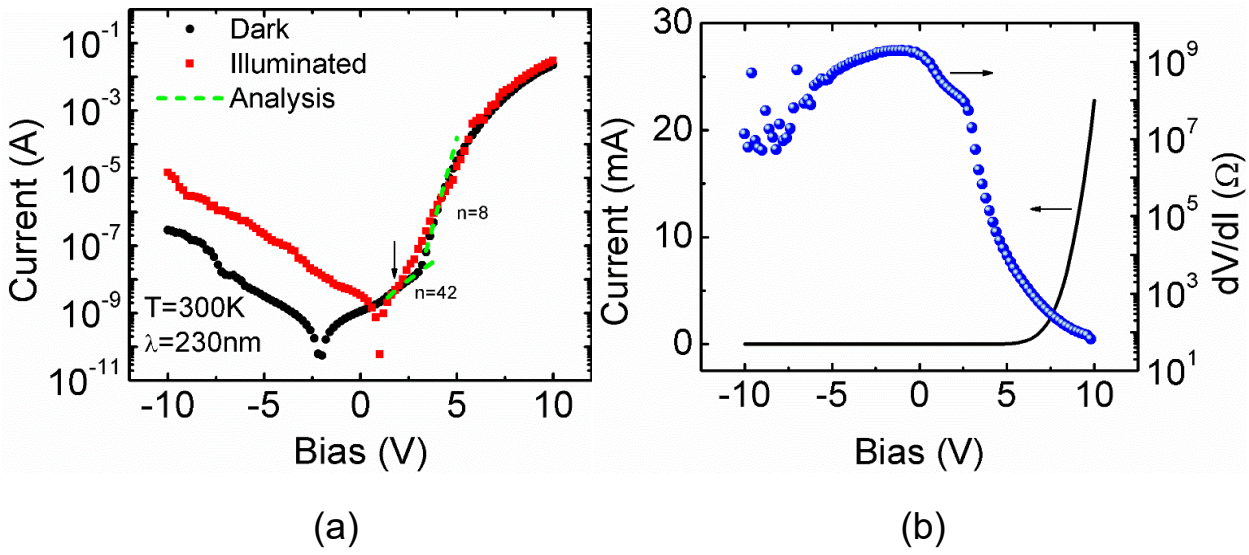

Figure 5.5 (a) Current-voltage characteristics of nanowire array photodiode under dark and illuminated conditions. Diode ideality factor analysis is shown for low and medium forward bias regions. Arrow indicates crossover voltage of 1.75 V. (b) Measured dynamic resistance in log scale and I-V characteristic in linear scale.

factor, n, is 42 while at moderate bias it decreases to 8. At low and high bias, the shunt and series resistance dominates, respectively, which causes the ideality factor to increase. At moderate bias, the space charge region controls the diode characteristics and the ideality factor is at a minimum. High values of the diode ideality factor are common in III-nitride heterostructures and are typically due to the existence of several junctions, as well as the high activation energy of Mg in $Al_xGa_{1-x}N$ which may cause p-doping difficulty, and non-idealities in the ohmic contacts [147-148]. The measured $1/C^2$ characteristics are shown in Figure 5.6 for the 1 mm^2 device.

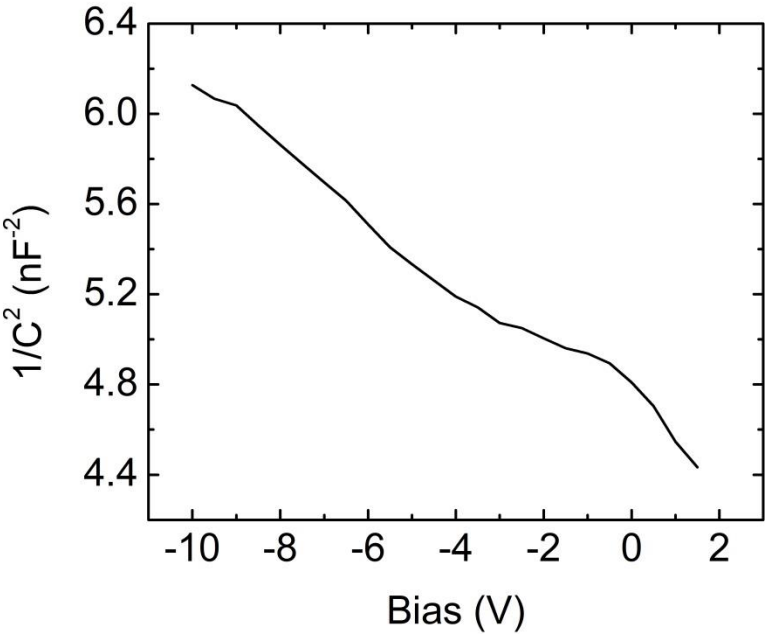

Figure 5.6 Measured room-temperature $1/C^2$ versus voltage characteristics under dark conditions for the 1 mm^2 device.

5.5 Photodiode Characteristics

Photocurrent spectra of the nanowire photodiode have been measured with a picoammeter and voltage source. Excitation is provided by focusing the output of a tunable xenon light source onto the top surface of the photodiode mounted on a thermoelectric cooler.

Measured spectra as functions of reverse bias and temperature are shown in Figures 5.7(a) and (b), respectively. The sharp cutoff below ~200 nm is due to the short wavelength limitation of the xenon light source. The general nature of the spectra are similar. The main peak is at 240 nm with weak shoulders at 206, 280 and ~360 nm. The overall photocurrent is generated by photoexcited carriers in the AlN nanowires and those from the ML GaN disks being emitted to the AlN nanowire regions and transported to the respective contacts. While carrier generation in

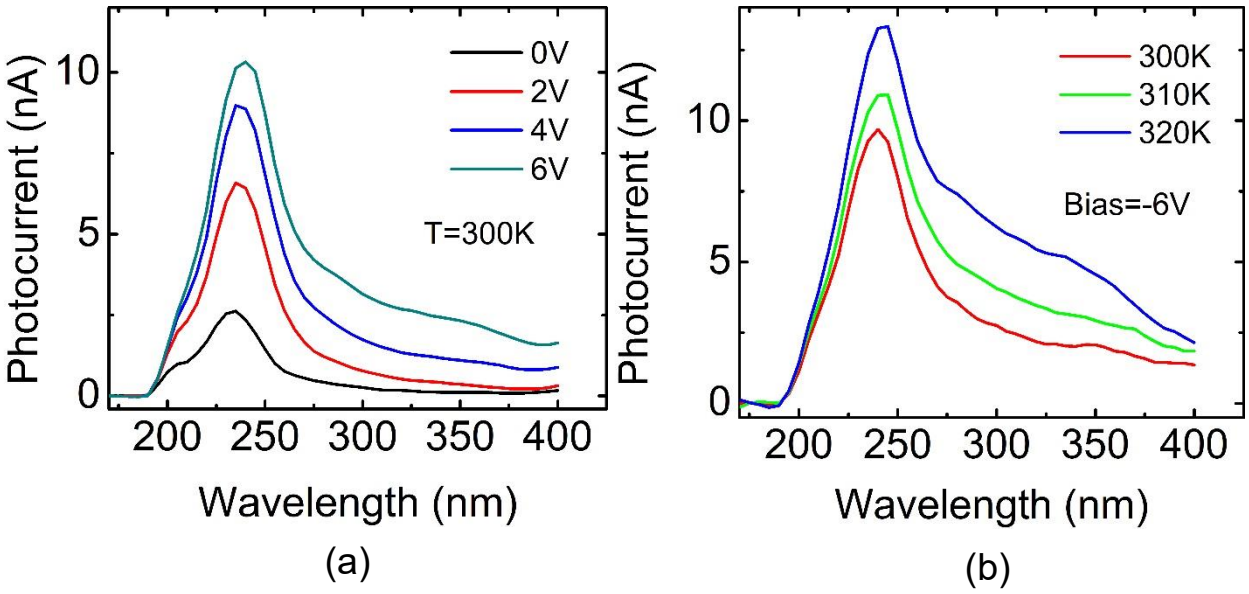

Figure 5.7 Measured photocurrent spectra (a) as a function of reverse bias at room temperature, and (b) as a function of temperature at 6 V reverse bias.

AlN nanowires is self-explanatory, the photocurrent from the ML GaN disks is not obvious. The exciton binding energy measured and calculated for 1-ML GaN disks are ~160-260 meV and 210 meV and for 2-ML GaN are ~230 meV and 170 meV, respectively [83, 91]. These energies are ~10X larger than kT at room temperature. The observed photocurrent from the ML GaN disk regions can only be attributed to free carriers resulting from exciton dissociation. A favorable mechanism for this is tunnel-assisted dissociation where the potential tunnel barrier formed at the GaN/AlN interface is of very small thickness due to the extremely large polarization field [83].

Photocurrent generation in monolayer Wse_2 has also been attributed to a similar tunnel-assisted dissociation of the two-dimensional excitons therein [149]. The small temperature dependence of the photocurrent from the disks at 240nm and 280nm observed in Figure 5.7(b) is attributed to thermally-assisted tunneling across the thin tunnel barrier. The peak of the photocurrent at 240 nm and the shoulder at 280 nm (which coincides with the PL peak of Figure 5.3(a)) are in excellent agreement with the values of the optical bandgap of 1 ML (5.23 eV) and 2 ML (4.52 eV) GaN surrounded by thick AlN barriers, derived from atomistic calculations based on density functional and many-body perturbation theories [82-83]. The shoulders at 206 and ~360 nm likely result from absorption in the AlN and GaN nanowire regions. The strong peak at 240 nm is a result of the large oscillator strength of the transition in 1 ML GaN disks and the weak peak at 280 nm is a reflection of the smaller oscillator strength, due to weaker electron-hole wavefunction overlap, in the 2 ML GaN disks. On the other hand, due to the lower energy, the transition at 280 nm is observed as a peak in the steady-state photoluminescence spectrum of Figure 5.3(a). From the bias-dependent photocurrent spectra in Figure 5.7(a), it is evident that the blue shift of the 240 nm peak is smaller than that of the 280 nm shoulder. The polarization field and the resulting quantum confined Stark effect (QCSE) are very large for the GaN/AlN heterostructure, but the blue shift will be small due to the extreme confinement. Therefore the blue shift is smaller for 1-ML GaN (240 nm) than that for 2-ML GaN (280 nm). The photocurrent near the 206 nm shoulder from the AlN region also saturates as the reverse bias increases. This can be explained by carriers in the AlN continuum reaching saturation velocity. The photoluminescence and photocurrent spectra confirm that the AlN nanowire array contains a mixture of 1-2ML-thick GaN disk regions, due to fluctuations in growth parameters, although the intended thickness of the disks was 2 ML. The strain should ideally be similar across all 3

disk regions despite the 1-2 ML fluctuation in growth. No photocurrent response was observed from 400-1700 nm.

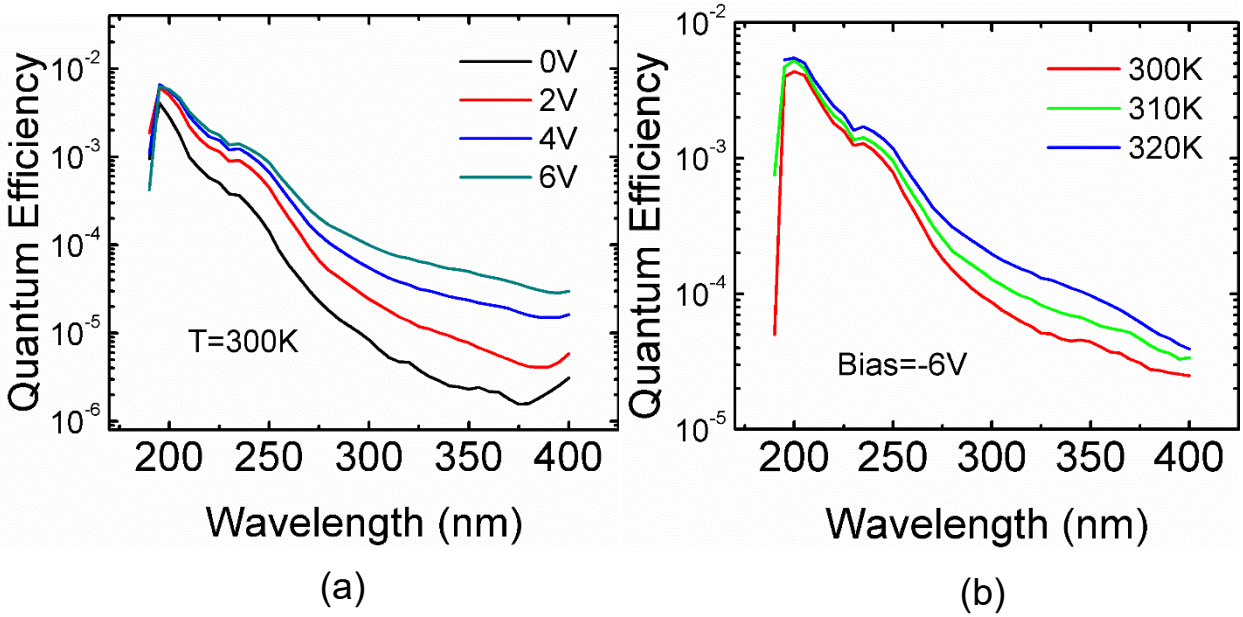

Figure 5.8 (a) Calculated quantum efficiency as a function of reverse bias. (b) Calculated quantum efficiency as a function of temperature at -6 V.

The quantum efficiencies calculated from the photocurrent data of Figure 5.7(a)-(b) are shown in Figure 5.8(a)-(b) respectively. First, the measured photocurrent is normalized by the power spectrum of the xenon light source at the sample, shown in Figure 5.9, to obtain the responsivity, $\mathscr{R}$, which is measured using a calibrated UV-enhanced silicon photodiode. Then, the quantum efficiency, η, is found from η = 1240 x ($\mathscr{R}$ / λ), where λ is the incident wavelength in nm. The noise equivalent power (NEP) can be found as $NEP = \frac{h\nu}{q\eta}\left[2q\left(I_{ph} + I_D\right) + \frac{4kT}{R}\right]^{1/2}$, where hν is the incident light energy, q is the elementary charge, I_{ph} is the photocurrent, I_D is the dark current, k is the Boltzmann constant, T is temperature, and R is the diode resistance. With a quantum efficiency of 0.6 % at 300 K for 6.2 eV incident light and 100 MΩ resistance at -6 V, and the sum of I_{ph} and I_D of 4.8 nA, the NEP is calculated to be 4.3×10^{-11} W/Hz$^{1/2}$. It is important

to note that the responsivity and quantum efficiency of the photodiode are largest for the AlN

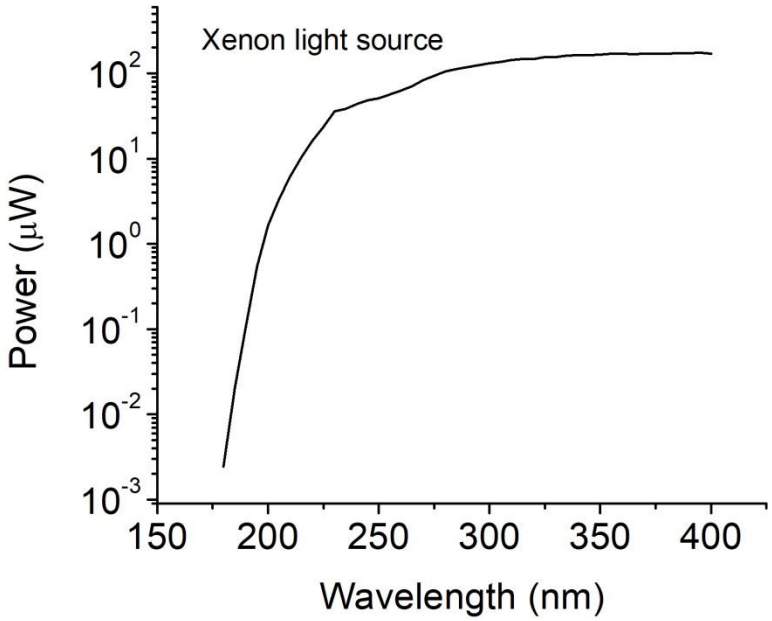

Figure 5.9 Measured output power of the xenon light source at the sample stage.

nanowire region of the photodiode and smaller for the GaN disk region because of the very small absorption thickness. A larger number of disks would result in higher photocurrent values. However, the objective in this study was to study the spectral nature of the photocurrent in comparison with calculated optical and electronic bandgaps of GaN disks of ML thickness with AlN barriers.

The frequency response of a 0.09 mm^2 photodiode, biased at 0 V, is measured using a lock-in amplifier and an AOM (acousto-optic modulator) with a bandwidth of 8 MHz. The smaller diode is chosen to minimize the RC time constant. The amplitude of the incident light is modulated using the AOM by varying the frequency. The light source is provided by ~100 μW of 6.2 eV emission from the Ti: sapphire laser. The response is shown in Figure 5.10. The -3 dB bandwidth is measured to be ~120 kHz. The measured zero-bias capacitance of this diode is 47

pF, as opposed to 460 pF for the larger 1mm^2 device. With a resistance of ~40 kΩ measured near the diode turn-on voltage at 4 V, the RC time constant is 1.9 μs. Assuming $f_{-3dB} \sim 1/2\pi\tau$, the cutoff frequency is estimated to be ~85 kHz, which is in good agreement with the measured bandwidth. Due to the large size of these devices, the photodiode bandwidth is believed to be RC-limited.

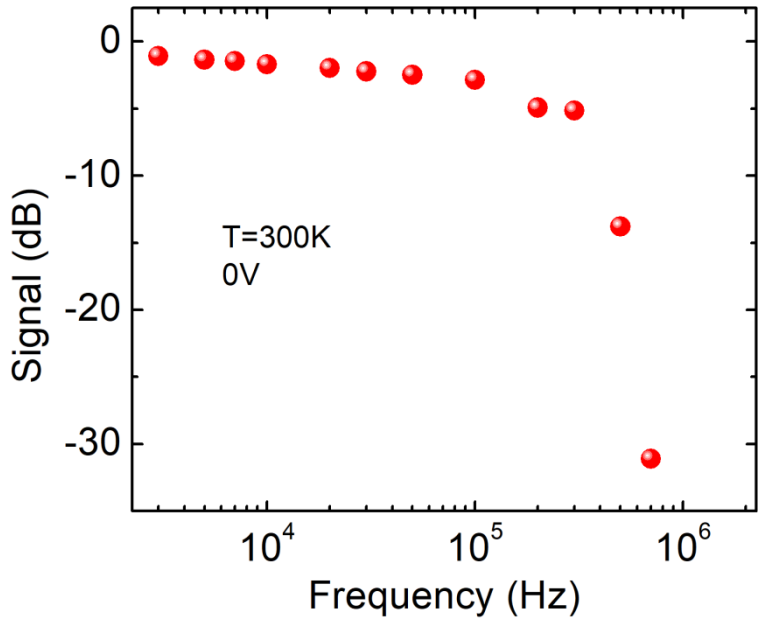

Figure 5.10 Measured frequency response of the monolayer GaN/AlN nanowire array photodiode at 0 V.

5.6 Summary

To summarize, the characteristics of AlN nanowire array p-n junction photodiodes have been investigated in which nominally 2-monolayer thick GaN disks are inserted as the light absorbing media. The nanowire arrays were grown on silicon substrates by plasma-enhanced molecular beam epitaxy. Photocurrent spectra have been measured with top illumination as a function of ambient temperature and bias and comparison of these with photoluminescence spectra from the same nanowire arrays suggests that both one- and two-monolayer thick GaN disks are present in the excitation volume. The observed photocurrent behavior has been

attributed to a thermally-assisted tunneling mechanism for exciton dissociation. With optimization of the device heterostructure and increased number of GaN disks, a high-efficiency deep-UV photodetector could be realized.

Chapter VI

InGaN Quantum Dot Characteristics and Photonic Devices on Silicon with Coalesced GaN Buffer Layers

6.1 Introduction

A reliable GaN-based heterostructure technology on inexpensive silicon substrates would be advantageous for high-power switching applications, visible silicon photonics and optoelectronic integration [12, 105, 107, 116, 146, 150-159]. Almost all electronic and optoelectronic GaN-based devices are grown on expensive sapphire and SiC substrates. Growth of high quality GaN on Si is difficult with the 17 % lattice mismatch and differences in thermal expansion coefficients and crystal structure. The growth technique most commonly used is organometallic vapor phase epitaxy (OMVPE). At the high growth temperatures used in this technique, a robust nitridation reaction results in the formation of an insulating Si_xN_y layer on all the exposed regions of the Si substrate [160]. Furthermore, when low-temperature GaN (LT-GaN) is used as a buffer layer to minimize the defect density, the generation of Ga between the LT-GaN and Si substrate can result in meltback etching of the substrate [161]. Intermediate, or seed layers such as AlN and AlGaN have been used to alleviate these problems [162-163]. Patterned substrates and compliant buffers have also been used with various degrees of success.

In the molecular beam epitaxy technique, epitaxial growth of III-nitride compounds is undertaken at relatively lower temperatures. Furthermore, this technique enables the growth of GaN, Ga(In)N and Al(In)N nanowire arrays, self-assembled or patterned, on Si or sapphire substrates [27, 93, 164-168]. The large surface-to-volume ratio of the nanowires leads to a

reduced density of extended defects [28, 169-170]. Strain relaxation during growth of the nanowires results in a smaller polarization field [93, 107]. III-nitride nanowire arrays and single nanowires grown on Si have therefore been attractive materials for the fabrication of lasers [63, 107, 171], light-emitting diodes [93, 104-105, 144, 172-173] and photodiodes [108, 116, 146, 174-175]. Controlled coalescence of GaN nanowire arrays during epitaxy on Si, ultimately leading to a planar GaN layer, has also been demonstrated together with their structural and optical properties [176-177]. However, the formation of cracks and a large defect density in these coalesced buffer layers have probably precluded the realization of electronic or optoelectronic devices on them. In the present study device-quality GaN buffer layer has been formed on Si substrates with an intermediate AlN seeding layer followed by coalescing of densely packed short GaN nanowires. InGaN/GaN quantum dot (QD) LED heterostructures have been grown and fabricated on the GaN/Si buffer layers and their characteristics are presented. In effect, a potentially promising technology for visible silicon photonics is presented. Lastly, pump-probe spectroscopy is performed on InGaN/GaN QDs grown on GaN/sapphire substrates. In this investigation the hot carrier relaxation dynamics have been studied in $In_{0.27}Ga_{0.73}N$/GaN quantum dot heterostructures by ultrafast pump-probe differential absorption ($\Delta\alpha$) spectroscopy. Both spectral and kinetic measurements have been made as a function of probe delay time, temperature and pump power. The results have been analyzed and discussed. Uniquely, very strong excited state absorption in the InGaN/GaN QD heterostructures is observed.

6.2 Coalescing of GaN Nanowires

The lateral growth rate of gallium nitride nanowires epitaxially-grown on silicon can be controlled in-situ during growth by carefully tuning the growth temperature. Continued growth

of GaN with this method leads to a controlled coalescence of the nanowires and eventually a planar GaN film. This method of growth is often called lateral epitaxial overgrowth (LEO) or pendeoepitaxy. By growing long GaN nanowires and lowering the growth temperature, one may take advantage of the coalescing mechanism during growth and achieve single-crystalline GaN templates on silicon. An example of this technique is shown here. Growth of GaN nanowires on silicon has been previously covered in Chapters 1-2. The GaN template starts with the growth of ~1.8 μm long GaN nanowires over (001) silicon at 800 °C with a Ga flux of $1.6x10^{-7}$ Torr. The N_2 and RF plasma power are held at 1 sccm and 380 W respectively. Following growth of the nanowires, the growth temperature is lowered to 600 °C while all other growth parameters remain unchanged. This enhances the lateral growth rate of the nanowires and starts the coalescence process. The thickness of the 2D coalesced template is ~1 μm. SEM images at 45 ° and at the edge are shown in Figures 6.1(a)-(b) respectively.

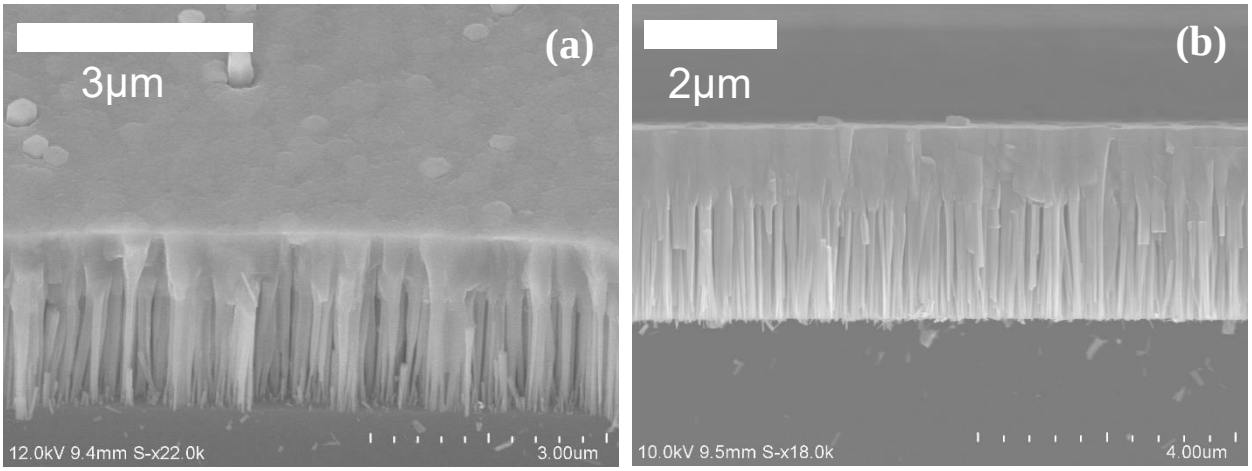

Figure 6.1 (a) Plan-view SEM image of the unannealed GaN template on silicon. (b) Edge-view of the GaN template.

Increasing the growth temperature as a final step in the growth process improves the crystallinity and anneals defects present in the low-temperature growth of the gallium nitride,

such as stacking faults caused by the nanowire coalescing. Growth was initiated as before with an additional growth step at 730 °C with a Ga flux of $1.8 \cdot 10^{-7}$ Torr for 2 hours. An SEM image of this annealed GaN template is shown in Figure 6.2. Continued growth would smoothen the surface and improve the crystallinity.

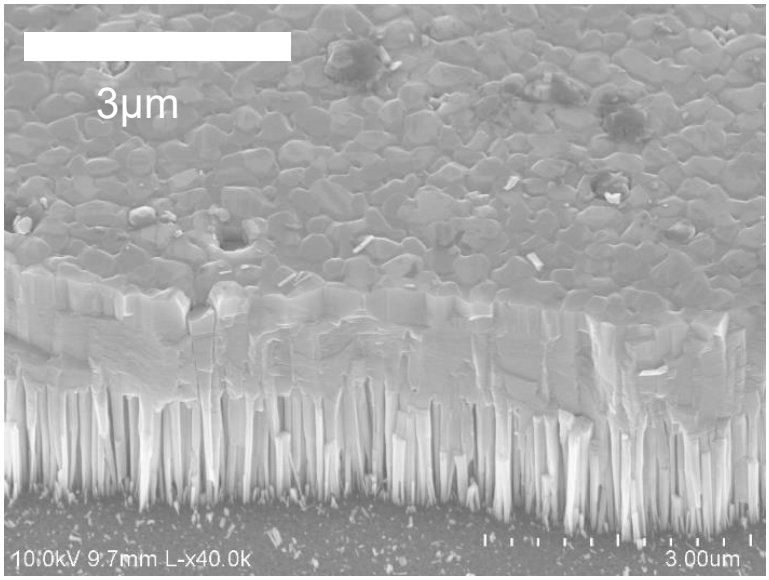

Figure 6.2 Plan-view SEM image of the annealed GaN template on silicon.

The photoluminescence spectra of the as-grown GaN nanowires at 10 K is shown in Figure 6.3. At low temperature, bulk-related exciton peaks emerge. Below 3.44 eV, there is a broad shoulder which is related to the surface states of the nanowires. These nanowires grow nearly defect-free along the c-axis in the Volmer-Weber growth mode. The PL spectra of the unannealed coalesced GaN template is shown in Figure 6.4. Low-temperature growth of this template results in a cubic phase (zinc-blende) GaN, with the luminescence peak at 384 nm (3.2 eV), which has been previously verified by the SAD (selected area diffraction) pattern by Dr. Wei Guo from our research group. The growth is not stable in this state and the material has a large density of defects. In addition, the PL intensity is weak and the linewidth broad compared to that of wurtzite GaN.

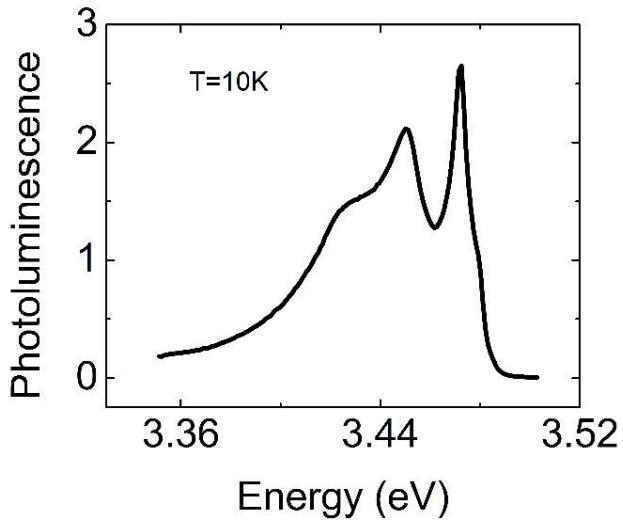

Figure 6.3 Photoluminescence of as-grown GaN nanowires at 10 K. The bulk-related excitons can be seen in the spectra. The broad shoulder below 3.44 eV is related to the surface.

After growing the template an additional two hours at 730 °C as an annealing step, the photoluminescence peak shifts to that of hexagonal (wurtzite) GaN and becomes narrower. The peak at room temperature is 364 nm and is shown in Figure 6.5 with the nanowire PL for comparison. Both are similar in intensity and linewidth, an indicator of good crystalline quality.

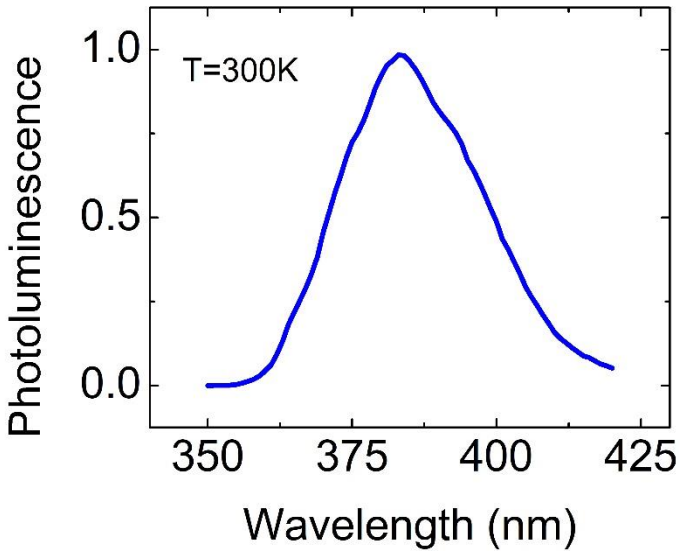

Figure 6.4 Room-temperature PL of the unannealed GaN template grown on (001) silicon.

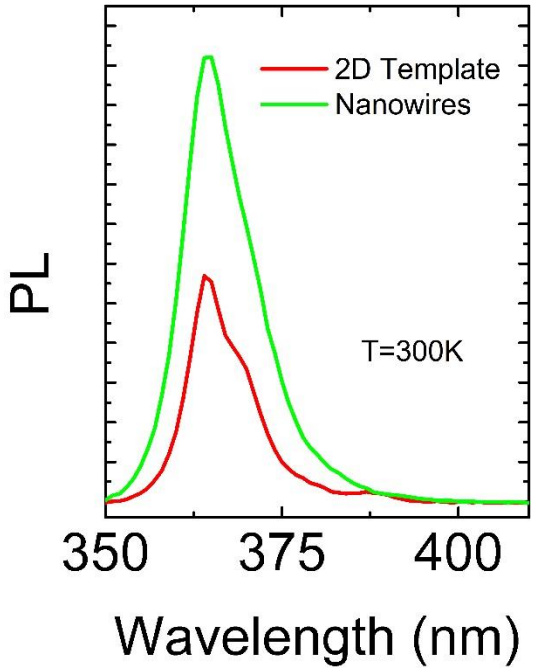

Figure 6.5 Room-temperature PL of the annealed GaN template grown on (001) silicon.

6.3 Epitaxy of GaN Buffer and InGaN Quantum Dots

Epitaxial growth of the GaN buffer layer and the following LED heterostructure on (111) Si substrates has been carried out in a Veeco Gen 930 MBE system equipped with a radio frequency (RF) nitrogen plasma source. The Si (111) plane is favorable for the growth of GaN along the c-axis in the wurtzite crystalline form. The buffer optimization was done in collaboration with Dr. Debabrata Das at The University of Michigan. The growth of the entire buffer layer was done at the relatively low temperature of 740 °C. A thin (~2 nm) AlN layer is first grown under nitrogen-rich conditions (Ga: $9x10^{-8}$ Torr; N: 1 sccm) to reduce the heteroepitaxial strain, followed by an array of short (10-15 nm) GaN nanowires with large area density. The low substrate temperature and nitrogen-rich ambient promote the increase of nanowire diameter and coalescence almost from the moment of initiation of nanowire growth. A planar GaN layer (~300-400 nm) is next grown on top of the coalesced nanowires. This layer is grown in six equal thickness steps with increasing III/V ratio, starting with Ga: $1x10^{-7}$ Torr, N:

0.8 sccm for the first step and ending with Ga: $2x10^{-7}$ Torr, N: 0.3 sccm for the last step. There is a 15 s pause every 5 min after each step for the removal of any surface Ga droplets and to get rid of GaN nanocrystals that may form due to the changing III/V ratio [178]. The thin GaN layers with varying III/V ratio and the interfaces in between effectively help in defect filtering. Finally a ~1 µm GaN layer is grown under Ga-rich conditions with multiple pauses in the growth for

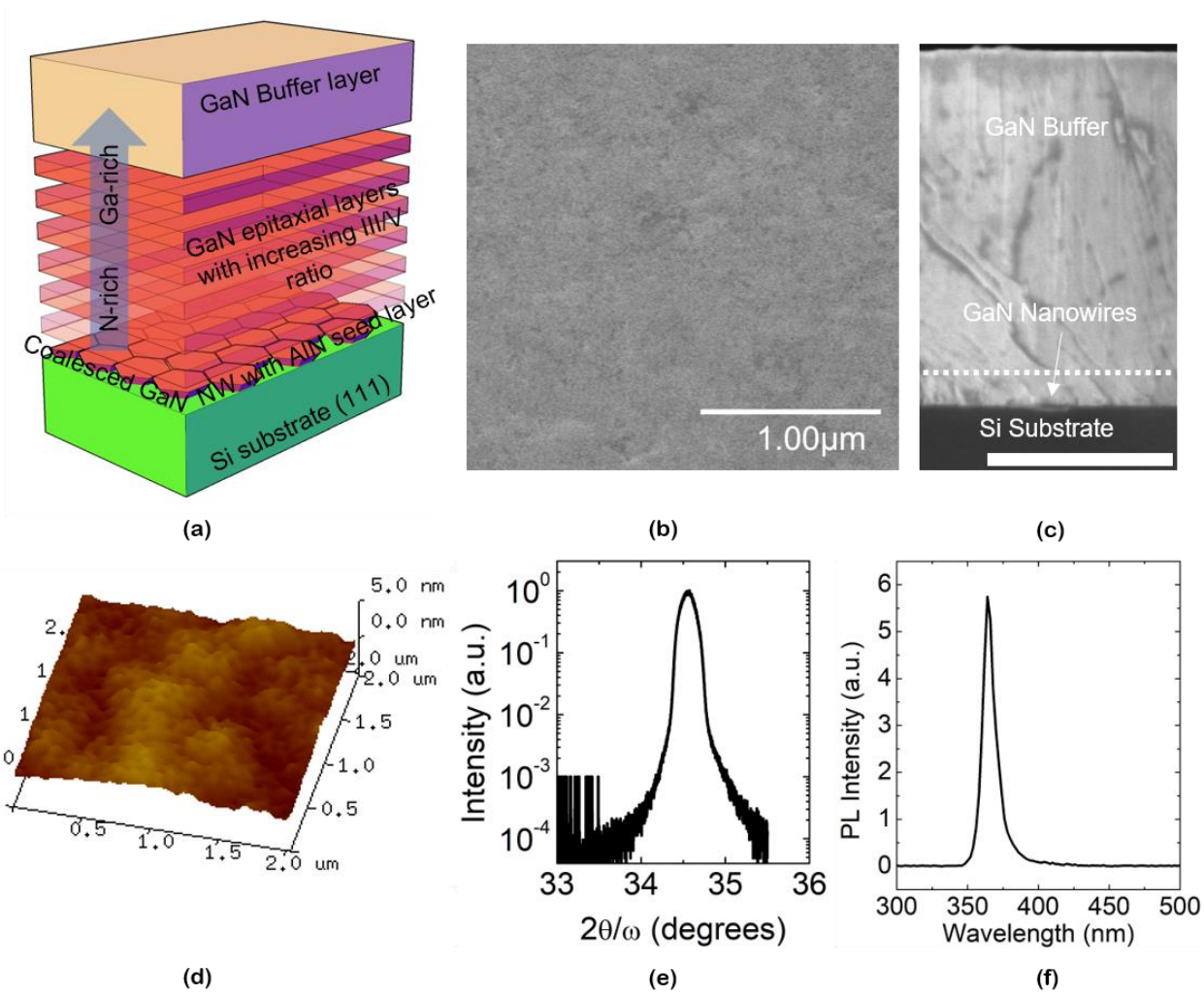

Figure 6.6 (a) Schematic of planar GaN buffer technique grown over a silicon substrate. (b) SEM image of final planar GaN buffer which shows smooth morphology. Image courtesy of Debabrata Das. (c) Cross-sectional SEM image of the full buffer structure. The dashed line indicates the transition between the GaN nanowires and the coalescing epitaxial layers. Scale bar is 500 nm. (d) 2 µm x 2 µm AFM image of the surface for the final GaN buffer. (e) XRD rocking curve of the final GaN buffer layer. Linewidth is 720 arcsec. (f) Room-temperature PL of the GaN buffer.

elimination of possible surface Ga droplets. The entire buffer heterostructure described above is schematically shown in Figure 6.6(a). The surface scanning electron microscope image of Figure 6.6(b) displays a smooth GaN surface and the cross-sectional SEM image of Figure 6.6(c) indicates a low density of extended defects. SEM imaging was done by Debabrata Das. A surface root mean square (rms) roughness of 0.562 nm is derived from the atomic force microscope image of Figure 6.6(d). The x-ray diffraction data of Figure 6.6(e) demonstrates the high crystalline quality of the GaN buffer layer and the excellent optical quality of the layer is confirmed by the room temperature photoluminescence spectrum of Figure 6.6(f). The peak of the spectrum is at 364 nm and linewidth (full width at half maximum) is 10 nm.

Six periods of $In_{0.23}Ga_{0.77}N$/GaN quantum dots were then grown atop the GaN/Si template. First, an undoped 200 nm GaN buffer was grown at 700 °C under slightly Ga-rich

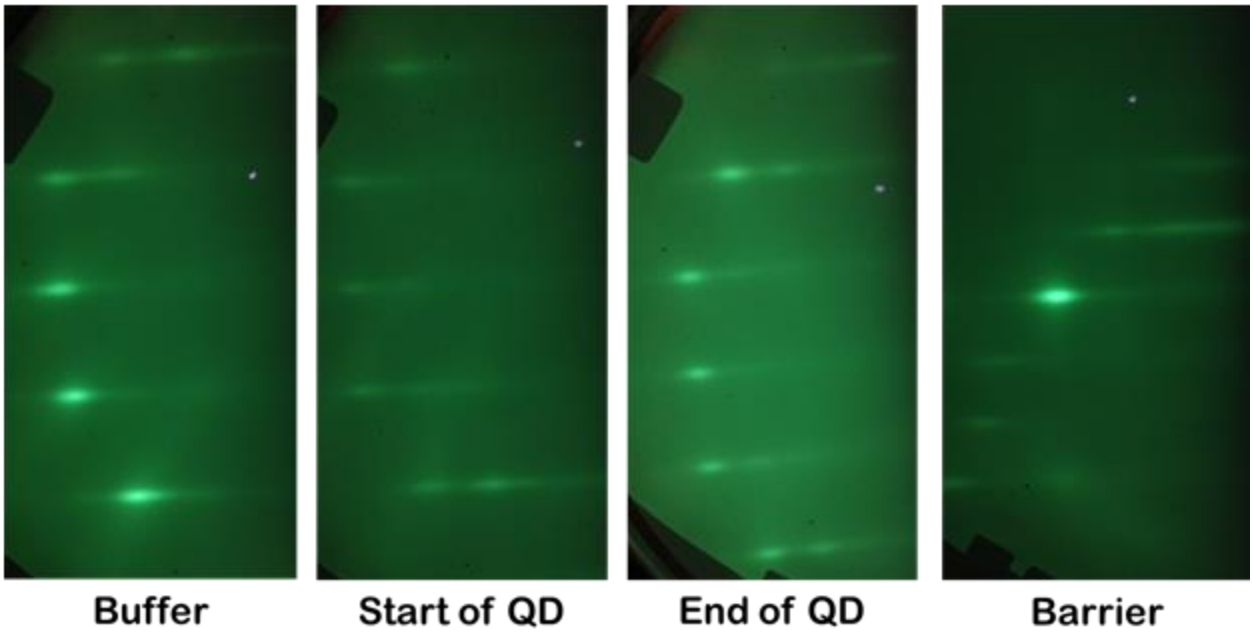

Figure 6.7 RHEED patterns during each layer of the heterostructure. Buffer and barrier images are taken at the end of the layer step.

conditions with periodic interruptions. The growth temperature was then lowered to 540 °C to allow sufficient In incorporation without degrading material quality and the $In_{0.23}Ga_{0.77}N$

quantum dots were grown under N-rich conditions at Ga and In beam equivalent pressures of $3.1x10^{-8}$ Torr and $1.3x10^{-7}$ Torr, respectively. Each dot layer was separated by a 10 nm GaN barrier grown under nearly stoichiometric conditions to recover a smooth surface while preventing any excess gallium from accumulating on the surface. The RHEED was closely monitored during each layer and the patterns are shown in Figure 6.7. The final dot layer was left uncapped for AFM imaging. An AFM image of the uncapped dots is shown in Figure 6.8. The surface is characterized with a rms roughness and average dot height of 0.941 nm and 2.5 nm, respectively. The area density is ~10^{10} cm^{-2}. Several of the dots appear to be merged into large clusters. This is a result of Ostwald ripening which occurs during the interruption step under

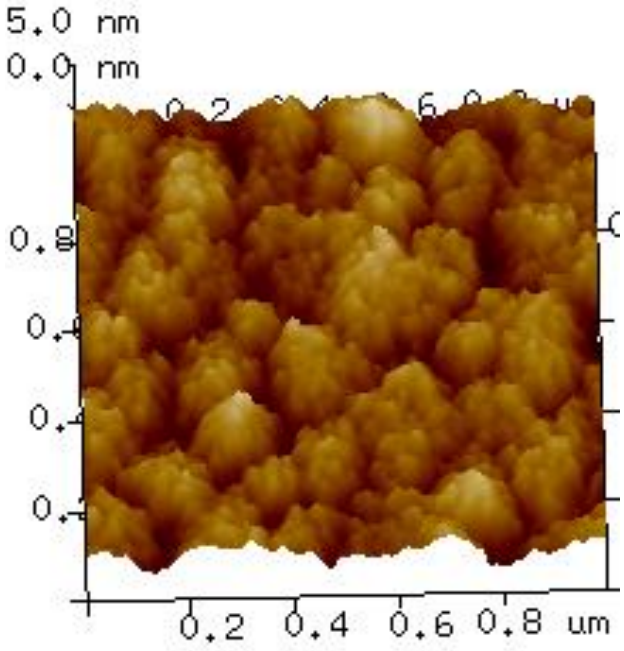

Figure 6.8 Atomic force microscopy 1 μm x 1 μm 3D scan of the uncapped InGaN/GaN quantum dots. AFM operated in-air with tapping mode.

nitrogen plasma. Temperature-dependent PL measurements were performed by mounting the sample in a closed-cycle He cryostat and excitation provided with 1 mW of the frequency-tripled 266 nm output of a Ti:sapphire laser. The measured data are shown in Figure 6.9(a). The room-temperature peak is centered at 475 nm. The internal quantum efficiency (IQE) is estimated to be

25 %, taken as the ratio of the integrated PL intensity at 300 K and 13 K. Strong oscillations are observed in the measured spectra due to reflections at the GaN/Si interface. Weak GaN emission is visible at lower temperatures, as most of the radiative recombination takes place within the quantum dots. The small peak at ~535 nm is from the exciting laser. The measured and analyzed integrated PL intensity versus inverse temperature is plotted in Figure 6.9(b), normalized to the intensity at 13 K. An activation energy of 53 meV is extracted, which agrees well with previous reports of InGaN quantum dots [179-180]. Temperature-dependent time-resolved

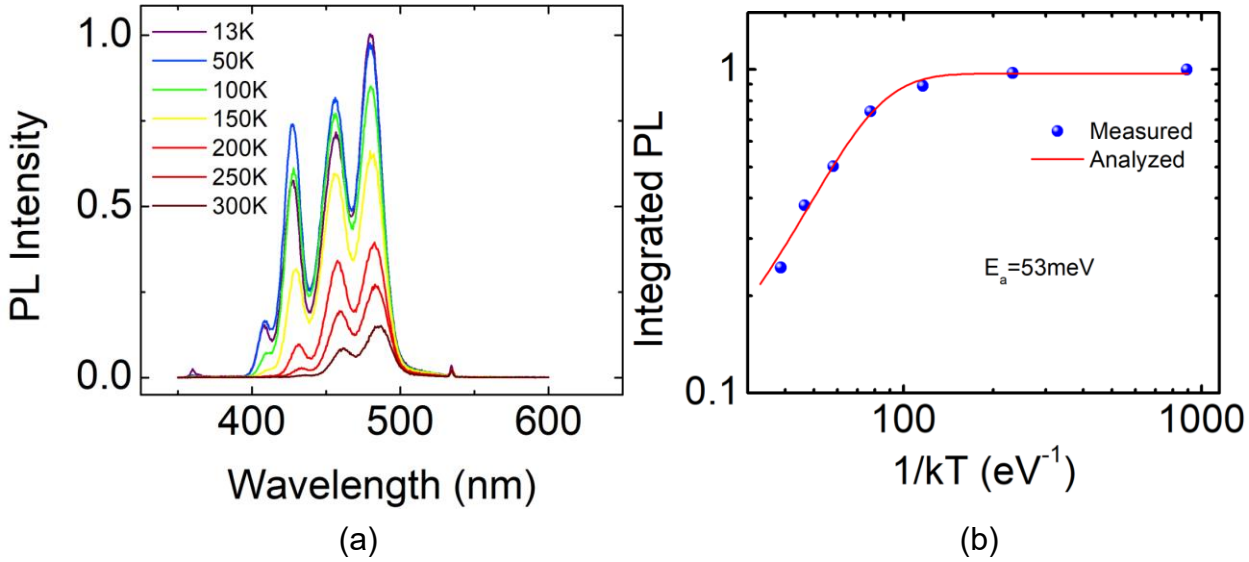

Figure 6.9 (a) Temperature-dependent photoluminescence of the InGaN/GaN quantum dots grown over the GaN/Si template. (b) Measured and analyzed Arrhenius plot of the integrated photoluminescence intensity. The extracted activation energy is 53 meV.

photoluminescence measurements were made on the quantum dots using the same laser excitation. The luminescence was detected using a high-speed single photon detector with a temporal resolution of ~50 ps. The recombination lifetime, τ, was extracted using the stretched exponential function, $I \propto \exp-(t/\tau)^{\beta}$, where I is the measured intensity and β is a measure of the polarization field and compositional fluctuations within the quantum dots. The value of β is ~0.7 in this analysis. At 300 K, the measured lifetime is 600 ps. The radiative lifetime, τ_r, is

calculated assuming all non-radiative channels are frozen at 13 K in accordance with $\tau_r = \tau/\eta$, where η is the IQE. The non-radiative lifetime, τ_{nr}, is calculated from $\frac{1}{\tau} = \frac{1}{\tau_r} + \frac{1}{\tau_{nr}}$. These are plotted in Figure 6.10. At 300 K, the radiative and non-radiative lifetimes are 2.4 ns and 800 ps,

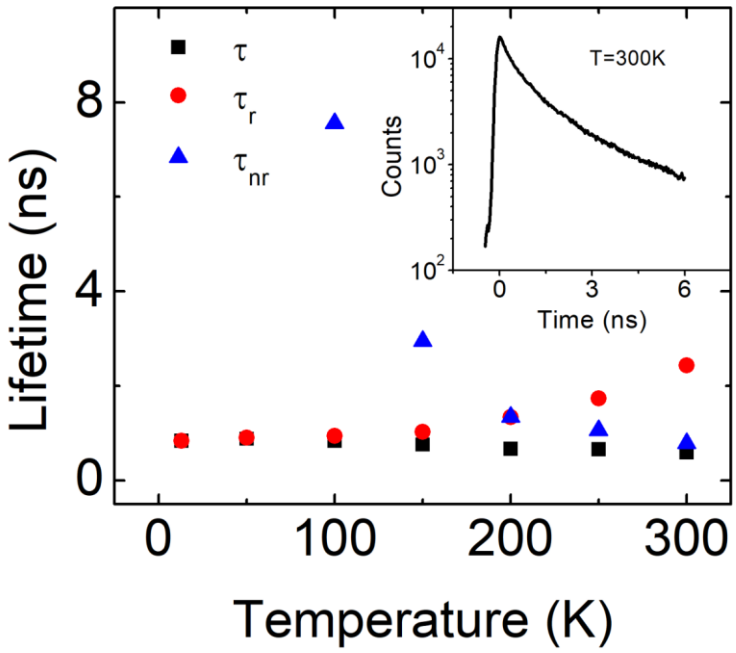

Figure 6.10 Time-resolved photoluminescence lifetimes as a function of temperature taken at the peak of the luminescence. Inset shows a measured transient at 300 K.

respectively. The transient PL signal measured at room-temperature is shown in the inset. The radiative lifetime increases with temperature, which has been previously observed in InAs/GaAs quantum dots [181-182] and InGaN/GaN dot-in-nanowires [28]. At low temperatures, holes in the ground state scatter with hot electrons. The electrons relax to the ground state and the holes are excited to higher energy levels, from which they relax rapidly by multi-phonon emission. However, as the temperature increases, some of the ground state holes are excited to higher energy levels, thus reducing the number of holes available to scatter with hot electrons. This causes a reduction in the electron-hole radiative recombination rate and an increase in τ_r.

6.4 Epitaxy and Fabrication of LED Heterostructure

A blue-green LED heterostructure, shown in Figure 6.11(a), was grown on the GaN/Si template and the device was fabricated. A 500 nm thick Si-doped n+ GaN (n ~1x10^{19} cm^{-3}) buffer layer was first grown, followed by 6 periods of $In_{0.23}Ga_{0.77}N$/10 nm GaN quantum dots under the growth conditions described above. An undoped 15 nm GaN layer was grown after the final dot layer. The growth temperature was then raised to 600 °C and a 20 nm-thick Mg-doped p+ $Al_{0.15}Ga_{0.85}N$ electron-blocking layer (EBL) was grown under slightly N-rich conditions, followed by 200 nm of Mg-doped p+ GaN (p ~ 2x10^{18} cm^{-3}). Square 0.0025 cm^2 mesas were defined by standard lithography and reactive-ion etching of the n-GaN layer. The p-contact was formed by depositing 5 nm/5 nm Ni/Au on top of the mesa. Finally, 25 nm/100 nm Ti/Au was deposited on the n-GaN and Ni/Au as contact pads. A photomicrograph of a fabricated LED is shown in Figure 6.11(b).

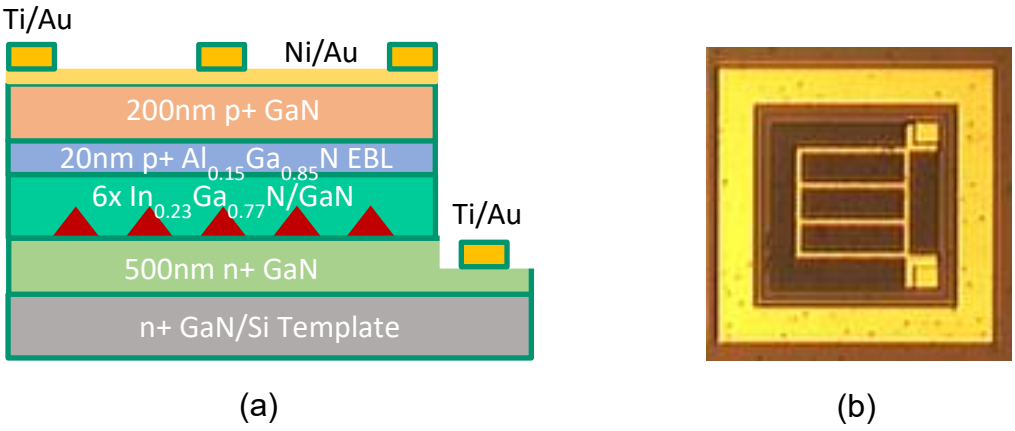

Figure 6.11 (a) Schematic of the LED structure and (b) top-view photograph of a fabricated 500 μm x 500 μm device.

6.5 LED Characteristics

The current-voltage characteristics are shown in Figure 6.12(a) and the corresponding series resistance is measured to be 27 Ω. Electroluminescence (EL) measurements were

performed at 300 K from 20 mA to 210 mA and the output was fiber-coupled to a charge-coupled device (CCD) spectrometer. The measured spectra are shown in Figure 6.12(b). The EL peaks at 477 nm at 20 mA, in good agreement with the measured PL. The light-current characteristics are

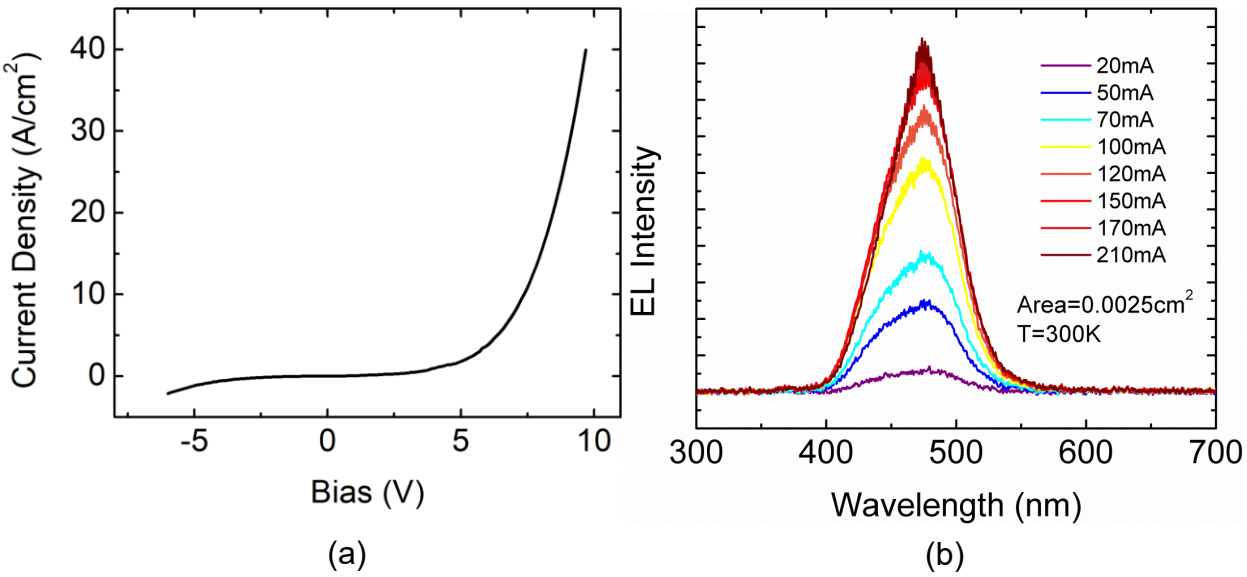

Figure 6.12 (a) I-V characteristics of LED. (b) Measured electroluminescence at 300K as a function of injection.

plotted in Figure 6.13(a). The EL intensity begins to saturate with injection above ~60 A/cm^2 which is believed to be due to carrier heating. There is also a small ~2.4 nm blueshift with injection that is observed and is shown in Figure 6.13(b). This blueshift is much smaller than that observed for blue/green emitting InGaN/GaN quantum wells grown along the c-axis [183]. The polarization field in the quantum dots is estimated to be ~50 kV/cm, which is much lower than that in comparable InGaN/GaN quantum wells [184]. A plot of the IQE, together with the external quantum efficiency (EQE) in arbitrary units, calculated from the light-current characteristics, is shown in Figure 6.14. The peak of the IQE is taken to be 0.25 from PL measurements. The IQE peaks at ~40 A/cm^2 after which a droop in efficiency is observed. Normally with quantum dots, the efficiency droop is significantly reduced compared to quantum wells due to the reduction in polarization field [185]. In this case, the reduction in efficiency is

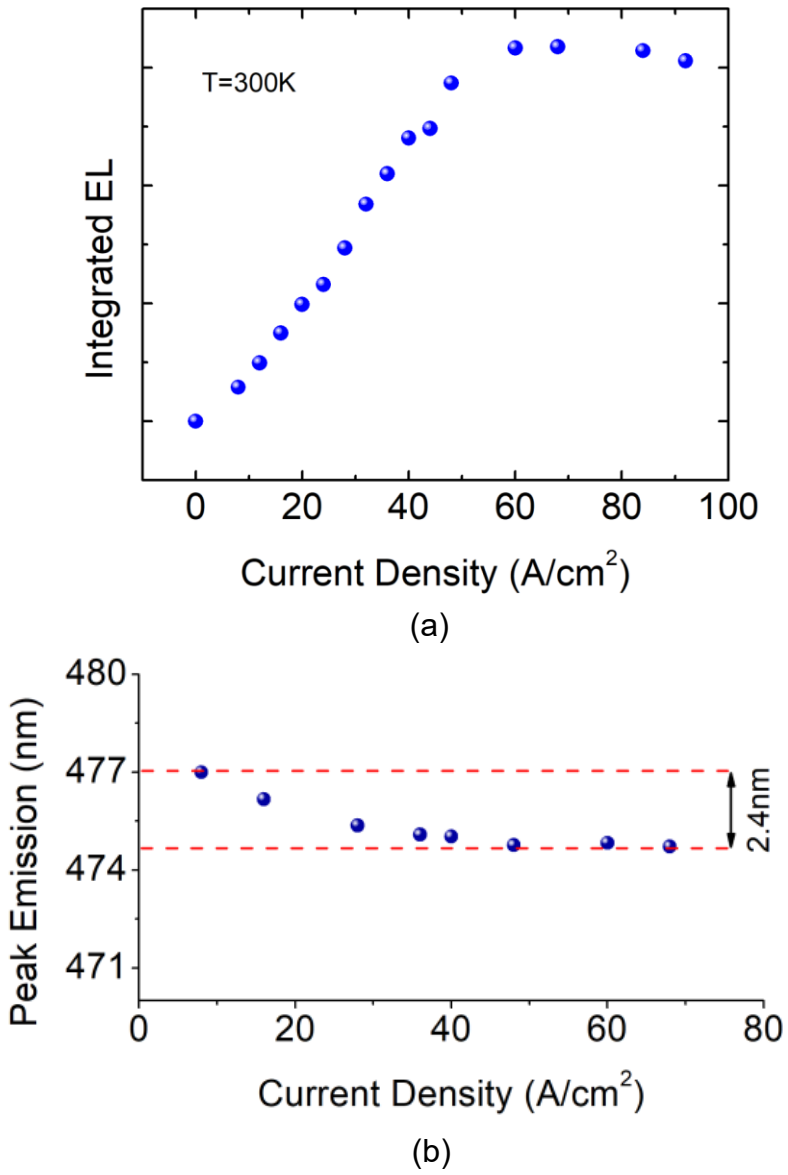

Figure 6.13 (a) Room-temperature integrated electroluminescence intensity. (b) Peak emission wavelength versus current density shows a 2.4nm blueshift with increasing injection which corresponds to 12.6meV.

believed to be due to carrier heating and enhanced defect-assisted Auger recombination [186], possibly due to the presence of threading dislocations originating from the GaN/Si template. Despite this reduction in performance, the present work demonstrates that InGaN/GaN quantum dot LEDs can be realized on the novel GaN/Si platform.

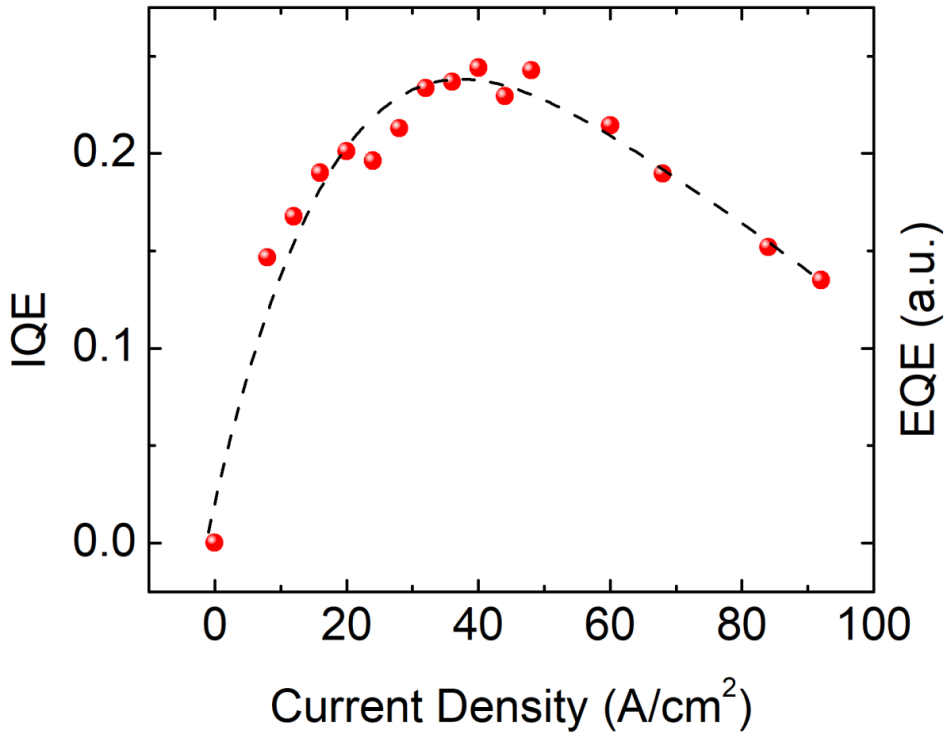

Figure 6.14 Measured internal quantum efficiency of LED. The dashed line is a guide to the eye. The external quantum efficiency is in arbitrary units because an integrating sphere was not used in the measurement.

6.6 Pump-Probe Spectroscopy of InGaN Quantum Dots

6.6.1 Epitaxy of Heterostructure

The InGaN/GaN quantum dot heterostructure was grown in a radio frequency plasma-assisted molecular beam epitaxy system equipped with standard Ga and In effusion cells and an RF nitrogen plasma source. The growth temperature was measured using an infrared pyrometer calibrated to the RHEED pattern 7x7 to 1x1 transition of (111) silicon. The heterostructure was grown on a hydride vapor phase epitaxy (HVPE) GaN/sapphire template indium mounted to a 3-inch silicon wafer. An undoped 220 nm GaN buffer layer was first grown at 700 °C under slightly metal-rich conditions. The growth temperature was then lowered to 540 °C for the InGaN/GaN quantum dots which were grown under N-rich conditions at a plasma power of 400 W and N flow rate of 1.1 sccm. The Ga and In beam-equivalent pressures were 3.1×10^{-8} Torr and

$1.2x10^{-7}$ Torr, respectively. The RHEED pattern became spotty after ~20 s, indicating the 2D-3D transition. 10 nm of GaN was grown between each quantum dot region. Six InGaN/GaN periods were grown, with the last layer left uncapped for atomic force microscopy. An AFM image is shown in the inset to Figure 6.15(a). The average dot height is 2.5 nm and the diameter ranges between 30-50 nm. The dot density is ~$2x10^{10}$ cm^{-2}.

6.6.2 Photoluminescence of Quantum Dots

Photoluminescence and time-resolved photoluminescence measurements were performed with the 266 nm 3rd harmonic of an 80 MHz/100 fs Ti:sapphire laser. The excitation density was fixed at ~300 W/cm^2. The luminescence was spectrally resolved with a 0.75 m monochromator with a resolution of 0.02 nm and detected with a photomultiplier tube (PMT). The transient signals were detected using a high-speed single photon detector and collected by a time-correlated single photon counting (TCSPC) module. The temporal resolution of the measurement system is ~50 ps. Temperature-dependent TRPL is performed by mounting the sample in a continuous-flow liquid-He cryostat. The measured photoluminescence spectrum at 300 K is shown in Figure 6.15(a). The peak of the luminescence is at 510 nm with a line width of ~280 meV. Oscillations in the spectra are due to reflections at the GaN/sapphire interface. The measured TRPL transient at 300 K is shown in Figure 6.15(b). A bi-exponential decay model is used to analyze the data. At 4 K, the fast and slow time constants are 600 ps and 2.4 ns and at 300 K they are 280 ps and 1.2 ns, respectively. The fast recombination lifetime is a measure of the screening of the built-in polarization field and thus better overlap of the electron and hole wave functions. The slow recombination lifetime is due to the restoration of the field as carriers recombine.

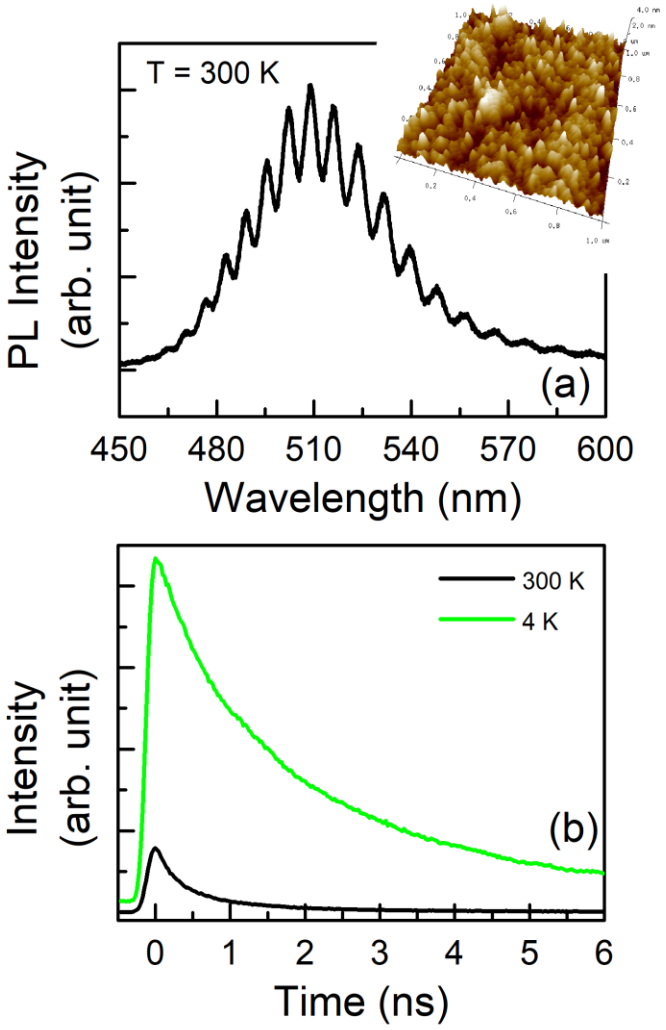

Figure 6.15 (a) Room temperature photoluminescence spectrum from InGaN/GaN quantum dot active region. The peak emission occurs at 510 nm. The oscillations in the spectrum are due to the reflections from the GaN/sapphire interface. A typical atomic force microscope image is shown in the inset. (b) Time resolved photoluminescence spectra at 4 K and 300 K are shown.

6.6.3 Differential Absorption Spectra

The carrier and photon dynamics are determined using femtosecond transient absorption spectroscopy (TAS). The pump-probe measurements were done in Prof. Dipankar Saha's group at IIT-Bombay and the data were analyzed and interpreted collaboratively. The samples are excited by a pump beam from a pulsed laser at 325 nm having 50 fs duration and 1 kHz repetition frequency. The probe beam is a low intensity white light. The measurement system is described in the Appendix according to [187]. The absorption spectra are captured with a time

resolution of 50 fs. Figure 6.16(a) shows a typical absorption spectrum at 12 ps delay between the pump and probe beam. The differential absorption is defined as $\Delta\alpha/\alpha = (\alpha_p - \alpha_o)/\alpha_p$, where α_p and α_o are absorption with and without pump, respectively. The absorption spectrum is fitted with Gaussian peaks to identify the different transitions in the quantum dot heterostructure. It shows absorption peaks at 431, 379, 372, 367, and 350 nm that correspond to the InGaN QD ground state (GS), first excited state, second excited state, GaN barrier and 2D wetting layer

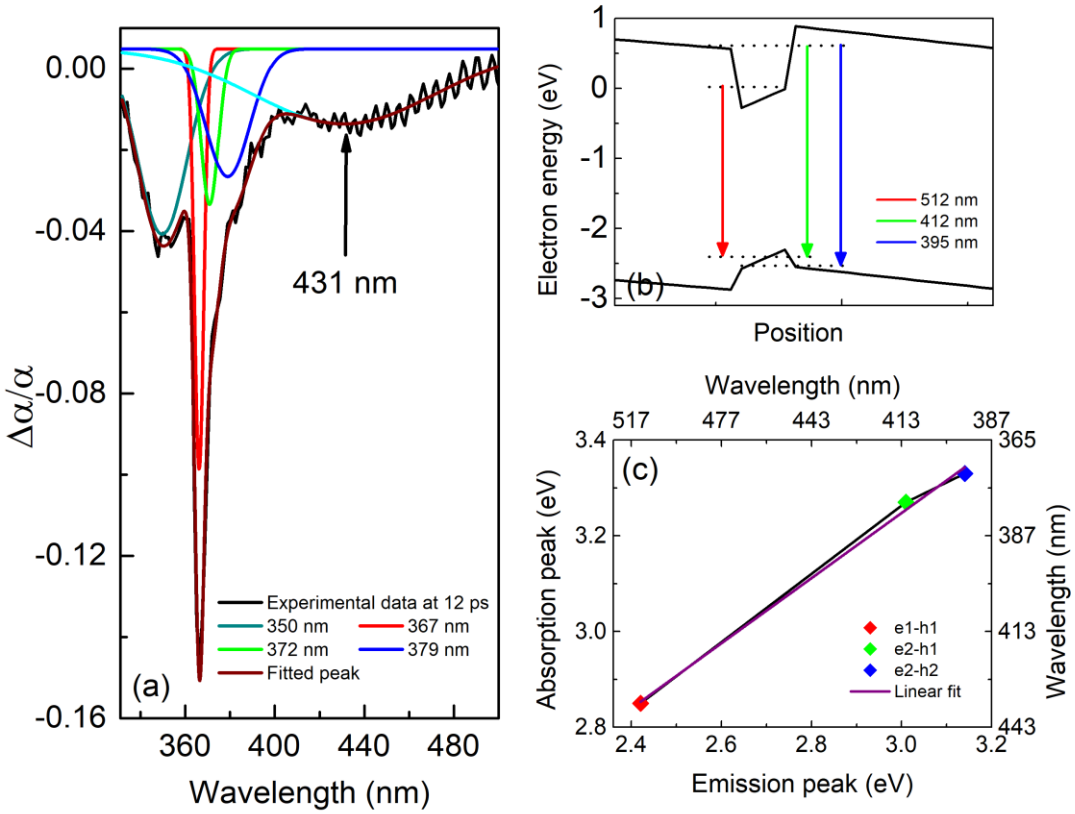

Figure 6.16 (a) Room temperature absorption spectrum at zero delay and 8.5 mW pump power is shown. Gaussian fitting identifies the absorption peaks for various transitions. (b) The energy band diagram showing the transition energies in the quantum dots. (c) Transition energy peaks as obtained from simulation versus absorption peaks are shown. A near linear relation is indicative of the Stokes shift.

transitions. The transition energy has been determined by solving a 6-band **k.p** formulation for electrons and holes. The quantum dots have been considered to be cylindrical in nature with a diameter of 50 nm and height of 2.5 nm, as observed in the AFM image. Figure 6.16(b) shows

the calculated radiative transition energies from the quantum dots. The ground state transition energy at 2.42 eV (510 nm) agrees well with that obtained from the PL data. It may be noted that the PL spectrum shows the GS transition peak only and higher order peaks are missing. This is due to the high pump power of the femtosecond laser that creates higher order band-filling. In addition, TAS exhibits transition peaks at spectral positions which are different from that obtained from the simulation. The difference between the luminescence and absorption peak is due to a Stokes shift, related to defects. It may also be noted that the energy difference between the electron ground state and first excited state is 590 meV, which is larger than the LO phonon energy. Figure 6.16(c) shows the calculated emission and experimentally measured absorption peaks for the sample. The approximately linear trend is a signature of the Stokes shift [188].

To study the dynamics of carriers and photons, the entire absorption spectra is measured and analyzed with Gaussian profiling for all the transition peaks as a function of wavelength. Figures 6.17(a)-(d) show the absorption spectra for 0, 20, 75, and 115 ps delays and highlight how the transition peaks at different wavelengths evolve with time. It is observed that both the GaN barrier (367 nm) and wetting layer (350 nm) peaks do not shift with increasing time delay, confirming that the spontaneous polarization is very small in these regions of the heterostructure, in comparison with the piezoelectric polarization in the quantum dots. The GS absorption peak is found to shift from 398 nm to 429 nm for a delay time of 20 ps. The peak shifts further towards longer wavelength with increasing time delay. The insets to Figure 6.17(b) plot the analyzed GS transition peak with increasing delay, confirming this trend. The inset to Figure 6.17(c) shows the peak energies of the GS absorption as a function of time. The peak is found to asymptotically shift to 435 nm for a long delay between pump and probe.

The temporal evolution of the spectra with delay time, shown in Figures 6.17(a)-(d),

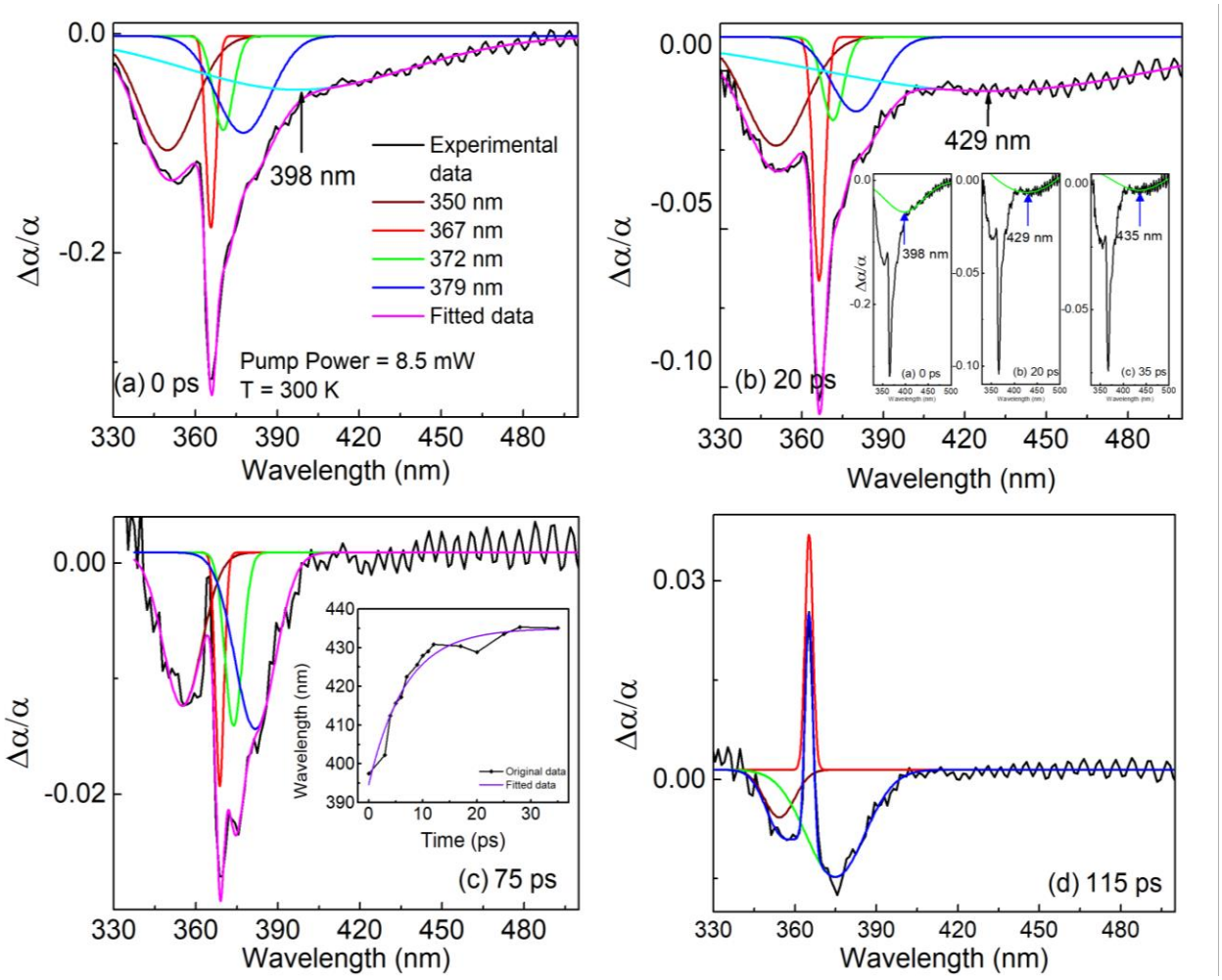

Figure 6.17 Room temperature absorption spectra at (a) 0 ps, (b) 20 ps, (c) 75 ps and (d) 115 ps delay and 8.5 mW pump power are shown. The corresponding Gaussian fittings are also shown alongside. Inset to (b) shows the evolving ground state transition peaks for 0, 20 and 35 ps. Inset to (c) shows the time evolution of the ground state transition peak.

exhibits some unique features, which have not been observed in differential transmission (ΔT/T) or differential absorption (Δα/α) spectroscopy of InAs/GaAs or InGaAs/GaAs quantum dots. First, it is important to elucidate the important processes that take pace sequentially after excitation with the pump beam, which excites electrons from higher valence band states to the higher states in the conduction band, creating electron-hole pairs. The holes thermalize rapidly to the lower energy states in the valence band by phonon scattering due to their heavy effective mass. The time constant of this process is <50 fs, which is the limit of resolution of the

measurement. The electrons excited to the higher energy states in the conduction band also thermalize to lower energy states in the two-dimensional wetting layer and barrier layer and, to a much smaller extent, into the confined states of the quantum dots. These processes take place before the probe beam excites the sample. Under these conditions the differential absorption with the probe beam is a sharp negative signal peak at the various transition energies. Direct thermalization of the higher energy electrons into the quantum dot states is insignificant due to the small dot volume [189]. This is also confirmed by selective sub-GaN bandgap excitation of the quantum dots. No significant change in the absorption coefficient is observed. Hence the conduction band electrons in the wetting and barrier layers largely determine the kinetics of the system.

With increasing probe delay, the kinetic behavior, dictated by the carrier dynamics, of the different transitions are distinctly different. With time, the density of hot carriers in the wetting layer monotonically decays by band-to-band radiative recombination, defect-assisted non-radiative recombination, carrier transfer to the GaN barrier layers and carrier capture into the quantum dot bound states. Hence the negative differential absorption ($\Delta\alpha$) peak of the wetting layer monotonically decreases in amplitude with time. The temporal carrier dynamics of the GaN barrier layer exhibits a different behavior. The excess carrier density initially decays by the same processes as described above for the wetting layer and the negative $\Delta\alpha$ peak decreases in amplitude with increasing probe delay time. However, the barrier transition exhibits a positive $\Delta\alpha$ peak at longer delay times. The $\Delta\alpha$ peaks corresponding to the quantum dot states also exhibit a positive $\Delta\alpha$ peak for large delays. This trend is discussed below. Also, as mentioned earlier, the additional feature in the $\Delta\alpha$ peaks related to the quantum dot states is their red shift with increasing delay, as shown in Figures 6.17(b)-(c) due to the quantum confined Stark effect

(QCSE). The large piezoelectric polarization in equilibrium leads to the band bending shown in Figure 6.16(b). The high carrier density at zero and small delays results in a large blue shift of the transition energy. With increasing probe delay, the resulting decreasing carrier density leads to a red-shift of the transitions to lower energies (longer wavelengths).

6.6.4 Temporal Dynamics of the Differential Absorption

The kinetics for the transitions related to the wetting layer, barrier and quantum dot states have also been determined and these are shown in Figures 6.18(a)–(d). All measurements have been made at room temperature. Figure 6.18(a) depicts the absorption coefficient at 350 nm, corresponding to the wetting layer, as a function of probe delay time. The initial negative $\Delta\alpha$ signal and its fast decay are ascribed to the carrier transfer processes described above and indicate that ground state bleaching (GSB) is dominant in this region. The carrier dynamics involved in GSB is described in Figure 6.19. The inset to Figure 6.18(a) shows the measured and analyzed data corresponding to the initial section of the transient. Figure 6.18(b) shows the measured $\Delta\alpha$ kinetics corresponding to the GaN barriers at 367 nm. The initial fast decay of the negative $\Delta\alpha$ signal (GSB) is due to radiative and non-radiative transitions and some carrier transfer to the quantum dot states. After that the $\Delta\alpha$ signal becomes positive, followed by a slow decay at longer delay times. The positive $\Delta\alpha$ signal most likely results from excited state absorption (ESA) wherein electrons are raised from the GaN conduction band edge to higher lying empty states, described in Figure 6.19. The relatively large population of the GaN conduction band edge results from the initial thermalization of carriers from the pump beam and transfer of carriers from the wetting layer. As a result, the ESA process competes with the GSB process initially and after the latter ceases, the former becomes more dominant. The inset to

Figure 6.18(a) shows a magnification of the initial kinetics.

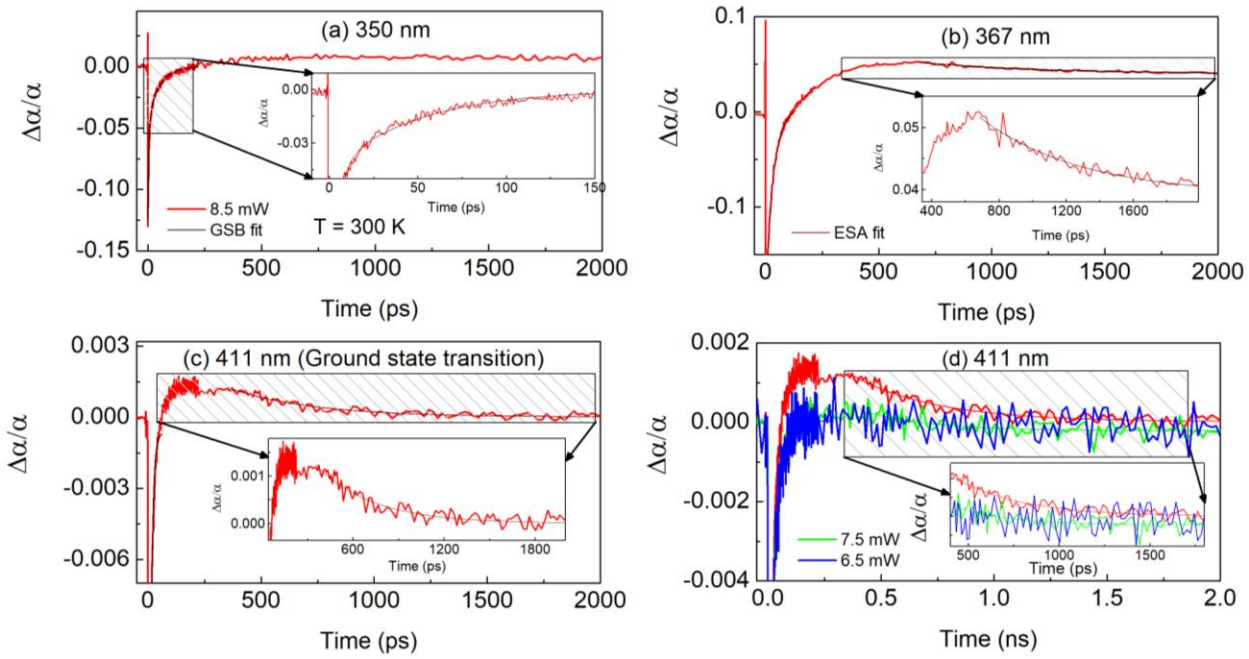

Figure 6.18 Room temperature kinetics for (a) wetting layer, (b) barrier layer, and (c) quantum dot ground state transitions are shown for a pump power of 8.5 mW. Inset to (a) shows an excited state absorption fitting to the experimental data. Inset to (b) and (c) show the respective fitting for the ground state bleaching. (d) Room temperature power dependent kinetics are shown for the ground state transition. The excited state absorption is more prominent for higher pump power.

The temporal variation of the Δα signal corresponding to the quantum dot ground state (GS) at 411 nm is shown in Figure 6.18(c). As shown in Figure 6.17(c), the GS transition energy changes with time due to the polarization field related QCSE. It is experimentally observed that the decay time constants do not vary much in the wavelength range of 398-435 nm for the GS transition. The general nature of the transient indicates a trend similar to that for the GaN barriers, an initial fast negative GSB signal followed by a slower ESA signal, an enlargement of the latter shown in the inset. The small equilibrium density of carriers in the ground state is augmented by carriers transferred from the barrier and wetting layer after the pump beam, which explains the initial negative GSB signal. While some of the excess carriers in the GS are rapidly

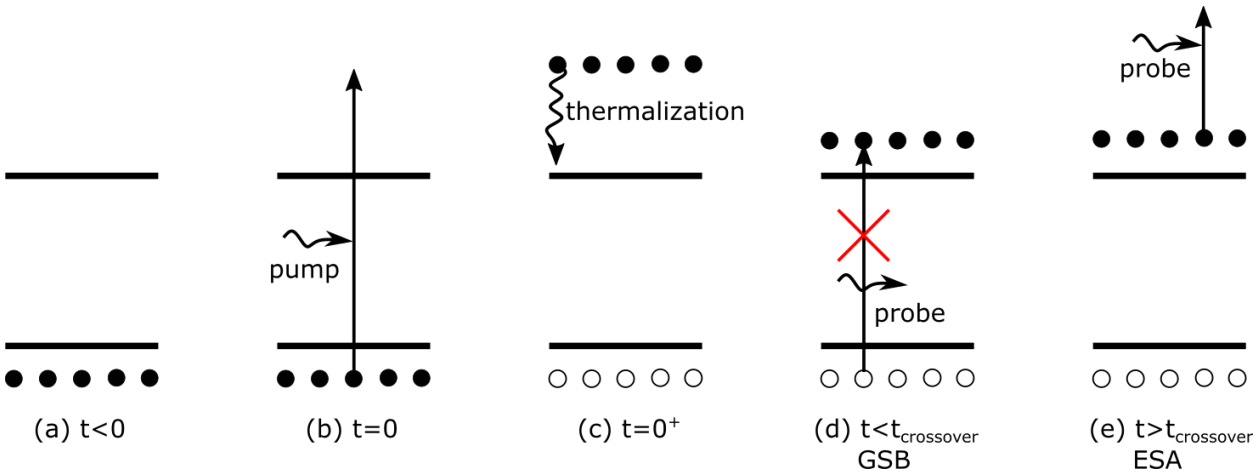

Figure 6.19 Schematic showing carrier dynamics in quantum dots. (a) Before pump the valence band is full of electrons and the conduction band is empty. (b) At t=0, pump beam creates electron-hole pairs. (c) After the pump, electrons quickly thermalize to the conduction band edge. (d) Low energy valence electrons are absent. The incoming probe pulse can no longer be absorbed due to the bleaching of electrons from the ground state ($\Delta\alpha<0$). (e) Near cross-over, electrons are populated in the excited state from the barrier and wetting layer. These electrons can absorb the probe beam by excited state absorption ($\Delta\alpha>0$).

lost, mostly by non-radiative recombination, and carrier transfer to localized states in the dots, the availability of empty states at higher energy levels in the conduction band promotes ESA from the electron GS and results in the positive signal with a slow decay. However, the number of available states in the quantum dots is much smaller than that in the GaN barrier layers. Therefore, the peak amplitudes of both GSB and ESA signals are smaller than those for the GaN barriers. It may also be noted that the peaks of the ESA signal occur at 352 ps and 682 ps for the quantum dot GS and the GaN barrier, respectively. This is attributed to easier band-filling in the dots. The general nature of the GSB and ESA signals is consistent and has been observed in other quantum dot heterostructures grown under similar conditions.

The quantum dot ground state kinetics measured as a function of pump powers of 6.5, 7.5 and 8.5 mW is shown in Figure 6.18(d). Since the amplitude of the ESA signal is dependent on the number of electrons in the ground state supplied from the wetting and barrier layers, it is expected to increase with increasing pump power. This is indeed observed in the data of Figure

6.18(d). Furthermore, the cross-over from GSB to ESA occurs at earlier delay times for higher pump powers owing to the larger supply of carriers. The inset to Figure 6.18(d) shows a magnified view of the measured and analyzed ESA signals for the three pump powers.

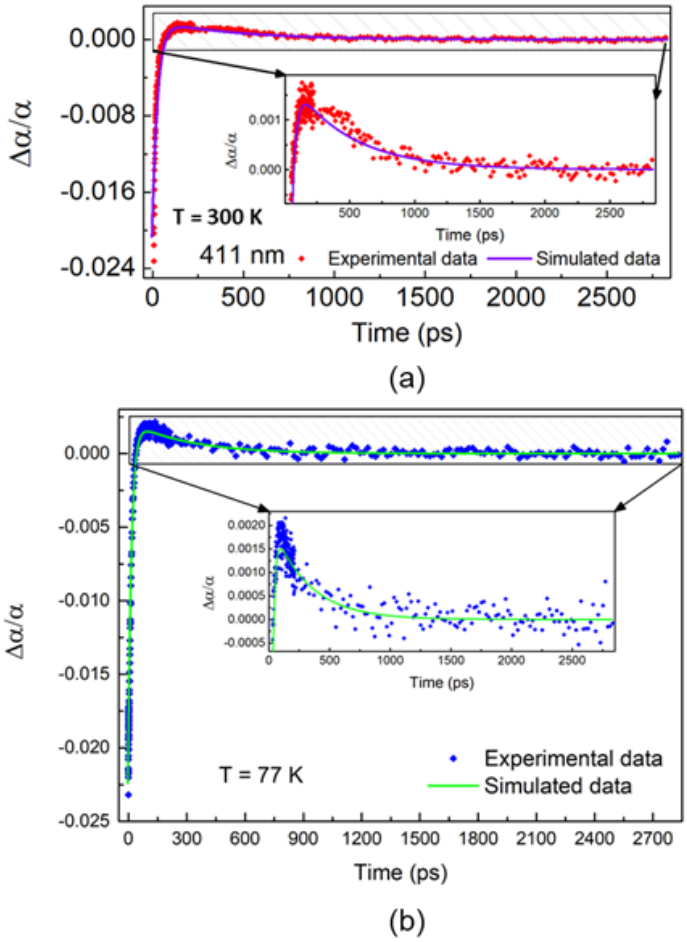

Figure 6.20 Measured and analyzed ground state (411 nm) differential absorption transient signals at (a) 300 K and (b) 77 K. Both insets are magnifications of the excited state absorption signal.

6.6.5 Rate Equation Modeling

Rate equation modeling of the GSB and ESA transient signals in the quantum dot region has been performed by Prof. Dipankar Saha's research group. The two competing processes of electron density increase due to carrier capture from the wetting layer and barrier and decrease of electron density via radiative and non-radiative recombination have been accounted for by

appropriate time constants. Equations (6.1) and (6.2) describe the kinetics of electrons in the quantum dot and effective transfer of electrons into the quantum dot region. Solving the coupled differential equations (6.1) and (6.2), the kinetics in the quantum dot region is obtained as Equation (6.3), where N and N' are electron density in the quantum dot and barrier regions, τ_1 is the effective decay time constant from the quantum dot, and τ_2 is the effective time constant for electron transfer into the well. τ_1 and τ_2 are considered to have different values.

$$\frac{dN}{dt} = -\frac{N}{\tau_1} - \frac{dN'}{dt} \tag{6.1}$$

$$\frac{dN'}{dt} = -\frac{N'}{\tau_2} \tag{6.2}$$

$$N(t) = \left[N(0) + \frac{N\prime(0)/\tau_2}{\left(\frac{1}{\tau_2}-\frac{1}{\tau_1}\right)}\right] e^{-t/\tau_1} - \frac{N\prime(0)/\tau_2}{\left(\frac{1}{\tau_2}-\frac{1}{\tau_1}\right)}\, e^{-\frac{t}{\tau_2}} \tag{6.3}$$

Figures 6.20(a)-(b) show the measured and calculated Δα kinetics at 300 K and 77 K, respectively, and the good agreement confirms the carrier dynamics outlined above.

The temperature dependence of the Δα spectra has also been studied since carrier capture into the quantum dots is mediated by phonons, whose density is dependent on temperature. Measurements have been made at 77 K with the sample in a continuous flow liquid nitrogen cryostat. The Δα spectra for different probe delays are plotted and compared with 300 K spectra in Figures 6.21(a)-(b). It is observed that the qualitative nature of the spectra at 77 K is the same as those at 300 K, with the expected blue shift of the peaks due to increase in bandgap with lowering of temperature. The transition corresponding to the higher order states in the dot also exhibits the change from GSB to ESA in the Δα spectra at pump power equal to or greater than 7.5 mW. The excited state transition is absent for lower pump powers. This suggests that carrier capture into the ground state from the higher energy levels in barriers and wetting layer is impeded by a reduced phonon scattering rate.

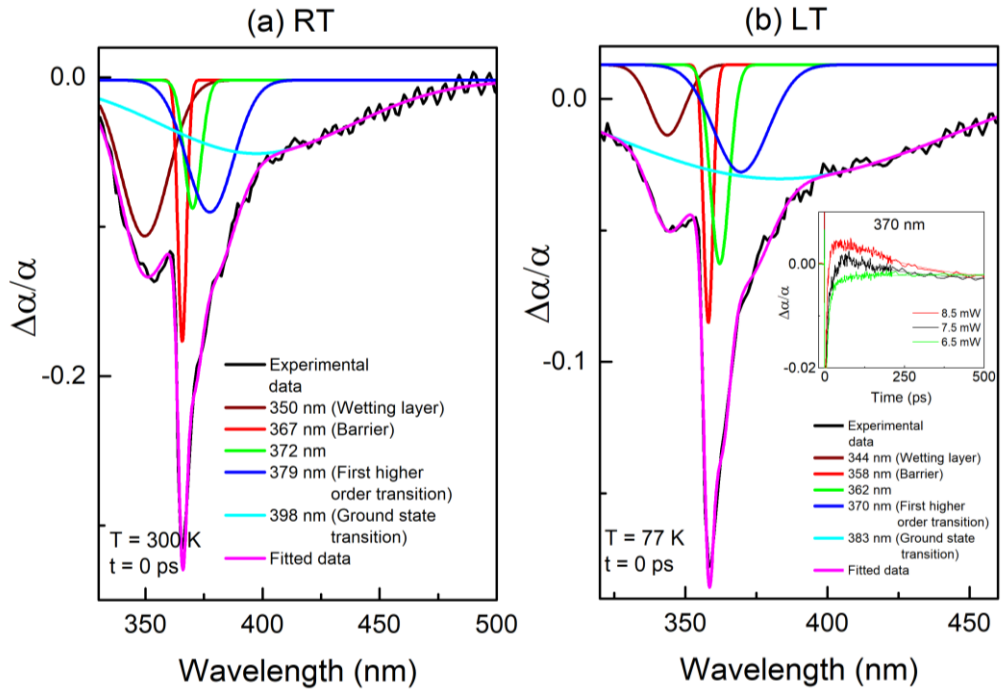

Figure 6.21 (a) Room temperature spectra at zero delay. (b) Low temperature spectra at zero delay showing blue shift due to an increase in the bandgap. Inset to (b) shows kinetics of the first excited state at various pump powers.

The time constants of the GSB and ESA processes have been derived from the measured transient kinetics by exponential curve fitting. Table 6.1 depicts the trend of these time constants for wetting layer, GaN barrier and dot ground state at 300 K and 77 K for a constant pump power of 8.5 mW. As described earlier, the fast GSB time constants of the dot wetting layer and GaN barrier transitions at 300 K reflect relaxation of carriers into lower energy barrier and dot states from the wetting layer and into the dot states from the barrier and wetting layers. The very fast relaxation of the dot GSB reflects transfer to a localized state, formed in the dots by compositional inhomogeneities, and non-radiative recombination at defects in the dot heterostructures. The ESA time constant is determined by a combination of carrier capture and carrier decay. For the GaN barriers, it is principally determined by the recombination lifetime. The increase of the time constant from 601 ps at 300 K to 655 ps at 77 K reflects the increasing

non-radiative recombination lifetime with decrease of temperature. This also agrees with the

TABLE 6.1 Time constants for the GSB and ESA processes corresponding to the different transition in InGaN/GaN quantum dot heterostructures measured with a constant pump power of 8.5 mW.

Transition Peak (nm)	GSB (ps)	ESA (ps)	
Temperature	300K	300K	77K
350 Dot Wetting Layer	49	-	-
367 GaN Barrier	37	601	655
411 Dot Ground State	14	448	207

trend of the recombination lifetimes determined from the TRPL measurements. In contrast, the ESA time constant is found to decrease with decrease in temperature for the dot GS transition. The rate of carrier capture from higher energy states will generally decrease with lowering of temperature. The recombination lifetime also increases with lowering of temperature. A possible explanation is rapid carrier relaxation from the GS to localized states in the dot, at a lower energy, with lowering of temperature.

Finally, it is important to discuss the positive excited state absorption signal in the $\Delta\alpha$ spectra and kinetics, which has hitherto not been observed in InGaN/GaN quantum wells [187] or in In(Ga)As/GaAs quantum dots. It has been observed in organic compounds, such as melanins [190], with large molecules. In comparing the In(Ga)As/GaAs and InGaN/GaN quantum dot heterostructures, it is evident that the density of states in the large-bandgap III-nitrides is larger than in the arsenides and that the band offsets are much larger in the latter, resulting in better confinement (localization) of the carrier wave functions within the dots. This

can increase the probability of ESA, even when the electrons are raised to continuum states in the dot conduction band.

6.7 Summary

In conclusion, a novel buffer, realized with coalescing GaN nanowires, has been realized for the growth and fabrication of InGaN/GaN quantum dot LEDs on silicon substrates. The measured structural and optical characteristics of the buffer layer and the LEDs are described and discussed. Further improvements in the epitaxy of the buffer layer will improve device characteristics and provide a path for future device applications. Finally, results are presented from femtosecond pump-probe differential absorption spectroscopy measurements made on InGaN/GaN quantum dot heterostructures. The samples were grown by plasma-assisted molecular beam epitaxy. The measurements have been made as a function of pump power and temperature. Excited state absorption is uniquely observed, in addition to ground state bleaching, for the different transitions corresponding to the 2D dot wetting layer states, the GaN barrier layers and the confined states in the dots. The time constants of the GSB and ESA processes for the different transitions have been analyzed and discussed. The results provide a window into the unique hot carrier dynamics in these important III-nitride quantum dot heterostructures.

Chapter VII

Conclusion and Future Work

7.1 Summary of Present Work

The research presented here was focused on the characterization of the optical and electrical properties of III-Nitride quantum wells, monolayer and disk-in-nanowire structures, and InGaN quantum dot heterostructures. The epitaxial methods were presented and discussed and structural characterization was performed to analyze interfaces and nanowire and quantum dot formation. Nanowires and quantum dots were grown on silicon as a demonstration for silicon photonic applications. Gallium nitride monolayers were grown both in planar and nanowire form and very high exciton binding energies on the order of ~200 meV were measured. Visible-blind photodetectors were demonstrated using InGaN/GaN disk-in-nanowires and the photocurrent properties were analyzed with the appropriate modeling. Deep-UV nanowire photodiodes on silicon were also shown using the GaN monolayers and their characteristics were analyzed. Growing a high-quality GaN platform on silicon is important for device applications. This was investigated and InGaN/GaN quantum dots were successfully grown on this platform and their luminescence properties analyzed. An LED was demonstrated using this structure. Finally, the differential absorption was measured in these quantum dots using pump-probe spectroscopy and a crossover between ground state bleaching and excited state absorption was observed.

An introduction into the III-Nitride materials was presented in Chapter 1. This material system is unique in that the InGaN, AlGaN, and InAlN ternaries completely cover the bandgap

range of ~0.7-6.2 eV, which is of particular interest for photonic applications. In addition, the In(Al)N material provides a large refractive index difference to that of In(Ga)N and Al(Ga)N and with the correct lattice-matching conditions, can provide an excellent solution for cladding layers in a laser heterostructure for optimal mode confinement. The III-Nitrides grow most stable along the c-axis with a hexagonal unit cell structure. This generates a built-in spontaneous polarization and causes band-bending in the electrical properties. Piezoelectric polarization may also be present under lattice mismatch and strain. This polarization, reaching orders of ~2 MV/cm in planar heterostructures, can cause issues with device operation, notably lasers and LEDs. Other structures such as nanowires and quantum dots alleviate this polarization and are promising for photonics. These structures are briefly introduced and their properties discussed. Some structures such as HEMTs have taken advantage of this large polarization as a channel for the 2DEG, both in Ga- and N-polar structures. Methods of reaching the deep-UV and solutions to p-doping in the III-Nitrides are also discussed.

Chapter 2 introduces the history of PAMBE and briefly describes the operational mechanics of a typical research-grade system. The PAMBE system is unique in the MBE community in that it generates the active nitrogen species using a RF plasma, necessary for III-Nitride epitaxy. The rest of the MBE system is quite similar to typical arsenide and phosphide systems, with the exception that the Nitrides often require higher operating temperatures, especially with Al(Ga)N growth. Extremely low background impurities, precise beam control and sharp interfaces, and improved p-doping characteristics are some of the hallmarks that MBE offers in comparison to MOCVD. Epitaxial techniques to grow different quantum structures such as quantum wells, nanowires, and quantum dots are presented and discussed. Interface characteristics for $Al_{0.56}Ga_{0.44}N/Al_{0.62}Ga_{0.38}N$ quantum well heterostructures are presented and

the interface roughness is analyzed. The interface roughness is such structures is found to range between 0.3-1 nm and these can act as radiative recombination centers, which affect the luminescence properties similar to a quantum dot confinement potential. The interface roughness is analyzed using a simple model based on photoluminescence linewidths.

The growth of GaN monolayers is presented in Chapter 3. These monolayers are grown in a planar GaN/$Al_{0.65}Ga_{0.35}N$ heterostructure and in a nanowire GaN/AlN form. Interface characteristics are analyzed from TEM imaging and these monolayers can range between 1-2 ML. Interface roughness also affects the planar structures in particular, as was shown in Chapter 2. Not only do these monolayers offer deep-UV emission along the c-axis, which is beneficial for light extraction compared to AlN which emits perpendicular, but the large wave function overlap and confinement produces extrememly large exciton binding energies on the order of ~200 meV. The exciton binding energy in the planar and nanowire structures is measured to be 95 meV and ~160-260 meV respectively. These are in excellent agreement with theoretical analysis from many-body theory. High exciton binding energies are advantageous for polariton devices and exciton lasers, in addition to deep-UV emitters which is achieved with these GaN monolayers.

Chapter 4 demonstrates a visible-blind InGaN/GaN disk-in-nanowire photodetector on silicon. These DINWs were briefly introduced and discussed in Chapters 1 and 2. They grow nearly defect-free on silicon substrates under nitrogen-rich conditions in the MBE chamber and the indium composition is selected such that the peak of the photoluminescence is near ~565 nm. The nanowires are ~500 nm in length and the area density is $2x10^{10}$ cm^{-2}. Several peaks are observed in the measured photocurrent which are attributed to interband transitions within the disks. The measured peak responsivity at 300 K is ~1500 A/W. The photocurrent is analyzed using appropriate drift and diffusion models with capture and escape times as fitting parameters.

A high gain in excess of 10^3 is also observed in these photodetectors, which is comprised of the conventional recycling of carriers and a nanowire surface modulation gain, the latter of which dominates. Though the carrier recombination lifetime from TRPL measurements is ~1 ns, the device transient behavior is much slower, a consequence of the large gain. The rise and decay times are measured to be 190 s and 454 s which are a measure of the carrier trapping and detrapping times respectively.

Chapter 5 presents another nanowire photodetector structure this time using the GaN/AlN monolayers. The AlN is again selected to be sufficiently thick (~10 nm) for highest confinement. However, instead of 1-ML GaN, a thickness of 2-ML GaN is chosen to improve the absorption/luminescence properties of the active region. A PiN photodiode is grown and fabricated. The same structure can also be used as a deep-UV emitter ~280 nm under forward bias conditions. TEM imaging confirms the GaN thickness to be 2 ML. The peak of the photoluminescence is 278 nm while that of the measured photocurrent is at 240 nm. A 1-2 ML fluctuation exists, which causes the absorption peak to be at 240 nm as opposed to the PL peak due to the larger oscillator strength that exists for 1-ML GaN. Due to the large exciton binding energy of 2-ML GaN measuring ~230 meV at 300 K, the measured photocurrent is attributed to free carriers from exciton dissociation within the disk regions. The photocurrent in the AlN bulk region is from the typical recycling of carriers in addition to modulation of the conducting nanowire volume as discussed in Chapter 4. The peak quantum efficiency is measured to be 0.6 % at 200 nm. The QE peaks at 200 nm due to the larger absorbing volume of AlN compared to 2 ML of GaN. The -3 dB bandwidth is measured to be ~120 kHz and RC-limited.

The epitaxy and characterization of InGaN/GaN quantum dots is described in Chapter 6. These dots are grown on silicon by first demonstrating a device-quality GaN buffer growth over

silicon. This is performed by a combination of two techniques using a thin AlN starting layer followed by the coalescence of GaN nanowires. Continued growth at higher temperatures results in a smooth, planar GaN template. The InGaN/GaN quantum dots are grown on this template followed by an LED heterostructure. AFM imaging and TRPL confirms the formation of quantum dots. The PL and EL peaks at ~480 nm. A small 2.4 nm blueshift in the EL peak corresponds to ~50 kV/cm polarization, a signature of quantum dots. Some droop is observed past 40 A/cm^2 which is likely attributed to defect-assisted Auger recombination. Further optimization of the GaN buffer layer will improve this. Lastly, pump-probe spectroscopy is performed in collaboration with IIT Bombay to analyze the carrier dynamics within InGaN/GaN quantum dots. These dots are grown over a standard GaN/sapphire HVPE substrate and exhibit a PL peak of ~500 nm. Transient absorption spectroscopy confirms carrier transfer between the GaN barrier, wetting layer, and quantum dot ground and excited states. Ground state bleaching and excited state absorption is observed in these structures. The measured transients are analyzed with the appropriate rate equations.

7.2 Suggestions for Further Research

Four topics are presented here as suggestions for future work related to this current research. A deep-UV laser is proposed using nanowires with GaN/AlN monolayers as the active region for ~240 nm emission with high exciton binding energies. An infrared electrically-injected room temperature single-photon source may be possible by isolating a single InGaN/GaN quantum dot, which has been previously shown at ~620 nm [191]. This can be done on the coalesced GaN/Si platform previously demonstrated. A HEMT grown and fabricated on this coalesced GaN/Si template is also proposed. Infrared $In_{0.34}Ga_{0.66}N$/GaN DINW photodiodes on

silicon is also proposed, with preliminary absorption data suggesting intraband transitions may be responsible.

7.2.1 Deep-UV Monolayer Exciton Laser

GaN monolayers have been shown to exhibit very strong electron-hole wavefunction overlap and very large exciton binding energies at room temperature, as discussed in Chapter 3. Deep-UV lasers are of interest in a wide variety of applications such as skin and eye treatment, sterilization and water purification, sensing, lithography, and scientific research. Current deep-UV lasers are often bulky or require multiple modules for photon conversion (i.e. excimer and Ti:sapphire lasers). The proposed design would use nanowires grown on silicon with GaN/AlN monolayers as the active region, with several periods to optimize light output and gain, and be electrically-injected. The refractive index at ~250 nm for GaN and AlN is 2.8 and 2.4. This is sufficient for waveguiding and cladding layers. LEDs have already been demonstrated [145]. A schematic of the proposed nanowire edge-emitting laser is shown in Figure 7.1.

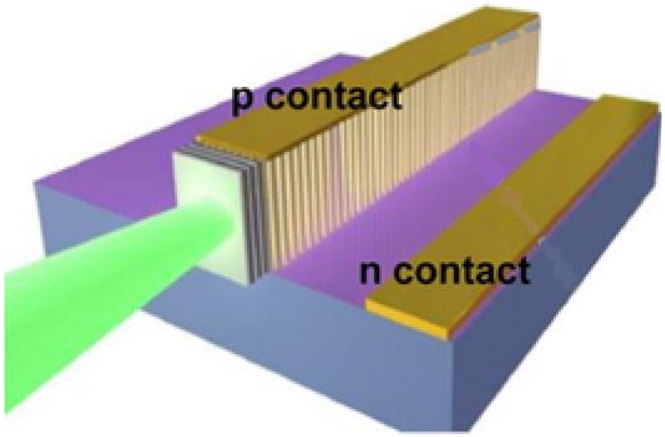

Figure 7.1 Schematic of GaN/AlN monolayer deep-UV nanowire edge-emitting laser on silicon, after [107].

7.2.2 Infrared Single-Photon Sources

Electrically-injected red-emitting single photon sources on GaN/sapphire have been demonstrated at room temperature [191]. The wavelength of 1.55 μm is of interest for telecommunications. In addition, the use of silicon substrates offers improved thermal conductivity for cooling requirements as well as for economic reasons. GaN templates of device-quality can be grown on silicon wafers, as previously demonstrated. InGaN/GaN quantum dots can be isolated by slightly increasing the metal fluxes to reduce the dot density, which allows for lithographic isolation of a single dot using aluminum apertures as discussed in [191]. This proposed design would go right to InN quantum dots. However, a graded InGaN region must be used to alleviate the strain between GaN. The structure is shown in Figure 7.2. Bulk InN emits at ~1.8 μm. With proper confinement (i.e. dot size, barrier composition, etc.) this can shift to 1.55 μm.

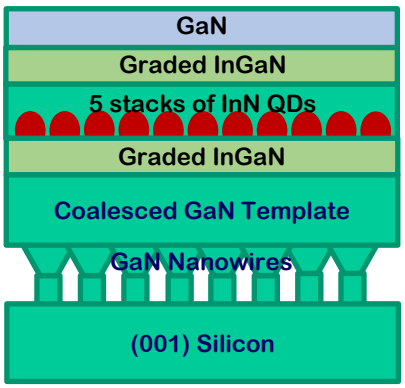

Figure 7.2 Proposed schematic of infrared single-photon source on silicon. The InN quantum dot heterostructure is grown on top of a coalesced GaN buffer layer on silicon.

7.2.3 High-Electron Mobility Transistors on Coalesced GaN/Si

GaN-based HEMTs are being widely pursued for applications involving switching and high-power. This potential design would use an AlGaN barrier over GaN/silicon. The design would involve many of the concepts previously demonstrated [15]. An example is shown in

Figure 7.3. The GaN would be grown unintentionally doped (UID). Fe- or C-doping can be used to make it more resistive if necessary. The AlGaN barrier thickness would range between 10-30 nm. Standard RIE would be used to etch the source and drain regions, taking care to not damage the crystal. Ion milling is also an option for a more delicate etch. Often, a silicon nitride passivation layer is deposited by LPCVD after epitaxy, to improve electrical characteristics and standard lithography defines the source, gate, and drain regions. Ni/Au/Ni can be used for the gate stack while Ti/Al/Ni/Au is common for the source and drain. Gate lengths ~1 μm can be investigated.

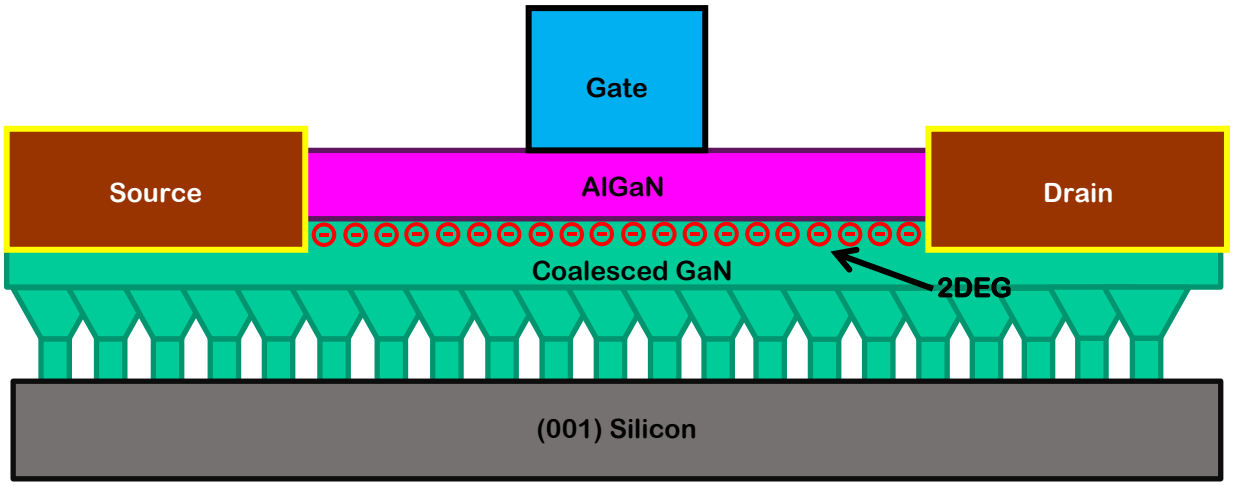

Figure 7.3 Schematic of an AlGaN/GaN HEMT epitaxially grown and fabricated on the coalesced GaN template on silicon.

7.2.4 Infrared Disk-in-Nanowire Photodiodes

Chapter 4 revealed that InGaN/GaN dot-in-nanowires on silicon behaved well as visible photodetectors and offer high responsivity at room temperature despite the large leakage current as an n-i-n photoconductor. We have recently shown that these dot-in-nanowires with a very similar In composition and green-emission have strong IR absorbance, likely due to various intersubband transitions. The absorbance data for $In_{0.34}Ga_{0.66}N$/GaN dot-in-nanowires on silicon is shown in Figure 7.4. A future objective may be to further investigate and optimize the growth

and fabrication conditions to produce an IR detector using these dot-in-nanowires on silicon.

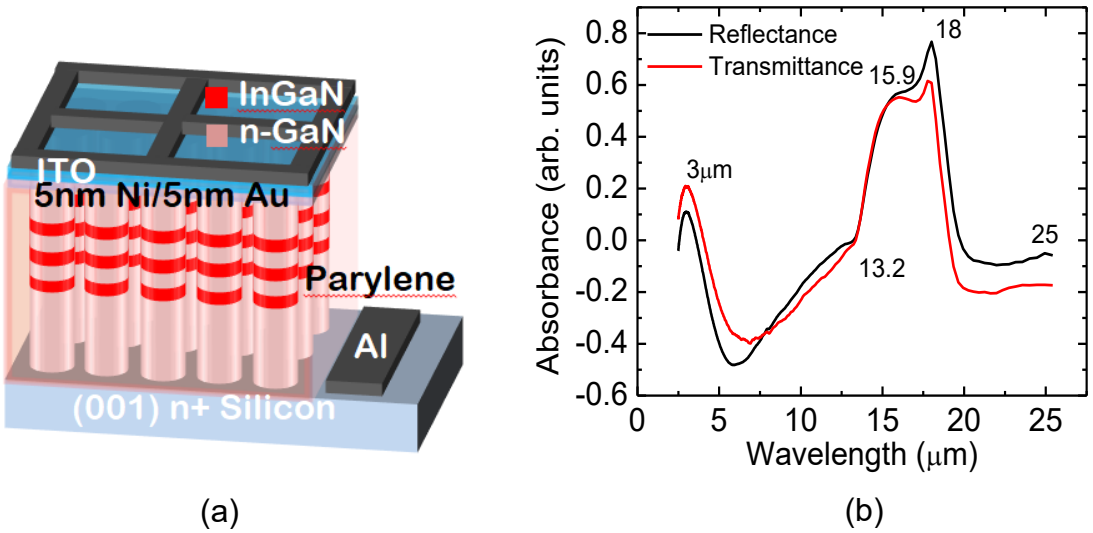

Figure 7.4 (a) Schematic of disk-in-nanowire infrared photodetector. The Ni/Au stack is optional and would improve IR transmission. (b) Absorption of as-grown $In_{0.34}Ga_{0.66}N$/GaN DINWs on silicon measured at 300 K.

APPENDICES

APPENDIX A

Microphotoluminescence

Microphotoluminescence (μPL) is a useful technique to focus and/or collect emission on a sample within a very tight beam size. This may be useful for small devices and nanostructures. It is important to characterize the beam size by measuring it. There are various methods, such as using a knife edge or a CCD camera. However, a CCD camera makes it difficult to align at the samples true surface, where the spot will be focused. Thus the knife-edge technique is ideal since one may physically measure across the sample surface location with a blade without disturbing the measurement setup. The formula for this technique is given in (A1), where P_0 is some offset power, x is blade translation, x_0 is some translation offset, w is beam waist (radius), and A is a fitting parameter. The experimental setup for μPL is schematically shown in Figure A1.

$$I(x) = I_0 + \left\{1 - \text{erf}[\sqrt{2} * \frac{x-x_0}{w}]\right\} * \frac{A}{2} \quad \text{(A1)}$$

A photo of the continuous-flow liquid-He cryostat for μPL is also shown in Figure A2(a). The objective lens may be exchanged for a deep-UV single lens. A CCD camera is installed here to allow viewing of the sample. Electrical connections can also be made to a sample within the cryostat and this is shown in Figure A2(b). Note the wires are neatly assembled and soldered in place to mitigate any thermal leakage. Silver paste must be used to fix sample securely and to allow thermal transfer.

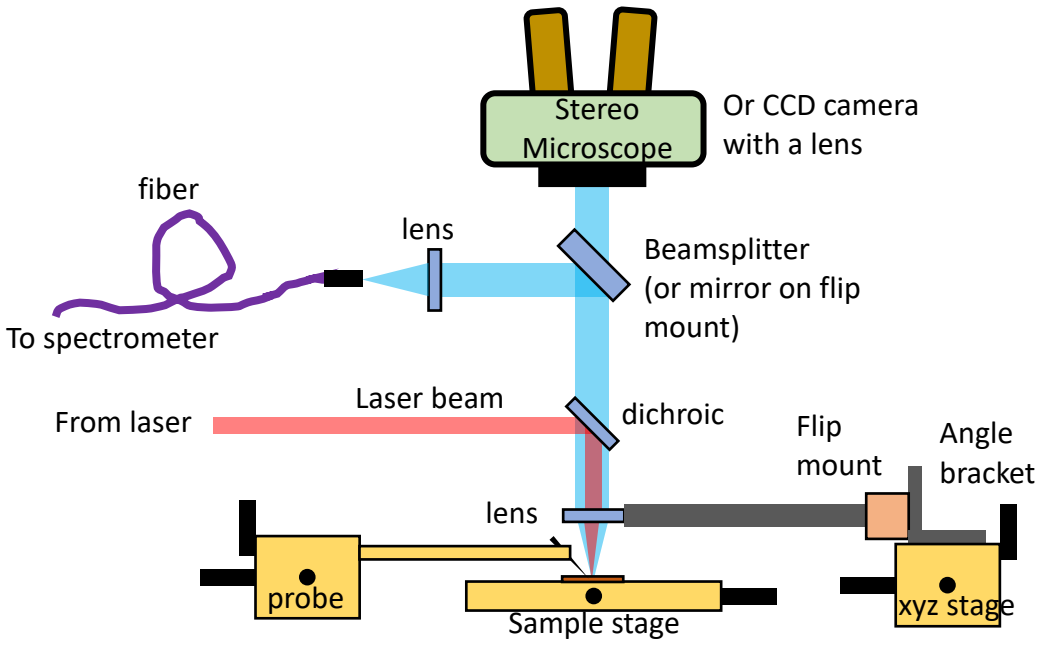

Figure A1 Microphotoluminescence experimental setup.

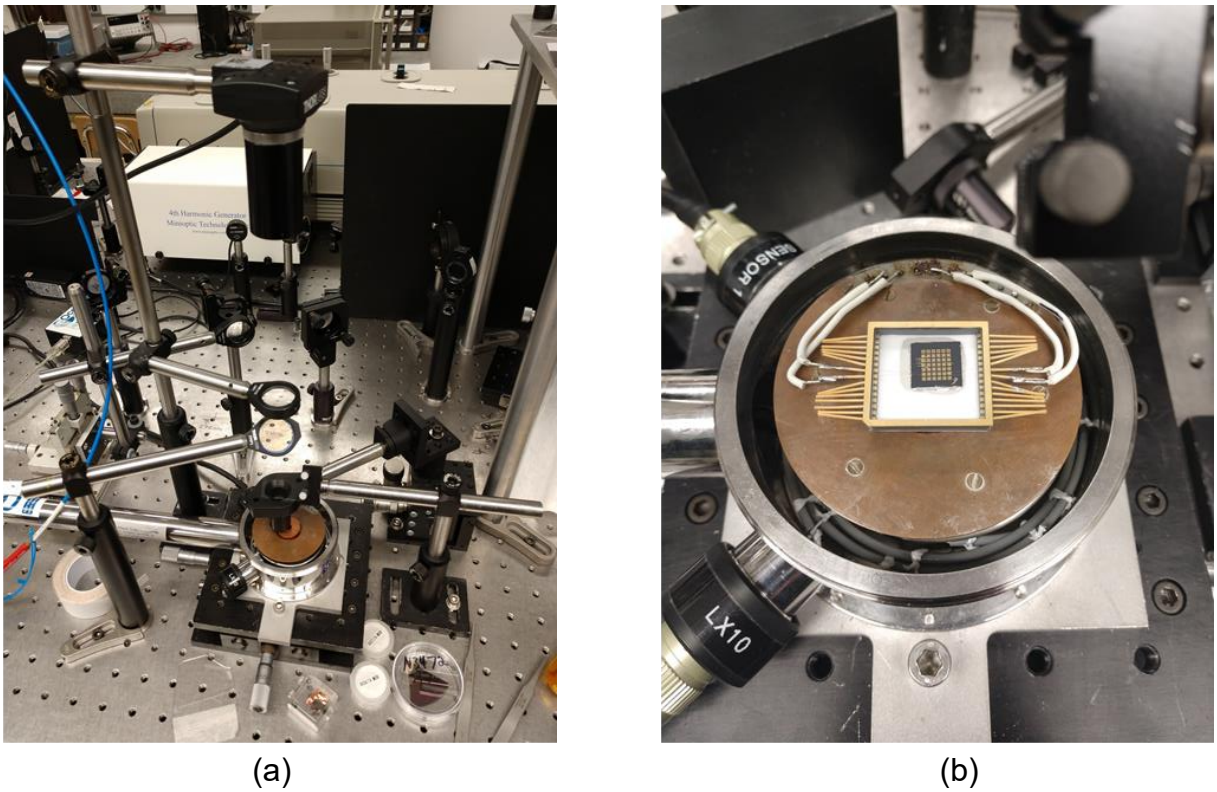

Figure A2 Photograph of continuous-flow liquid-He cryostat for (a) microphotoluminescence and (b) electrical connections to a device.

APPENDIX B

Time-Resolved Photoluminescence

TRPL is an experimental technique to study the carrier dynamics of a material. An ultrafast laser (oscillator) is typically used and if higher photon energy is required, such as that for wide-bandgap materials, the oscillating frequency may be converted to 2ω, 3ω, or even 4ω by means of non-linear crystals and/or a time-delay stage to achieve temporal overlap. The experimental setup is shown in Figure B1. If 4ω is required, the output of the tripler must then pass to a 4th harmonic generator and then the 4ω can be collected and passed to the sample. The Acton 2750 can be any monochromator and the id100 can be any single photon detector (SPD) or single photon counting module (SPCM). It is important to excite the sample such that the bands are not saturated with carriers. This can be done using a low to moderate excitation density, calculated using (B1).

$$n_{3D} = (1 - R)AI_p/\left(f_p \hbar\omega \pi r^2 L\right) \tag{B1}$$

R is reflectivity, A is absorbance in %, I_p is pump power, f_p is the pump frequency, $\hbar\omega$ is photon energy of the pump, r is excitation radius (beam waist measured from knife-edge), and L is the thickness of the absorbing material. One may obtain a 2D form by removing L from (B1).

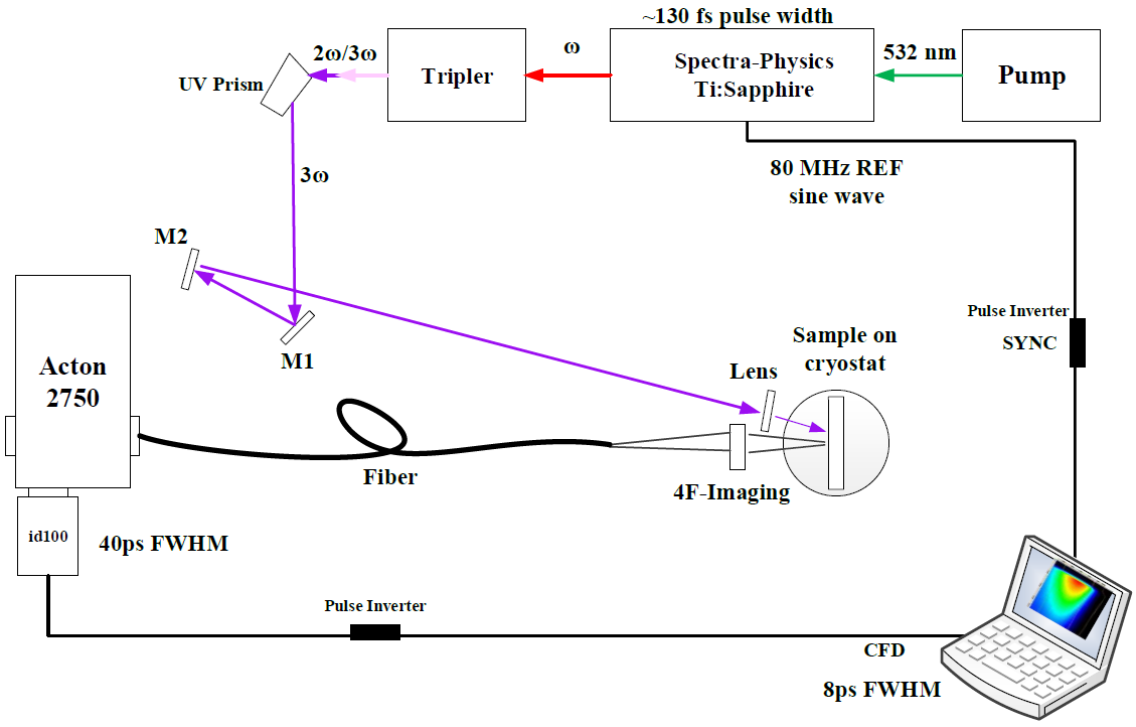

Figure B1 Schematic of time-resolved photoluminescence setup.

APPENDIX C

Measurement of Photocurrent Spectra

A photo of the photodetector measurement setup is shown in Figure C1. The device is mounted on a thermoelectric cooler probe platform. A stereomicroscope is inserted for probing and then swung out of position for the photocurrent measurement. A xenon light source illuminates the input slit of the monochromator and the output monochromatic light is directed to the device with a series of mirrors and focused by a lens at the stage.

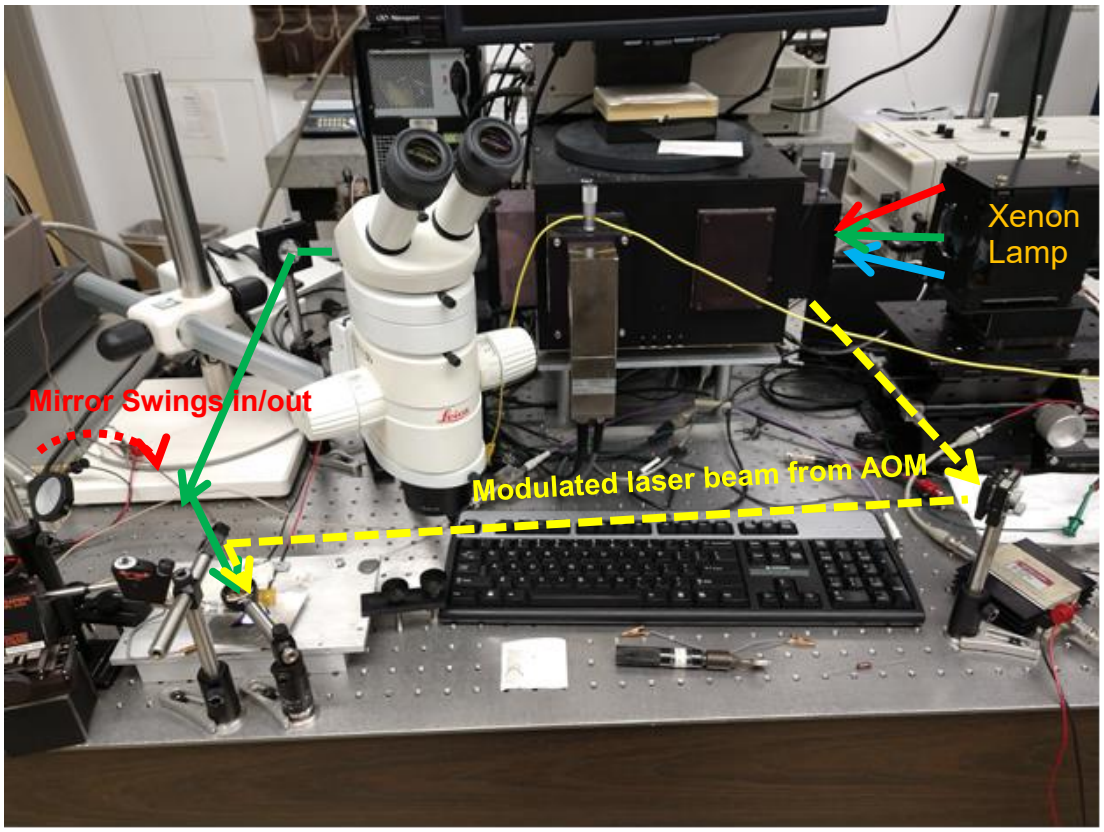

Figure C1 Photo of the experimental setup for photodetector characterization.

For high-speed measurements where the light must be modulated or chopped, an AOM can be used to chop a laser beam, which can then be directed to the device. This is also shown in Figure C1. A photo of the AOM is shown in Figure C2. It must be angled and rotated at the correct Bragg angle so a diffraction pattern can be observed. Mounting it on an XYZ-θ stage allows for ease of alignment. Then the desired order is picked off and directed to the sample.

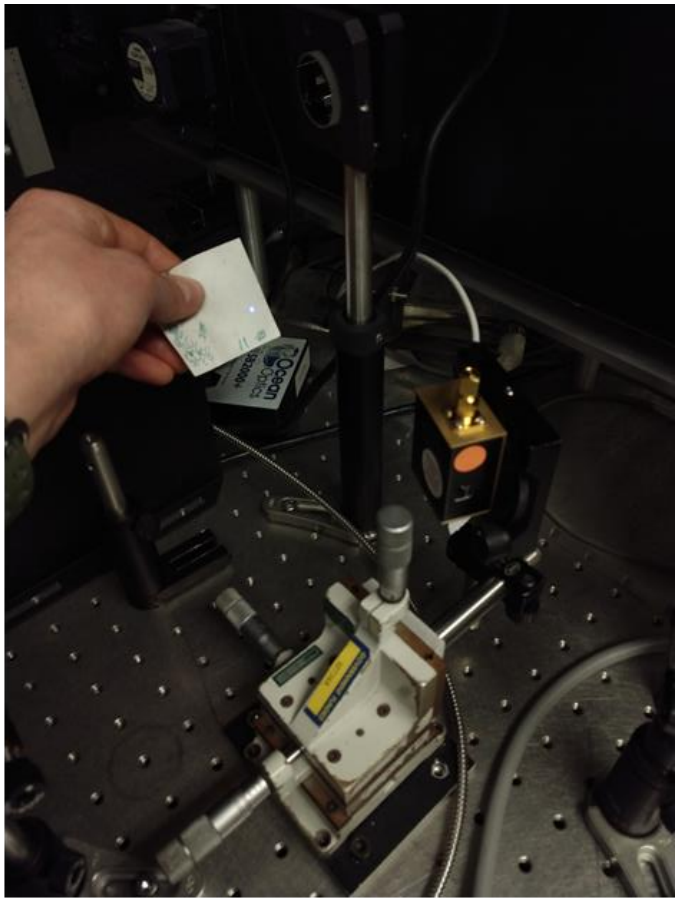

Figure C2 Photo of the acousto-optic modulator near the Bragg angle. Resulting diffraction pattern of the laser is viewable at the output.

APPENDIX D

Transient Absorption Spectroscopy

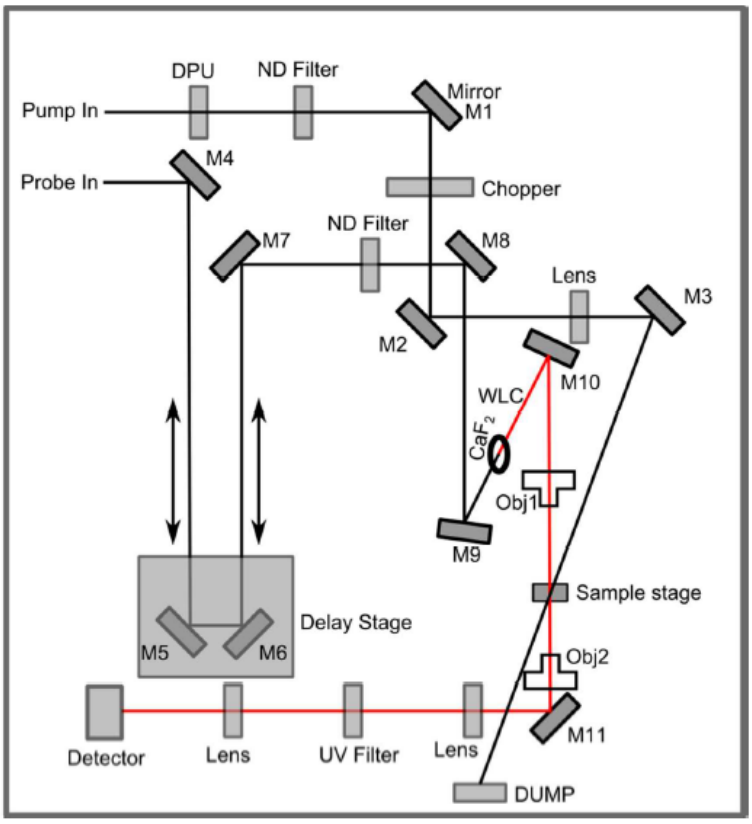

Figure D1 Schematic of HELIOS transient absorption spectrometer from Ultrafast Systems after [187]. Pump and probe signals are generated from a pulsed laser with a 1 kHz repetition rate and 50 fs pulse width. Energy per pulse is approximately 4 mJ. Probe signal passes from sample to a grating spectrometer for further processing. Probe delay is controlled by a motorized linear stage and the white light continuum (WLC) at 350-800 nm is generated from a CaF_2 crystal. DPU = depolarizing unit, ND = neutral density, Mx = mirror where 'x' is a number, and Obj = objective lens.

APPENDIX E

Nanowire Detector/LED Fabrication

1. Parylene-C Planarization and Passivation
   1.1. Parylene deposition
      1.1.1. PDS 2035 with silicon monitor piece
   1.2. Plasma Etch
      1.2.1. LAM 9400 to expose nanowire tips for p-contact. Etching calibration done with SEM imaging.
2. Defining Mesa
   2.1. Solvent Clean
      2.1.1. Acetone 5 min.
      2.1.2. IPA 5 min.
      2.1.3. DI rinse 5 min.
   2.2. Lithography (S1813 in parentheses)
      2.2.1. Dehydration bake 2 min, 115°C
      2.2.2. Photoresist manual coat, SPR-220-3.0, 4kRPM (or S1813 2kRPM)
      2.2.3. Soft Bake 90 sec, 115°C (60 sec)
      2.2.4. Exposure, 6 sec MJB3 contact aligner (9 sec)
      2.2.5. Post exposure bake 90 sec, 115°C (none)
      2.2.6. Development, AZ 726 MIF, 60-60 DP
      2.2.7. DI rinse 1 min.
      2.2.8. (Hard bake S1813 before a wet etch)
   2.3. Plasma Etch
      2.3.1. LAM 9400 Cl_2-based dry etch, ~5nm/sec
      2.3.2. Etch 600 μm x 600 μm mesa
      2.3.3. SEM imaging
   2.4. Resist Strip
      2.4.1. YES plasma stripper 300sec, 200W, 250mT, O_2
      2.4.2. Acetone 5 min.
      2.4.3. IPA 5 min.
      2.4.4. DI rinse 5 min.
3. P-contact
   3.1. Solvent Clean
      3.1.1. Acetone 5 min.
      3.1.2. IPA 5 min.
      3.1.3. DI rinse 5 min.
   3.2. Lithography (S1813 in parentheses)
      3.2.1. Dehydration bake 2 min, 115°C
      3.2.2. Photoresist manual coat, SPR-220-3.0, 4kRPM (or S1813 2kRPM)

3.2.3. Soft Bake 90 sec, 115°C (60 sec)
3.2.4. Exposure, 6 sec MJB3 contact aligner (9 sec)
3.2.5. Post exposure bake 90 sec, 115°C (none)
3.2.6. Development, AZ 726 MIF, 60-60 DP
3.2.7. DI rinse 1 min.
3.2.8. (Hard bake S1813 before a wet etch)

3.3. Descum
3.3.1. YES plasma stripper 90 sec, 90W, 250mT, O_2

3.4. Oxide Removal
3.4.1. HCl:DI water 1:1, 2 min.
3.4.2. DI rinse 5 min.

3.5. Ammonium Sulfide $(NH_4)_2S_x$ Treatment (optional)
3.5.1. 5 min.
3.5.2. DI rinse 5 min.

3.6. Metal Deposition
3.6.1. Angstrom Engineering/SJ-20 E-beam Ni/Au 5nm/5nm

3.7. Metal Deposition
3.7.1. Kurt Lesker Lab 18 sputtering, ITO, 230nm

3.8. Lift-off
3.8.1. 24 hours acetone
3.8.2. IPA 5 min.
3.8.3. DI rinse 5 min.

3.9. Anneal
3.9.1. JetFirst 150 RTP 550°C, 2 min, N_2:O_2 4:1 ambient

4. N-contact

4.1. Solvent Clean
4.1.1. Acetone 5 min.
4.1.2. IPA 5 min.
4.1.3. DI rinse 5 min.

4.2. Lithography (S1813 in parentheses)
4.2.1. Dehydration bake 2 min, 115°C
4.2.2. Photoresist manual coat, SPR-220-3.0, 4kRPM (or S1813 2kRPM)
4.2.3. Soft Bake 90 sec, 115°C (60 sec)
4.2.4. Exposure, 6 sec MJB3 contact aligner (9 sec)
4.2.5. Post exposure bake 90 sec, 115°C (none)
4.2.6. Development, AZ 726 MIF, 60-60 DP
4.2.7. DI rinse 1 min.
4.2.8. (Hard bake S1813 before a wet etch)

4.3. Descum
4.3.1. YES plasma stripper 90 sec, 90W, 250Mt, O_2

4.4. Metal Deposition
4.4.1. Angstrom Engineering/SJ-20 E-beam Al/Au 100nm/10nm

4.5. Lift-off
4.5.1. 24 hours acetone
4.5.2. IPA 5 min.
4.5.3. DI rinse 5 min.

APPENDIX F

Planar LED Fabrication

1. HCl clean metal off sample, 10 min.
2. Defining Mesa
   - 2.1. Solvent Clean
     - 2.1.1. Acetone 5 min.
     - 2.1.2. IPA 5 min.
     - 2.1.3. DI rinse 5 min.
   - 2.2. Lithography (S1813 in parentheses)
     - 2.2.1. Dehydration bake 2 min, 115°C
     - 2.2.2. Photoresist manual coat, SPR-220-3.0, Thin, 4kRPM (or S1813 2kRPM)
     - 2.2.3. Soft Bake 90 sec, 115°C (60 sec)
     - 2.2.4. Exposure, 6 sec MJB3 contact aligner (9 sec)
     - 2.2.5. Post exposure bake 90 sec, 115°C (none)
     - 2.2.6. Development, AZ 726 MIF, 60-60 DP
     - 2.2.7. (Hard bake S1813 before a wet etch)
     - 2.2.8. Microscope inspection
     - 2.2.9. Dektak XT step height BEFORE etch for PR thickness
   - 2.3. Plasma Etch
     - 2.3.1. LAM 9400 Cl_2-based dry etch, ~5-8nm/sec, Recipe GaN_2mT_150W_Abanerji (Oxford RIE is much more gentle; use recipe GaN_Ayush3, etch rate is ~2.8 nm/s)
     - 2.3.2. Dektak XT step height for etch rate (take into account PR thickness)
     - 2.3.3. Etch 600 μm x 600 μm mesa
   - 2.4. Resist Strip
     - 2.4.1. YES plasma stripper Recipe 2, 360sec, 800W, 250mT, O_2
     - 2.4.2. Microscope inspection
3. P-contact
   - 3.1. Solvent Clean
     - 3.1.1. Acetone 5 min.
     - 3.1.2. IPA 5 min.
     - 3.1.3. DI rinse 5 min.
   - 3.2. Lithography (S1813 in parentheses)
     - 3.2.1. Dehydration bake 2 min, 115°C
     - 3.2.2. Photoresist manual coat, SPR-220-3.0, Thin, 4kRPM (or S1813 2kRPM)
     - 3.2.3. Soft Bake 90 sec, 115°C (60 sec)
     - 3.2.4. Exposure, 6 sec MJB3 contact aligner (9 sec)
     - 3.2.5. Post exposure bake 90 sec, 115°C (none)
     - 3.2.6. Development, AZ 726 MIF, 60-60 DP
     - 3.2.7. (Hard bake S1813 before a wet etch)

3.2.8. Microscope inspection

3.3. Oxide Removal

3.3.1. HCl, 2 min.

3.3.2. DI rinse 5 min.

3.4. Metal Deposition

3.4.1. Angstrom Engineering/SJ-20 E-beam/ Lab-18 Ni/Au 5nm/5nm

3.5. Lift-off (30 min. in hot Remover PG first and then lightly rubbing with foam swab helps process)

3.5.1. Hot Acetone

3.5.2. IPA 5 min.

3.5.3. DI rinse 5 min.

3.5.4. Microscope inspection

3.6. Anneal

3.6.1. JetFirst 150 RTP 550°C, 2 min, N_2:O_2 4:1 ambient, Recipe PKB_pGaN

4. N-contact

4.1. Lithography (S1813 in parentheses)

4.1.1. Dehydration bake 2 min, 115°C

4.1.2. Photoresist manual coat, SPR-220-3.0, Thin, 4kRPM (or S1813 2kRPM)

4.1.3. Soft Bake 90 sec, 115°C (60 sec)

4.1.4. Exposure, 6 sec MJB3 contact aligner (9 sec)

4.1.5. Post exposure bake 90 sec, 115°C (none)

4.1.6. Development, AZ 726 MIF, 60-60 DP

4.1.7. (Hard bake S1813 before a wet etch)

4.1.8. Microscope inspection

4.2. Oxide Removal

4.2.1. HCl, 2 min.

4.2.2. DI rinse 5 min.

4.3. Metal Deposition

4.3.1. Angstrom Engineering/SJ-20 E-beam/Lab-18 Ti/Au 25nm/100nm

4.4. Lift-off

4.4.1. Hot Acetone

4.4.2. IPA 5 min.

4.4.3. DI rinse 5 min.

4.4.4. Microscope inspection

APPENDIX G

Fabrication for Proposed Single Photon Source

1. Deposition of Alignment Mark
   - 1.1. Remove metal after growth; Solvent clean 10 min acetone, 10 min IPA, DI rinse 2 min
   - 1.2. Lithography
     - 1.2.1. Dehydrate bake: 2 min, 115C hotplate
     - 1.2.2. HMDS – YES Image Reversal Oven
     - 1.2.3. Resist coating: SPR 220-3.0 4.0 krpm, 30 sec, Soft Bake: 90 sec at 115C on hotplate
     - 1.2.4. Exposure: 0.38 sec in stepper (GCA AS200 AutoStep stepper – job: PKBSPS)
     - 1.2.5. Post-exposure bake: 90 sec at 115C
     - 1.2.6. Resist development: AZ 726 Piece DP 60-60 sec
   - 1.3. Descum
     - 1.3.1. YES plasma stripper, 20 sec, 100 W, 250mT, 17% O_2
   - 1.4. Metal Deposition
     - 1.4.1. E-beam Ti/Au 10 nm/30 nm
   - 1.5. Lift-off in Acetone/Remover PG
2. P-contact
   - 2.1. Solvent clean
   - 2.2. Lithography
   - 2.3. Descum
   - 2.4. HCl dip, 2 min
   - 2.5. Metal Deposition
     - 2.5.1. E-beam Ni/Au 5 nm/5 nm
   - 2.6. Lift-off
3. 200 nm Apertures
   - 3.1. Solvent Clean
   - 3.2. Lithography
     - 3.2.1. Overexpose (0.4 sec)
   - 3.3. Descum
   - 3.4. Metal Deposition
     - 3.4.1. E-beam Al 300 nm
   - 3.5. Lift-off
4. Defining Mesa
   - 4.1. Solvent Clean
   - 4.2. Lithography
   - 4.3. Plasma etch Oxford Plasmalab RIE recipe: GaN_Ayush3, etch rate ~2.8 nm/s
   - 4.4. Resist strip
   - 4.5. Dektak measure height

5. N-contact and contact pads
    5.1. Lithography
    5.2. Descum
    5.3. Metal Deposition
        5.3.1. E-beam Ti/Au 25 nm/300 nm
    5.4. Lift-off

BIBLIOGRAPHY

[1] N. Holonyak and S. F. Bevacqua, Appl. Phys. Lett. **1**, 82 (1962).

[2] S. Nakamura, M. Senoh, and T. Mukai, Jpn. J. Appl. Phys. **32**, L8 (1993).

[3] H. Amano, N. Sawaki, I. Akasaki, and Y. Toyoda, Appl. Phys. Lett. **48**, 353 (1986).

[4] H. Amano, M. Kito, K. Hiramatsu, and I. Akasaki, Jpn. J. Appl. Phys. **28**, L2112 (1989).

[5] Y. Xie, http://www.seas.ucla.edu/smrl/GaN.html (2015).

[6] US DOE, apps1.eere.energy.gov/buildings/publications/pdfs/ssl/ssl_mypp2012_web.pdf (2020).

[7] US DOE, https://www.energy.gov/sites/prod/files/2020/01/f70/ssl-rd-opportunities2-jan2020.pdf (2020).

[8] S. Nakamura, M. Senoh, S. Nagahama, N. Iwasa, T. Yamada, T. Matsushita, Y. Sugimoto, and H. Kiyoku, Appl. Phys. Lett. **69**, 4056 (1996).

[9] Y. Enya, Y. Yoshizumi, T. Kyono, K. Akita, M. Ueno, M. Adachi, T. Sumitomo, S. Tokuyama, T. Ikegami, K. Katayama, and T. Nakamura, Appl. Phys. Exp. **2**, 082101 (2009).

[10] T. Frost, A. Banerjee, K. Sun, S. L. Chuang, and P. Bhattacharya, IEEE J. Quant. Electron. **49**, 923 (2013).

[11] P. Bhattacharya, T. Frost, S. Deshpande, Z. Baten, A. Hazari, and A. Das, Phys. Rev. Lett. **112**, 236802 (2014).

[12] A. Hazari, F. C. Hsiao, L. Yan, J. Heo, J. M. Millunchick, J. M. Dallesasse, and P. Bhattacharya, IEEE J. Quant. Electron. **53**, 6300109 (2017).

[13] E. Monroy, F. Calle, and E. Muñoz, Appl. Phys. Lett. **74**, 3401 (1999).

[14] S. Keller, C. S. Suh, Z. Chen, R. Chu, S. Rajan, N. A. Fichtenbaum, M. Furukawa, S. P. DenBaars, J. S. Speck, and U. K. Mishra, J. Appl. Phys. **103**, 033708 (2008).

[15] S. W. Kaun, M. H. Wong, U. K. Mishra, and J. S. Speck, Semicond. Sci. Technol. **28**, 074001 (2013).

[16] M. H. Wong, S. Keller, N. S. Dasgupta, D. J. Denninghoff, S. Kolluri, D. F. Brown, J. Lu, N. A. Fichtenbaum, E. Ahmadi, U. Singisetti, A. Chini, S. Rajan, S. P. DenBaars, J. S. Speck, and U. K. Mishra, Semicond. Sci. Technol. **28**, 074009 (2013).

[17] T. Zhu and R. A. Oliver, Phys. Chem. Chem. Phys. **14**, 9558 (2012).

[18] M. C. Schmidt, K.-C. Kim, R. M. Farrell, D. F. Feezell, D. A. Cohen, M. Saito, K. Fujito, J. S. Speck, S. P. DenBaars, and S. Nakamura, Jpn. J. Appl. Phys. **46**, L190 (2007).

[19] G. Namkoong, E. Trybus, K. K. Lee, M. Moseley, W. A. Doolittle, and D. C. Look, Appl. Phys. Lett. **93**, 172112 (2008).

[20] M. Zhang, P. Bhattacharya, W. Guo, and A. Banerjee, Appl. Phys. Lett. **96**, 132103 (2010).

[21] J. S. Speck, https://www.winton.phy.cam.ac.uk/JimSpeckWintonEnergySymposium.pdf (2020).

[22] A. Pandey, W. J. Shin, J. Gim, R. Hovden, and Z. Mi, Photonics Res. **8**, 331 (2020).

[23] S. M. Islam, K. Lee, J. Verma, V. Protasenko, S. Rouvimov, S. Bharadwaj, H. Xing, and D. Jena, Appl. Phys. Lett. **110**, 041108 (2017).

[24] S. Tamariz, G. Callsen, and N. Grandjean, Appl. Phys. Lett. **114**, 082101 (2019).

[25] X. Liu, S. Zhao, B. H. Le, and Z. Mi, Appl. Phys. Lett. **111**, 101103 (2017).

[26] S. Jahangir, *III-Nitride Self-Assembled Nanowire Light Emitting Diodes and Lasers on (001) Silicon*, Dissertation, University of Michigan (2015).

[27] S. Fernández-Garrido, J. Grandal, E. Calleja, M. A. Sánchez-García, and D. López-Romero, Appl. Phys. Lett. **106**, 126102 (2009).

[28] S. Deshpande, T. Frost, L. Yan, S. Jahangir, A. Hazari, X. Liu, J. M. Millunchick, Z. Mi, and P. Bhattacharya, Nano Lett. **15**, 1647 (2015).

[29] G. Koblmüller, S. Fernández-Garrido, E. Calleja, and J. S. Speck, Appl. Phys. Lett. **91**, 161904 (2007).

[30] A. Aiello, A. Pandey, A. Bhattacharya, J. Gim, X. Liu, D. A. Laleyan, R. Hovden, Z. Mi, and P. Bhattacharya, J. Cryst. Growth **508**, 66 (2019).

[31] M. J. Paisley, Z. Sitar, B. Yan, and R. F. Davis, J. Vac. Sci. Technol. B **8**, 323 (1990).

[32] A.Y. Cho, M.B. Panish, and I. Hayashi, Proceedings of the Third International Symposium on GaAs and Related Compounds **18**, London: Institute of Physics (1970).

[33] Molecular Beam Epitaxy Materials and Applications for Electronics and Optoelectronics, Edited by H. Asahi and Y. Horikoshi, Hoboken, Wiley (2019).

[34] S. Yoshida, S. Misawa, and A. Itoh, Appl. Phys. Lett. **26**, 461 (1975).

[35] M. J. Paisley, Z. Sitar, J. B. Posthill, and R. F. Davis, J. Vac. Sci. Technol. A **7**, 701 (1989).

[36] G. Koblmüller, J. R. Lang, E. C. Young, and J. S. Speck, Molecular Beam Epitaxy of Nitrides for Advanced Electronic Materials. In Handbook of Crystal Growth, Thin Films and Epitaxy: Basic Techniques, Amsterdam, Elsevier (2015).

[37] P. A. Bennett and M. W. Webb, Surf. Sci. **104**, 74 (1981).

[38] C. Adelmann, J. Simon, G. Feuillet, N. T. Pelekanos, B. Daudin, and G. Fishman, Appl. Phys. Lett. **76**, 1570 (2000).

[39] H. Hirayama, T. Yatabe, N. Noguchi, T. Ohashi, and N. Kamata, Appl. Phys. Lett. **91**, 071901 (2007).

[40] M. Kneissl, T. Kolbe, C. Chua, V. Kueller, N. Lobo, J. Stellmach, A. Knauer, H. Rodriguez, S. Einfeldt, Z. Yang, et al., Semicond. Sci. Technol. **26**, 014036 (2011).

[41] S. Vilhunen, H. Särkkä, and M. Sillanpää, Environ. Sci. Pollut. Res. **16**, 439 (2009).

[42] T. Wang, C. Tasi, C. Lin, and D. Wuu, Scientific Reports **7**, 14422 (2017).

[43] T. Takano, T. Mino, J. Sakai, N. Noguchi, K. Tsubaki, and H. Hirayama, Appl. Phys. Express **10**, 031002 (2017).

[44] V. N. Jmerik, A. M. Mizerov, A. A. Sitnikova, P. S. Kop'ev, S. V. Ivanov, E. V. Lutsenko, N. P. Tarasuk, N. V. Rzheutskii, and G. P. Yablonskii, Appl. Phys. Lett. **96**, 141112 (2010).

[45] Y. Liao, C. Thomidis, C. Kao, and T. D. Moustakas, Appl. Phys. Lett. **98**, 81110 (2011).

[46] K. Ban, J. Yamamoto, K. Takeda, K. Ide, M. Iwaya, T. Takeuchi, S. Kamiyama, I. Akasaki, and H. Amano, Appl. Phys. Express **4**, 052101 (2011).

[47] T. Kyono, H. Hirayama, K. Akita, T. Nakamura, M. Adachi, and K. Ando, J. Appl. Phys. **99**, 114509 (2006).

[48] J. E. Northrup, J. Neugebauer, R. M. Feenstra, and A.R. Smith, Phys. Rev. B **61**, 9932 (2000).

[49] T. D. Moustakas and A. Bhattacharyya, Phys. Status Solidi C **9**, 580 (2012).

[50] A. Bhattacharyya, T. D. Moustakas, L. Zhou, D. J. Smith, and W. Hug, Appl. Phys. Lett. **94**, 181907 (2009).

[51] I. Friel, C. Thomidis, and T. D. Moustakas, Appl. Phys. Lett. **85**, 3068 (2004).

[52] I. Friel, C. Thomidis, Y. Fedyunin, and T. D. Moustakas, J. Appl. Phys. **95**, 3495 (2004).

[53] P. G. Eliseev, P. Perlin, J. Lee, and M. Osinski, Appl. Phys. Lett. **71**, 569 (1997).

[54] J. Singh, *Electronic and Optoelectronic Properties of Semiconductor Structures* (Cambridge University Press, Cambridge, UK, 2003).

[55] I. Vurgaftman and J. R. Meyer, J. Appl. Phys. **94**, 3675 (2003).

[56] P. Reddy, I. Bryan, Z. Bryan, J. Tweedie, S. Washiyama, R. Kirste, S. Mita, R. Collazo, and Z. Sitar, Appl. Phys. Lett. **107**, 091603 (2015).

[57] W. Wei-Ying, L. Gui-Peng, J. Peng, M. De-Feng, L. Wei, W. Zhan-Guo, T. Wu, and C. Chang-Qing, Chin. Phys. B **23**, 117803 (2014).

[58] J. Singh and K. K. Bajaj, J. Appl. Phys **57**, 5433 (1985).

[59] N. Chand and S. N. G. Chu, Appl. Phys. Lett. **57**, 1796 (1990).

[60] K. Kamath, N. Chervela, K. K. Linder, T. Sosnowski, H-T. Jiang, T. Norris, J. Singh, and P. Bhattacharya, Appl. Phys. Lett. **71**, 927 (1997).

[61] W. Yang, R. R. Lowe-Webb, H. Lee, and P. Sercel, Phys. Rev B **56**, 13314 (1997).

[62] A. Banerjee, T. Frost, E. Stark, and P. Bhattacharya, Appl. Phys. Lett **101**, 041108 (2012).

[63] A. Hazari, A. Aiello, T. Ng, B. Ooi, and P. Bhattacharya, Appl. Phys. Lett. **107**, 191107 (2015).

[64] Y. Taniyasu, M. Kasu, and T. Makimoto, Nature **441**, 325 (2006).

[65] A. Khan, K. Balakrishnan, and T. Katona, Nat. Photonics **2**, 77 (2008).

[66] M. S. Shur and R. Gaska, IEEE Trans. Electron Devices **57**, 12 (2010).

[67] P. S. Ramanujam and R. H. Berg, Appl. Phys. Lett. **85**, 1665 (2004).

[68] K. G. Lindenauer and J. L. Darby, Water Res. **28**, 805 (1994).

[69] H. Tsuzuki, F. Mori, K. Takeda, T. Ichikawa, M. Iwaya, S. Kamiyama, H. Amano, I. Akasaki, H. Yoshida, M. Kuwabara, Y. Yamashita, and H. Kan, Phys. Status Solidi A **206**, 1199 (2009).

[70] X. Xu, J. Zhong, H. So, A. Norvilas, C. Sommerhalter, D.G. Senesky, and M. Tang, AIP Adv. **6**, 115016 (2016).

[71] K. B. Nam, J. Li, M. L. Nakarmi, J. Y. Lin, and H. X. Jiang, Appl. Phys. Lett. **81**, 1038 (2002).

[72] J. Li, K. B. Nam, J. Y. Lin, and H. X. Jiang, Appl. Phys. Lett. **79**, 3245 (2001).

[73] Y. H. Liang and E. Towe, J. Appl. Phys. **123**, 095303 (2018).

[74] Y. H. Liang and E. Towe, Appl. Phys. Rev. **5**, 011107 (2018).

[75] Y. Taniyasu and M. Kasu, Appl. Phys. Lett. **96**, 221110 (2010).

[76] M. Suzuki, T. Uenoyama, and A. Yamane, Phys. Rev. B **52**, 8132 (1995).

[77] Y. Taniyasu and M. Kasu, Appl. Phys. Lett. **99**, 251112 (2011).

[78] K. Kamiya, Y. Ebihara, K. Shiraishi, and M. Kasu, Appl. Phys. Lett. **99**, 151108 (2011).

[79] S. M. Islam, V. Protasenko, K. Lee, S. Rouvimov, J. Verma, H. Xing, and D. Jena, Appl. Phys. Lett. **111**, 091104 (2017).

[80] H. Kobayashi, S. Ichikawa, M. Funato, and Y. Kawakami, Adv. Opt. Mater. **7**, 1900860 (2019).

[81] B. Peng, H. Zhang, H. Shao, K. Xu, G. Ni, L. Wu, J. Li, H. Lu, Q. Jin, and H. Zhu, ACS Photonics **5**, 4081 (2018).

[82] D. Bayerl, S. M. Islam, C. M. Jones, V. Protasenko, D. Jena, and E. Kioupakis, Appl. Phys. Lett. **109**, 241102 (2016).

[83] N. Sanders, D. Bayerl, G. Shi, K. A. Mengle, and E. Kioupakis, Nano Lett. **17**, 7345 (2017).

[84] D. Bayerl and E. Kioupakis, Appl. Phys. Lett. **115**, 131101 (2019).

[85] G. Christmann, R. Butté, E. Feltin, A. Mouti, P. A. Stadelmann, A. Castiglia, J.-F. Carlin, and N. Grandjean, Phys. Rev. B **77**, 085310 (2008).

[86] S. Christopoulos, G. B. H. v. Högersthal, A. J. D. Grundy, P. G. Lagoudakis, A. V. Kavokin, and J. J. Baumberg, Phys. Rev. Lett. **98**, 126405 (2007).

[87] A. Das, J. Heo, M. Jankowski, W. Guo, L. Zhang, H. Deng, and P. Bhattacharya, Phys. Rev. Lett. **107**, 066405 (2011).

[88] M. Knupfer, Appl. Phys. A **77**, 623 (2003).

[89] D. M. Bagnall, Y. F. Chen, Z. Zhu, T. Yao, S. Koyama, M. Y. Shen, and T. Goto, Appl. Phys. Lett. **70**, 2230 (1997).

[90] B. Zhu, X. Chen, and X. Cui, Sci. Rep. **5**, 9218 (2015).

[91] A. Aiello, Y. Wu, A. Pandey, P. Wang, W. Lee, D. Bayerl, N. Sanders, Z. Deng, J. Gim, K. Sun, R. Hovden, E. Kioupakis, Z. Mi, and P. Bhattacharya, Nano Lett. **19**, 7852 (2019).

[92] W. Guo, A. Banerjee, P. Bhattacharya, and B. S. Ooi, Appl. Phys. Lett. **98**, 193102 (2011).

[93] W. Guo, M. Zhang, A. Banerjee, and P. Bhattacharya, Nano Lett. **10**, 3355 (2010).

[94] N. H. Tran, B. H. Le, S. Zhao, and Z. Mi, Appl. Phys. Lett. **110**, 032102 (2017).

[95] Y. Wu, Y. Wang, K. Sun, and Z. Mi, J. Cryst. Growth **507**, 65 (2019).

[96] L. Rigutti, L. Mancini, W. Lefebvre, J. Houard, D. Hernàndez-Maldonado, E. Di Russo, E. Giraud, R. Butté, J.-F. Carlin, N. Grandjean, D. Blavette, and F. Vurpillot, Semicond. Sci. Technol. **31**, 095009 (2016).

[97] A. Zunger, S.-H. Wei, L. G. Ferreira, and J. E. Bernard, Phys. Rev. Lett. **65**, 353 (1990).

[98] A. van de Walle, P. Tiwary, M. de Jong, D. L. Olmsted, M. Asta, A. Dick, D. Shin, Y. Wang, L.-Q. Chen, and Z.-K. Liu, CALPHAD: Comput. Coupling Phase Diagrams Thermo- chem. **42**, 13 (2013).

[99] Y. P. Varshni, Physica **34**, 149 (1967).

[100] H. Schömig, S. Halm, A. Forchel, and G. Bacher, Phys. Rev. Lett. **92**, 106802 (2004).

[101] J. Ma, X. Ji, G. Wang, X. Wei, H. Lu, X. Yi, R. Duan, J. Wang, Y. Zeng, J. Li, F. Yang, C. Wang, and G. Zou, Appl. Phys. Lett. **101**, 131101 (2012).

[102] E. Muñoz, E. Monroy, J. L. Pau, F. Calle, F. Omnes, and P. Gibart, J. Phys.: Condens. Matter **13**, 7115 (2001).

[103] C. Rivera, J. L. Pau, A. Navarro, and E. Muñoz, IEEE J. Quant. Electron. **42**, 51 (2006).

[104] S. Jahangir, M. Mandl, M. Strassburg, and P. Bhattacharya, Appl. Phys. Lett. **102**, 071101 (2013).

[105] S. Jahangir, T. Schimpke, M. Strassburg, K. A. Grossklaus, J. M. Millunchick, and P. Bhattacharya, IEEE J. Quant. Electron. **50**, 530 (2014).

[106] S. Deshpande, A. Das, and P. Bhattacharya, Appl. Phys. Lett. **102**, 161114 (2013).

[107] T. Frost, S. Jahangir, E. Stark, S. Deshpande, A. Hazari, C. Zhao, B. S. Ooi, and P. Bhattacharya, Nano Lett. **14**, 4535 (2014).

[108] R. Calarco, M. Marso, T. Richter, A. I. Aykanat, R. Meijers, A. Hart, T. Stoica, and H. Luth, Nano Lett. **5**, 981 (2005).

[109] J. Pereiro, C. Rivera, A. Navarro, E. Muñoz, R. Czernecki, S. Grzanka, and M. Leszczynski, IEEE J. Quant. Electron. **45**, 617 (2009).

[110] L. Rigutti, M. Tchernycheva, A. Bugallo, G. Jacopin, F. H. Julien, L. F. Zagonel, K. March, O. Stephan, M. Kociak, and R. Songmuang, Nano Lett. **10**, 2939 (2010).

[111] A. Bugallo, M. Tchernycheva, G. Jacopin, L. Rigutti, F. H. Julien, S. T. Chou, Y. T. Lin, P. H. Tseng, and L. W. Tu, Nanotechnology **21**, 315201 (2010).

[112] A. Bugallo, L. Rigutti, G. Jacopin, F. H. Julien, C. Durand, X. J. Chen, D. Salomon, J. Eymery, and M. Tchernycheva, Appl. Phys. Lett. **98**, 233107 (2011).

[113] F. Gonzalez-Posada, R. Songmuang, M. D. Hertog, and E. Monroy, Nano Lett. **12**, 172 (2012).

[114] H. Zhang, A. V. Babichev, G. Jacopin, P. Lavenus, F. H. Julien, A. Y. Egorov, J. Zhang, T. Pauporte, and M. Tchernycheva, J. Appl. Phys. **114**, 234505 (2013).

[115] G. Jacopin, A. Bugallo, L. Rigutti, P. Lavenus, F. H. Julien, Y. T. Lin, L. W. Tu, and M. Tchernycheva, Appl. Phys. Lett. **104**, 023116 (2014).

[116] A. Aiello, A. K. M. H. Hoque, M. Z. Baten, and P. Bhattacharya, ACS Photonics **6**, 1289 (2019).

[117] E. Monroy, F. Omnes, and F. Calle, Semicond. Sci. Technol. **18**, R33 (2003).

[118] F. Urbach, Phys. Rev. **92**, 1324 (1953).

[119] R. W. Martin, P. G. Middleton, K. P. O'Donnell, and W. Van der Stricht, Appl. Phys. Lett. **74**, 263 (1999).

[120] J. A. Garrido, E. Monroy, and E. Muñoz, Semicond. Sci. Technol. **13**, 563 (1998).

[121] N. A. Sanford, P. T. Blanchard, K. A. Bertness, L. Mansfield, J. B. Schlager, A. W. Sanders, A. Roshko, B. B. Burton, and S. M. George, J. Appl. Phys. **107**, 034318 (2010).

[122] M. Vallone, M. Goano, F. Bertazzi, and G. Ghione, J. Appl. Phys. **121**, 123107 (2017).

[123] W. H. Fan, S. M. Olaizola, T. Wang, P. Parbrook, J. Wells, D. J. Mowbray, M. S.

Skolnick, and A. M. Fox, Phys. Status Solidi B **240**, 364 (2003).

[124] A. Hazari, A. Bhattacharya, T. Frost, S. Zhao, Z. Baten, Z. Mi, and P. Bhattacharya, Opt. Lett. **40**, 3304 (2015).

[125] P. Bhattacharya, Semiconductor Optoelectronic Devices, 2nd ed., Prentice-Hall: Upper Saddle River (1997).

[126] Hamamatsu Si Photodiodes. https://www.hamamatsu.com/us/en/product/optical-sensors/photodiodes/si-photodiodes/index.html (accessed Apr 14, 2019).

[127] M. A. Krainak, X. Sun, G. Yang, and W. Lu, Proc. SPIE **7681**, 76810Y (2010).

[128] Roithner Laser UV Photodiodes. http://www.roithner-laser.com/pd_uv.html (accessed Apr 14, 2019).

[129] Q. Chen, J. W. Yang, A. Osinsky, S. Gangopadhyay, B. Lim, M. Z. Anwar, and M. Asif Khan, Appl. Phys. Lett. **70**, 2277 (1997).

[130] G. Y. Xu, A. Salvador, W. Kim, Z. Fan, C. Lu, H. Tang, H. Morkoç, G. Smith, M. Estes, B. Goldenberg, W. Yang, and S. Krishnankutty, Appl. Phys. Lett. **71**, 2154 (1997).

[131] A. Osinsky, S. Gangopadhyay, J. W. Yang, R. Gaska, D. Kuksenkov, H. Temkin, I. K. Shmagin, Y. C. Chang, J. F. Muth, and R. M. Kolbas, Appl. Phys. Lett. **72**, 551 (1998).

[132] Y. Yu, Y. Zhang, Z. Zhang, H. Zhang, X. Song, M. Cao, Y. Che, H. Dai, J. Yang, J. Wang, H. Zhang, and J. Yao, J. Phys. Chem. Lett. **8**, 445 (2017).

[133] Y. Che, Y. Zhang, X. Cao, H. Zhang, X. Song, M. Cao, Y. Yu, H. Dai, J. Yang, G. Zhang, and J. Yao, ACS Appl. Mater. Interfaces **9**, 32001 (2017).

[134] H. Zhang, Y. Zhang, X. Song, Y. Yu, M. Cao, Y. Che, Z. Zhang, H. Dai, J. Yang, G. Zhang, and J. Yao, ACS Photonics **4**, 584 (2017).

[135] Y. Yu, Y. Zhang, X. Song, H. Zhang, M. Cao, Y. Che, H. Dai, J. Yang, H. Zhang, and J. Yao, ACS Photonics **4**, 950 (2017).

[136] L. Jin, Y. Zhang, Y. Yu, Z. Chen, Y. Li, M. Cao, Y. Che, and J. Yao, Adv. Opt. Mater. **6**, 1800639 (2018).

[137] Y. Yu, Y. Zhang, X. Song, H. Zhang, M. Cao, Y. Che, H. Dai, J. Yang, H. Zhang, and J. Yao, Adv. Opt. Mater. **5**, 1700565 (2017).

[138] H. Zhang, Y. Zhang, X. Song, Y. Yu, M. Cao, Y. Che, H. Dai, J. Yang, X. Ding, G. Zhang, and J. Yao, Adv. Opt. Mater. **5**, 1600434 (2017).

[139] W. Xu, Y. Shi, F. Ren, D. Zhou, L. Su, Q. Liu, L. Cheng, J. Ye, D. Chen, R. Zhang, Y. Zheng, and H. Lu, Photonics Res. **7**, B48 (2019).

[140] X. Qiu, Z. Wang, X. Hou, X. Yu, and D. Yang, Photonics Res. **7**, 351 (2019).

[141] M. -H. Ji, J. Kim, T. Detchprohm, R. D. Dupuis, A. K. Sood, N. K. Dhar, and J. Lewis, IEEE Photonics Technol. Lett. **28**, 2015 (2016).

[142] Z. G. Shao, D. J. Chen, H. Lu, R. Zhang, D. P. Cao, W. J. Luo, Y. D. Zheng, L. Li, and Z. H. Li, IEEE Electron Device Lett. **35**, 372 (2014).

[143] M. Z. M. Yusoff, A. Mahyuddin, Z. Hassan, H. A. Hassan, M. J. Abdullah, M. Rusop, S. M. Mohammad, and N. M. Ahmed, Mater. Sci. Semicond. Process. **29**, 231 (2015).

[144] A. T. M. G. Sarwar, B. J. May, M. F. Chisholm, G. J. Duscher, and R. C. Myers, Nanoscale **8**, 8024 (2016).

[145] Y. Wu, X. Liu, P. Wang, D. A. Laleyan, K. Sun, Y. Sun, C. Ahn, M. Kira, E. Kioupakis, and Z. Mi, Appl. Phys. Lett. **116**, 013101 (2020).

[146] A. Aiello, Y. Wu, and P. Bhattacharya, Appl. Phys. Lett. **116**, 061104 (2020).

[147] D. Zhu, J. Xu, A. Noemaun, J. Kim, E. Schubert, M. Crawford, and D. Koleske, Appl. Phys. Lett. **94**, 081113 (2009).

[148] K. Lee, P. Parbrook, T. Wang, J. Bai, F. Ranalli, R. Airey, and G. Hill, Phys. Status. Solidi B **247**, 1761 (2010).

[149] M. Massicotte, F. Vialla, P. Schmidt, M. Lundeberg, S. Latini, S. Haastrup, M. Danovich, D. Davydovskaya, K. Watanabe, T. Taniguchi, V. Fal'ko, K. Thygesen, T. Pedersen, and F. Koppens, Nat. Commun. **9**, 1633 (2018).

[150] M. H. Wong and U. K. Mishra, Semicond. Semimetals **102**, 329 (2019).

[151] T. Kikkawa, T. Hosoda, K. Shono, K. Imanishi, Y. Asai, Y. Wu, L. Shen, K. Smith, D. Dunn, S. Chowdhury, P. Smith, J. Gritters, L. McCarthy, R. Barr, R. Lal, U. Mishra, and P. Parikh, 2015 IEEE International Reliability Physics Symposium, Monterey, CA, 6C.1.1 (2015).

[152] Z. Li, J. Waldron, R. Dayal, L. Parsa, M. Hella, and T. P. Chow, 2012 24th Int. Symp. Power Semicond. Devices ICs, Bruges, 45 (2012).

[153] R. Quay, D. Schwantuschke, E. Ture, F. van Raay, C. Friesicke, S. Krause, S. Müller, S. Breuer, B. Godejohann, and P. Brückner, Phys. Status Solidi A **215**, 1700655 (2018).

[154] S. Deshpande, J. Heo, A. Das, and P. Bhattacharya, Nat. Commun. **4**, 1675 (2013).

[155] M. Brubaker, P. T. Blanchard, J. B. Schlager, A. W. Sanders, A. Roshko, S. M. Duff, J. M. Gray, V. M. Bright, N. A. Sanford, and K. A. Bertness, Nano Lett. **13**, 374 (2013).

[156] X. Li, Y. Wang, K. Hane, Z. Shi, and J. Yan, Opt. Commun. **415**, 47 (2018).

[157] X. Li, Y. Jiang, J. Li, Z. Shi, G. Zhu, and Y. Wang, Opt. Laser Technol. **114**, 103 (2019).

[158] T. Kamei, T. Kamikawa, M. Araki, S. P. DenBaars, S. Nakamura, and J. E. Bowers, Phys. Status Solidi A **1900770** (2019).

[159] N. V. Triviño, R. Butté, J. -F. Carlin, and N. Grandjean, Nano Lett. **15**, 1259 (2015).

[160] R. M. C. de Almeida and I. J. R. Baumvol, Phys. Rev. B **62**, R16255 (2000).

[161] M. Khoury, O. Tottereau, G. Feuillet, P. Vennégues, and J. Z.- Pérez, J. Appl. Phys. **122**, 105108 (2017).

[162] A. Dadgar, J. Christen, T. Riemann, S. Richter, J. Bläsing, A. Diez, and A. Krost, Appl. Phys. Lett. **78**, 2211 (2001).

[163] H. Ishikawa, G. -Y. Zhao, N. Nakada, T. Egawa, T. Jimbo, and M. Umeno, Jpn. J. Appl. Phys. **38**, L492 (1999).

[164] B. H. Le, S. Zhao, X. Liu, S. Y. Woo, G. A. Botton, and Z. Mi, Adv. Mater. **28**, 8446 (2016).

[165] K. A. Bertness, A. Roshko, N. A. Sanford, J. M. Barker, and A. V. Davydov, J. Cryst. Growth **287**, 522 (2006).

[166] K. Kishino, K. Nagashima, and K. Yamano, Appl. Phys. Exp. **6**, 012101 (2013).

[167] M. Yoshizawa, A. Kikuchi, M. Mori, N. Fujita, and K. Kishino, Jpn. J. Appl. Phys. **36**, L459 (1997).

[168] M. A. Sanchez-Garcia, E. Calleja, E. Monroy, F. J. Sanchez, F. Calle, E. Muñoz, and R. Beresford, J. Cryst. Growth **183**, 23 (1998).

[169] S. D. Hersee, A. K. Rishinaramangalam, M. N. Fairchild, L. Zhang, and P. Varangis, J. Mater. Res. **26** 2293 (2011).

[170] F. Limbach, T. Gotschke, T. Stoica, R. Calarco, E. Sutter, J. Ciston, R. Cusco, L. Artus, S. Kremling, S. Höfling, L. Worschech, and D. Grützmacher, J. Appl. Phys. **109**, 014309 (2011).

[171] J. Heo, W. Guo, and P. Bhattacharya, Appl. Phys. Lett. **98**, 021110 (2011).

[172] A. Kikuchi, M. Kawai, M. Tada, and K. Kishino, Jpn. J. Appl. Phys **43**, L1524 (2004).

[173] M. D. Brubaker, K. L. Genter, J. C. Weber, B. T. Spann, A. Roshko, P. T. Blanchard, T. E. Harvey, K. A. Bertness, Proc. SPIE **10725**, 1072502 (2018).

[174] A. Hazari, M. Z. Baten, L. Yan, J. M. Millunchick, and P. Bhattacharya, Appl. Phys. Lett. **109**, 191102 (2016).

[175] M. Tchernycheva, A. Messanvi, A. de Luna Bugallo, G. Jacopin, P. Lavenus, L. Rigutti, H. Zhang, Y. Halioua, F. H. Julien, J. Eymery, and C. Durand, Nano Lett. **14**, 3515 (2014).

[176] Y. Wu, Y. Wang, K. Sun, A. Aiello, P. Bhattacharya, and Z. Mi, J. Cryst. Growth **498**, 109 (2018).

[177] P. Dogan, O. Brandt, C. Pfüller, A. -K. Bluhm, L. Geelhaar, H. Riechert, J. Cryst. Growth **323**, 418 (2011).

[178] C. Adelmann, J. Brault, D. Jalabert, P. Gentile, H. Mariette, G. Mula, and B. Daudin, J. Appl. Phys. **91**, 9638 (2002).

[179] Ž. Gačević, A. Das, J. Teubert, Y. Kotsar, P. K. Kandaswamy, Th. Kehagias, T. Koukoula, Ph. Komninou, and E. Monroy, J. Appl. Phys. **109**, 103501 (2011).

[180] B. Damilano, N. Grandjean, S. Dalmasso, and J. Massies, Appl. Phys. Lett. **75**, 3751 (1999).

[181] P. Bhattacharya, K. K. Kamath, J. Singh, D. Klotzkin, J. Phillips, H. -T. Jiang, N. Chervela, T. B. Norris, T. Sosnowski, J. Laskar, and M. R. Murty, IEEE Trans. Electron. Dev. **46**, 871 (1999).

[182] R. Heitz, M. Veit, N. N. Ledentsov, A. Hoffmann, D. Bimberg, V. M. Ustinov, P. S. Kop'ev, and Zh. I. Alferov, Phys. Rev. B **56**, 10435 (1997).

[183] D. Queren, A. Avramescu, G. Brüderl, A. Breidenassel, M. Schillgalies, S. Lutgen, and U. Strauß, Appl. Phys. Lett. **94**, 081119 (2009).

[184] Y. D. Jho, J. S. Yahng, E. Oh, and D. S. Kim, Phys. Rev. B **66**, 035334 (2002).

[185] M. Zhang, P. Bhattacharya, and W. Guo, Appl. Phys. Lett. **97**, 011109 (2010).

[186] Y. C. Shen, G. O. Mueller, S. Watanabe, N. F. Gardner, A. Munkholm, and M. R. Krames, Appl. Phys. Lett. **91**, 141101 (2007).

[187] S. Chouksey, S. Sankaranarayanan, V. Pendem, P. K. Saha, S. Ganguly, and D. Saha, Nano Lett. **17**, 4596 (2017).

[188] Y. Zhang, R. M. Smith, Y. Hou, B. Xu, Y. Gong, J. Bai, and T. Wang, Appl. Phys. Lett. **108**, 031108 (2016).

[189] S. Chouksey, S. Sreenadh, S. Ganguly, and D. Saha, Nanotechnology **30**, 194003 (2019).

[190] M. J. Simpson, J. W. Wilson, F. E. Robles, C. P. Dall, K. Glass, J. D. Simon, and W. S. Warren, J. Phys. Chem. A **118**, 993 (2014).

[191] S. Deshpande, T. Frost, A. Hazari, and P. Bhattacharya, Appl. Phys. Lett. **105**, 141109 (2014).